Terrestrial Paleoclimate of the Cenozoic: Insights from and Developments of the Soil Carbonate Clumped Isotope Thermometer

Julia R Kelson

A dissertation
submitted in partial fulfillment of the
requirements for the degree of

Doctor of Philosophy

University of Washington
2019

Reading Committee:
Katharine Huntington, Chair
Alexis Licht
Ethan Hyland

Program Authorized to Offer Degree:
Department of Earth and Space Sciences

University of Washington

Abstract

Terrestrial Paleoclimate of the Cenozoic:

Insights from and Developments of the Soil Carbonate Clumped Isotope Thermometer

Julia R Kelson

Chair of the supervisory committee:

Dr. Katharine W. Huntington

Earth and Space Science Department

Land temperature at the surface of the Earth is a first-order parameter used to describe climate, but reliable and widespread measurements of this basic parameter through geologic time has eluded geochemists and geologists for decades. The carbonate clumped isotope geothermometer, which uses the bond-ordering of the carbon and oxygen isotopes in a carbonate mineral, is a relatively new tool that can be used to measure surface temperature on geologic timescales. Chapter 1 introduces carbonate clumped isotope geochemistry. In the subsequent four research chapters, this thesis first refines fundamental methodologies, then improves our understanding of the proxy-system by examining modern soil carbonates, and finally applies the thermometer to reconstruct terrestrial paleoclimate in the early Paleogene.

In Chapter 2, I empirically create a clumped isotope-temperature relationship that can be used to estimate the growth temperature of natural carbonates. I rule out the two primary

hypotheses that were proposed to explain discrepancies between existing Δ_{47} -temperature calibrations: 1) synthesis methods caused kinetic isotope effects in calibration samples, and/or 2) the temperature of the acid which was used to digest the calcite for analysis created an analytical artifact. I precipitated >56 synthetic calcite samples at known temperatures, replicating the methodologies used by previously published discrepant calibrations. I analyzed the samples by digesting the calcite at both 90 °C and 25 °C. My results showed that the temperature-Δ_{47} relationship does not vary with precipitation method or acid digestion temperature. Instead, I suggest that the previously observed variations in empirical calibrations were largely due to poor sample replication and small number statistics. I also show the importance of using appropriate constants in the calculation of Δ_{47} to correct for the mass interference between ^{13}C and ^{17}O during mass spectrometry (as described in companion paper, Schauer, Kelson et al., 2016). Through this research, I produced a new and robust empirical calibration that can be used to calculate growth temperatures from natural calcite materials.

Chapter 3 investigates the seasonal bias in soil carbonates by re-examining in aggregate the published Δ_{47} -temperature data from >200 Holocene soil carbonate samples. In this synthesis, I re-calculate and update Δ_{47} values to reflect modern standards in methodology. The updated data confirm the general assumption that most soil carbonates have a Δ_{47} temperature that is warm-season biased. However, importantly, I show that modern soil carbonates have Δ_{47}-temperatures that differ from mean annual air temperatures by -5 to 24 °C. The variation in the magnitude of seasonal bias can be partially explained by differences in the annual timing of rain/snow, the texture of the host soil matrix, and vegetative cover. This variation in seasonal bias has profound implications for using soil carbonate Δ_{47} in paleoclimate applications and underscores the need for a process-based understanding of soil carbonate formation.

Chapter 4 builds an understanding of soil carbonate formation that is based in soil physics and chemistry by numerically predicting the timing of calcite growth in a 1D soil profile. Using a software package called HYDRUS-1D (Šimůnek et al., 2009), I calculate soil water content, soil temperatures, soil CO_2 productions and concentrations, and carbonate chemistry. I show that the timing of large rain events controls the timing of carbonate accumulation in a soil profile. During storms, soil respiration increases, which increases soil CO_2 and dissolves soil carbonate. The subsequent re-precipitation of soil carbonate as soil CO_2 decreases post-storm makes up the majority of the total preserved soil carbonate. This result undermines the existing assumption that soil carbonates form slowly during evaporation during dry periods. I show that soil texture and the timing and character of rainfall will control the seasonal bias recorded by soil carbonates. This process-based understanding of soil carbonate formation will enable more nuanced and accurate interpretations of paleo-temperatures and meteoric waters.

Chapter 5 uses the clumped isotope composition of fossilized soil carbonates collected in the Tornillo Basin of Big Bend National Park, Texas (30°N) to investigate the greenhouse climate of the Paleocene and early Eocene. I first use a combination of textural evidence and thermal modeling to identify that the isotopic signatures of the soil carbonates collected reflect primary environmental signals. The clumped isotope temperature record derived from these carbonates show an increase from 25 ± 4 to 32 ± 2 °C from the Paleocene to the Eocene, respectively, and a corresponding increase in calculated $\delta^{18}O$ of soil waters. These temperatures are lower than the temperatures predicted by global circulation models given the high pCO_2 conditions and the subtropical location; they are also similar to modern summer temperatures. These results may suggest habitable, near-coast environments persisted even during the peak-CO_2 conditions of the early Cenozoic.

In conclusion, this thesis expands the ability to reconstruct terrestrial paleoclimates with carbonate clumped isotope thermometry and highlights future challenges. Applications of clumped isotope thermometry are no longer limited by analytical precision in most settings. Instead, robust paleoclimate reconstructions hinge upon accurate characterizations of the seasonal bias of the proxy and diagenetic alteration. A more complete understanding of the evolution of Cenozoic climate on land awaits further analyses from stratigraphic sections that are spatially diverse and temporally overlapping.

Table of Contents

List of Figures

List of Tables

Acknowledgements

My time at the University of Washington was enjoyable and productive largely due to the support from a broad community of faculty and graduate students. First, I would like to recognize the immense support and guidance that my advisor, Kate Huntington, has offered throughout graduate school. Kate gently steered me towards productive research directions but also allowed me to explore numerous tangents. She taught me that how to write and re-write. I admire her ability to identify clear research questions and herding the collaborators to make it happen. Thank you, Kate.

I am also grateful to the members of my committee: Alex Gagnon, Ethan Hyland, Alexis Licht, Casey Saenger, and Eric Steig. Thanks to Alex Gagnon for surpassing involvement expectations for a Graduate School Representative by truly engaging in the material of the thesis and for suggesting the use of carbonic anhydrase. Thanks to Ethan Hyland for initially pointing out that Eocene paleoclimate is interesting, then encouraging me to pursue that avenue of research and providing field expertise. Thanks to Alexis for always having an idea or three, to Casey for providing advice and scientific feedback, and to Eric Steig for providing the diverse viewpoint as the only non-clumper on my committee.

I would also like to acknowledge Andrew Schauer, the manager of IsoLab, for not only teaching me everything about mass spectrometry and gas purification, but also for contributing to the science and research. Andy provided endless creativity and enthusiasm for solving both technical and research problems.

The graduate students at UW made this experience enjoyable. Thanks to fellow Supergroupers: Sarah Schanz, Sarah Harbert, Camille Collett, Landon Burgener, Sean Lahusen, Cassie Brigham, Megan Mueller, Philip Schoettle-Greene, Mike Turzewski, Susannah Morey,

Keith Hodson and Max Needle – you all provided an intellectual community that was both inquisitive and supportive. Special thanks to friends who constantly reminded me that life is about having fun and building strong friendships: Max, Shelley, Kelley, Emma, Todd, Anabelle. Thanks to David Lilien for cooking me dinner most nights, teaching me that I can climb mountains, and for being there for me always.

Thanks to my incredibly supportive family: Mom, Dad, Suzanne and Kyle. You encouraged me to take advantage of every educational opportunity and you have been excellent role models as curious and caring scientists.

Chapter 1 Introduction

1.1 Motivation

Knowledge of how ancient climates and atmospheres changed in the past is crucial to contextualize present climate change. In particular, information about temperature at the Earth's surface through geologic time can provide the opportunity to test our understanding of climate physics (Braconnot et al., 2012; Eagle et al., 2013b; Huber, 2008; Huber and Caballero, 2011; Lunt et al., 2013, 2017; Pagani et al., 2006; Sewall and Sloan, 2006; Sloan and Barron, 1990), including the sensitivity of the Earth system to greenhouse gases (Fischer et al., 2018; Rohling et al., 2012; von der Heydt et al., 2016; Zeebe, 2011). Understanding temperature on land is particularly interesting given that environments on land are more sensitive to carbon cycle perturbations than the ocean (Diffenbaugh and Field, 2013; Harrison et al., 2015). Additionally, land surface temperatures can provide important context for understanding biotic evolution through geologic time (Burgener et al., 2019; Jaramillo et al., 2006; Mulch, 2016; Passey et al., 2010; Tobin et al., 2014; Wing et al., 2005) as well as paleoaltimetry estimates needed to test tectonic models of orogenesis (Ehlers and Poulsen, 2009; Fan et al., 2014; Garzione et al., 2008, 2014; Ghosh et al., 2006b; Huntington et al., 2010, 2015; Huntington and Lechler, 2015; Lechler et al., 2013; Mix et al., 2016; Snell et al., 2014).

For many decades, land surface temperatures have been investigated through semi-quantitative estimates of temperature and environmental conditions, such as leaf shapes and sizes (Bailey and Sinnott, 1915; Meyer, 1992; Peppe et al., 2011; Wing and Greenwood, 1993; Wolfe, 1995), soil textures and major elemental compositions (Gallagher and Sheldon, 2013; Retallack,

2007; Sheldon et al., 2002; Sheldon and Tabor, 2009; Stinchcomb et al., 2016), and/or traditional carbon and oxygen stable isotopes ($\delta^{13}C$ and $\delta^{18}O$) of carbonate materials (Cerling, 1984; McCrea, 1950). These methods have led to exciting discoveries and hypotheses about terrestrial climate in the Cenozoic like the existence of hyperthermals, the puzzle of the equable Eocene, and the transition from greenhouse to icehouse environments (seminal works include MacGinitie, 1953; Greenwood and Wing, 1995; Koch et al., 1995; Markwick, 1998; Sheldon et al., 2002; Wing et al., 2005, and others that are too numerous to exhaustively cite). However, these terrestrial climate and ecosystem reconstructions are placed into a global and geologic context through comparison to the quantitative estimates of ocean temperatures derived from the $\delta^{18}O$ of foraminifera (Zachos et al., 2008, 2001). The absence of a reliable and widespread method to quantitatively estimate Earth surface temperatures on land has led to a perspective of Cenozoic temperature evolution that is dominated by an oceanographic lens, hampering our ability to fully understand the climate system (Finnegan et al., 2011; Huber and Caballero, 2011; Mulch et al., 2008).

Initial measurements of clumped isotopes in carbonates the mid-2000s promised to fulfill this demand for quantitative estimates of terrestrial Earth surface temperatures (Came et al., 2007; Eiler, 2007; Ghosh et al., 2006a). Clumped isotope thermometry provides a thermodynamically-based estimate of the growth temperature of a mineral. The term 'clumped isotopes' refers to the co-existence of two rare heavy isotopes in a single molecule – or, if the reader prefers a mouthful – a 'doubly substituted isotopologue'. This double substitution of heavy isotopes is energetically favorable due to the slight increase in bond strengths (reduction in vibrational energy) with the increased mass in the molecule. Clumping is increasingly energetically favorable at low temperatures, while at high temperatures the heavy isotopes are

randomly distributed (Affek, 2012; Guo et al., 2009; Schauble et al., 2006; Wang et al., 2004). In a carbonate mineral, the relevant isotopes are carbon (^{12}C vs ^{13}C) and oxygen (^{16}O vs ^{18}O). Measuring the clumped isotope composition of a solid carbonate mineral first requires that the mineral is digested in acid; the resulting CO_2 gas is analyzed on a mass spectrometer. Thus, the Δ_{47} notation refers to the atomic mass of the analytical target (^{13}C-^{18}O-^{16}O). The Δ_{47} value is calculated as the anomaly from the stochastic distribution of heavy isotopes (Huntington et al., 2009). This thermometer is extremely useful because it does not require knowledge of the isotopic composition of the source fluid (as in traditional $\delta^{18}O$ thermometry). Also, because it is based on thermodynamics, in principle its calibration can be extrapolated beyond specific organisms or interlaboratory effects (Eiler, 2011). Furthermore, carbonate minerals are common in the geologic record and appear to have Δ_{47} compositions that form in near-equilibrium and thus reflect near-surface temperatures, including soil carbonates (Quade et al., 2007a, 2011), tufa (Kele et al., 2015), limestones (Huntington et al., 2010), and some fossil shells (Came et al., 2014; Henkes et al., 2013; Peral et al., 2018; Zaarur et al., 2011).

However, as with all proxies, the clumped isotope thermometer required significant refinement before it could be widely adopted. Its usefulness was limited by disagreement about the empirically-estimated temperature sensitivity (Dennis and Schrag, 2010; Eiler, 2011; Fernandez et al., 2014; Henkes et al., 2013; Petrizzo et al., 2014; Wacker et al., 2014; Zaarur et al., 2013), the specter of kinetic or pH effects during carbonate precipitation (Daëron et al., 2011; Hill et al., 2014; Saenger et al., 2012; Spooner et al., 2016; Tang et al., 2014; Tripati et al., 2015; Watkins and Hunt, 2015), and a myriad of analytical challenges stemming from the need for low precision to detect the small Δ_{47} signal (~ 20 ppm) (Daëron et al., 2016; Defliese et al., 2015; Dennis et al., 2011; He et al., 2012; e.g., Huntington et al., 2009; Petersen et al., 2015; Petrizzo

and Young, 2014; Schauer et al., 2016; Wacker et al., 2013; Yeung et al., 2018). Furthermore, the development of this new proxy generated a need to understand the formation processes of natural carbonate minerals in the modern. In particular, one emerging research goal is to understand how and when soil carbonates form, and by extension, how to interpret the stable oxygen, carbon, and clumped isotope composition of soil carbonates (Burgener et al., 2016, 2018; Gallagher and Sheldon, 2016; Hough et al., 2014; Huth et al., 2019; Oerter and Amundson, 2016; Peters et al., 2013; Quade et al., 2011; Ringham et al., 2016). Despite these initial challenges in carbonate clumped isotope thermometry, Δ_{47} analyses of ancient soil carbonates (and other carbonate materials) have already begun to answer longstanding questions about terrestrial Cenozoic climate, including the high-CO_2 climate regimes addressed in this thesis (Burgener et al., 2019; Csank et al., 2011; Hyland et al., 2018; Kelson et al., 2018; Lechler et al., 2018; Licht et al., 2017; Methner et al., 2016; Page et al., 2019; Passey et al., 2010; Snell et al., 2013; Tobin et al., 2014; VanDeVelde et al., 2013). This thesis develops fundamentals of clumped isotope geochemistry, explores the soil-carbonate proxy system, and applies these tools to understand high-CO_2 climates on land during the early Paleogene.

1.2 Thesis Organization

The remaining four chapters of this dissertation are organized to mimic the arc of the development of a novel proxy: I start with fundamental methods development, move to research on the soil carbonate proxy system, and finally use the clumped isotope composition of soil carbonates to explore terrestrial climate during the Paleogene. Two of the chapters have been previously published in peer-reviewed journals; those articles are included as-published in this dissertation (save formatting).

In Chapter 2, I progress the clumped isotope geothermometer towards a universal, empirical calibration by synthesizing >56 synthetic carbonate samples at known temperatures. I show that a temperature-Δ_{47} relationship is not sensitive to various carbonate synthesis methods or to acid digestion temperature. I also demonstrate the appropriate ^{17}O correction parameters should be used when calculating Δ_{47}. This work was published in *Geochimica et Cosmochimica Acta* (Kelson et al., 2017).

Next, I address how to accurately interpret the clumped isotope composition of natural, pedogenic carbonates. In Chapter 3, I combine previously published clumped isotope measurements of Holocene soil carbonates (about 200) and provide additional environmental constraints (seasonality of rain/snow, soil grain size, and land cover). While most soil carbonates appear to have isotopic compositions that are warm-season biased, the magnitude of this bias is variable. I show that some of the variation in observed seasonal biases can be explained through seasonal timing of hydrology and/or soil grain size. This chapter will be submitted to *Quaternary Science Reviews*.

In Chapter 4, I promote a process-based understanding of soil carbonate formation with numerical modeling, building upon hypotheses developed through empirical observations in Chapter 3. I use HYDRUS-1D, a free open-source software package, to calculate physical and chemical parameters in a soil profile. I test the hypothesis that the annual timing of soil carbonate formation is sensitive to changes in soil moisture. I show the importance of soil texture and rainfall patterns in controlling soil moisture and soil carbonate formation. I plan to submit a manuscript based on the work in this chapter to *Earth and Planetary Science Letters*.

In Chapter 5, I apply the improved calibrations of the clumped isotope thermometer and an understanding of the formation processes of soil carbonates to investigate past climate using

fossilized soils from the Tornillo Basin, Texas, USA (30 °N). I analyze soil carbonates with primary isotopic compositions (i.e., not diagenetically altered) that are from the late Paleocene to early Eocene. I estimate relatively mild summertime temperatures during this hothouse, high-CO_2 climate and show a shift in surface temperatures that is approximately contemporaneous with changing hydrologic conditions and an increase in atmospheric CO_2 concentrations. This chapter was published in *Paleoceanography and Paleoclimatology* in a Special Section *Climatic and Biotic Events of the Paleogene: Earth Systems and Planetary Boundaries in a Greenhouse World* (Kelson et al., 2018).

I conclude with reflections on the state of using clumped isotope geochemistry to reconstruct terrestrial paleoclimates. Supplementary materials for the four research chapters are included as Appendices A-D. Additional large spreadsheets are included in Excel format.

Chapter 2 Toward a Universal Carbonate Clumped Isotope Calibration: Diverse Synthesis and Preparatory Methods Suggest a Single Temperature Relationship

Abstract. Carbonate clumped isotope (Δ_{47}) thermometry has been applied to a wide range of problems in earth, ocean and biological sciences over the last decade, but is still plagued by discrepancies among empirical calibrations that show a range of Δ_{47}-temperature sensitivities. The most commonly suggested causes of these discrepancies are the method of mineral precipitation and analytical differences, including the temperature of phosphoric acid used to digest carbonates. However, these mechanisms have yet to be tested in a consistent analytical setting, which makes it difficult to isolate the cause(s) of discrepancies and to evaluate which synthetic calibration is most appropriate for natural samples. Here, we systematically explore the impact of synthetic carbonate precipitation by replicating precipitation experiments of previous workers under a constant analytical setting. We (1) precipitate 56 synthetic carbonates at temperatures of 4-85 ºC using different procedures to degas CO_2, with and without the use of the enzyme carbonic anhydrase (CA) to promote rapid dissolved inorganic carbon (DIC) equilibration; (2) digest samples in phosphoric acid at both 90 °C and 25 °C; and (3) hold constant all analytical methods including acid preparation, CO_2 purification, and mass spectrometry; and (4) reduce our data with ^{17}O corrections that are appropriate for our samples. We find that the CO_2 degassing method does not influence Δ_{47} values of these synthetic carbonates, and therefore probably only influences natural samples with very rapid degassing rates, like speleothems that precipitate out of drip solution with high pCO_2. CA in solution does not influence Δ_{47} values in this work, suggesting that disequilibrium in the DIC pool is negligible. We also find the Δ_{47} values of samples reacted in 25 and 90 °C acid are within error of each other (once corrected with a constant acid fractionation factor). Taken together, our

results show that the Δ_{47}-temperature relationship does not measurably change with either the precipitation methods used in this study or acid digestion temperature. This leaves phosphoric acid preparation, CO_2 gas purification, and/or data reduction methods as the possible sources of the discrepancy among published calibrations. In particular, the use of appropriate ^{17}O corrections has the potential to reduce disagreement among calibrations. Our study nearly doubles the available synthetic carbonate calibration data for Δ_{47} thermometry (adding 56 samples to the 74 previously published samples). This large population size creates a robust calibration that enables us to examine the potential for calibration slope aliasing due to small sample size. The similarity of Δ_{47} values among carbonates precipitated under such diverse conditions suggests that many natural samples grown at 4 - 85 °C in moderate pH conditions (6-10) may also be described by our Δ_{47}-temperature relationship.

2.1 Introduction

Carbonate clumped isotope (Δ_{47}) thermometry is applied to an increasing range of natural systems, contributing to discoveries in areas such as paleoclimate, paleoaltimetry, and basinal fluid migration (Affek, 2012; Eiler, 2007, 2011; Eiler et al., 2013, 2014; Huntington and Lechler, 2015). Δ_{47} thermometry estimates mineral growth temperature using the thermodynamic tendency for ^{13}C and ^{18}O to bond in carbonate molecules at lower temperatures (e.g., Schauble et al., 2006). The Δ_{47} value of CO_2, derived from phosphoric acid digestion of carbonate minerals, measures the abundance of ^{13}C and ^{18}O in the same molecule in excess of what would occur by random chance (Ghosh et al., 2006a; Schauble et al., 2006). The temperature dependence of ^{13}C-^{18}O clumping in carbonates has been studied from a theoretical perspective (Schauble et al., 2006; Guo et al., 2009; Passey and Henkes 2012, Hill et al., 2014; Tripati et al., 2015). However,

given the as of yet imperfect knowledge of carbonate precipitation processes, acid fractionation effects, and analytical artifacts, accurate empirical Δ_{47}-temperature calibrations are necessary to apply the thermometer with confidence. Many empirical calibrations have been published based on analyses of carbonates with known growth temperatures, including synthetic carbonates (Daëron et al., 2011; Defliese et al., 2015; Dennis and Schrag, 2010; Fernandez et al., 2014; Ghosh et al., 2006a; Kluge et al., 2015; Passey and Henkes, 2012; Tang et al., 2014; Tripati et al., 2015; Zaarur et al., 2013) and natural biogenic and abiogenic carbonates (Ghosh et al., 2007; Eagle et al., 2010; Tripati et al., 2010; Thiagarajan et al., 2011; Saenger et al., 2012; Henkes et al., 2013; Grauel et al., 2013; Eagle et al., 2013; Came et al., 2014; Wacker et al., 2014; Petrizzo et al., 2014; Kele et al., 2015; Tripati et al., 2015; Eagle et al., 2015).

Despite the extensive body of research on calibrating the Δ_{47} thermometer, unresolved discrepancies of up to 10-15 °C exist among published empirical calibrations (Table 2-2). The first two published synthetic calcite calibrations differ in their temperature sensitivity: Ghosh et al. (2006) report a steep Δ_{47}-temperature slope ($m= 0.0636 \times 10^6/T^2$), while Dennis and Schrag (2010) report a relatively shallower slope ($m = 0.0362 \times 10^6/T^2$) (both slopes as reported in the absolute reference frame in Dennis et al., (2011)). More recent calibrations have slopes that fall between these two end-members, such that a spectrum of temperature sensitivities has been published (Table 2-2). These discrepancies in slope and resulting temperature estimates are large enough to significantly change interpretations of Δ_{47} measured in natural samples. Yet it is unclear if these calibrations disagree because of true differences in the Δ_{47} values of carbonates synthesized or because of differences in laboratory analysis methods.

Previous workers have suggested that calibrations diverge because different carbonate precipitation methods cause calibration samples to have Δ_{47} values that reflect variables other

than growth temperature (e.g. Dennis and Schrag, 2010; Dennis et al., 2011; Henkes et al., 2013; Zaarur et al., 2013; Fernandez et al., 2014; Tang et al., 2014). Most notably, opposing views have been expressed about which method of CO_2 degassing during synthetic calcite growth (passive degassing or active degassing with N_2, sensu Kim and O'Neil (1997) and Dennis and Schrag (2010)) favors clumped isotope disequilibrium (Affek and Zaarur, 2014; cf. Fernandez et al., 2014). Recent publications have shown that Δ_{47} values can also be influenced by growth rate, pH, and DIC disequilibrium (Hill et al., 2014; Tang et al., 2014; Tripati et al., 2015; Watkins and Hunt, 2015).

However, the influence of carbonate precipitation methods used by previous workers to create empirical Δ_{47}-temperature calibrations remains to be systematically evaluated in a single analytical setting, making it difficult to determine if calibration discrepancies arise due to differences in carbonate precipitation techniques or analysis techniques. Differences in analysis methods that could cause calibrations to diverge could occur at multiple steps in the sample preparation and measurement process including: digestion of the carbonate sample to produce CO_2 gas for analysis (e.g., Wacker et al., 2013; Fernandez et al., 2014; Came et al., 2014; Wacker et al., 2014; Petrizzo et al., 2014; Defliese et al., 2015), sample gas purification, data processing and absolute reference frame construction (Dennis et al., 2011; Daëron et al., 2016; Olack and Colman, 2016; Schauer et al., 2016), or background measurements (He et al., 2012; Bernasconi et al., 2013; Fiebig et al., 2016).

Here, we systematically explore the influence of carbonate precipitation methods on Δ_{47} values. We precipitate carbonate at known temperatures using various methods, including the methods used in previously published synthetic carbonate clumped isotope calibrations over the temperature range 4-85 °C. We then digest samples in phosphoric acid at both 90 °C and 25 °C,

but control for other preparatory and analytical variables by purifying and measuring the resulting CO_2 using identical procedures. Our results support previous findings that rule out acid digestion temperature as the cause of the calibration discrepancies (Defliese et al., 2015). Most importantly, our large dataset (56 samples; 200 individual sample analyses bracketed by extensive equilibrated CO_2 and carbonate standard measurements) shows that synthetic carbonate precipitation methods are unlikely to be responsible for previous calibration discrepancies. Furthermore, we define a robust Δ_{47}-temperature calibration that is appropriate for estimating temperature from natural, abiogenic carbonates precipitated via a variety of pathways. Our findings point toward specific analytical and data correction methods that contribute to discrepancies among previous calibrations, including ^{17}O corrections (Daëron et al., 2016; Olack and Colman, 2016; Schauer et al., 2016). Normalizing these methods across laboratories will be required to decrease dispersion among calibration data and correctly interpret Δ_{47} data across the broad range of research questions to which they are applied.

2.2 Materials and Methods

We investigate how precipitation methods can influence Δ_{47} values by replicating techniques used in previous synthetic carbonate Δ_{47} calibration studies at temperatures <100 °C. We conduct experiments with and without the use of a bovine enzyme carbonic anhydrase (CA); measure solution pH and isotopic composition at the start and end of each experiment; confirm sample mineralogy with XRD; measure mineral grain size with microprobe imaging; measure carbonate isotopic composition; and evaluate the fractionation that occurs during phosphoric acid reactions at 25 and 90 °C. All analytical, reference frame, and data reduction methods except the

acid digestion procedure were held constant to facilitate direct comparison of carbonate precipitation methods.

2.2.1 Carbonate Precipitation Methods

We grew carbonates at known temperatures of 4-85 °C using precipitation methods chosen to replicate the previous calibration studies of Dennis and Schrag (2010), Zaarur et al. (2013), Ghosh et al., (2006), and Kim and O'Neil (1997) in a consistent analytical setting. We assume that by replicating the methods used in these previous studies we replicate to the extent possible the conditions that control kinetics of DIC equilibration and carbonate precipitation. In addition to replicating these previously published experiments, we conducted additional experiments to isolate the effects of specific variables (e.g., concentration of salts, and catalyzing DIC equilibration).

In all experiments, solutions were placed in an Erlenmeyer flask and allowed to thermally equilibrate in a temperature-controlled oil bath or refrigerator. The temperature was continuously logged with a thermocouple (Campbell Scientific data logger CR10X with thermocouple type T or an Onset Hobo U-Series data logger with a TMC1-HD temperature sensor, manufacturer's accuracy of ±0.5 °C). The thermocouples were calibrated to the freezing and boiling points of water. The standard deviation of hot plate temperature was ± 0.7 °C, while that of the refrigerators (4 and 8 °C experiments) was ± 0.2 °C.

Synthetic calcium carbonates were precipitated (1) by combining $NaHCO_3$ and $CaCl_2$ in solution (e.g. Kim and O'Neil, 1997; Dennis and Schrag, 2010) or (2) by dissolving $CaCO_3$ in water whose pH had been lowered by CO_2 bubbling, and then filtering out un-dissolved crystals (e.g., Kim and O'Neil, 1997; and Zaarur et al., 2013). The $NaHCO_3$ used in the experiments had a $\delta^{13}C$ value of -3.3 ‰ (VPDB, measured using a Kiel III carbonate device coupled to a

Finnegan DeltaPlus Isotope Ratio Mass Spectrometer). The CO_2 gas that was bubbled through the experimental solutions had a $\delta^{13}C$ value of -36.5 ‰ (VPDB). CO_2 was removed from solution, which increased its pH and saturation state, causing carbonate to precipitate. CO_2 was removed either actively by bubbling N_2 through solutions (e.g., Ghosh et al., 2006; Zaarur et al., 2013), or passively by allowing CO_2 to degas into the atmosphere (e.g., Dennis and Schrag, 2010; Affek and Zaarur, 2014). As in previous studies, the solution was not stored before degassing was initiated in any of the methods (i.e., no DIC equilibration time allowed prior to degassing).

Experiments were allowed to proceed until enough material for Δ_{47} analysis precipitated; about one week for higher temperature samples and up to six weeks for lower temperature samples. All sample types were collected with a rubber spatula and were vacuum filtered from solution (Whatman #40 8 µm filter paper). The samples were freeze-dried overnight prior to acid digestion, purification and analysis. Table 2-1 provides the names and a detailed comparison of the precipitation methods used in this work.

In two of the filtered crystal method experiments (Table 2-1), we observed thin films of carbonate floating on the air-water interface. Previous experiments that did not stir the solution (unlike our filtered crystal experiments, which were stirred gently with N_2 bubbles) also observed floating carbonates, and because of their morphology, called them rafts (Affek and Zaarur, 2014). These rafts likely formed when they experienced rapid CO_2 degassing at the surface (Affek and Zaarur, 2014). We collected the raft morphology material and analyzed it separately from other precipitate material.

In several experiments, we added the enzyme CA before the addition of salts in order to promote isotopic equilibrium among the DIC species (Table A-1). Uchikawa and Zeebe (2012)

found that at 25 °C and pH of 8.3, CA reduces the time it takes DIC species reach isotopic equilibrium from ~600 minutes to less than 200 minutes. CA has previously been used in carbonate synthesis experiments (Tripati et al., 2015; Watkins et al., 2014, 2013). CA is most active at 60 °C, and fully inactive above 80 °C (DeLuca et al., 2013). We determined that the CA was working in our experimental conditions by measuring the isotopic composition of CO_2 gas as it equilibrated at room temperature with a solution identical to our precipitation solution. CO_2 gas approached oxygen isotopic equilibrium faster when CA was in solution (equilibration rate of 0.45 ‰/minute with CA, as opposed to a rate of 0.30 ‰/minute) (Figure A-1).

We also analyzed an eggshell from a domestic chicken. We use the body temperature of a chicken (42 °C, Randall and Hiestand, 1939) to represent the growth temperature of the shell material (Wacker et al., 2014; Eagle et al., 2015).

2.2.2 Mineralogy and grain size analytical methods

Samples were analyzed for their mineralogy using a Bruker F8 Focus Powder X-Ray Diffractometer at the Materials Sciences Department at the University of Washington. The spectral signatures were analyzed using JADE™ software and mineral database. Grain size of select calcite samples was measured using imagery of the samples as described by Tobin et al. (2011). The images were taken with a JEOL 733 electron microprobe using secondary and backscattered electron signals (Figure A-3). The 50^{th} percentile (d50) grain size is considered the representative grain size.

2.2.3 Stable isotope analytical methods

2.2.3.1 Measurements of $\delta^{18}O$ and pH of solution

The solution from which the calcium carbonates precipitated was sampled for water $\delta^{18}O$ and pH measurements at the start and end of each experiment. pH was measured using a Mettler Toledo FG2 FiveGo Portable pH meter (pH accuracy quoted by the manufacturer of ±0.01). Water $\delta^{18}O$ was measured at the University of Washington IsoLab using a Picarro L2120i wavelength-scanned cavity ring-down spectrometer (Gupta et al., 2009). Water samples were referenced to the VSMOW scale using two bracketing internal reference waters that were measured against VSMOW and SLAP using GISP as a quality control reference.

2.2.3.2 Measurements of Δ_{47}, $\delta^{18}O$, and $\delta^{13}C$ of calcium carbonates

Clumped, carbon, and oxygen isotopic compositions of the calcium carbonate samples were measured at the University of Washington IsoLab. The details of the automated vacuum line and sample purification methods used in IsoLab are described in Burgener et al. (2016). In this work, 6-9 mg of sample were reacted for 10 minutes in a common bath of 90 °C phosphoric acid with a starting specific gravity of 1.904 - 1.970 g/cm^3 (multiple batches of acid were used throughout the course of this work). Some samples were also reacted overnight at 25 °C in McCrea-type reaction vessels (McCrea, 1950) with 1.5-2 mL of the same phosphoric acid.

A solid calcium carbonate reference material was run for every ~4 sample unknowns including: NBS19, three in-house calcites with disparate bulk compositions (C64 and C2, both reagent-grade; and Coral, a tropical *Porites* coral sample). C64 was also reacted in 25 °C phosphoric acid and purified then analyzed with the samples reacted at 25 °C. Apart from monitoring Δ_{47}, standards C64, C2, and Coral were used to place all $\delta^{13}C$ and $\delta^{18}O$ values on the VPDB scale (see data reduction code in Schauer et al., 2016). These three materials have been

calibrated to NBS19, LSVEC, and NBS18 using a Kiel III Carbonate device coupled to Finnegan DeltaPlus Isotope Ratio Mass Spectrometer. The values of our calcium carbonate standards can be found in the Tables S2, S4, S6, and S7.

Purified CO_2 break seals were placed on an automated 10-port tube cracker inlet system on a Thermo MAT 253 configured to measure *m/z* 44-49 inclusive. To start each sample analysis, sample and reference gas bellows were fully expanded and evacuated. Sample gas was filled into the sample bellows and pressure was measured. Reference gas bellows were automatically filled to a pressure equal to the sample bellows pressure (this is done by modifying the sample introduction and reference refill scripts as described in Schauer et al., 2016). The CO_2 reference gas is from a corn fermentation plant ($\delta^{13}C$ -10.2 ‰, $\delta^{18}O$ -6.0 ‰, versus NBS-19). Sample and reference signals were balanced on *m/z* 47 to a signal of 2.55 V from installation of the MAT 253 until April 2015 (as recommended by Thermo because of irreconcilable noise issues). After April 2015 Thermo installed a newly designed amplifier power supply and we began pressure balancing on *m/z* 44 to a signal of 16 V (approximately 2.55 V on *m/z* 47). Pressure base line (PBL) was automatically measured while CO_2 is flowing at 80 V left of peak center before each sample measurement (similar to He et al., 2012; code in Schauer et al., 2016). Our background measurement is used instead of the default IsoDat background, and all V signals (44-49) are corrected for the background before they are output (code in Schauer et al., 2016). Sample CO_2 *m/z* 44-49 were measured against reference CO_2 for 6 acquisitions of 10 sample-reference comparisons cycles with 26-second integration times, for a total of 1560 seconds of counting. Standard amplifications were used for m/z 44-46 ($3x10^8$, $3x10^{10}$, $1x10^{11}$ Ω, respectively); *m/z* 47-49 were measured with $1x10^{12}$ Ω amplification. After the 6 sample-

reference comparison cycles, water backgrounds were measured by peak centering on *m/z* 18 of both sample and reference.

Δ_{47} was calculated using previously established methods (Eiler and Schauble, 2004; Affek and Eiler, 2006; Huntington et al., 2009; Dennis et al., 2011), with the exception of ^{17}O abundance correction values. The λ (0.528) and K (0.01022461) values recommended by Brand et al. (2010) were used to correct for ^{17}O interference in $\delta^{13}C$ measurements made with a mass spectrometer (Daëron et al., 2016; Schauer et al., 2016). Traditionally, the ^{17}O parameters that are used to calculate Δ_{47} values come from Huntington et al. (2009), which are indistinguishable from those of Santrock et al. (1985). The Brand et al. (2010) values are likely more appropriate than the Santrock et al. (1985) values for most natural and synthetic samples because they are based on measurements of meteoric water, rather than meteorites (Schauer et al., 2016). Additionally, using the Brand et al. (2010) parameters minimizes an apparent dependency of Δ_{47} on $\delta^{13}C$, as described in Schauer et al. (2016). Δ_{47} values are corrected for their dependence on δ_{47} with the slope of the reference frame gases, then projected into the absolute reference frame (ARF) (Dennis et al., 2011). Our reference frame gases are made by heating CO_2 in a quartz break seal to 1000 °C, or by equilibrating CO_2 with water of various isotopic compositions at 4 and 60 °C in a Pyrex break seal (Tables S1, S3, and S5). The heated and equilibrated gases were purified using the same vacuum line and method as the carbonate-derived CO_2 samples, and were measured regularly throughout the period of analysis.

Samples that were reacted at 90 °C are presented without an acid fractionation factor (AFF) (i.e., they are presented in the '90 °C reference frame'). When projecting samples into the 25 °C reference frame for comparison purposes in this paper, we used an AFF of 0.082 ‰ (Defliese et al., 2015). The Defliese et al. (2015) AFF is within error of the value we calculate

based on a smaller dataset from this study, but we choose to use the more robust Defliese et al. (2015) AFF because their value is based on a large number of replicates of many samples with diverse compositions reacted at different temperatures.

The data span three distinct reference frames, each continually constructed with reference gases during the analysis period. The break between the first and second reference frames was established because the stainless steel tubing of the cryogenic traps was replaced with nickel tubing to reduce water contamination in the vacuum line. The break between the second and third reference frames was established in April 2015 because we started to pressure balance on *m/z* 44 instead of *m/z* 47. The Δ_{47} values of the calcium carbonate standards measured in these three reference frames are indistinguishable within measurement error (Tables S2, S4, S6).

Peirce's criterion was used to identify and remove data outliers (Ross, 2003; Zaarur et al., 2013); 7 out of 207 total analyses were removed. The average Δ_{47} internal mass spectrometer uncertainty is ~0.008 ‰, and the total internal uncertainty due to both the mass spectrometer and the projection into the reference frame for each replicate is 0.012 ‰ on average (code in Schauer et al., 2016). External reproducibility, which we calculate as the standard deviation of replicates, is usually larger (~0.015 ‰), so we report that larger uncertainty. The final uncertainty that we report for samples is the standard error, calculated as the larger value between 1) the standard deviation of all C64 replicates for the relevant reference frame divided by the square root of the number of sample replicates, or 2) the standard deviation of the sample replicates divided by the square root of the number of sample replicates. We use C64 to represent error because it is the laboratory standard that was analyzed most regularly and is a homogenous material that allows us to monitor long-term errors of our methods.

An ordinary least squares regression is used to calculate linear regressions. A model II regression that considers the errors in both the predictor and response variables (i.e., York et al., 2004) is not needed because the error in our solution temperature measurements is relatively small (Wacker et al., 2014).

2.3 Results

2.3.1 Solution chemistry, mineralogy, and grain size

Details of each precipitation experiment can be found in Table A-1. pH values at the start of experiments range from 5.36 to 8.77. pH values at the end of experiments range from 5.84 to 8.73 (Table A-1). The average increase in pH from start to end of experiment is 0.5 (an average change in pH of 9 %). The $\delta^{18}O$ of Seattle DI tap water is -10.5 ‰ (VSMOW), and the measured $\delta^{18}O$ of the solutions was close to this value. Minimal evaporation occurred during precipitation experiments, and the $\delta^{18}O$ of the solution did not change significantly.

XRD analyses confirm that most of the samples precipitated are 100 % calcite. Some of the higher temperature samples are aragonite or some mixture of calcium carbonate polymorphs (Table A-1). Our non-calcite samples are within measurement error (1 standard error, SE) of calcite samples grown at the same temperature (Figure A-2), consistent with recent work by Defliese et al. (2015) showing that mineralogy does not measurably influence the Δ_{47} values, despite theoretical calculations to the contrary (Guo et al., 2009). Linear regressions through the calcite-only sample types are within one standard error of regressions through all samples (Table 2-2). Therefore, we have included the non-calcite samples for the purpose of drawing more robust conclusions over larger temperature ranges.

Grain size d50 values of the subset of synthetic calcites analyzed range from 2.8-9.0 µm. Aragonite samples display the expected needle-like structure, and therefore are not included in the grain size comparison (Figure A-3). Each calcite sample has grains of uniform size (standard deviation of 2-3 µm). In samples that were measured, grain size does not vary systematically with growth temperature.

2.3.2 Stable isotope values of synthetic calcium carbonates

200 total individual analyses of 56 synthetic calcium carbonates were performed. 166 analyses were conducted by digesting each of the 56 samples in 90 °C acid for a total of 2 to 4 replicates per sample. 34 analyses were conducted by digesting 11 of the total 56 samples in 25 °C acid for a total of 2 to 4 replicates per sample. At least 3 replicates per sample were performed, unless insufficient material limited our number of replicates.

The $\delta^{13}C$ values (VPDB) of the samples range from 1.6 to -25.7 ‰ with an average standard error (SE) of 0.13 ‰. The $\delta^{18}O$ values (VPDB) of samples range from -6.5 to -20.8 ‰ with an average SE of 0.08‰ (Table A-2). The regressions for mineral-water oxygen isotope fractionation versus temperature for the different sample types are statistically the same; an ancova analysis accepts the null hypothesis ($p = 0.12$ and greater).

The Δ_{47} values of samples reacted at 90 °C range from 0.457 to 0.691 ‰ with an average SE of 0.015‰ on replicate analyses of the same sample (no AFF applied). The Δ_{47} values of samples reacted at 25 °C range from 0.558 to 0.792 ‰ with an average SE of 0.014 ‰ (no AFF applied) (Figure 2-3).

The samples grown with and without CA for a given growth temperature have Δ_{47} and $\delta^{18}O$ water-calcite fractionation values that are the same within measurement uncertainty (1 SE)

(Figure 2-1, Figure 2-2) (Table A-2). A t-test accepts the null hypothesis that the sample populations with CA and without CA have the same mean Δ_{47} values ($p = 0.81$). Our results show that CA does not influence Δ_{47} even at optimum enzyme temperatures (<80 °C) (Figure 2-1). For the rest of this paper, the samples with CA ($n = 13$) are grouped with samples without CA when discussing Δ_{47}-temperature relationships.

The Δ_{47} of samples grown with different methods at approximately the same temperature are indistinguishable from one another within measurement error (1 SE) (Figure 2-4). The different sample populations are not statistically different (null hypothesis of the t-test accepted at 95% confidence level for all comparisons). The slope and intercept values of the regression through each of the sample types are within error of the others (Table 2-2). An analysis of covariance (ancova) test also accepts the null hypothesis that the linear regressions are the same at the 95% confidence level ($p = 0.21$ and greater). When the Δ_{47} of samples grown at nominally the same temperature using all of the different precipitation methods are averaged, the standard deviations of those averages range from 0.010 to 0.024 ‰. For comparison, these values are better than or as good as the reproducibility of individual replicates of our in-house calcite standards during the same time period as the samples (C64: standard deviation (SD) $\Delta_{47} = 0.023$ ‰; Coral: SD $\Delta_{47} = 0.025$ ‰). This suggests that the spread of measured Δ_{47} values reflects the expected analytical variability.

Because all sample types yield Δ_{47} results that are indistinguishable within measurement error, we combine the 56 samples to produce a linear relationship that can be used as a calibration for samples reacted at 90 °C with growth temperatures approximately between 4 and 85 °C (Table 2-2):

$$\Delta_{47} = 0.0417 \pm 0.0013 \times 10^6/T^2 + 0.139 \pm 0.014 \qquad \text{Equation 2-1}$$

The mean AFF calculated for the 11 samples reacted at both 25 and 90 °C is 0.098 ± 0.025 ‰ (error is propagated from the SE of replicates of samples). This estimate overlaps with previous estimates (Defliese et al., 2015; Guo et al., 2009; Henkes et al., 2013; Passey et al., 2010; Wacker et al., 2013). The same trends in Δ_{47} vs. temperature persist for the different sample types when reacted at 25 °C, and the measurements made after 25 °C and 90 °C reaction are within error of each other when projected into the 25 °C reference frame (Figure 2-3). The choice of AFF does not change this result. Although the 25 °C acid digestion data are sparse, all of the Δ_{47} - temperature regressions are similar to those observed for the data produced using 90 °C acid digestion (Table 2-2).

2.4 Discussion

Our results shed light on several aspects of carbonate precipitation that have been proposed to affect $\delta^{18}O$ and Δ_{47}, including the results of (1) experiments replicating previous studies while providing ancillary information that is not typically reported (e.g., pH), (2) new experiments isolating variables that differed among previous studies and using CA to promote DIC equilibration. At first, we hold analytical methods constant, and then we change acid digestion temperature, and use the Brand et al. (2010) ^{17}O correction parameters.

2.4.1 Insights into carbonate precipitation variables that do not influence measured Δ_{47}

Previous workers have suggested that carbonate Δ_{47}-temperature calibrations diverge because of disequilibrium carbonate precipitation (e.g. Dennis and Schrag, 2010; Dennis et al., 2011; Henkes et al., 2013; Zaarur et al., 2013; Fernandez et al., 2014; Tang et al., 2014). Indeed, isotopic equilibrium is unlikely to be achieved in laboratory experiments (Watkins et al., 2014),

and can occur among the DIC species in solution, at the solution-air boundary layer, or between solution and the mineral surface (Zeebe, 1999; Fenter and Sturchio, 2004; Geissbühler et al., 2004; Zeebe, 2007; Fenter and Sturchio, 2012; Affek, 2013; Affek and Zaarur 2014; Fenter et al., 2013; Tripati et al., 2015). Several of our observations eliminate specific precipitation methods as the cause of calibration discrepancies by showing that these methods do not cause divergences in measured Δ_{47}.

First, our observation that the use of CA in solution does not measurably influence $\delta^{18}O$ or Δ_{47} values of calcium carbonates grown in this study (Figure 2-1, Figure 2-2) suggests that disequilibrium in the DIC pool does not exist, or is not large enough to cause measurable isotope effects in the precipitate material of this work or in those of the previous work whose methods we replicated. DIC species take about 5 hours to equilibrate at 25 °C and a pH of 7 (Uchikawa and Zeebe, 2012b; Wang et al., 2009; Zeebe, 1999). For many of our room temperature samples, we first observed precipitate material in approximately that amount of time, so it seems possible that the calcium carbonate could inherit some of the original isotopic composition of the $NaHCO_3$ and $CaCO_3$ from DIC species that are not fully equilibrated (e.g., Henkes et al., 2013). We speculate that we do not observe a change in $\delta^{18}O$ or Δ_{47} values when we add CA because only a small fraction of all calcite precipitated during the early periods when water-DIC disequilibrium may occur.

DIC disequilibrium also may be caused by rapid CO_2 degassing, but our results suggest that the precipitation methods used in previous studies and replicated here do not inherently cause dissimilar Δ_{47} values through this mechanism. It has been suggested that actively degassing solution could cause faster degassing rates, faster precipitation rates, and thus kinetic isotope effects (Fernandez et al., 2014). In contrast, it has also been suggested that the open-

atmosphere passive degassing method causes disequilibrium because the carbonate represents a mix of surface and bulk solution conditions (Affek and Zaarur, 2014). Our experiments are the first to vary active vs. passive degassing under a constant analytical setting. The passively and actively degassed samples, for which the only difference is N_2 bubbling, have Δ_{47} values that are statistically indistinguishable for a given precipitation temperature (Figure 2-4). The mixed solution samples, which do not have N_2 or CO_2 bubbling, are within measurement error of the other sample types. Our ability to resolve disequilibrium effects is limited by the SE of the individual samples and the SE of the calibration equations. Nevertheless, agreement within 1 SE of our samples that replicate previously published precipitation methods indicates that disequilibrium due to CO_2 degassing is unlikely to explain the calibration slope discrepancies. Taken together, observations from our CA experiments and N_2 bubbling comparisons support the idea that disequilibrium among DIC species in solution is less important than the kinetics of transporting, attaching, and detaching DIC species at the mineral surface in causing Δ_{47} disequilibrium when it occurs (Affek and Zaarur 2014; Watkins and Hunt, 2015).

While our findings suggest that DIC disequilibrium and CO_2 degassing are not the cause of calibration discrepancies in previous studies, we note isotope effects due to rapid CO_2 degassing have been observed in other samples. Rapid CO_2 degassing has been shown to cause a decrease in Δ_{47} values and an increase in $\delta^{13}C$ and $\delta^{18}O$ values in some natural inorganic calcites like speleothems (Affek et al., 2014; Daëron et al., 2011; Kluge et al., 2013; Kluge and Affek, 2012; Mickler et al., 2004), as well as in synthetic calcium carbonates precipitated in the bulk solution (Guo, 2009) and as rafts at the water-surface interface (Affek and Zaarur, 2014). We therefore expected the raft carbonates of this study to have Δ_{47} values that differed from the other sample types because they grew at the solution surface, presumably during rapid CO_2 degassing

(Affek and Zaarur, 2014). However, the raft Δ_{47} values were not different from the other samples grown in bulk solution (i.e., samples that had to be scraped off the bottom of the flask) (Figure 2-4). Watkins and Hunt (2015) predict that kinetic effects in Δ_{47} can be as small as 0.01 ‰, which is within our measurement uncertainty. Therefore, it is possible that these raft carbonates experienced Δ_{47} disequilibrium that cannot be resolved with current analytical precision. It also may be possible that, despite their floating raft morphology, these samples were not formed due to rapid CO_2 degassing at the surface boundary layer, although we are not aware of a process that forms floating carbonates other than rapid degassing at the surface. Finally, we note that the raft carbonates precipitated in this study and those of Affek and Zaarur (2014) were produced by similar, but not identical methods. The two raft carbonates formed in the present study were unintentionally produced from solutions that were (gently) stirred with N_2 bubbles, while the 14 raft calcites of Affek and Zaarur (2014) were precipitated from solutions that were not stirred at all; stirring can change the thickness of the surface boundary layer. Nevertheless, our observations raise the possibility that the large kinetic effects observed by Guo (2009) and Affek and Zaarur (2014) are not inherent to all carbonate materials formed floating at the solution-air interface in synthetic carbonate experiments.

Recent work raises the possibility that solution pH, ionic concentration and carbonate growth rate could contribute to differences among previous calibrations (e.g., Affek and Zaarur, 2014; Hill et al., 2014; Tang et al., 2014; Watkins and Hunt, 2015; Tripati et al., 2015). To the extent possible, our experiments provide insight into the effects of these variables on Δ_{47} in previous calibration studies whose experiments we replicated, and by isolating the effect of ionic concentration in new experiments.

Our findings are consistent with theoretical predictions that the pH effect on Δ_{47} is likely too small to be resolved in carbonate precipitated from solutions in the pH range we investigated, and suggest that previous calibration studies were likely conducted in the same pH range (Hill et al., 2014; Tripati et al., 2015; Watkins and Hunt, 2015). Most previous carbonate Δ_{47}-temperature calibration studies do not report pH. However, the pH values we report here likely represent the pH range of previous calibration studies whose methods we replicated. pH in calibration samples could vary systematically with carbonate growth temperature because CO_2 solubility depends on temperature; therefore variability in pH could affect Δ_{47}-temperature sensitivity. pH can influence Δ_{47} values of carbonate by changing DIC speciation. HCO_3^- dominates at pH ~5-10, and CO_3^{2-} dominates at higher pH values (depends on temperature and salinity; Hill et al., 2014; Tripati et al., 2015). CO_3^{2-} has a lower Δ_{47} than HCO_3^-, so calcium carbonate minerals precipitated at high pH are expected to have lower Δ_{47} (Hill et al., 2014; Tripati et al., 2015). Our samples are within the pH range where HCO_3^- is dominant (range of 5.67 to 8.77). The calculations of Watkins and Hunt (2015) suggest that in this pH range, Δ_{47} is expected to vary by <0.01 ‰ at typical experimental growth rates. Consistent with these predictions, we observe no measurable pH effect on Δ_{47} values (Hill et al., 2014; Tang et al., 2014; Watkins and Hunt, 2015). These observations indicate pH should not have a significant influence on measured Δ_{47} in our experiments—or on previous <100 °C calibrations, which are likely within the same pH range.

Our results are consistent with previous empirical studies that have shown that growth rate does not measurably influence Δ_{47} within the range of experimental growth rates (Kele et al., 2015; Tang et al., 2014). A process-based isotope model suggests that growth rate may influence Δ_{47} values, but not by a measurable amount in a pH range of 7 to 9 (Watkins and Hunt, 2015).

We lack measurements of growth rate for each sample (apart from knowing total mass collected and experiment run time). Qualitatively, we observe that the mixed solution and filtered crystal sample types grow, on average, more slowly than the actively and passively degassed sample types at a given temperature. These limited observations combined with our finding that the Δ_{47} values agree among all sample types support previous work suggesting that growth rate within the range observed in laboratory experiments does not influence Δ_{47}.

Our experiments also suggest that ionic strength and stoichiometric proportions are not likely responsible for previous calibration discrepancies. Stoichiometric excess of Ca^{2+} could enhance kinetic isotope fractionations at the mineral surface (suggested by Affek and Zaarur, 2014). We precipitate samples that start with both balanced stoichiometry and unbalanced stoichiometry (excess of Ca^{2+}), and in a range of salt concentrations of 7 to 20 mM (Table A-1). The samples grown with lower ionic concentration and unbalanced-stoichiometry have Δ_{47} values that are within measurement error of the other samples grown with a higher ionic concentration and stoichiometric balance (Figure 2-4) (Table A-1). The ionic strength and unbalanced stoichiometry likely does not influence Δ_{47} in our samples, or in those of previous calibrations whose methods we replicated, perhaps because Δ_{47} is not sensitive to growth rate within the range observed in laboratory experiments (Tang et al., 2014; Affek and Zaarur 2014; Watkins and Hunt 2015).

In summary, our approach of analyzing synthetic carbonates in a single laboratory circumvents many complications that make it difficult to directly compare the results of previous studies—enabling us to rule out calcium carbonate precipitation method as the cause of calibration discrepancies. It is difficult to envision an untested sample preparation method that might disproportionately affect samples with high Δ_{47} values to change the calibration slope.

However, future calcite precipitation experiments that more closely monitor pH throughout the experiment, and quantify growth rate of carbonates and solution degassing rate could shed light on some of the variability that is observed in calibration samples.

2.4.2 $\delta^{18}O$ Fractionation between synthetic calcium carbonates and water

The calcite-water oxygen isotope fractionation factors calculated for all samples can be compared to previous predictions. True oxygen isotope equilibrium that is likely exemplified by the slow-growing Devils Hole calcite (Coplen, 2007) is unachievable for calcites grown at laboratory growth rates (Watkins et al., 2014). Our samples fall approximately within the range of expected fractionation factors for samples grown at laboratory growth rates (Watkins et al., 2014), which is also near the values of Kim and O'Neil (1997) (Figure 2-2). The spread among our samples is likely due to small variations in solution pH and growth rate (Watkins et al., 2014); precision for $\delta^{18}O$ measurements allows better resolution of these effects where the precision for Δ_{47} does not currently allow for observation of these effects. The spread we observe is comparable to that observed in calcite-water fractionation in the studies of Zaarur et al. (2013), Affek and Zaarur (2014), and Dennis and Schrag (2010). For our samples, deviation from the Kim and O'Neil (1997) relationship does not correlate with deviation from Δ_{47} predictions (the choice of Δ_{47} calibration or theoretical curve from which to measure Δ_{47} deviation does not matter). This suggests that Δ_{47} is not measurably influenced by the small changes in pH and growth rate that influence $\delta^{18}O$ fractionation. Because the samples in this study plot near previous $\delta^{18}O$ carbonate-water predictions, they likely precipitated from a DIC pool that was isotopically equilibrated, even if there was no solution storage time. This hypothesis is further supported by agreement between our samples grown with or without CA.

2.4.3 Acid digestion temperature does not change Δ_{47}-temperature sensitivity

Our observation that the Δ_{47} values of samples reacted in 25 and 90 °C acid show the same Δ_{47}-temperature sensitivity confirms that acid temperature is not responsible for slope discrepancies (Figure 2-3, Defliese et al., 2015). Historically, laboratories that reacted samples offline in individual acid vessels at 25 °C mostly display a steeper Δ_{47}-temperature calibration slope (e.g., Ghosh et al., 2006; Zaarur et al., 2013) compared to laboratories that react samples at 90 °C in a common acid bath (e.g., Dennis and Schrag, 2010; Wacker et al., 2014). However, exceptions to this pattern further show that acid digestion temperature is not a simple explanation for calibration discrepancies. For example, Tripati et al. (2015) reacted samples at 90 °C but report a slope that is within error of the slope of Zaarur et al. (2013), who reacted at 25 °C (Table 2-2; Tripati et al. (2015) calibration that includes all samples). Also, Petrizzo et al. (2014) reacted at 25°C, but report a slope of 0.0358 ± 0.0060, which is within error of the slope of Dennis and Schrag (2010). This pattern could potentially be explained by the observation that reacting small (< 5 mg samples) in a vessel at 25 °C can produce higher Δ_{47} values (Wacker et al., 2013).

All of the samples in our study were reacted in 6-9 mg aliquots avoiding such potential complications, but grain size did vary among the samples. It is conceivable that AFF could depend on grain size because smaller grains could more easily equilibrate with water present in the phosphoric acid (similar to the small grain size re-equilibration observed in the Kiel devices by Tobin et al., 2011). If this effect was significant and grain size was correlated with precipitation temperature, using a constant AFF to project samples in the 25 °C reference frame would produce slope inaccuracies. However, the AFF that we measure does not appear to depend

on calcium carbonate grain size. A linear regression between grain size and AFF has an r^2 of 0.01, p = 0.79; other types of regressions (logarithmic, polynomial, etc.) do not yield better fits. This observation suggests that grain size and texture may not influence AFF, but a more thorough investigation should be undertaken given that we tested a small range of grain sizes and reacted a relatively small number (n = 11; 2 to 4 replicates each) of samples at both 25 and 90 °C.

2.4.4 Comparison to previously published Δ47 –temperature calibrations processed using Santrock et al. (1985) parameters

We compare our samples to previously published calibration data, taking into account the effects of ^{17}O correction parameters on Δ_{47} values to the extent possible. To our knowledge, previously published carbonate clumped isotope calibration studies processed data using the traditional Santrock et al. (1985) parameters to correct for ^{17}O interference in $\delta^{13}C$ measurements by mass spectrometry (e.g., Affek and Eiler, 2006; Huntington et al., 2009). Visual inspection of our samples re-calculated with the traditional Santrock et al. (1985) parameters plotted with calibration samples from previous work highlights the spread in measured Δ_{47} for a given temperature (up to 0.1 ‰) (Figure 2-5) (values in Table A-3). None of our samples are able to replicate the high Δ_{47} values at lower temperatures reported by Ghosh et al. (2006), even by precipitating samples using almost identical methods (dissolve and filter $CaCO_3$, actively degas CO_2 with N_2) (Figure 2-5, Table 2-2). Kluge et al. (2015) also uses very similar precipitation methods, but do not produce calibration slopes that are as steep as the Zaarur et al. (2013) calibration. Together, these observations may suggest that precipitation method is not responsible for the relatively high Δ_{47} observed by Ghosh et al. (2006) at low temperatures, consistent with the results of our study. However, these comparisons are inherently flawed

because they rely on Δ_{47} data that may be inaccurate to some degree due to the choice of ^{17}O correction parameters.

2.4.5 The influence of ^{17}O correction parameters on measured Δ_{47} values and comparison to calibration data processed using Brand et al. (2010) parameters

Having ruled out precipitation method and acid digestion method as likely causes of calibration discrepancies, we discuss the potential implications for calibration data of the recent finding that the choice of ^{17}O abundance corrections used to calculate Δ_{47} influences the accuracy of sample and absolute reference frame data (Daëron et al., 2016; Olack and Colman, 2016; Schauer et al., 2016). If the Santrock et al. (1985) ^{17}O correction values are used and the $\delta^{13}C$ composition of the reference frame gases, mass spectrometer working gas and/or sample gas differ, inaccuracies in calculated Δ_{47} values emerge (Daëron et al., 2016; Schauer et al., 2016). Thus differences in the isotopic compositions of synthetic carbonates, the mass spectrometer working gas, and/or the equilibrated gases used to construct the absolute reference frame could compromise the validity of inter-laboratory comparisons. Using the parameters recommended by Brand et al. (2010) to correct for ^{17}O abundance in CO_2 has been shown to minimize these inaccuracies (Daëron et al., 2016; Olack and Colman, 2016; Schauer et al., 2016).

Our dataset highlights the potential for the choice of ^{17}O correction parameters to influence calibration accuracy and agreement. In this study we present data processed using the parameters recommended by Brand et al. (2010) (Figure 2-4). Schauer et al. (2016) show that re-processing our data using the Santrock et al. (1985) values traditionally used in clumped isotope studies causes up to 0.06 ‰ bias in some of our sample Δ_{47} values, and results in a large and spurious apparent disagreement between the mixed solution and other sample Δ_{47} data (Figure 2-5, Figure 2-6, Table A-3; see Schauer et al., 2016, for details). It is not straightforward to

predict how re-processing previously published data using the Brand et al. (2010) values will influence calibration samples from different laboratories; the magnitude and direction of change likely depend on the bulk composition of the absolute reference frame gases, the working gas, and the sample gas (Daëron et al., 2016). However, examination of our data provides strong evidence that other calibration samples could be affected significantly.

We also present the chicken eggshell as a biogenic data point available that has been processed with both Santrock et al. (1985) and Brand et al. (2010) ^{17}O parameters (Figure 2-6). The egg displays closer agreement with the UW synthetic calibration samples when processed with the Brand et al. (2010) parameters (Figure 2-6). In contrast, Eagle et al. (2015) suggest that their eggshell calibration agrees well with the Ghosh et al. (2006) synthetic calibration as published originally (presumably with the Santrock et al. (1985) values). It remains to be determined if this agreement will hold when/if both calibrations are reprocessed with Brand values. Without further analysis, it seems that the choice in ^{17}O corrections is not the only variable that controls agreement between synthetic and biogenic data. Our single data point (the egg) does not allow for a comprehensive discussion of how biogenic data and their agreement with synthetic calibrations may be affected by the choice of ^{17}O parameters, but we hope that it may be a helpful reference for future workers.

A handful of synthetic carbonate data have been calculated using the Brand et al. (2010) ^{17}O correction factors and can be directly compared with our data (Figure 2-6) to demonstrate how the choice of ^{17}O parameters influences calibration data. Daëron et al. (2016) recalculate the Δ_{47} values of 5 of the 7 synthetic carbonate samples analyzed at Yale University by Zaarur et al. (2013) and 5 previously unpublished synthetic carbonates analyzed at LSCE (University of Paris-Saclay) using the Brand et al. (2010) parameters. Daëron et al. (2016) show that the slopes

of the LSCE and Yale calibrations are not affected by the choice of ^{17}O parameters, but that the intercepts move further apart when reprocessed with the Brand et al. (2010) values. Similarly, the slope of our calibration is not affected by using the Brand et al. (2010) parameters. In contrast with Daëron et al. (2016), the dispersion of intercepts in our dataset is reduced (Figure 2-4, Figure 2-6, Eq. 1.; Schauer et al., 2016). These observations suggest that inaccuracies due to the choice ^{17}O correction parameter may explain some of the large dispersion among previous calibration data, but they likely do not explain the large slope discrepancies in previous clumped isotope calibrations.

However, we suggest the approach of focusing on slopes to compare calibration data may be inappropriate because regression slopes are easily influenced by aliasing due to small sample population size. The calibration comparison in Figure 2-6 and the large population size of our dataset make it possible to evaluate this issue quantitatively. For example, when we repeat 10,000 times the exercise of randomly selecting 5 of our 56 calibration samples and fitting a line through them, 11% of the resampled populations produce a slope that is within error of the Yale calibration slope (0.055 ± 0.007), and 54% of the resampled populations produce a slope that is within error of the LSCE calibration slope (0.0388 ± 0.0046). Results are similar when the exercise is performed with a randomly selected sample size of 13, which is the number of samples used in the Dennis and Schrag (2010) calibration. Future workers who wish to differentiate between calibration lines should employ statistical tests that consider the sample population size. Instead of differentiating between calibrations, we believe that the calibration equation that is most robust to outliers and small population sizes is one that considers all available calibration sample data generated in different laboratories using comparable data processing methods. We present a calibration equation that combines our samples with those

from LSCE and Yale processed with Brand et al. (2010) in the 25 °C reference frame (n = 66, r^2 = 0.942):

$$\Delta_{47} = 0.0422 \pm 0.0013 \times 10^6/T^2 + 0.215 \pm 0.014 \quad \text{Equation 2-2}$$

We note that a source of unquantifiable error in this equation is the choice of AFF; here we use 0.082 ‰ (Defliese et al., 2015) to correct the UW and LSCE data, but recognize that this AFF may change when/if it is re-calculated with the Brand et al. (2010) parameters. We offer the above equation with the caveat that a community effort to reprocess all calibration and AFF samples with the Brand et al. (2010) parameters and/or produce new calibration data that can be compared in the same framework will result in a more accurate calibration equation. We advocate that this effort is the most promising approach for arriving at a calibration that is universal to all laboratories.

2.4.6 Additional Possible Analytical and Data-Processing Controls on Δ_{47} disagreements

While we think that using appropriate ^{17}O correction parameters may significantly improve inter-laboratory agreement, we discuss other differences in analysis techniques that could potentially change measured Δ_{47} values that merit systematic evaluation. These analytical differences may not directly influence calibration slopes, but they may have with implications for dispersion in calibration data.

First, the precise density of the phosphoric acid used could influence oxygen exchange during carbonate dissolution and is not currently well documented (Colman and Olack, 2015; Defliese et al., 2015). Similarly, the distance from the acid bath to the water traps on preparation lines could contribute to CO_2 gas re-equilibration with water (as observed in acid vessels in Wacker et al., 2013). Also, methods used to remove contaminants vary or are not used (e.g., the

use of gas chromatograph or packed columns, with or without He carrier gas, operating at different temperatures; Ghosh et al., 2006; Dennis and Schrag, 2010; Bernasconi et al., 2013; Petersen et al., 2016). Laboratories that use a gas chromotagraphy (GC) column report similar calibrations (e.g., Zaaur et al., 2013; Tripati et al. 2015 (all samples)), whereas laboratories that use a vacuum line Porpak Q trap report similar calibrations (e.g., this work; Kluge et al., 2015; Dennis and Schrag, 2010). Laboratories also vary the method of storing or transferring purified CO_2 to the mass spectrometer for analysis (e.g., using a break seal or not). Additionally, there may be artifacts that arise from differences in the way laboratories measure backgrounds (i.e., backgrounds measured with or without gas flowing into the mass spectrometer source; He et al., 2012; Bernasconi et al., 2013; Fiebig et al., 2016) that remain to be explored systematically. The influence of these analytical differences on measured Δ_{47} values remains to be explored systematically.

2.4.7 Implications for isotope effects in natural abiogenic carbonates

Our unique dataset shows consistent Δ_{47} values for calcium carbonates synthesized with diverse precipitation conditions, suggesting that natural abiogenic calcium carbonates preserved in geologic archives should also reliably record temperature over a variety of precipitation conditions. Reliable carbonate geothermometers can be found in environments that host solutions where HCO_3^- is the dominant DIC species (~pH 5 to 10, such as soil waters). Small changes in solution chemistry in these environments will still result in Δ_{47} values that can be directly compared to abiogenic laboratory precipitation experiments (Tripati et al., 2015). Critically, we also show that carbonates produced in solutions that are not necessarily in DIC equilibrium (all of our experiments that do not have CA) have isotopic compositions that are indistinguishable

from samples produced in known DIC equilibrium (all of our experiments that do have CA). This observation indicates that small changes in the source DIC pool should not significantly influence the isotopic compositions of natural samples. Disequilibrium Δ_{47} values, when observed, instead likely result from cases where DIC species are far from equilibrium, or from kinetic processes at the solution-mineral interface (Kluge et al., 2014; Tripati et al., 2015), although the magnitude, and even direction, of such effects remain highly uncertain (Watkins and Hunt, 2015).

Our samples may offer insight into the effect of CO_2 degassing on natural samples. Despite degassing CO_2 with different methods, our Δ_{47} results are consistent. We do not reproduce large kinetic effects that might be expected from degassing, even in our raft-morphology carbonates (e.g., as observed in the raft carbonates of Affek and Zaarur, 2014). This may suggest that Δ_{47} equilibrium of other natural samples is likely unaffected by degassing unless the carbonates are precipitated in solutions that have high concentrations of CO_2 compared to ambient air, or where the water-air interface is large compared to the reservoir, such as in speleothems (e.g., Daëron et al., 2011; Kluge and Affek, 2012).

Our carbonate synthesis experiments are most similar to the formation processes of natural samples such as travertines, tufas, and vein, soil and lake carbonates. Vent and open-air pool travertines/tufas precipitate during the initial degassing of a small fraction of the CO_2 dissolved in solution, and thus are similar to our samples in that they do not experience measurable kinetic effects due to degassing (Kele et al., 2015). Similarly, pedogenic carbonates typically grow in soil waters that are slowly degassed and become supersaturated during drying events, and are thought to precipitate in near-equilibrium conditions (e.g., Quade et al., 2007; Breecker et al., 2009; Quade et al., 2013; Burgener et al., 2016). Our calibration samples are also

analogous to open lake carbonates that form in response to degassing caused by biotic removal of CO_2 (Hren and Sheldon, 2012). In contrast, carbonates grown in closed, evaporative lakes may grow under a relatively higher degree of supersaturation and pH (Reddy, 1995), which could invalidate the comparison with our calibration samples. Similarly, alkaline spring carbonates may have isotope values that are influenced by hydroxylation of CO_2 and other kinetic effects (Falk et al., 2016). We suggest through these comparisons that our samples likely represent processes relevant to natural, inorganic samples grown in physiochemical conditions that can be found in a variety of geologic settings. As such, we anticipate that the calibration we present in Equation 2-1 can be used to estimate the growth temperature of a wide variety of natural carbonates even when their precipitation pathway is highly variable.

2.5 Conclusions

Several suites of calcites, grown using various precipitation methods and acid digestion temperatures, while holding other analytical methods constant, suggest a constant Δ_{47}-temperature relationship. Our findings corroborate previous work showing that changing the temperature of acid digestion does not change the temperature sensitivity of the Δ_{47}-temperature relationship. We further suggest that calibration discrepancies are not a direct result of the precipitation methods used by previous workers; these methods do not appear to cause measurable Δ_{47} differences due to disequilibrium in the DIC species or CO_2 degassing method.

Our observations suggest that natural samples grown in moderate pH (5-10) and near-equilibrium conditions between 4 and 85°C can be represented by a calibration that includes the synthetic samples from this work (Equation 2-1, Table 2-2). The similarity of isotopic compositions among our samples even with diverse precipitation methods suggests that many

natural carbonates can be used as dependable geothermometers. The large number of data points (n = 56 samples) makes this calibration robust to outliers and illustrates that the approach of using slopes to compare calibration regressions is vulnerable to aliasing. However, the dispersion of some calibration data exceeds that which can be explained by analytical error and acid fractionation uncertainties. This work highlights the need for systematic study of how CO_2 gas purification, acid preparation, background corrections, and most importantly ^{17}O correction parameters assumed during Δ_{47} calculations could influence measured Δ_{47} values.

Acknowledgements

We thank Associate Editor Hagit Affek for her invaluable conversations and reviews that greatly improved our discussion of kinetics and the implications of our work to clumped isotope calibrations. We also thank Jens Feibig and two anonymous reviewers for their comments that improved this manuscript. This material is based on work supported by the National Science Foundation Graduate Research Fellowship Program under Grant No. DGE-1256082 to JRK. We also gratefully acknowledge funding from the National Science Foundation under grants EAR-1156134 and EAR-0955309 to KWH and from the Geological Society of America under a Graduate Student Research Grant to JRK. CS acknowledges support from the UW School of Oceanography. We thank Rebecca Smith, Adrienne Scott, and Paul Tosello for their assistance in the laboratory and with grain size analyses. We thank Scott Kuehner for assistance with microprobe imaging of our samples. We also acknowledge Tuesday Kuykendall and Tatyana Galenko (UW Materials Sciences and Engineering) for their assistance in acquiring and analyzing XRD data.

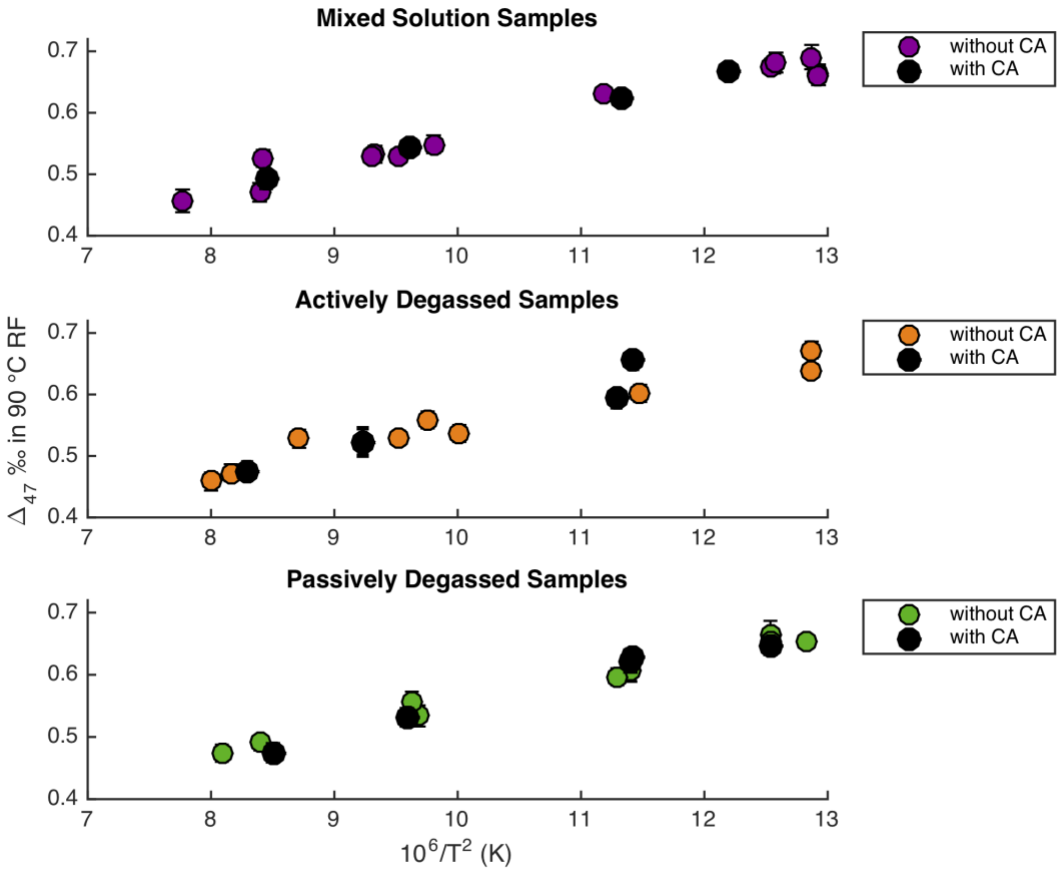

Figure 2-1: Synthetic carbonate samples grown with and without carbonic anhydrase.

Synthetic carbonate samples grown with carbonic anhydrase (black) and without (color). Δ_{47} (‰) plotted against growth temperature. Error bars are 1 SE and are generally smaller than the symbol.

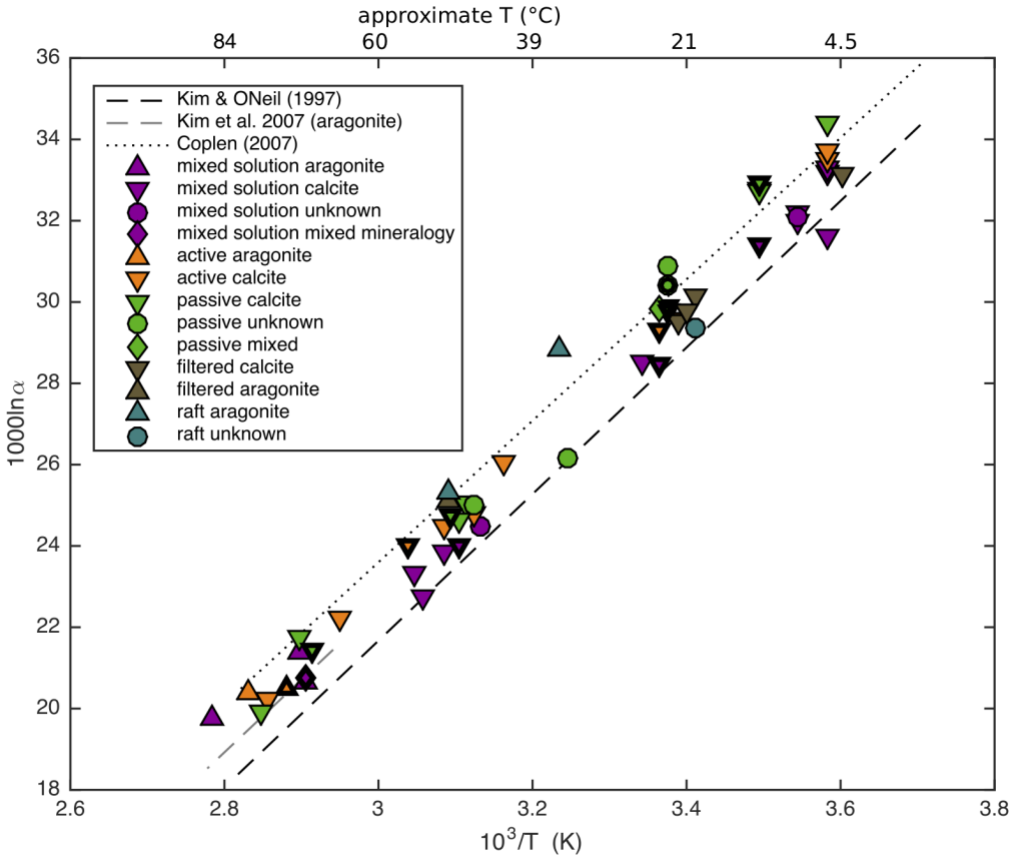

Figure 2-2: Carbonate mineral-water fractionation in oxygen isotopes.

Error bars are smaller than marker size. Colors indicate precipitation method and shape indicates mineralogy. Samples with bold outline were grown in the presence of CA (n = 13). Our samples mostly fall between the Kim and O'Neil (1997) relationship measured in synthetic carbonates and the Coplen (2007) relationship measured from Devils Hole calcite, and they fall within the range expected for carbonates grown at laboratory growth rates (Watkins et al. 2014).

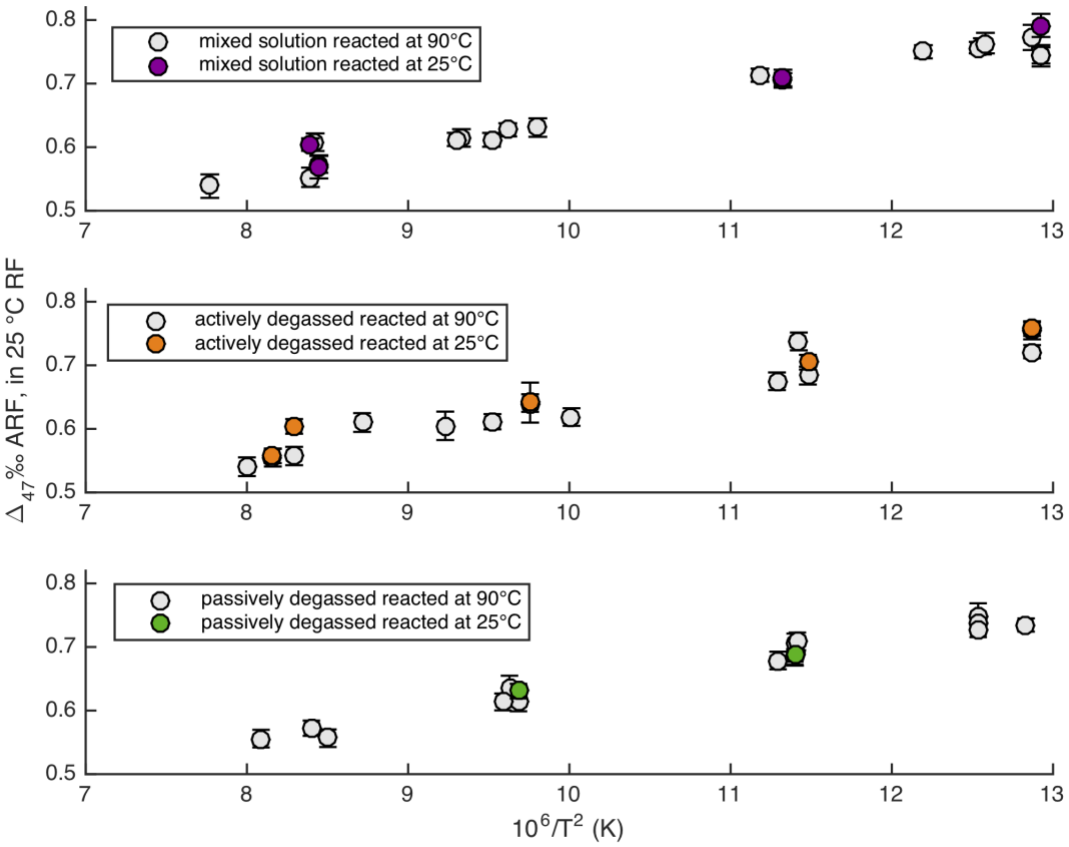

Figure 2-3: Δ_{47} values of samples digested in 25 and 90 °C phosphoric acid.

Error bars are 1 SE. The measured Δ_{47} value for samples after digestion at 25 °C is within error of the measured Δ_{47} value after digestion at 90 °C (samples reacted at 90 °C are corrected with the AFF of 0.082 ‰ from Defliese et al. (2015)) (Table A-2).

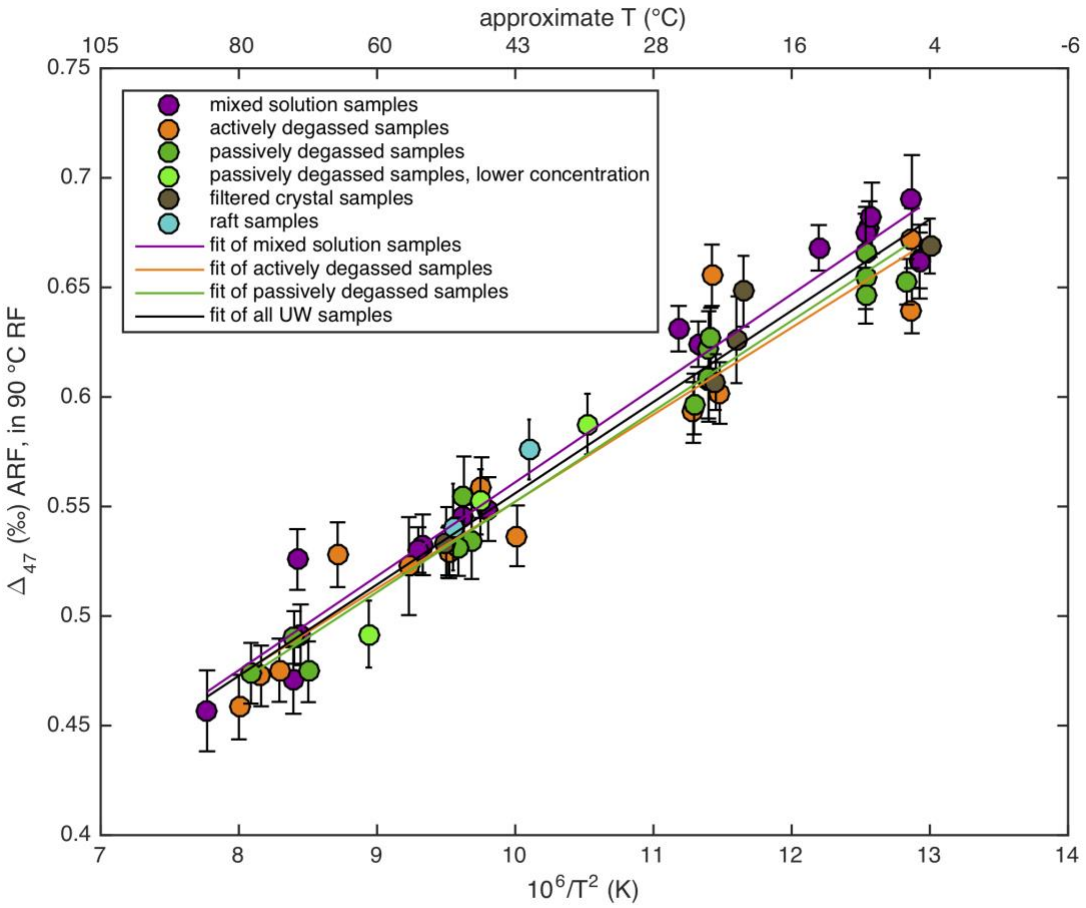

Figure 2-4: Δ_{47} – temperature relationship for synthetic carbonate samples from this work.

Error bars are 1 SE. The black regression is the regression through all UW samples processed with Brand et al. (2010) values (Equation 1).

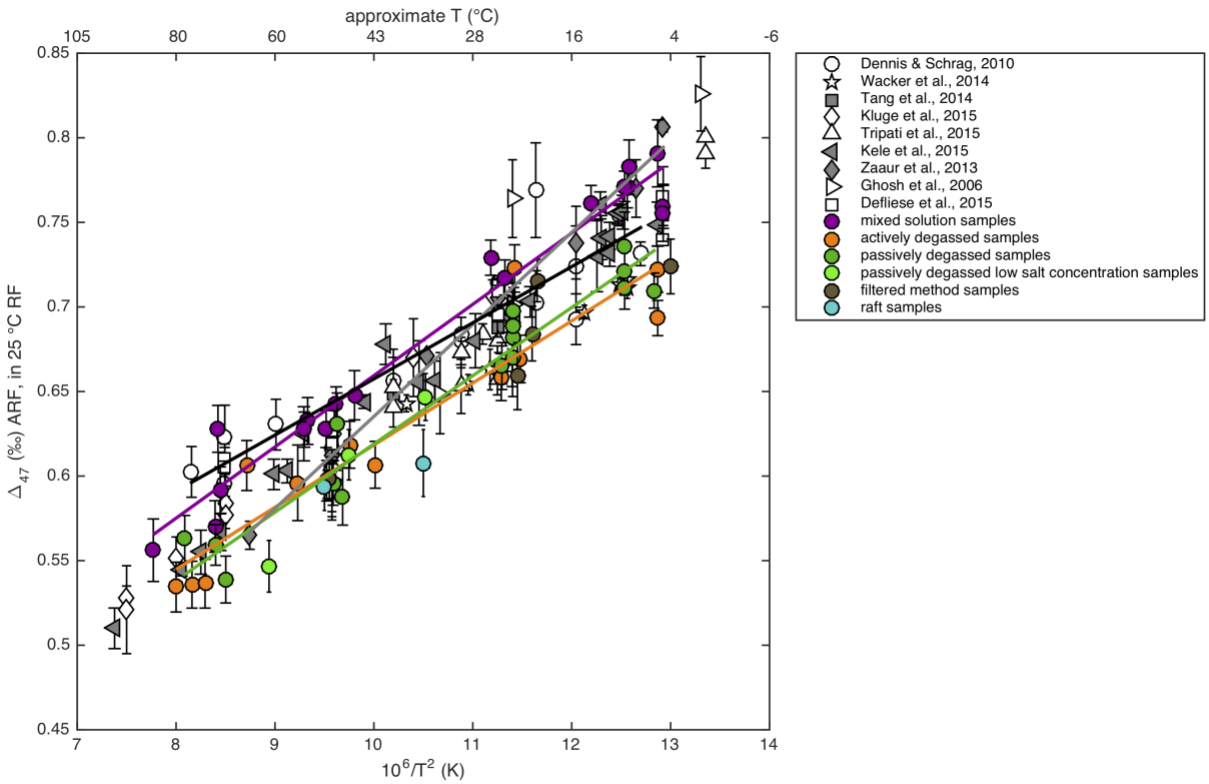

Figure 2-5: Comparison of Δ_{47} values of synthetic carbonates from this work and others.

Δ_{47} vs. growth temperature for synthetic carbonate samples from this work, and previous synthetic and abiogenic calibration samples. Colored samples and linear regressions are from this work. The solid gray line is the Zaaurur et al., (2013) calibration and the solid black line is the Dennis and Schrag (2010) calibration. In order to compare our samples with those from previous work, the Δ_{47} values of our carbonate samples in this figure have been calculated using ^{17}O correction values of Santrock et al. (1985) (Schauer et al., 2016).

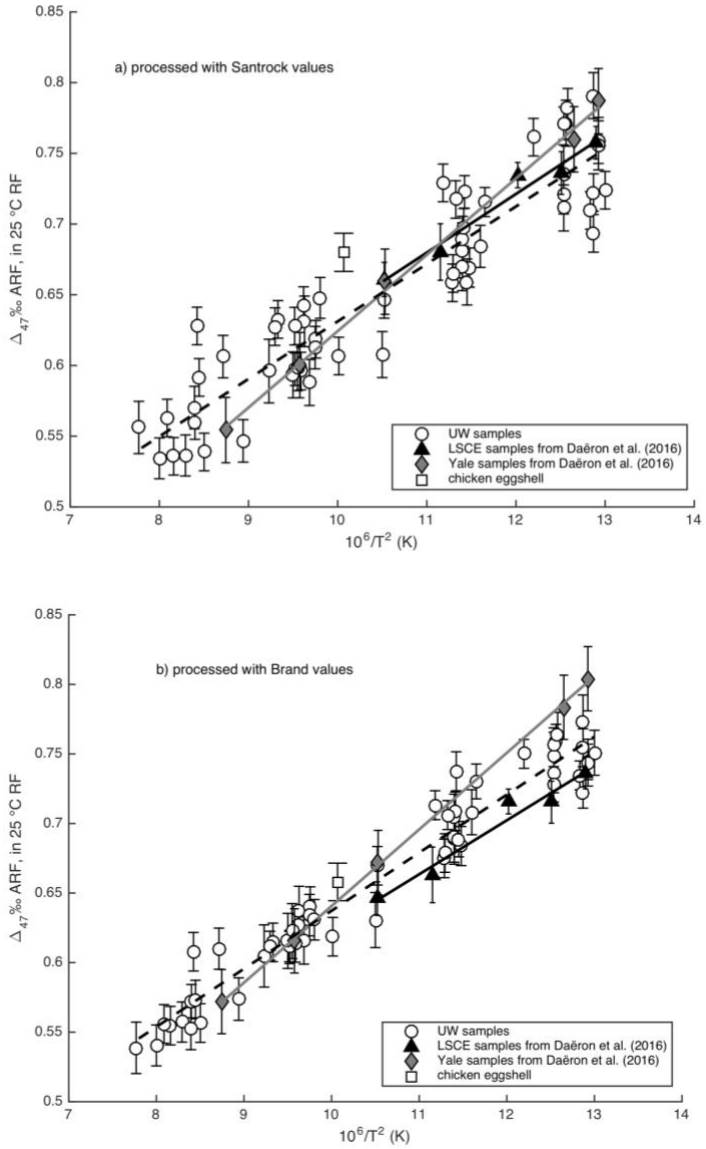

Figure 2-6: Δ_{47} values of synthetic carbonates from this work and others, recalculated with Brand et al. (2010) ^{17}O correction parameters.

LSCE and Yale samples as presented in Daëron et al. (2016). Values are presented in the 25 °C reference frame (UW and LSCE samples reacted at 90 °C are corrected with the AFF of 0.082 ‰ from Defliese et al. (2015). The solid gray line is the fit to the Zaarur et al. (2013) samples, the dashed black line is the fit to the UW samples, and the solid black line is the fit to the Paris samples. **a)** Samples processed using the Santrock et al. (1985) ^{17}O correction parameters. **b)** Samples processed using the Brand et al. (2010) ^{17}O correction parameters.

Table 2-1: Synthetic Carbonate Precipitation Methods Used in this Work

Method	"active degassing"	"passive degassing"[a]	"mixed solution"	"filtered crystal"
Citation replicated	Kim and O'Neil (1997)	modified after Kim and O'Neil (1997); Dennis and Schrag (2010)	Dennis and Schrag (2010)	Zaarur et al., (2013); Ghosh et al. (2006)
Adding reagents	CO_2 bubbled for 10 minutes, $NaHCO_3$ was added, CO_2 bubbled for an additional 10 minutes, $CaCl_2*2H_2O$ was added, CO_2 was bubbled for an additional 10 minutes	CO_2 bubbled for 10 minutes, $NaHCO_3$ was added, CO_2 bubbled for an additional 10 minutes, $CaCl_2*2H_2O$ was added, CO_2 was bubbled for an additional 10 minutes	Thermally equilibrated solutions of $NaHCO_3$ and $CaCL_2*2H_2O$ were slowly combined in ~5 mL quantities	CO_2 bubbled for 1 hour, then 1 g of in-house calcite standard, C64, was added. CO_2 bubbled until $CaCO_3$ dissolved
CA added?	After salts were added, in some experiments (Table A1)	After salts were added, in some experiments (Table A1)	After solutions were combined, in some experiments (Table A-1)	No
Filtering	NA	NA	NA	Filtered with Whatman #40 8 um filter paper
Stirring	Magnetic stir bar	Magnetic stir bar	Magnetic stir bar	N_2 bubbles
Degassing	N_2 bubbled (20 bubbles/30 seconds) with a pasteur pipe to actively degas CO_2	CO_2 allowed to passively degas into the atmosphere, through 1 hole at the top of the beaker	CO_2 allowed to passively degas into the atmosphere, through 1 hole at the top of the beaker	N_2 bubbling (20 bubbles/30 seconds) with a pasteur pipe to actively degas CO_2
Carbonate observation	in suspension and coating the bottom of the flask	in suspension and coating the bottom of the flask	attached to the bottom of the flask (had to be scraped aggressively to remove)	coating the bottom of the flask and floating rafts

[a] The passive degassing method does not strictly replicate either Kim and O'Neil (1997) or Dennis and Schrag (2010). Kim and O'Neil (1997) /the "active degassing" method bubbled both N_2 and CO_2, while Dennis and Schrag, (2010)/ the "mixed solution method" bubble neither. This method only bubbles CO_2 in order to isolate the influence of bubbling CO_2 in solution. Additionally, we have varied the stoichiometry and ionic concentrations in some of these samples (Table A-1).

Table 2-2: Synthetic and abiogenic Δ_{47}-temperature calibrations

Regresssion	Slope x $10^6/T^2$ ± 1 SE	Intercept ± 1 SE	r^2	Acid Dig. T °C (AFF)[a]	Calib. Range °C	n (samples)
This work – all samples digested in 90 °C acid						
actively degassed	0.0396 ± 0.0035	0.155 ± 0.035	0.921	90 (0)	6 to 80	13
passively degassed	0.0412 ± 0.0018	0.139 ± 0.019	0.970	90 (0)	6 to 80	18
mixed solution	0.0429 ± 0.0020	0.132 ± 0.021	0.967	90 (0)	6 to 85	18
filtered	0.0384 ± 0.0063	0.179 ± 0.073	0.924	90 (0)	4 to 50	5
all sample types (Eq. 1)	**0.0417 ± 0.0013**	**0.139 + 0.014**	**0.95**	**90 (0)**	**4 to 85**	**56**
This work - calcite only, samples digested in 90 °C acid						
actively degassed	0.0372 ± 0.0047	0.183 ± 0.050	0.887	90 (0)	6 to 77	10
passively degassed	0.0407 ± 0.0019	0.144 + 0.021	0.975	90 (0)	6 to 78	12
mixed solution	0.0420 ± 0.0028	0.142 + 0.032	0.957	90 (0)	6 to 55	12
all sample types	0.0408 ± 0.0017	0.148 + 0.019	0.941	90 (0)	4 to 78	38
This work - samples digested in 25 °C acid						
actively degassed	0.0383± 0.0041	0.266 ± 0.042	0.966	25 (0)	6 to 80	5
passively degassed	0.0327 ± 0	0.313 ± 0	NaN	25 (0)	23 to 48	2
mixed solution	0.0447 ± 0.0052	0.209 ± 0.054	0.974	25 (0)	6 to 80	4
all sample types	0.0407 ± 0.0030	0.242+ 0.031	0.95	25 (0)	6 to 77	11
Synthetic & Abiogenic Calibrations (in order of shallow to steep slope)						
Wacker et al. 2014	0.0327 ± 0.0026	0.303 ± 0.03	0.9915	90 (0.069)	9 to 38	7
Defliese et al. 2015	0.0348 ± 0.00229	0.3031 ± 0.0244	0.8778	75 (0.067)	5 to 70	8
Dennis & Schrag (2010)[b]	0.0362 ± 0.0018	0.292 ± 0.0194		90 (0.081)	7.5 to 77	15
Kluge et al. 2015	0.038 ±0.007	0.259 ± 0.006		70/90 (various)	23 to 250	29
Tang et al. 2014	0.0387 ± 0.0072	0.2532 ± 0.0829		90 & 100	5 to 40	23
Kele et al. 2015	0.044 ± 0.005	0.205 ± 0.47	0.96	70 (0.064)	5.6 to 95	25
Tripati et al. 2015, excluding low T	0.046 ± 0.0074	0.1649 ± 0.0786		90 (0.092)	25 to 50	10
Affek and Zaarur 2014	0.048 ± 0.0028	0.2149 ± 0.0295	0.84	25 (0)	7 to 69	14
Tripati et al. 2015	0.0505 ± 0.0034	0.1185 ± 0.038		90 (0.092)	0.5 to 50	12
Zaarur et al. 2013	0.0526 ± 0.0025	0.052 ± 0.0284	0.93	25 (0)	1 to 60	14
Ghosh et al. 2006[b]	0.0636 ± 0.0049	0.005 ± 0.062		25 (0)	1 to 50	7

[a] Values in parenthesis are the acid fractionation factors used by the studies' authors to calculate the calibration.
[b] Values recalculated in Dennis et al. (2011)

Chapter 3 A proxy for all seasons? A synthesis of clumped isotope data from Holocene soil carbonates

Abstract. Despite the importance of soil carbonates as paleoclimate archives, interpretations of their isotopic compositions (δ18O, δ13C, and Δ47) is hampered by uncertainty in when and how soil carbonates accumulate. Several previous studies have paired modern air/soil temperatures with temperatures estimated from the clumped isotopic composition (TΔ47) of Holocene soil carbonates to infer the timing of soil carbonate accumulation. Here, we synthesize these previous studies in order to identify which environmental conditions are critical to controlling the seasonal bias of carbonate formation. Considering recent improvements in the standardization of clumped isotope methods, we recalculate Δ47 values where possible and only examine Δ47 data that adheres to modern standards. Most soil carbonates record TΔ47 values higher than mean annual air temperature, but the residual varies from -8 to 24 °C. Depth in the soil profile does not explain this variance: most observed soil profiles have Δ47 profiles that are uniform with depth. We find that the grain size of the soil matrix, timing of precipitation and presence of vegetation each explain a portion of the observed variance in seasonal bias. This result is consistent with the hypothesis that changes in soil moisture can drive soil carbonate accumulation. We observe that, in aggregate, the δ18O values of soil water calculated from δ18O of soil carbonates and TΔ47 best agrees with the δ18O of mean annual rainfall. Where possible, reconstructions of paleoclimates and paleoaltimetry should consider the timing of rain, soil texture, and vegetative cover to aid in identifying the seasonal bias of stable isotopic compositions of soil carbonates.

3.1 Introduction

The ability to reconstruct ancient climates on land is critical for investigating the evolution of habitats, ecology, climate, tectonics, and landforms. Soil carbonates are an important archive of terrestrial paleoenvironments because they are widespread through space and time in the geologic record and form near the Earth's surface. For example, past studies have used the carbon isotope composition ($\delta^{13}C$) of soil carbonate to reconstruct changes in the composition of Cenozoic plant communities (e.g., the proportion of C3 and C4 vegetation; Cerling et al., 1989; Wang et al., 1993; Quade et al., 1995; Ding and Yang, 2000; Monger et al., 2009; Levin et al., 2011) and changes in atmospheric CO_2 concentrations throughout the Phanerozoic ((Bowen and Beerling, 2004; Breecker et al., 2010; Cotton and Sheldon, 2012; Ekart et al., 1999; Leier et al., 2009; Mintz et al., 2011; Mora et al., 1996; e.g., Mora and Driese, 1993; Myers et al., 2016; Nordt et al., 2003; Retallack, 2009; Tabor et al., 2013). The oxygen isotope composition of soil carbonates ($\delta^{18}O_c$) is commonly used to infer changes in local meteoric waters and/or local temperature (Behrensmeyer et al., 2007; Cerling and Hay, 1986; Dworkin et al., 2005; Fox and Koch, 2004; Garzione et al., 2000; Kaakinen et al., 2006; Koch et al., 1995; Liu et al., 1996; Monger et al., 1998; Nordt et al., 2003; Sikes and Ashley, 2007; Smith et al., 1993; Wang et al., 1996). The more recent development of the ability to measure the temperature-dependent abundance of ^{18}O-^{13}C bonds in a carbonate molecule, called clumped isotope thermometry (Δ_{47}), has allowed for a thermodynamically-based estimate of the growth temperature of carbonate minerals. This measurement of temperature from Δ_{47} allows the worker to solve for $\delta^{18}O$ of growth water, and thus allows for quantitative reconstruction of both temperature and changes in meteoric waters with a single analysis. Δ_{47} analysis of paleosol carbonates has improved paleoaltimetry (Fan and Carrapa, 2014; Garzione et al., 2014; Huntington and Lechler, 2015;

Ingalls et al., 2018; Lechler et al., 2013; Leier et al., 2013), improved reconstructions of terrestrial temperatures and hydrology, especially that of abrupt climate events (Burgener et al., 2019; Eagle et al., 2013b; Hyland et al., 2018; Kelson et al., 2018; Lechler et al., 2018; Methner et al., 2016; Page et al., 2019; Snell et al., 2013; Suarez et al., 2011; Tobin et al., 2014), improved atmospheric pCO_2 reconstructions (Ji et al., 2018), and enabled characterization of habitats of human evolution (Passey et al., 2010). These and many other studies using carbonates of modern and ancient soils have advanced geomorphology, paleoclimatology, ecology, evolutionary biology and tectonics research.

Despite their value to paleoclimatology, significant uncertainty remains about how and when carbonates accumulate in soils. Because the seasonal and diurnal range in surface temperature on land is generally much larger than the secular changes in temperature through geologic time that most studies of terrestrial paleoclimate wish to address, even slight changes in the seasonal bias of a terrestrial climate record must be recognized in order to establish high fidelity climate records. This uncertainty in the seasonality of carbonate formation leads to ambiguity in the interpretation of carbonate isotopic compositions and limits the usefulness of terrestrial paleoclimate reconstructions that use soil carbonates (Breecker et al., 2009; Burgener et al., 2016; Gallagher and Sheldon, 2016; Hough et al., 2014; Huntington and Lechler, 2015; Huth et al., 2019; Oerter and Amundson, 2016; Peters et al., 2013; Ringham et al., 2016). Understanding the seasonal bias of soil carbonate formation is paramount for interpreting Δ_{47} temperatures and has implications for interpreting $\delta^{18}O$ and $\delta^{13}C$ values of soil carbonates.

Comparison between the clumped isotope temperature (here $T\Delta_{47}$) and measured local temperatures in modern to Holocene soil carbonates can identify seasonal biases of soil carbonate formation and thus elucidate formation processes (Ghosh et al., 2006b; Peters et al.,

2013; Quade et al., 2013). Here, we synthesize existing clumped isotope (Δ_{47}) data from Holocene soil carbonates with the goal of deciphering which, if any, environmental factors emerge as primary drivers of the annual timing of soil carbonate formation. We compare measured Δ_{47} temperatures to local mean annual temperatures to assess seasonal bias. We seek to compare the seasonal bias to environmental parameters that could be deciphered from paleosols or climate models, and thus are useful to paleoclimatologists. We first rule out artifacts in Δ_{47} measurement and calculation as the cause of the varied seasonal biases reported in the literature. Then, we explore other variables including depth in soil column, seasonal precipitation patterns, vegetation cover, and soil texture, all of which relate to the idea that changes in soil moisture drive soil carbonate formation. Lastly, we discuss implications for interpretations of isotopic values of paleosol carbonates in the geologic record.

3.2 Background: Soil Carbonate Formation and Isotopic Composition

Pedogenic carbonate forms *in situ* in soils in arid to sub-humid environments (Birkeland, 1984; Jenny, 1941). The precipitation of carbonate in a soil is thought to be controlled by soil water, soil temperature, and soil CO_2, which can be encapsulated by the expression for the activity of calcium carbonate (a_{CaCO_3}):

$$a_{CaCO_3} = \frac{4m_{Ca^{2+}}^3}{pCO_2}\left(\frac{K_2}{K_1 K_{cal} K_{CO_2}}\right) \qquad \text{Equation 3-1}$$

where m_{Ca2+} is the concentration of Ca^{2+} ions in solution, pCO_2 is the partial pressure of CO_2 in the soil gas, K_{CO2} is the Henry's law constant for CO_2 and K2, K1, K_{cal} are the temperature-dependent equilibrium constants for the following reactions, respectively:

$$HCO^{3-} \leftrightarrow H^{+} + CO_3^{2-} \qquad \text{Equation 3-2}$$

$$H_2CO_3 \leftrightarrow H^{+} + HCO^{3-} \qquad \text{Equation 3-3}$$

$$Ca^{2+} + CO_3^{2-} \leftrightarrow CaCO_3 \qquad \text{Equation 3-4}$$

Calcite will precipitate when a_{CaCO_3} = 1 at thermodynamic equilibrium (Breecker et al., 2009; Drever, 1982). Equation 1 demonstrates that calcite precipitation in soils can be driven by increased concentrations of Ca^{2+}, decreased concentrations of CO_2, and/or increased temperatures (due to temperature dependence of K values). It is generally assumed that soil carbonates form when the solution in pore space reaches superstation with respect to calcite, but organic carbon can poison nucleation sites and promote supersaturation with respect to calcite in natural soils (Inskeep and Bloom, 1986; Lebrón and Suárez, 1998; Suarez and Šimůnek, 1997). It is also generally assumed that soil carbonates precipitate in isotopic equilibrium with the soil water because of the slow accumulation rates of calcite in soil (Cerling and Quade, 1993; Marion and Schlesinger, 1994). However, long-term accumulation rates do not preclude fast short-term precipitation rates. Isotopic disequilibrium in carbonates can arise in the dissolved inorganic carbon (DIC) pool and as carbonate ions attach to the surface of calcite crystals (DePaolo, 2011). Complete isotopic equilibrium is likely never achieved in natural carbonate systems (Daëron et al., 2019; Gabitov et al., 2012), but the relatively fast rate of DIC equilibration at the moderate pH values of soil waters likely conspire to produce apparent equilibrium Δ_{47} values in soil carbonates (Watkins et al., 2014; Watkins and Hunt, 2015). Indeed, kinetic effects have only

been documented in natural soil carbonates from cold environments that form though cryogenically induced precipitation (Burgener et al., 2018, 2016).

In apparent equilibrium conditions, the $\delta^{13}C$ values of soil carbonates are derived from the $\delta^{13}C$ of soil CO_2, which is a mixture of biogenically-respired soil and atmospheric CO_2 (Amundson and Lund, 1987; Breecker et al., 2009; Cerling et al., 1991; Cerling and Quade, 1993). In most soils, $\delta^{13}C$ values of soil carbonates decrease with depth (e.g., Cerling, 1984; Cerling and Quade, 1993; Quade et al., 1989). Seasonal biases of $\delta^{13}C$ are generally not considered, although seasonal variations in plant growth and soil respiration would impart a seasonal bias in $\delta^{13}C$ of soil CO_2 (Breecker et al., 2012). Soil carbonate $\delta^{18}O$ values (here $\delta^{18}O_c$) are controlled by the oxygen isotope composition of the soil water ($\delta^{18}O_{sw}$) and the temperature of calcite precipitation (Cerling and Quade, 1993; Quade et al., 2007a). $\delta^{18}O$ values of soil water are primarily controlled by $\delta^{18}O$ values of rainfall (Tan et al., 2017), but can also be affected by evaporation in the near-surface (Breecker et al., 2009; Huth et al., 2019; Liu et al., 1996; Oerter and Amundson, 2016; Oshun et al., 2015), as well as freezing, or storage and mixing with other local waters like snowmelt (Gazis and Feng, 2004; Sprenger et al., 2018). Agreement between $\delta^{18}O$ values of local meteoric waters (rivers or rain) and $\delta^{18}O_{sw}$ calculated from $\delta^{18}O_c$ and an assumed temperature (usually mean annual air temperature) has been observed, with little discussion of seasonal bias in $\delta^{18}O_c$ (Cerling and Quade, 1993; Hoke et al., 2009; Peters et al., 2013; Quade et al., 2007a). However in some locations, the calculated $\delta^{18}O_{sw}$ is most similar to $\delta^{18}O$ values of meteoric waters (rain or soil water) from the assumed month of soil carbonate formation (Gallagher and Sheldon, 2016; Hough et al., 2014; Huth et al., 2019), suggesting that $\delta^{18}O_c$ may be seasonally biased in some environments not only because of temperature of formation but also because of seasonal changes in the $\delta^{18}O$ value of soil waters.

The Δ_{47} value of a carbonate mineral is a thermodynamically-based estimate of its growth temperature. Δ_{47} refers to a measurement of the concentration of ^{13}C-^{18}O bonds relative to their expected concentration if the isotopes were randomly distributed among isotopologues. ^{13}C-^{18}O bonds are more energetically favorable at lower temperatures, so their concentration can be used as a thermometer (Eiler, 2007, 2011; Ghosh et al., 2006a; Schauble et al., 2006). Assuming isotopic equilibrium is achieved, the Δ_{47} value of soil carbonate is controlled by the ambient temperature of the soil. Daily and seasonal temperature fluctuations at the surface decrease in amplitude with depth in a soil column, as described by heat diffusion equations (Hillel, 1982; Quade et al., 2013; Radcliffe and Šimůnek, 2010). Thus it has been predicted that the Δ_{47} value of soil carbonates should depend on the season and depth of formation (Peters et al., 2013; Quade et al., 2013).

Comparisons between environmental conditions (e.g., air and soil temperature) and Δ_{47} values of Holocene soil carbonates have been made in various settings (Figure 3-1) with the purpose of deciphering seasonal biases of carbonate formation (Burgener et al., 2016, 2018; Gallagher and Sheldon, 2016; Hough et al., 2014; Huth et al., 2019; Passey et al., 2010; Peters et al., 2013; Quade et al., 2011, 2013; Ringham et al., 2016). Initial observations suggested that carbonate formation was warm-season biased (Breecker et al., 2009; Passey et al., 2010; Quade et al., 2013). Many early TΔ_{47} values were similar to peak summer temperatures or even hotter, interpreted to be due to radiative solar heating of the ground surface (Burgener et al., 2016; Hough et al., 2014; Passey et al., 2010; Quade et al., 2013; Ringham et al., 2016). In New Mexico, calcite solubility was measured to be lowest during periods of increasing soil temperature (Equation 3-1) (Breecker et al., 2009), consistent with empirical evidence for a warm season bias in carbonate formation. However, subsequent observations showed soil

carbonates yield growth temperatures similar to mean annual temperature in certain locales (Burgener et al., 2016; Gallagher and Sheldon, 2016; Peters et al., 2013). These inconsistencies point to a need to re-evaluate the often-assumed summer bias in soil carbonate formation and consider alternative processes that could promote formation at other times of the year.

One hypothesis that has emerged from studies of modern soil carbonates is that the annual timing of changes in soil moisture governs the timing of carbonate formation (Burgener et al., 2016; Gallagher and Sheldon, 2016; Huth et al., 2019; Meyer et al., 2014; e.g., Peters et al., 2013). For example, differences in the timing of rainfall were used to explain the variation in $T\Delta_{47}$ biases across a precipitation-seasonality divide in the Andes (Peters et al., 2013). Timing of snow melt was invoked to explain $T\Delta_{47}$ values similar to MAAT at high altitudes in the Chilean Andes (Burgener et al., 2016). A related hypothesis is that the rate of change in soil moisture content will be moderated by the soil texture (Blodgett, 1988; Burgener et al., 2018). Fine-grained soils (silt or finer) retain moisture, while coarse-grained soils (sand or coarser) dry relatively quickly after rain events (Bouma and Bryla, 2000). Also, the timing of plant growth could be important as plants respire CO_2 and their roots uptake water (Meyer et al., 2014; Ringham et al., 2016). These previous studies of Δ_{47} in Holocene soil carbonates each developed hypotheses to explain site-specific observations and point to the importance of understanding soil moisture. However, a holistic understanding for how to interpret Δ_{47}, $\delta^{13}C$, and $\delta^{18}O$ values of soil carbonates has not yet emerged. Here we synthesize existing soil carbonate Δ_{47} data with the goal of deciphering broad patterns in environmental conditions that can explain varied seasonal biases in a global dataset of Holocene soil carbonates.

3.3 Methods: Datasets Considered

3.3.1 Compiling Isotopic and Environmental Data

We compiled all studies that have published Δ_{47} (and concurrent $\delta^{13}C$, $\delta^{18}O$ measurements) of Holocene soil carbonates that are accompanied with meteorological data from *in situ* monitoring and/or nearby weather stations. Table 3-1 lists the studies considered and the type of meteorological data. We trust the assumption made by the previous studies that the soil carbonates formed at a constant depth and under conditions similar to the monitoring period of the environmental data. The methods used to identify and date Holocene carbonates vary by study: methods range from identifying and sampling young soils based on landscape position to radiocarbon dating of soil carbonate. We do not include samples that the original studies identified as having precipitated in isotopic disequilibrium and/or as a statistical outlier (the cryogenic and outlier samples from Burgener et al. (2016) and Burgener et al. (2018)).

Each sample was assigned a mean annual air temperature (MAAT) and mean warm season temperature (MWST, defined as the mean temperature of the warmest three months, which is either JJA or DJF in all places except the tropics, where it is MJJ). The air temperature data come from a variety of sources: at best, carbonate samples were collected from soil pits with weather monitoring stations (Burgener et al., 2016; Peters et al., 2013; Ringham et al., 2016). For most samples, temperature data come from weather stations at a similar elevation that are within a few kilometers of the sample collection site (Table 3-1). In some cases, temperatures were extrapolated between elevations to estimate a more accurate temperature at the given sample site. Although soil temperature differs from air temperature, we have gathered air temperature data to compare to $T\Delta_{47}$ data because air temperature is generally the parameter of interest for paleoclimate reconstructions, and because direct observations of local soil temperature were not available for all samples.

We assigned the primary season of precipitation (defined as the season (JJA vs. DJF) that has the highest proportion of annual precipitation) to each sample based on examining local weather station records. The $\delta^{18}O$ value of precipitation at each sample location was estimated using the Oxygen Isotopes in Precipitation Calculator (OIPC) (Bowen and Revenaugh, 2003), which is an algorithm that interpolates between point measurements of $\delta^{18}O$ values of rainfall (from the Global Network of Isotopes in Precipitation, GNIP (IAEA/WMO, 2019)) to produce global maps of $\delta^{18}O$ values. We consider $\delta^{18}O$ values of mean warm season rainfall ($\delta^{18}O_{MWS}$), and $\delta^{18}O$ values of annual rainfall (weighted by monthly precipitation, $\delta^{18}O_{ann}$).

Vegetative cover at each location was determined using the MODIS landcover dataset (Friedl et al., 2010), which uses an algorithm to classify satellite into land cover types at 500m resolution. Various algorithms exist that differ in how to categorize vegetative cover types for the sites examined, but the schemes that we examined all agreed in their classification of the of barren/non-vegetated sites. Thus, we simplify the land cover classification and describe our sites as vegetated vs. non-vegetated. This simplification allows us to avoid making assumptions about the stability of the type of vegetation cover, like the proportion C3/C4 plants through the Holocene at a given sampling site (Ringham et al., 2016), and also circumvents the need to re-classify with sites that are classified as 'urban' or 'cropland' – categories that are likely not pertinent to the carbonate that have been forming in soils before human occupation. This simplification is also consistent with a compilation of air and soil temperature data that show little difference in radiative heating amongst vegetation categories (Burgener et al., 2019). The sites that are categorized as 'non-vegetated' likely have some sparse vegetation.

Soil texture of the matrix surrounding each sample was evaluated from descriptions in supplementary material, photographs of the soil pits, field notes, and personal communication

with authors (Table 3-1). Each sample is assigned a soil texture category, where 'fine' indicates clay/silt, 'medium' indicates silt loam/sand (can contain minor gravels, as is the case for pendant samples), 'coarse' indicates matrix-supported gravels (gravels of about 50% or more of matrix, identified visually from pictures or in descriptions), and 'very coarse' indicates clast-supported gravels. In the case of carbonate pendants, the soil texture refers to the average matrix grain size, not the size of the clast on which the carbonate pendants formed.

3.3.2 Updating Clumped Isotope Temperatures to Modern Standards

The Δ_{47} data in this compilation were acquired during a time of rapid methods development. We take several steps to update all data to be consistent with modern standards for number of replicate analysis and methods of calculation and standardization.

The first relatively recent advancement was the development of the 'absolute reference frame' or carbon dioxide equilibrium scale (CDES), created to enable interlaboratory comparison (Dennis et al., 2011). Many of the first analyses of modern soil carbonates were performed and published before the establishment of the CDES and are presented in the 'Ghosh' or 'Caltech' reference frame, which references sample data to measurements of carbon dioxide equilibrated at 1000 °C (e.g., Huntington et al., 2009); Δ_{47} data referenced in this way include analyses in Passey et al. (2010). Some Δ_{47} values were retroactively projected into the CDES for publication (Quade et al., 2013; Peters et al., 2013; Hough et al., 2014). We include these data in our compilation but acknowledge that these Δ_{47} values might have additional, unquantifiable uncertainties.

Early clumped isotope studies reported a single analysis for a sample (an analysis is defined as a single acid digestion of carbonate and measurement of the resulting CO_2). Now it is recognized that the small size of the Δ_{47} signal mandates more than a single analysis to produce

robust data (Fernandez et al., 2017). Three or more replicates is typically considered a minimum to achieve the desired precision (Petersen et al., 2019; Spencer and Kim, 2015) and in some cases 5-6 replicate analyses are performed (~14 is considered a minimum for the LIDI analysis method, Müller et al., (2017)). We therefore conservatively remove Δ_{47} data for samples with only a single replicate from all studies (Figure 3-2).

Recent work shows that the importance of the choice of parameters used to correct for the presence of ^{17}O-bearing CO_2 molecules that interfere with the measurement of ^{13}C- and ^{18}O-bearing CO_2 molecules values: these values effect the accuracy of Δ_{47} values (Daëron et al., 2016; Kelson et al., 2017; Schauer et al., 2016). Clumped isotope workers originally used the ^{17}O correction parameters recommended by Santrock et al. (1985) (Huntington et al., 2009). However, these values, which are based on terrestrial water and rock data for the quartz-water system, can produce spurious Δ_{47} values for carbonates (Daëron et al., 2016; Schauer et al., 2016). The ^{17}O values recommended by IUPAC (Brand et al., 2010) are more appropriate for carbonates and largely eliminate such errors; it is recommended that all future studies use those parameters (Daëron et al., 2016; Petersen et al., 2019; Schauer et al., 2016). Here, we recalculate $\delta^{13}C$, $\delta^{18}O$, and Δ_{47} values using the ^{17}O correction parameters recommended by IUPAC (Brand et al., 2010) where possible (Table 3-1, Figure 3-2).

To calculate temperatures from Δ_{47} values that were calculated with the IUPAC parameters, an empirical calibration that was constructed using measurements made with IUPAC parameters should be used. In most cases, this requires the use of a T-Δ_{47} calibration that differs from that used in the original publication of the Δ_{47} data. Most recent empirical calibrations are converging on a similar Δ_{47} -temperature sensitivity of approximately 0.04 ‰/°C, but some discrepancies still remain among labs, particularly in intercept (Bonifacie et al., 2017; Kele et al.,

2015; Kelson et al., 2017; Levitt et al., 2018; Peral et al., 2018; Petersen et al., 2019). Thus, for each dataset, we use a T-Δ_{47} calibration that was produced in the same laboratory as the soil carbonate data and that has been calculated with the IUPAC parameters (Table B-4). These calibrations were reported in the supplementary table 5 of Petersen et al. (2019). In all cases, we use an acid fractionation factor (AFF, $\Delta^*_{25\text{-}90}$) of 0.088 ‰ to project samples reacted at 90 °C into the 25 °C reference frame, and an AFF of 0.072 ‰ to project samples reacted at 75 °C into the 25 °C reference frame ($\Delta^*_{25\text{-}75}$), based on AFFs recalculated from 4 studies using IUPAC parameters (Petersen et al., 2019).

Analytical error in the Δ_{47} values is reported as the standard error of the mean (S.E.) of replicate analyses of each carbonate sample (S.E. is defined as the standard deviation (S.D.) divided by the square root of the number of replicates). To calculate S.E., most studies employed the long-term S.D. of a carbonate standard (carbonate standard information is listed in footnote of Table 3-1). Any natural variability or heterogeneity is in addition to this analytical error. Where relevant, the oxygen isotopic composition of the soil water from which the soil carbonate grew ($\delta^{18}O_{sw}$) is recalculated using the IUPAC-recalculated $\delta^{18}O_c$ values and TΔ_{47} and the fractionation factor from Kim & O'Neil (1997).

3.4 Results

3.4.1 Updated TΔ_{47} Values

Of the 208 published Δ_{47} values from Holocene/recent soil carbonates, a total of 129 samples have >1 replicate analysis (study-specific information in Table 3-1). The data necessary to recalculate Δ_{47} values with updated ^{17}O parameters were available from supplementary data or personal communication with authors of the following studies: Burgener et al. (2016), Ringham

et al. (2016), Hough et al. (2014), and Gallagher and Sheldon (2016) (Table 3-1). The Δ_{47} values of the samples in Burgener et al. (2018) were initially published using the Brand et al. (2010) parameters, so no re-calculation was needed. We were not able to recalculate the Δ_{47} values from Passey et al. (2010), Quade et al. (2013), or Peters et al. (2013). These data are included despite not being recalculated because the data from those studies were generated at Caltech and due to the isotopic composition of the reference gases used in that laboratory, the data likely do not have significant systematic errors from the use of the Santrock et al. (1985) parameters (Bonifacie et al., 2017; Schauer et al., 2016). Two soil carbonate samples from Peters et al. (2013) (D2-50 and C-50) each had a single additional analysis performed at the University of Washington Isolab in 2015 that were reported in Ringham et al. (2016). However, we have do not consider their Δ47 values because they are not replicated.

As predicted by Daëron et al. (2016) and Schauer et al. (2016), the magnitude and direction of change in Δ_{47} due to using Brand et al. (2010) parameters depends on the isotopic composition of the natural sample and of the standards used by each laboratory and each analysis session (Figure B-1). The largest observed changes in final calculated temperature ($T\Delta_{47}$) were in samples from Burgener et al. (2016) (up to 11 °C change), Hough et al. (2014) (up to 9 °C change), and Ringham et al. (2016) (up to 8 °C change) (Appendix B).

3.4.2 Carbonate sample locations, carbonate types, and soil texture

The 119 samples that that have more than one replicate are biased both in the geographic location and type of Holocene soil carbonates. Most soil carbonates were collected from North and South America, with only seven sample collection sites from Asia, three from Africa, and one from the Arctic (Svalbard). Most of the soil carbonates in this compilation are carbonate

rinds (pendants) that form on the underside of large clasts. Only a handful of the samples are carbonate nodules (all 11 samples from Gallagher and Sheldon (2016); the Inner Mongolia and California samples from Passey et al. (2010)).

Table B-1 summarizes the soil texture classification for each sample. Most of the samples are categorized as medium, coarse or very coarse-grained substrates (27, 34, and 33 samples, respectively). Only six samples are categorized as fine-grained substrates, most of which come from the Gallagher and Sheldon (2016) study.

The MWST, MAAT, primary season of precipitation, and $\delta^{18}O$ values of precipitation ($\delta^{18}O_{MWS}$ and $\delta^{18}O_{ann}$) for each location can also be found in Table B-1, Table B-2, and Table B-3. Quade et al. (2013) only reported hottest month mean temperature for their locations, so that value is used instead of MWST.

Comparison between $T\Delta_{47}$ and ambient air temperatures suggests significant variability in the seasonal timing of carbonate formation (Figure 3-2). Most samples exhibit a warm-season bias, with $T\Delta_{47}$ values that are larger than MAAT: the mean exceedance from MAAT is 9 °C, and the mean exceedance from MWST is 2°C (Table 3-2). However, the difference between $T\Delta_{47}$ values and MAAT ranges from -8 to 24 °C, demanding an explanation for the observed significant variation in seasonal bias.

3.5 Discussion

Previous studies have hinted that soil moisture, and more specifically the timing of soil drying, is a primary control of the timing of soil carbonate formation. If soil moisture is important, it follows that soil texture and season of precipitation should directly influence the timing of soil carbonate formation, and that the presence/absence of vegetation might also play a

role. We evaluate the ability of precipitation seasonality and soil texture to explain the observed variability in the seasonal bias of $T\Delta_{47}$ values. The compiled and updated data suggest that most soil carbonates record a temperature that is biased towards the warm season, but there is variability in the magnitude of this bias. We show that updating Δ_{47} and $T\Delta_{47}$ values to modern standards does not explain this variability (Figure 3-2); an improved process-based understanding of soil carbonate formation is required. Therefore, we explore how $T\Delta_{47}$ relates to depth below ground surface, soil texture, season of precipitation, and presence of vegetation.

3.5.1 Updating Δ47 values does not fully explain the variable magnitude of difference between MAAT and Δ47 temperatures

Recalculating Δ_{47} values with updated ^{17}O correction parameters and corresponding temperature calibrations and culling data based on lack of replication might be expected to reduce variability in the residual between $T\Delta_{47}$ and mean annual air temperature. The culling step that makes the most difference is removing samples with only one replicate analysis: this step reduces the mean residual from mean annual temperatures ($T\Delta_{47}$ – MAAT) from 12.0 to 9.8 °C) and also reduces the standard deviation of that residual from 7.3 to 6.2 °C (Figure 3-2). This reduction in the mean residual and its variance comes from the removal of 43 single-analysis samples with $T\Delta_{47}$ that exceeded MAAT by >10 °C, 16 of which exceeded MAAT by >20 °C (most of which are from the earliest two studies, Passey et al. (2010) and Quade et al. (2013), Figure 3-2). These extremely high $T\Delta_{47}$ values were previously explained by local radiative heating (Passey et al., 2010; Quade et al., 2013). However, given this reanalysis it seems that the hot temperatures previously reported are better explained by the use of an overly sensitive T-Δ_{47} calibration and/or poor analytical replication. The idea that radiative heating should not be commonly recorded in soil carbonate growth temperatures agrees with monitored soil

temperatures: a comparison of soil and air temperatures from the Soil Climate Analysis Network (SCAN) suggests that soil temperatures only exceed summer air temperatures by 5 °C at shallow depths in extremely arid conditions (MAP 0 to 30 cm/year) (Burgener et al., 2019). On average, soil temperatures at depths >20 cm do not exceed surface temperature by more than 3 °C in all land cover types (Burgener et al., 2019). This observation is consistent with other direct field measurements of ground temperatures that exceed air temperatures by <4 °C (Bartlett et al., 2006; Breshears et al., 1998; Cermak et al., 2017; Passey et al., 2010).

For samples with >1 replicate, the step of recalculating the Δ_{47} values using IUPAC ^{17}O parameters does not significantly change the mean or variance of the observed residual from MAAT. The $T\Delta_{47}$ for some individual samples and studies changes by up to 11 °C, but the magnitude and direction of change varies on a sample-basis (Supplementary Text S1, (Figure 3-2). The as-published and recalculated $T\Delta_{47}$ values for replicated samples are characterized by a mean warm-season residual ($T\Delta_{47}$ minus MWST) of 9.8 and 9.0 °C, respectively (S.D. = 6.2 °C for both) (Figure 3-2). The variation in observed seasonal bias is large compared to the ~2 °C precision usually desired to adequately reconstruct paleoclimate conditions, making the interpretation of $T\Delta_{47}$ of paleosol carbonates uncertain. In the following sections, we explore the extent to which variance in the relationship between air temperature (MAAT and MWST) and the observed $T\Delta_{47}$ values can be explained by sample depth, soil texture, and seasonality of precipitation.

3.5.2 Relationship between $T\Delta_{47}$ and depth in a soil column

Soil temperature varies with depth and time as fluctuations in temperature at the surface propagate downward. Daily and seasonal temperature fluctuations decrease in amplitude with

depth in a soil column by a characteristic exponential factor: soil temperatures in the upper ~40 cm vary on a daily basis while temperatures at depths of ~40-300 cm vary on a seasonal basis (Quade et al., 2013). We might therefore expect systematic warm-season bias in soil carbonate accumulation to result in carbonate temperature increasing toward the surface in the upper 100 cm of soil; such an increase in carbonate temperature toward the surface was observed by Quade et al. (2013) in one of the first studies of Δ_{47} of soil carbonates. However, subsequent workers found that $T\Delta_{47}$ does not vary systematically with depth within a single soil profile (Burgener et al., 2016; Peters et al., 2013; Ringham et al., 2016). We re-evaluate the variation of $T\Delta_{47}$ with depth in the updated compilation.

The compiled $T\Delta_{47}$ depth profiles of soil pits includes the majority of data from Peters et al. (2013), Burgener et al. (2016) and Ringham et al. (2016), as well as the Huachuca pit from Quade et al. (2013). Unfortunately, the Quade et al. (2013) data that showed systematic warming of carbonate formation temperatures near the surface were based on un-replicated Δ_{47} analyses. Within the 15 soil pits with replicated data, $T\Delta_{47}$ does not vary systematically with depth (from 0 to 150 cm) within measurement error (Figure 3-3, Figure B-2). 68 of the 75 individual carbonate samples in the updated compilation of depth profiles have a $T\Delta_{47}$ value that is within 1 S.E. of the mean temperature of the profile (Figure B-2). Only one shallow sample has a $T\Delta_{47}$ value that exceeds summer air temperatures by an amount that suggests radiative heating has affected shallow soil temperatures (CAN01-10, from Ringham et al., 2016, $T\Delta_{47} = 42 \pm 4$ °C vs. MWST = 25 °C). The observed uniform $T\Delta_{47}$ values within a soil column could result from the following end-member scenarios: 1) soil carbonate accumulates approximately simultaneously at all depths during times when temperature is uniform with depth in a soil, or 2) soil carbonate formation occurs at different times at different depths but result in the same growth temperature within

measurement precision (usually ± 2 °C). Either scenario should be consistent with the available Δ_{47}, $\delta^{13}C$, and $\delta^{18}O$ values.

The simplest explanation for the observed uniform $T\Delta_{47}$ values with depth is that soil carbonate at all depths form simultaneously when temperatures are uniform. Such uniform temperatures at depth in a soil column can occur following rain events as percolating rainwater moves downward, especially in coarse-grained soils where minimal rainwater-bulk soil contact could allow rainwater to percolate without changing temperature (as shown in meteorological data collected by Ringham et al., 2016). The $\delta^{13}C$ and $\delta^{18}O$ data are not necessarily consistent soil carbonate formation following rain/wetting events. $\delta^{13}C$ values increase toward the surface and generally resemble the prediction for $\delta^{13}C$ with depth that is calculated from a CO_2 production-diffusion model (described in Quade et al. (1989); Cerling (1984)) (this is especially true for the pits Elq13-1300, A Peters, Eql3-2700, D2 Peters, DL01 Ringham, CA Passey, see Figure B-2). This systematic $\delta^{13}C$ decrease with depth might suggest that soil carbonate is forming under conditions of time-constant or time-averaged soil respiration. However, soil respiration can spike following wetting events (Borken et al., 2003; Bowling et al., 2011; Lee et al., 2004; Liu et al., 2002; Tang and Baldocchi, 2005) – so perhaps the $\delta^{13}C$ data is inconsistent with carbonate formation after storms when soil CO_2 is changing rapidly. Furthermore, we might expect such percolation of rainwater to remove or dampen the near-surface evaporative enrichment in ^{18}O, but the soil pit data do show an increase in $\delta^{18}O$ values toward the surface (Figure B-2).

Given this isotopic evidence, it remains equally possible that soil carbonates form at different times at different depths but result in near-uniform $T\Delta_{47}$ profiles. This might occur because near-surface soil carbonates are more vulnerable to daily fluctuations in

temperature/precipitation and form during drying after small rain events throughout the year, while deeper carbonate only form after large rain events and/or during seasonal drying (McFadden and Tinsley, 1985; Retallack, 2005; Ringham et al., 2016). This process of soil carbonate formation implies that near-surface carbonates (0-39 cm in depth, where 40 cm is maximum depth affected by daily temperature fluctuations) record an isotopic signal that is more variable and more challenging to interpret than carbonates at depths >40 cm. This variation in timing of formation, even within a single soil pit, could explain some of the variance in soil carbonate $\delta^{13}C$ and $\delta^{18}O$ data, which can be rather large even at a single depth within a single soil.

This dataset suggests that $T\Delta_{47}$ is uniform with depth in the studied environments but further research is necessary to explain why. Given this uncertainty, and the documented variability in $\delta^{13}C$ and $\delta^{18}O$ values, we maintain the longstanding recommendation that near-surface carbonate samples (approximately 0-40 cm in depth) should be avoided for use in paleoclimate reconstructions (Cerling and Quade, 1993; Quade et al., 2007a, 2013). We simplify the remainder of the discussion by conservatively disregarding the samples collected from 0–39 cm in depth. Removing these near-surface samples from the compilation dataset increases the mean bias between soil carbonate $T\Delta_{47}$ and MAAT from 9.0 to 9.3 °C and reduces the S.D. from 6.2 to 5.6 °C (Figure 3-2). We note that most of the difference in the mean and S.D. from removing near-surface samples comes from the exclusion of 7 of the shallow (30 cm deep) carbonate samples from Gallagher and Sheldon (2016) with exceptionally low $T\Delta_{47}$ values. It is possible that the unusual $T\Delta_{47}$ values of these shallow samples is due to their relatively fine-grained matrix texture, carbonate type or some other factor, rather than their depth.

3.5.3 Soil texture and TΔ_{47} values

The grain size of a soil matrix is a primary control its hydraulic properties (e.g., Carsel and Parrish, 1988; Fredlund and Xing, 1994) so it has been suggested that grain size could influence the timing of soil carbonate formation (Burgener et al., 2018). Because fine-grained soils retain moisture better than coarse-grained soils, the timing of soil drying should differ with soil texture. Also, the coefficient for CO_2 diffusion out of a soil column also depends on grain size, such that if all else is equal soil CO_2 concentrations will decrease more slowly in fine-grained soils (Bouma and Bryla, 2000; Suarez and Šimůnek, 1997). Thus, coarse-grained soils could dry and degas faster than fine-grained soils, which may cause soil carbonate in coarse-grained soils to form sooner after rain events. We examine the compiled dataset for patterns in TΔ_{47} that relate to soil texture.

The four samples that are fine-grained (silty clay) are statistically different from the other sample populations. The fine-grained samples have a mean TΔ47 – MAAT residual of -4 °C (S.D. = 3 °C) (Table 3-2), which is a statistically colder bias than the other texture categories (Table 3-3). Furthermore, a KS-test shows that the fine-grained sample group are unlikely to have come from the same continuous underlying distribution as the other sample types (Table 3-3, Figure 3-4). However, three of the four fine-grained samples are from a single study (Gallagher and Sheldon, 2016) and the fourth sample is from Ethiopia (Passey et al., 2010), where there is no seasonal range in temperature. These data hint that soil carbonates in clay-rich substrates are more likely to have a growth temperature that is closer to MAAT than those from coarse soils, but additional data on soil carbonates from fine-grained soils are needed to rigorously test this hypothesis.

TΔ_{47} data from soil carbonates in the other soil-texture categories (medium, coarse, and very coarse-grained), also suggest that soil texture can explain some of the variability in seasonal bias. Carbonates from the medium, coarse, and very-coarse grained soils have mean seasonal

biases that increase with coarseness in soil texture (mean bias 7.5, 9.5, and 10.5 °C, respectively) (Table 3-2) (Figure 3-4). Although the carbonate samples from these groups likely came from the same continuous distribution (see KS test results in Table 3-2), the means of medium and very coarse are significantly different (*t*-test in Table 3-2) (Figure 3-4). Nonetheless, the trend among texture categories and the significant difference between the means of fine, medium and very coarse textured soils suggests that coarser soils are more likely to have a larger seasonal bias.

In summation, these data suggest that coarser soils are more likely to yield carbonates with a warm season bias compared to clay-rich soils. The difference in seasonal bias is less pronounced when comparing carbonates in adjacent categories from medium- to coarse-grained soils. This reduced difference in seasonal bias when comparing adjacent grain size categories could be due to other environment factors, or perhaps because grain size will slow/speed up soil drying on timescales of days to hours, which is important for determining equilibrium/non-equilibrium formation (Burgener et al., 2018) but not for determining seasonal bias. Another limitation of this current analysis is that we are qualitatively describing soil texture based on photographs and field notes; measurements of grain size distributions are necessary.

3.5.4 Primary season of precipitation and TΔ_{47} values

Previous workers have proposed that soil carbonates form during soil drying, and thus formation should occur after the wettest season of the year (Gallagher and Sheldon, 2016; Peters et al., 2013) or during seasonal warming in especially dry years (Breecker et al 2009). The former predicts that soil carbonates in environments with primarily winter rain are more likely to form in the spring or summer (Peters et al., 2013). Conversely, an overabundance of summer

rain would prevent carbonate formation in that season and would yield carbonates with reduced seasonal biases.

If the annual timing of rain/snow influences the timing of carbonate formation, we should be able to observe a difference in the $T\Delta_{47}$ in this compiled dataset. If this prediction held true, carbonates from environments with winter-dominated rain/snow would yield $T\Delta_{47}$ hotter than MAAT (near agreement with MWST), while carbonates from environments with summer rain would yield $T\Delta_{47}$ more similar to MAAT. The mean residual between $T\Delta_{47}$ and MAAT for the winter rain/snow samples is 11.1 ℃ (n = 43, S.D. = 5 ℃) (Table 3-2) (Figure 3-5), a value that is indeed consistent with a warm season bias at mid latitudes. The mean residual between $T\Delta_{47}$ and MAAT for the summer-rain samples is 7.7 ℃ (n = 43, S.D. = 5 ℃) (Table 3-2) (Figure 3-5), a value that is closer to MAAT and 3.4 ℃ less than that of the winter-rain/snow samples (95 % CI in difference of means from a t-test, (Table 3-2). The warm season bias is less pronounced in the summer-rain samples, upholding the idea that the timing of carbonate formation differs in response to the timing of seasonal rainfall. The observed difference in mean residuals between summer and winter rain/snow samples is true even if the fine-grained samples with a statistically smaller $T\Delta_{47}$-MAAT residual are removed from the sample set (samples come from populations with different means at 95% CI, Table 3-2). Additionally, soil physics might justify cooler soil temperatures for the summer-rain samples: ample rain during the summer months might reduce maximum soil temperatures through higher heat capacity of soil and evaporative cooling (Seneviratne et al., 2010) and, speculatively, through increased vegetative cover (Geiger et al., 2009). Furthermore, the samples with winter precipitation that falls as snow might have relatively higher soil temperatures because insulation from snowpack would increase winter

temperatures, and the corresponding reduction in seasonal amplitude could be propagated to depths.

3.5.5 Vegetation Cover and TΔ47 values

Because plants change water, solute, and CO_2 content in soils, their presence and the timing of their activity has been predicted to influence the timing of soil carbonate formation (Meyer et al., 2014; Noy-Meir, 1973; Ringham et al., 2016; Young et al., 2009). No evidence for significantly different $T\Delta_{47}$ values was found in soils that differed in the proportion of C3/C4 vegetation (Ringham et al., 2016), so we simplify this hypothesis to explore if the compiled $T\Delta_{47}$ values exhibits variation given the presence or absence of vegetation.

The mean residual between $T\Delta_{47}$ and MAAT for sites that are vegetated is statistically smaller than that of the non-vegetated sites (7.5 °C vs. 11.6 °C, different at 95% confidence interval with p = 1.84e-4 in a *t*-test) (Table 3-2, Table 3-3) (Figure 3-6). The lower $T\Delta_{47}$-MAAT residual for vegetated sites could be because plant activity promotes carbonate formation during the spring through rootwater uptake and changing soil CO_2 concentrations, even without the benefit of long warm dry spells (Breecker et al., 2009; Meyer et al., 2014). The lower $T\Delta_{47}$-MAAT residual could also be because the shade of vegetated might reduce radiative heating of ground temperatures in the summer (Cermak et al., 2017; Geiger et al., 2009; Passey, 2012). We prefer the former explanation because the depth profiles in this compilation show little evidence for radiative heating (see above) and other empirical evidence that soil temperatures at depths > 50 cm are not affected by radiative heating (Burgener et al., 2019).

3.5.6 No environmental factor is isolated: interactions between season of rain, soil texture, and presence of vegetation that influence the bias in TΔ47

While the environmental factors explored in this paper each explain a portion of the variation in TΔ47 biases, they are not precise predictors of the seasonal bias of soil carbonates: a~20 ℃ range in residual from MAAT exists within each category (Figure 3-4, Figure 3-5, Figure 3-6). Furthermore, regional comparisons highlight the differences in TΔ47 bias even in similar environments: samples from Wyoming at elevations of about 2000 m have $T\Delta_{47}$ values that exceed MAAT by about 10 ℃ (consistent with summer formation) (three carbonate pendant samples from Hough et al., 2014), while samples from New Mexico at similar elevations yield $T\Delta_{47}$ values that are about 5 ℃ colder than MAAT (three carbonate nodules from fine-grained soils sampled by Gallagher and Sheldon, 2016) (Figure B-2). These discrepancies could be explained by a difference in soil texture and/or carbonate type. A similar discrepancy can be found by comparing the samples at elevations of about 1000 m in the eastern Andes: the bias ranges from 0 – 15 ℃ even within samples that are a few kilometers apart (samples from Ringham et al. (2016) and Peters et al. (2013)) (Figure B-3), even in a consistent summer precipitation regime. Those authors suggest that landscape position, such as proximity to an active channel and related seasonal flooding, might explain these apparent differences in $T\Delta_{47}$ (Ringham et al., 2016). An analysis of variance amongst categories fails in part because the variance in $T\Delta_{47}$ due to soil texture overwhelms the variance explained by other factors (driven by the small number of fine-grained samples all with low $T\Delta_{47}$ values). We lack data from fine-grained soils in winter-rain environments or from non-vegetated environments. We also lack samples from non-vegetated environments, especially in summer-rain environments.

However, we can make some hypotheses about how these environmental factors would interact to affect seasonal bias. For example, we might predict that the timing of carbonate

accumulation is sensitive the spacing between rain events but modulated by soil texture: particular spacing between rain events might promote soil drying given coarse but not fine-grained soil texture. In other climates, adequately long dry spells might allow for carbonate accumulation during the summer regardless of soil texture, or plentiful summer rain would prevent summertime carbonate formation regardless of soil texture. Snowpack depth and the timing of snowmelt and its percolation into the soil column may be another important factor that is not explicitly considered in our interpretation of this dataset (Burgener et al., 2016). The annual timing (and type) of precipitation likely influences vegetative cover and type, which in turn influences soil temperatures and timing of carbonate formation (Meyer et al., 2014). Experiments that can isolate the environmental factors that control soil moisture is a logical next step to understanding the timing of soil carbonate formation. Such controlled experiments might include numerical modeling (Huth et al., 2019), and laboratory and outdoor experiments with controlled environmental conditions.

3.5.7 No seasonal bias observed in comparing $\delta^{18}O$ values of carbonates and rainfall

It has long been assumed that $\delta^{18}O_{sw}$ values calculated from soil carbonate $\delta^{18}O_c$ values reflects $\delta^{18}O$ values of meteoric waters. This agreement has been observed even without the benefit of a precise carbonate growth temperature estimate from $T\Delta_{47}$ (Breecker et al., 2009; Cerling and Quade, 1993; Hoke et al., 2009; Quade et al., 2011), and maintained with measurement of $T\Delta_{47}$ (Burgener et al., 2016; Peters et al., 2013; Ringham et al., 2016). Hough et al. (2014) and Gallagher and Sheldon (2016) put forth the idea that $\delta^{18}O_{sw}$ reflects $\delta^{18}O$ values of precipitation during the month of proposed carbonate formation. Here we use the compiled dataset to investigate apparent seasonal biases in $\delta^{18}O_{sw}$ (compared to $\delta^{18}O$ values of

precipitation) and explore if soil texture and precipitation season explain some of the variability in the bias in $\delta^{18}O_{sw}$ values.

The compiled data show agreement between $\delta^{18}O_{sw}$ and $\delta^{18}O$ values of average annual precipitation (weighted by monthly precipitation) ($\delta^{18}O_{ann}$) (Figure 3-7). Over half of the $\delta^{18}O_{sw}$ values (51 of the 91) are closer to the $\delta^{18}O_{ann}$ values than the $\delta^{18}O$ values of warm season precipitation ($\delta^{18}O_{MWS}$). The r^2 values for linear regressions between $\delta^{18}O_{sw}$ and either $\delta^{18}O_{ann}$ or $\delta^{18}O_{MWS}$ are decent for natural systems ($r^2 = 0.542$, $p = 9.12e^{-17}$, and $r^2 = 0.445$, $p = 5.34e^{-13}$, respectively), but indicate the isotopic composition of rainfall alone does not explain all of the variability in $\delta^{18}O_{sw}$.

There are a multitude of reasons why $\delta^{18}O_{sw}$ values should not be a perfect reflection of (or vary seasonally with) $\delta^{18}O$ values of rainfall, and why carbonate might record $\delta^{18}O_{sw}$ values that are most similar to $\delta^{18}O_{ann}$ values. For example, seasonal variations in $\delta^{18}O$ values of rain could be dampened in soil as rainwater mixes with water stored in soil pores (Mathieu and Bariac, 1996). The rate at which rainwater percolates through the soil depends on rain intensity, depth in the soil, and soil texture. Also, evaporation will likely be depth-and texture-dependent, and overprints all of these soil-hydrology processes (Oerter and Amundson, 2016). Thus, soil texture and timing of rainfall likely both influence $\delta^{18}O_{sw}$ values and shift the value away from $\delta^{18}O$ value of rainfall. We find that the mean residual between $\delta^{18}O_{sw}$ and $\delta^{18}O_{ann}$ values is statistically different for samples from fine-grained vs. coarser-grained samples (Table 3-2, *t*-test results in Table 3-3). Also, the mean residual between $\delta^{18}O_{sw}$ and $\delta^{18}O_{ann}$ values is statistically different for the samples in winter and summer precipitation regimes (Table 3-3). Thus, variations in $\delta^{18}O$ values of soil water (and thus $\delta^{18}O_c$ and $\delta^{18}O_{sw}$) are affected by seasonality of rainfall and soil texture. These environmental conditions likely can either increase or decrease

$\delta^{18}O_{sw}$ compared to $\delta^{18}O$ of rainfall but sum to create $\delta^{18}O_{sw}$ that is similar to $\delta^{18}O_{ann}$ in any given soil.

3.5.8 Implications for paleoclimate reconstructions of the soil-moisture framework for predicting timing of carbonate formation

At present, the apparent variations in seasonal biases have prevented the development of a clear framework for how to interpret paleosol carbonate clumped isotope temperatures. Most workers assume a warm-season bias (Burgener et al., 2019; Ghosh et al., 2006b; Hyland et al., 2018; Ingalls et al., 2018; Lechler et al., 2018; Snell et al., 2013, 2014; Suarez et al., 2011; Újvári et al., 2019), but detailed considerations of environmental factors that would influence that bias are often not included. Increasingly, researchers recognize a varied season bias in soil carbonate formation either due to environmental factors like monsoon rainfall patterns (Licht et al., 2017), or because a shift in seasonal bias is required to explain observed temperature shifts (Page et al., 2019). As soil carbonate Δ_{47} analysis becomes more common, it is likely that secular change in seasonal bias of carbonate formation will be encountered – especially considering the large changes in seasonal precipitation patterns that can occur on million-year time scales as a result of changes in atmospheric concentrations of greenhouse gases (Carmichael et al., 2015; Fricke et al., 2010; Sewall and Sloan, 2006) or changes in topography (Huber and Goldner, 2012; Licht et al., 2014, 2017). Major changes in soil texture through a sedimentary record should be taken into consideration when interpreting seasonal bias. Here we show that the existing Holocene soil carbonate samples from fine-grained soils have $T\Delta_{47}$ values that are similar to MAAT, but Cenozoic soil carbonates from fine-grained paleosols have been interpreted as consistent with MWST (Burgener et al., 2019; Hyland et al., 2018; Kelson et al., 2018). This discrepancy highlights the need for further studies of carbonates from fine-grained

soils. When possible, climate model output could be used to inform relevant precipitation patterns. Apparent differences in the seasonal bias of modern carbonates collected within a kilometer of each other (compare samples collected by Ringham et al. (2016) and Peters et al. (2013)) highlight that robust climate interpretation should rely on analyses of multiple carbonates and/or multiple proxies. Continued efforts to build a process-based understanding of soil carbonate formation will allow future workers to leverage the varied seasonal bias in soil carbonate formation to investigate past temperature seasonality. Paleoclimate reconstructions will be most robust if specific factors that control bias can be identified in a paleosol, or if soil carbonate $T\Delta_{47}$ is combined with temperature estimates from other proxies (Burgener et al., 2019; Hyland et al., 2018; Snell et al., 2013).

3.6 Conclusions

The recalculated dataset compiled here shows that most of the available data from Holocene soil carbonates record $T\Delta_{47}$ values higher than mean annual air temperature. The average bias in $T\Delta_{47}$ in this sample suite suggests that soil carbonates are often representative of mean summer or warm season conditions. However, some $T\Delta_{47}$ values are within error of mean annual air temperature, and when $T\Delta_{47}$ exceeds mean annual air temperature that exceedance can be as high as 24 °C. Within the dataset, $T\Delta_{47}$ does not decrease systematically with depth in the soil, despite the fact that average soil temperatures do decrease with depth in the soil during the warm season. Differences in soil texture, seasonal timing of precipitation, and vegetative cover explain some of the variance in apparent seasonal bias in the global dataset. Despite observing a general warm season bias in $T\Delta_{47}$, we observed that $\delta^{18}O_{sw}$ (calculated from $\delta^{18}O_c$) is better correlated with the

$\delta^{18}O$ value of mean annual of precipitation than the $\delta^{18}O$ value of mean warm season precipitation. Put together, this analysis upholds the hypothesis that the timing of changes in soil moisture likely controls the timing of soil carbonate formation.

For paleoclimate purposes, this dataset suggests that one cannot simply assume that the $T\Delta_{47}$ represents an easily defined climate parameter such as mean summer temperature or peak summer temperature. Changes in environmental conditions (especially rainfall), substrate grain size, and the presence of vegetation through a sedimentary section should be documented and taken into consideration. Further developing a process-based understanding of soil carbonate formation would allow paleoclimate workers to leverage the varied seasonal bias in the isotopic composition of soil carbonates to learn about various seasonal aspects of paleoclimate.

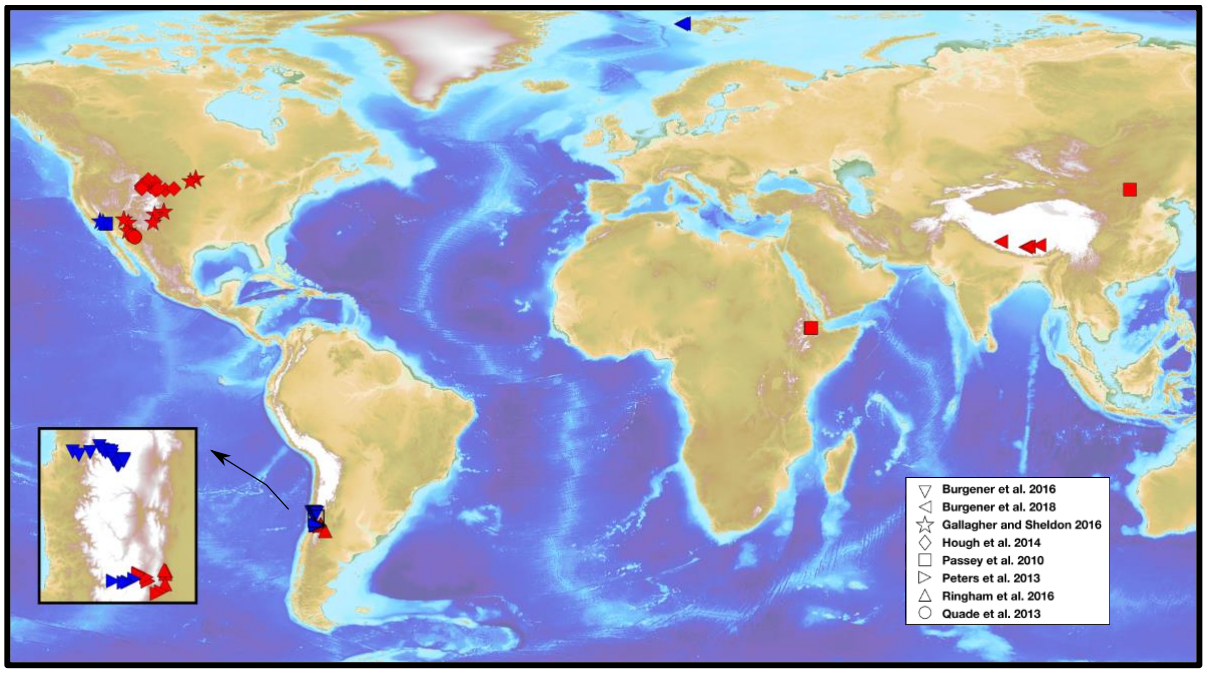

Figure 3-1: Map of modern soil carbonate localities.

Map of localities considered in this study. Red symbol indicates that summer is the primary season of precipitation. Blue symbol indicates that winter is the primary season of precipitation.

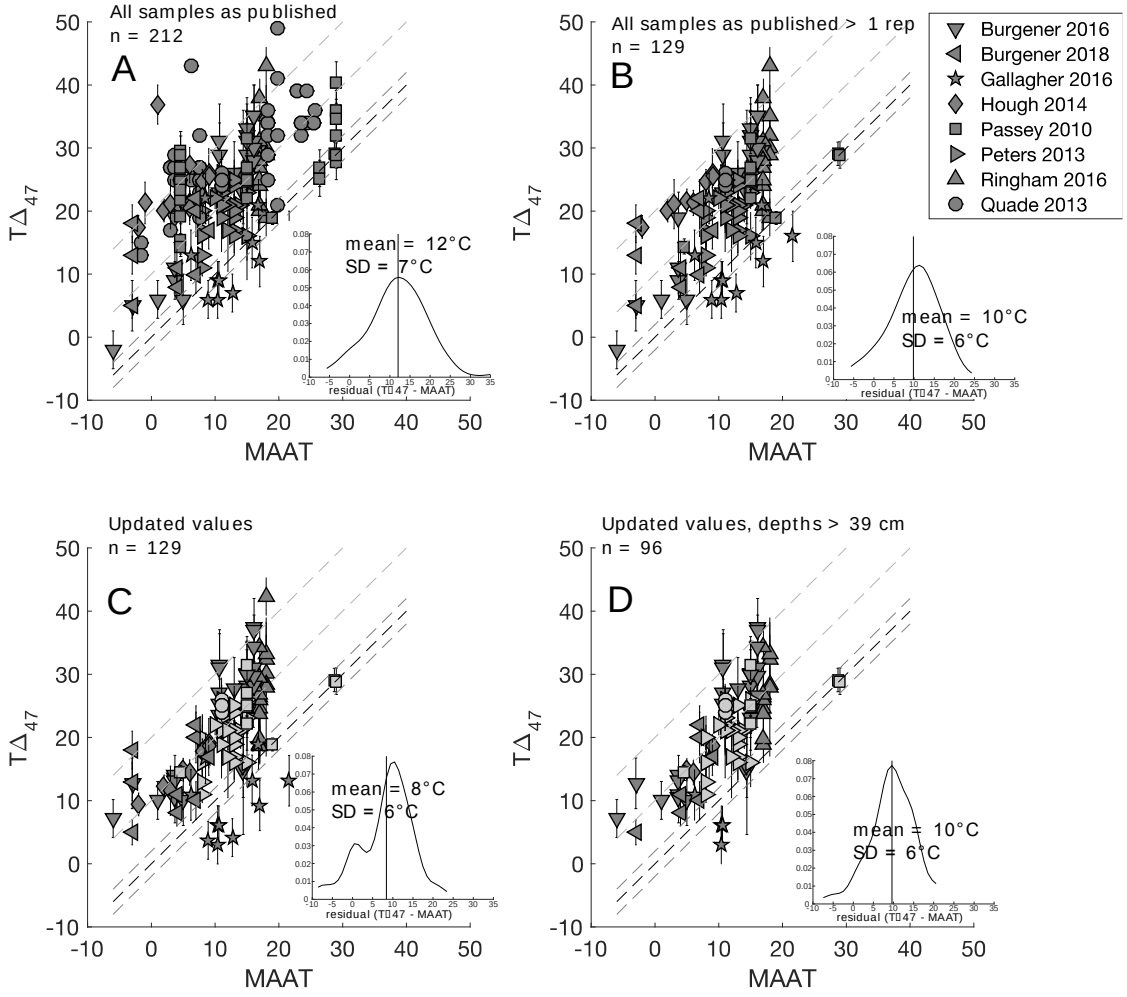

Figure 3-2: Clumped isotope temperature vs MAAT for all Holocene soil carbonate samples included in this work.

In all panels, the dark gray dashed line is 1:1 line and light gray dashed lines are ± 2, +10, and +20 °C. Subplots are kernel density estimates of the residual between MAAT and $T\Delta_{47}$, with mean residual (±1 S.E.) plotted as gray band. **a)** All samples as published in original work. **b)** Only samples that have more than a single Δ_{47} replicate analysis, with $T\Delta_{47}$ values as published in original studies. **c)** As in B, but dark gray samples indicate $T\Delta_{47}$ values have been recalculated to reflect modern standards as described in Section 2.2. Light gray samples are not recalculated (lacked necessary data). **d)** Recalculated $T\Delta_{47}$ data from samples >39 cm in depth.

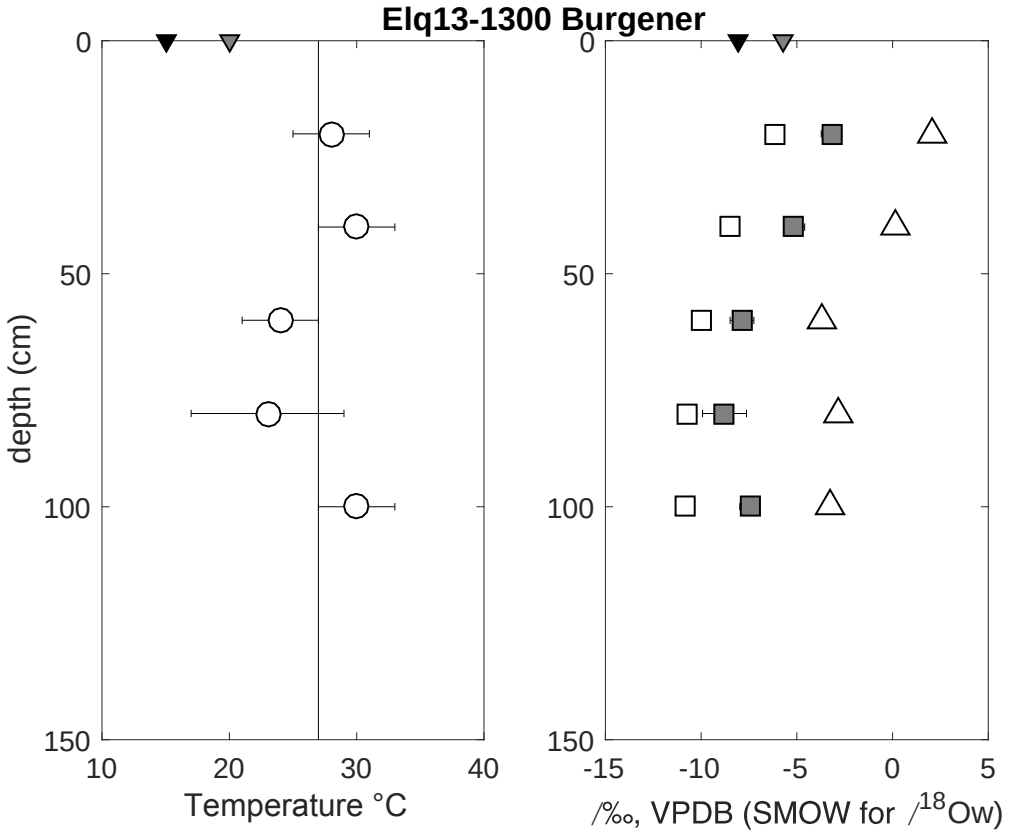

Figure 3-3: Stable isotope depth profiles for soil pit Elq13-1300 (Burgener et al., 2016). Left panel: open circles are $T\Delta_{47}$ values at specific depths. Vertical Gray band is soil pit mean $T\Delta_{47}$ ± 1 S.E. Black/gray triangles on top of plot are MAAT/MWST. Right panel: open squares are $\delta^{18}O_c$, gray squares are calculated $\delta^{18}O_{gw.}$ Black/gray triangles on top of plot are $\delta^{18}O_{ann}/\delta^{18}O_{JJA}$ of rain from OIPC. Open triangles are $\delta^{13}C$.

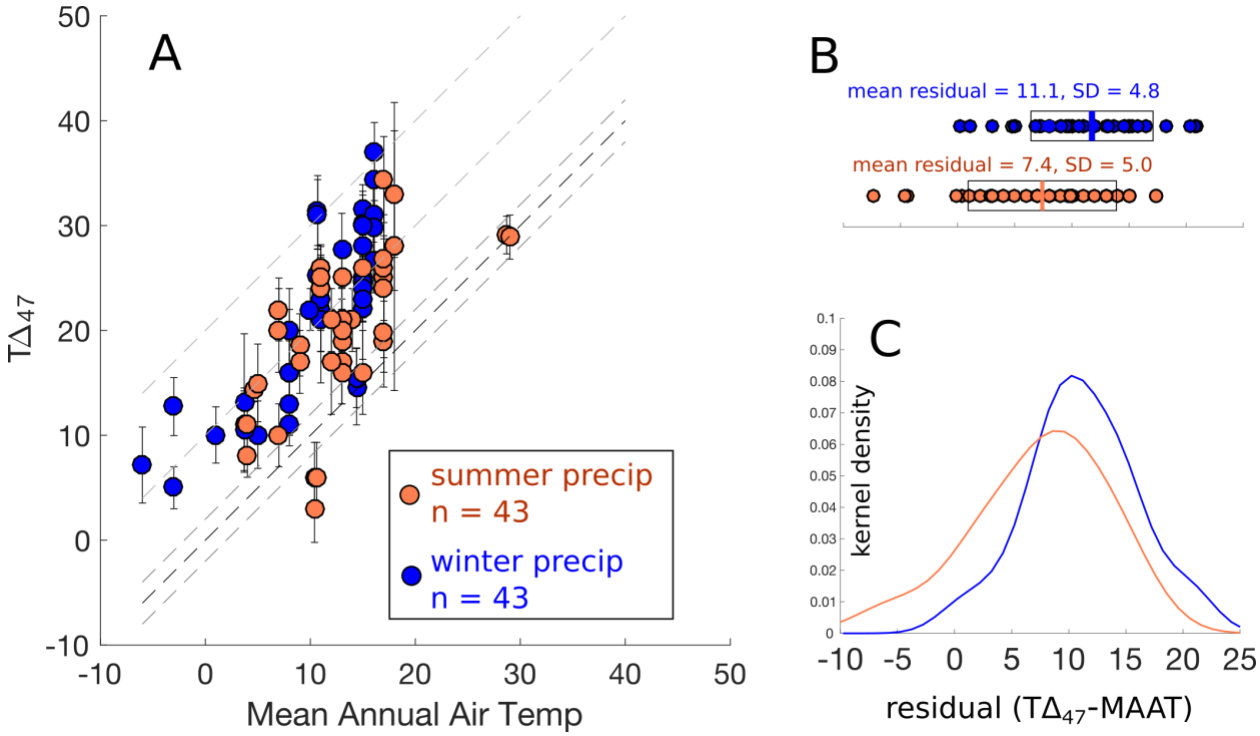

Figure 3-4: Precipitation season and seasonal bias of $T\Delta_{47}$ of soil carbonates

Blue symbol color indicates that the soil carbonate is from an environment with winter-dominated precipitation. Red symbol color indicates that the soil carbonate is from an environment with summer-dominated precipitation. A) Clumped isotope temperature vs mean annual air temperature for carbonates from compiled dataset. Dark gray dashed line is 1:1 line, light gray dashed lines are ± 2, +10, and +20 °C. B) residual between $T\Delta_{47}$ and MAAT for each carbonate sample, binned by season of precipitation. C) Kernel density of the residual.

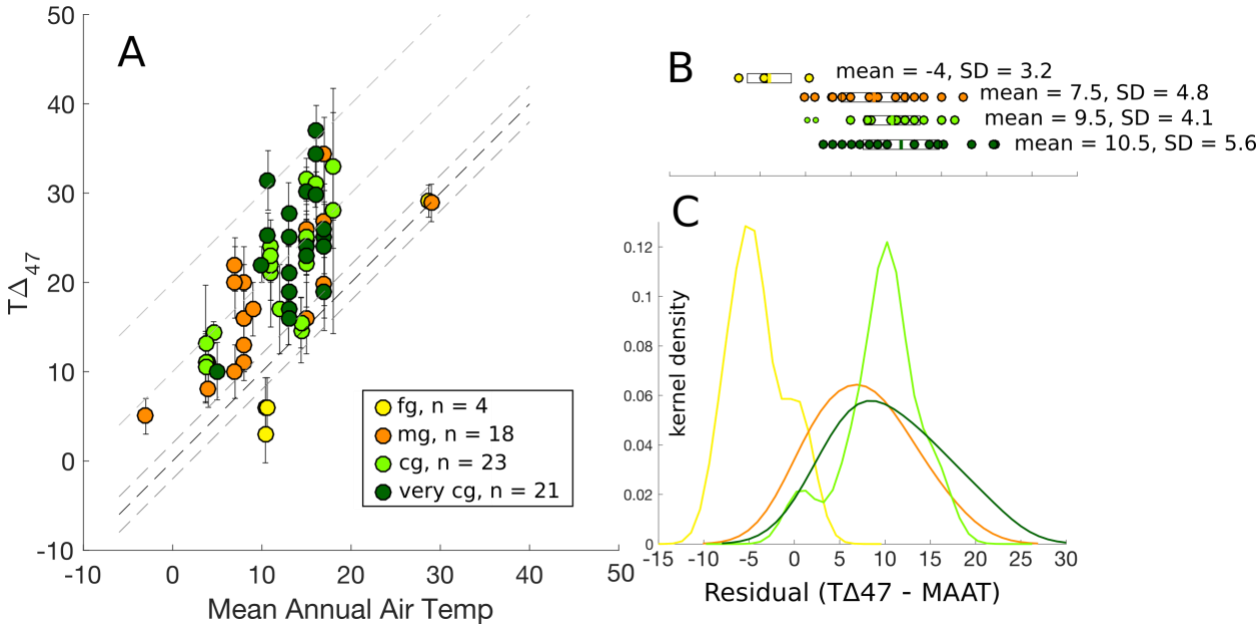

Figure 3-5: Soil texture and the seasonal bias of $T\Delta_{47}$ of soil carbonates

Symbol color indicates soil texture (fine, medium, coarse, and very coarse-grained matrix). A) Clumped isotope temperature vs mean annual air temperature for carbonates from compiled dataset. Dark gray dashed line is 1:1line, light gray dashed lines are ± 2, +10, and +20 °C. B) residual between $T\Delta_{47}$ and MAAT for each carbonate sample, binned by texture. C) Kernel density of the residual.

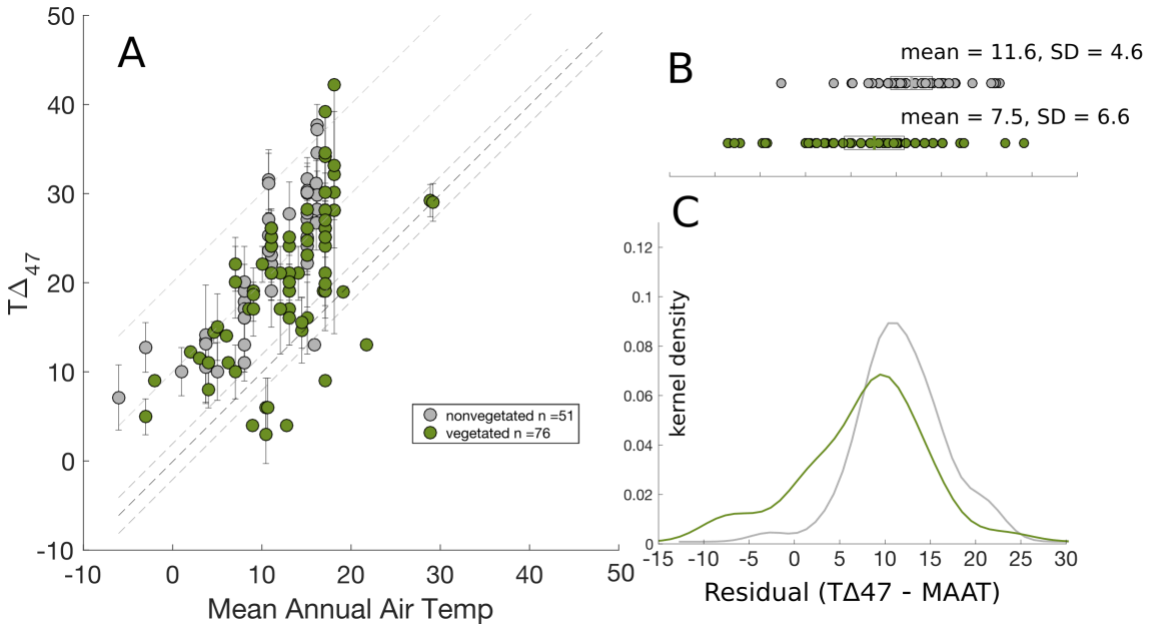

Figure 3-6: Land cover and the seasonal bias of $T\Delta_{47}$ of soil carbonates

Symbol color indicates land cover (green is vegetated, gray is non-vegetated). A) Clumped isotope temperature vs mean annual air temperature for carbonates from compiled dataset. Dark gray dashed line is 1:1 line, light gray dashed lines are ± 2, +10, and +20 °C. B) residual between $T\Delta_{47}$ and MAAT for each carbonate sample, binned by land cover. C) Kernel density of the residual.

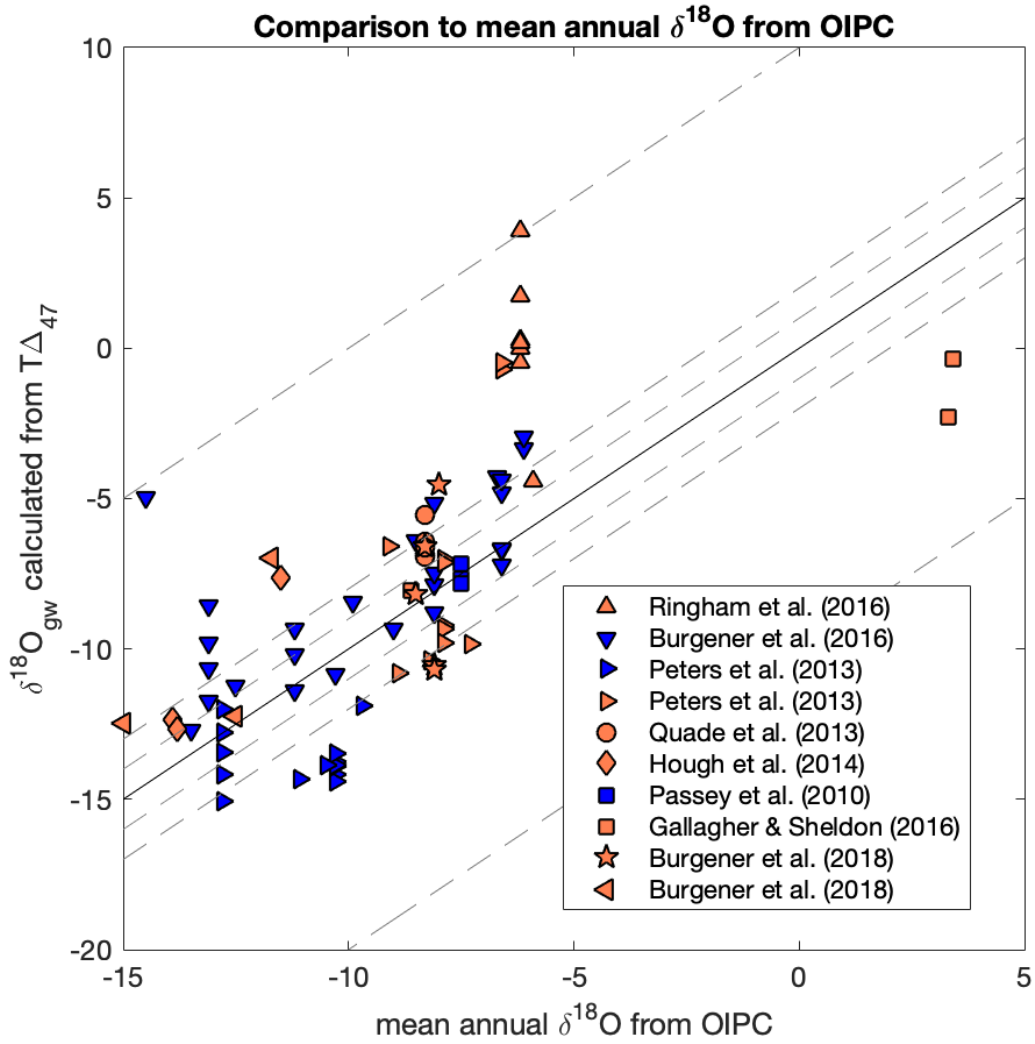

Figure 3-7: Calculated $\delta^{18}O_{gw}$ and $\delta^{18}O$ of rain water for soil carbonate samples.

X-axis is the annual $\delta^{18}O$ of precipitation (weighted by amount). The dark gray dashed line is a 1:1 line and the light gray dashed lines are ± 1, ±2, and ±20 ‰. Blue symbol color indicates that the soil carbonate is from an environment with winter-dominated precipitation. Red symbol color indicates that the soil carbonate is from an environment with summer-dominated precipitation.

Table 3-1 Studies included, meteoric & soil texture data sources, and data quality

Study	Meteoric Data Source	Soil Texture Data Source	Samples with > 1 replicate	Updated with IUPAC 17O parameters?	Soil Texture[a]	Primary Season of Precipitation[b]
Passey et al. (2010)	Soil temperatures in Table S3 of paper, monthly mean air temperatures from local weather stations in Table S1 of paper	Descriptions of soils in supplement of original publication	9 of 28	no	fine/medium/ coarse	summer / winter
Quade et al. (2013)	Soil and air temperaure from Fig 2d of original paper	Not available	5 of 52	no	coarse	summer
Peters et al. (2013)	Soil temperature from Fig 5 in original paper (only for select locales). Air temperature from local weather stations, extrapolated by elevation.	Field notes, photographs of soil pits, personal communication with authors	33 of 34	no	medium/ coarse/very coarse	summer / winter
Hough et al. (2014)	Soil and air temperature from nearby SCAN sites. Used elevation-temperature relationship from Fig 3 of paper.	Not available for sample matrix	8 of 24	yes	-	summer
Burgener et al. (2016)	Soil and air temperature measured *in situ* for some sites, extrapolated by elevation for others. Data from supplemental tables in paper.	Field notes, photographs of soil pits, personal communication with authors	36 of 36	yes	coarse/ very coarse	winter
Ringham et al. (2016)	Soil and air temperature measured in situ for some sites, extrapolated by elevation for others. Data from supplemental tables in paper.	Field notes, photographs of soil pits, personal communication with authors	22 of 24	yes	medium/ coarse/very coarse	summer
Gallagher & Sheldon (2016)	Air temperature normals from nearby NCDC weather stations, provided in paper.	From NRCS soil series descriptions from sites, provided by T.G.	11 of 11	yes	fine/medium/ coarse	summer / winter
Burgener et al. (2018)	Air temperaure from original paper Table 2 (local weather station data)	Categorized by texture In original publication	9 of 9	yes	medium	summer / winter

a - Soil texture for individual samples is given in Table A-1

b - Primary season of precipitation for individual samples is given in Table A-1

Table 3-2: Seasonal Bias of Clumped Isotope Temperatures and $\delta^{18}O$

	fine-grained	medium-grained	coarse-grained	very coarse-grained	winter	summer	summer (no fg)	vegetated	barren
num.samples in group	4	18	28	22	43	43	39	76	51
Mean residuals from MAAT ($T\Delta_{47}$-MAAT, in °C)									
Mean residuals	-4.0	7.6	9.8	11.0	11.1	7.7	8.9	7.5	11.6
S.D.	3	5	4	6	5	5	4	6.6	4.6
Mean residuals from MWST ($T\Delta_{47}$-MWST, in °C)									
Mean residuals	-12.9	0.68	3.22	4.7	5.47	0.5198	0.75	-0.75	5.7
S.D.	7	5	4	7	4.9	6.1	4.4	7.2	5.2
Mean residual from $\delta^{18}O_{ann}$ ($\delta^{18}O_{gw}$ - $\delta^{18}O_{ann}$, in ‰)									
Mean residuals	-2.6	0.8	1.3	1.4	0.2	1.8	2.2	2.4	0.7
S.D.	2.4	2.6	3.4	3.2	2.7	3.5	3.3	3.89	2.9

Table 3-3: Statistical Comparisons (KS test and *t*-test) Between Sample Populations

	fg vs. mg	fg vs cg	fg vs vcg	mg vs cg	mg vs vcg	cg vs vcg	winter vs. summer precip	winter vs. summer precip, without fg	veg vs. non veg
				*KS test results - comparisons of $T\Delta_{47}$-MAAT**					
h	**1**	**1**	**1**	**1**	0	0	0	0	**1**
p	**0.0017**	**8.09E-04**	**5.70E-04**	**0.0311**	0.4648	0.3719	0.0569	0.2451	**0.0041**
ks-stat	**0.9444**	**0.9643**	**1**	**0.4167**	0.2576	0.25	0.2791	0.2194	**0.3109**
	*t-test results - comparisons of $T\Delta_{47}$-MAAT for each population **								
h	**1**	**1**	**1**	**1**	**1**	0	**1**	**1**	**1**
p	**2.90E-04**	**1.70E-07**	**3.82E-05**	**3.07E-02**	**4.97E-02**	7.32E-01	**0.0037**	**0.0343**	**1.86E-04**
difference in means ± 95% CI (°C)	**11.5 ± 5.4**	**14.54±4.4**	**15.0 ± 6.2**	**2.9 ± 2.7**	**3.4 ± 3.4**	0.48 ± 2.8	**3.4 ± 2.2**	**2**	**-4 ±2**
	*KS test results - comparisons of $\delta^{18}Ogw$ -$\delta^{18}Oann$ **								
h	**1**	0	**1**	0	0	0	0	**1**	**1**
p	**0.0439**	0.1454	**3.49E-02**	0.4605	0.8639	0.421	0.1005	**0.0319**	**0.0356**
ks-stat	**0.6944**	0.5652	**0.7045**	0.256	0.1818	0.251	0.2558	**0.3083**	**0.2505**
	*t-test results -comparisons of $\delta^{18}Ogw$ -$\delta^{18}Oann$ **								
h	**1**	**1**	**1**	0	0	0	**1**	**1**	**1**
p	**3.09E-02**	**3.09E-02**	**2.86E-02**	5.36E-01	5.36E-01	9.22E-01	**0.0203**	**0.0029**	**0.0109**
difference in means ± 95% CI (°C)	**3.0107**	**3.0107**	**3.594**	NA	NA	NA	**-1.6 ± 1.3**	**2.0±1.3**	**1.6 ± 1.2**

* Tests the null hypothesis that the residual (TD47-MAAT) data are from the same continuous distribution, using the two-sample Kolmogorov-Smirnov test. If h = 1, it rejects the null hypothesis at the 5% significance level (different distributions, in bold)

**Tests the null hypothesis that the residual (TD47-MAAT) data are from the populations with the same mean. If h = 1, it rejects the null hypothesis at the 5% significance level (different means, in bold)

Chapter 4 Predicting the timing of Soil Carbonate Accumulation with Numerical Modeling (HYDRUS-1D)

Abstract

Soil carbonates from fossilized soils are widely used to investigate paleoclimates and paleoenvironments, however, the annual timing of their accumulation is poorly understood. One common hypothesis is that the timing of soil carbonate accumulation is controlled by changes in soil-water balance, which in turn are driven by the timing and pattern of seasonal rainfall. Here, we seek to test the soil-water balance hypothesis by predicting the seasonal bias of soil carbonate accumulation using a numerical model of soil physics and carbonate chemistry (HYDRUS-1D). We simulate soil CO_2 contents, water contents, temperature, and calcite precipitation/dissolution in a single dimension soil profile for 5 years. We start by using soil and meteorological boundary conditions that resemble a location in New Mexico, USA. We find that calcite accumulation in most model simulations forms during large dissolution-reprecipitation events; these events usually occur as a result of changing CO_2 concentrations during large rain/storm events. Given that soil CO_2 is sensitive to soil texture and water content in HYDRUS, we test the sensitivity of calcite accumulation to those two factors. We run simulations parametrized as clay loam ('fine-grained'), sandy clay loam, and sandy loam ('coarse-grained'). While we observe higher CO_2 contents and larger changes in soil CO_2 with decreasing grain size, the clumped isotope temperature is similar in all three soil texture scenarios. Then we alter the input rainfall to test the hypothesis that the timing and seasonal evenness in rainfall influence the timing of calcite formation. We shift the New Mexico rainfall by 6 months – this results in a shift in the timing of calcite accumulation. Next, we force the simulations with annually uneven rainfall (derived from

New Delhi, India) and annually even rainfall (derived from Prince Rupert, BC, Canada). In the uneven rainfall simulation, calcite accumulates at the end of the rainy season and/or after large storms, similar to New Mexico. In the even rainfall simulation, calcite forms sporadically throughout the year. These rainfall-sensitivity experiments show that a change in the rainfall regime in geologic time will affect the seasonal bias of the soil carbonate proxy. We estimate a 7 °C difference in clumped isotope temperature in these simulations. These initial numerical simulations show that HYDRUS could be used to model the soil carbonate proxy system and could enhance our ability to interpret their isotopic composition.

4.1 Introduction

Pedogenic carbonate from fossilized soils (paleosols) is widely used to investigate ancient climates and environments of continents, commonly through measurement of carbonate stable isotopic composition ($\delta^{13}C$, $\delta^{18}O$, and Δ_{47}). However, the utility of paleosol carbonates in paleoclimate reconstructions has been limited by an incomplete understanding of the environmental processes that control the timing of its formation; seasonal variations in the formation of carbonate could impart a bias that is larger than the paleoclimate signal of interest. An understanding of the seasonal bias in the stable isotopic composition of soil carbonates is critical to understanding the evolution of climate on land through geologic time.

While the formation processes of soil carbonates have been studied extensively since as early as the 1940s (see review by Zamanian et al., 2016), until more recently the annual timing of those processes was not explicitly considered (Breecker et al., 2009). The development of the clumped isotope thermometer (Δ_{47}) has simultaneously motivated a need to understand the annual timing of carbonate formation in order to accurately interpret temperature reconstructions,

as well as provided a new way to constrain annual timing through comparison between temperatures measured *in situ* with temperature estimated through clumped isotope analyses. Several workers studying the Δ_{47} composition of Holocene soil carbonates have suggested that soil moisture balance is a primary control on carbonate formation—and that therefore soil texture and the timing and character of rainfall should be important in controlling the timing of carbonate formation (Burgener et al., 2016; Gallagher and Sheldon, 2016; Peters et al., 2013). However, we lack a systematic understanding of how these environmental factors influence carbonate formation.

Here, we explore how soil texture and changes in precipitation regime individually affect the annual timing of carbonate formation. We use a soil physics and chemistry numerical modeling software package, HYDRUS-1D, to predict calcite formation and other physical and chemical parameters (Šimůnek et al., 2009). Numerical modeling allows us to control for other environmental factors and vary rainfall patterns in ways that are not possible or efficient through examination of natural soil carbonates. We test the hypothesis that the timing and processes of carbonate formation are sensitive to 1) seasonal timing of rainfall and 2) annual evenness of rainfall.

4.2 Background

4.2.1 Carbonate chemistry and accumulation in soils

Calcium carbonate ($CaCO_3$) precipitates and dissolves according to the following equations (e.g., Birkeland, 1984; White, 2003):

$$Ca^{2+}_{(aq)} + 2HCO^{-}_{3\,(aq)} \Leftrightarrow CaCO_{3\,(s)} + CO_{2\,(g)} + H_2O \qquad \text{Equation 4-1}$$

$$CO_{2\,(g)} + H_2O \Leftrightarrow H_2CO_{3\,(aq)} \Leftrightarrow H^+_{(aq)} + HCO^{3-}{}_{(aq)} \Leftrightarrow 2H^+_{aq} + CO_3^{2-}{}_{(aq)} \quad \text{Equation 4-2}$$

When soil CO_2 content increases, gaseous CO_2 dissolves into soil water where it disassociates into dissolved inorganic carbon (DIC) species (Equation 4-2). The dissolution of CO_2 creates a weak acid, which drives Equation 4-1 to the left and promotes dissolution of $CaCO_3$ into the surrounding soil. As soil CO_2 content decreases, Equation 4-1 is driven to the right, promoting the precipitation of $CaCO_3$. Because CO_2 is more soluble at colder temperatures, $CaCO_3$ solubility has an inverse relationship with temperature: $CaCO_3$ is more likely to precipitate at higher temperatures. Accordingly, changes in the CO_2 concentration in soil pores influence calcite solubility. In a soil, CO_2 gas is produced through plant and microbial respiration and from the diffusion of atmospheric CO_2 (Birkeland, 1984; Cerling et al., 1991; Cerling and Quade, 1993; Quade et al., 1989). The Ca^{2+} ions are sourced primarily from calcium-bearing dust particles that are deposited on the landscape surface (Birkeland, 1984; Gile et al., 1966; Harden et al., 1991; McFadden, 2013; McFadden et al., 1991; Reheis et al., 1989) and from Ca^{2+} ions in rain (Machette, 1985).

Calcite horizons form in soils likely via two end-member processes: the *per descensum* process and/or the *per ascensum* process (Blodgett, 1988; Goudie, 1973; Li et al., 2018; Marion and Schlesinger, 1994; Zamanian et al., 2016). According to the *per descensum* process, calcite forms as Ca^{2+} is mobilized in meteoric water and percolates downward into the soil column (Birkeland, 1984; Gile et al., 1966; Machette, 1985). When the Ca^{2+} ions reach sufficient depths/ low soil pCO_2 conditions, it is precipitated out of solution as $CaCO_3$. In this *per descensum* framework, the timing and depth of calcite precipitation will be controlled by the timing of

rainfall and by the percolation of that water, which is moderated by soil texture (Burgener et al., 2016, 2018; e.g., Jenny, 1941; Peters et al., 2013). Supersaturation could occur as a result of evaporation of soil water, which is most likely to occur during periods of net negative soil moisture (Arkley, 1963; Gallagher and Sheldon, 2016), often during the warm and dry months of the year (Breecker et al., 2009; Peters et al., 2013). In the *per ascensum* framework, carbonate forms through uptake of soil water by roots and/or capillary draw (Blodgett, 1985; Goudie, 1973). This process is controlled by plant and microbial activity, both through uptake of water and through respiration that causes changes in CO_2 concentrations at rooting depths. This process could explain how calcite forms even during water-saturated conditions (Mintz et al., 2011), and implies that calcite precipitation in soils will be sensitive to timing of plant activity (Meyer et al., 2014; Ringham et al., 2016). Natural soil carbonates likely form as a result of both *per descensum* and *per ascensum* processes.

Mathematical models have been previously used to simulate the formation of $CaCO_3$ horizons in soils (Hirmas et al., 2010; Marion et al., 1985; Marion and Schlesinger, 1994; Mayer et al., 1989; McDonald et al., 1996; McFadden and Tinsley, 1985; Meyer et al., 2014). Most previous workers have focused on understanding the relationship between climate and depth-distribution of $CaCO_3$ in a soil profile, largely with the purpose of relating observed depths of $CaCO_3$ horizons to changes in Quaternary climate (both precipitation and temperature) (Mayer et al., 1989; McDonald et al., 1996; McFadden and Tinsley, 1985). However, the models from the late 1980s and early 1990s do not explicitly discuss the annual timing of carbonate formation and do not seasonally vary soil CO_2. HYDRUS-1D is well-suited to explore the seasonal timing of carbonate formation because making calculations with hourly timesteps is trivial and because soil CO_2 is dynamically calculated considering environmental parameters (Suarez and Šimůnek,

1993, 1997). Additionally, HYDRUS-1D incorporates relatively sophisticated soil physics (i.e., unsaturated flow); these physics may be important in calculating timing of carbonate formation and will provide more accuracy than soil-moisture balance calculations (Gallagher and Sheldon, 2016; Huth et al., 2019; Šimůnek et al., 2009). Meyer et al. (2014) first use HYDRUS-1D to predict the seasonal timing of carbonate formation by considering the importance of the timing of plant growth. We expand on their use of HYDRUS-1D with the purpose of testing the hypothesis that seasonal timing and distribution of rainfall controls the timing of soil carbonate formation.

4.3 HYDRUS-1D: Model description and parameterization

4.3.1 Modeling approach

Here we use a finite-element model, HYDRUS-1D, to decipher the environment conditions and processes that control the timing of carbonate formation and dissolution. We attempt to identify the timing of the formation of 'accumulated calcite,' which is calcite that would be preserved in the geologic record (i.e., not re-dissolved). We initially parameterize the numerical model to best describe a site in central New Mexico, USA (Adams Ranch), for which environmental- and soil-monitoring data exist. We test the model's ability to reproduce observed soil moisture and soil temperature (Appendix C). Then we vary parameters that most affect soil CO_2 content in HYDRUS (Suarez and Šimůnek, 1993): soil texture and water content. Keeping all other model parameters constant, we vary soil texture from clay loam, sandy clay loam, to sandy loam – a range of soil texture parameters that is numerically stable in HYDRUS. Again, keeping all other model parameters constant, we vary water content by altering the rainfall

inputs. Specifically, we examine how the seasonality and distribution of rainfall influences the annual timing of carbonate formation.

4.3.2 HYDRUS-1D: governing equations

HYDRUS-1D is a numerical modeling software package that solves for heat and water transport and carbonate chemistry in a 1-dimensional soil profile. In HYDRUS, water flow in a soil column is calculated with the modified Richards equation for transport in variably saturated conditions:

$$\frac{\partial \theta}{\partial t} = \frac{\partial}{\partial x}\left[K\left(\frac{\partial h}{\partial x} + \cos\alpha\right)\right] - S \qquad \text{Equation 4-3}$$

where h is pressure head (L), θ is volumetric water content (L^3L^{-3}), t is time (T), x is the spatial coordinate (L), S is the sink term ($L^3L^{-3}T^{1}$), α is the angle between the flow direction and the vertical axis (allows for vertical, horizontal, and inclined flows), and K is the unsaturated hydraulic conductivity of the soil material (LT^{-1}) (Šimůnek et al., 2009). Water enters the soil profile as rainfall, and no surface ponding, runoff, or snowpack is considered. Root water uptake is calculated using the Feddes equation (Feddes, 1978; Šimůnek et al., 2009); root water uptake is incorporated as a sink term at each node where roots are present.

Heat transport in a soil profile is calculated with a convective-dispersion equation:

$$C_p(\theta)\frac{\partial T}{\partial t} = \frac{\partial}{\partial x}\left[\lambda(\theta)\frac{\partial T}{\partial x}\right] - C_w q\frac{\partial T}{\partial x} \qquad \text{Equation 4-4}$$

where λ(θ) is the coefficient of the apparent thermal conductivity of the soil ($MLT^{-3}K^{-1}$), and $C_p(\theta)$ and C_w are the volumetric heat capacities ($ML^{-1}T^{-2}K^{-1}$) of the porous medium and the

liquid phase, respectively. This equation considers heat flow due to conduction and heat transport from flowing water, including energy uptake from plant root water uptake (Šimůnek et al., 2009).

HYDRUS calculates CO_2 transport in liquid and gas phase. CO_2 production by plant roots and soil microorganisms are estimated using empirical relationships that are dependent on depth in soil profile, pressure head, soil temperature, and soil CO_2 concentration (i.e., O_2 deficiency) (Šimůnek et al., 2009).

In this study we use the UNSATCHEM module of HYRDUS-1D, which calculates calcite dissolution/precipitation in a soil (Suarez and Šimůnek, 1997). Kinetics of the reaction rate, which are affected by the surface area of calcite and dissolved organic carbon (DOC) concentrations, can be considered in HYDRUS (Suarez and Šimůnek, 1997), but are excluded in this work for simplification (as in Meyer et al., 2014). Here we assume that calcite precipitates under equilibrium conditions, i.e., when the solution reaches saturation with respect to calcite according to Equation 4-1 and Equation 4-2.

4.3.3 Model parametrization

4.3.3.1 Site Selection: simulations inspired by central New Mexico

Model parameters are chosen to best describe a Soil Climate Analysis Network (SCAN) station in New Mexico called Adams Ranch (34.25N 105.42W, 1880 m in elevation, https://wcc.sc.egov.usda.gov/nwcc/site?sitenum=2015). Adams Ranch is a logical place to use as a basis for these experiments for a few reasons. First, this location is similar in environment to the central New Mexico locale modeled in HYDRUS by Meyer et al. (2014), allowing us to easily build on their work. Second, although our goal is not to fully explain or reproduce

clumped isotope data from specific Holocene soil carbonate samples, it is beneficial to choose a location that has nearby clumped isotope data from fine-grained soils. Some of the few Holocene soil carbonates with published clumped isotope analyses of nodules from fine-grained soils are in New Mexico (the Plughat, Witt, and Montecito sites from Gallagher and Sheldon (2016)). The model parameters described below are based on the conditions and SCAN data from Adams Ranch.

4.3.3.2 Soil profile, chemical initial conditions, and other time-constant parameters

The model is parameterized with a soil profile geometry, soil material, and initial chemistry. We model a 250 cm deep soil profile with calculation nodes every 2.5 cm (Table 4-10). Based on the soil pit description at Adams Ranch, we model a single soil material that consists of sandy clay loam. For the experiments that vary soil texture, we also consider a clay loam (fine-grained end member) and a sandy loam (coarse-grained end member). The water flow and heat transport parameters for the soil materials are listed in Table 4-1 and Table 4-5. We start the simulations with 10 meq/kg (500 mg/kg) of solid calcite at all depths in the soil column and a calcite surface area of 0.007 m^2/dm^3 (McFadden and Tinsley, 1985; Meyer, 2012; Meyer et al., 2014) (Table 4-4). While this initial configuration is not representative of natural soils, it is necessary to starting with seed calcite throughout the profile to ensure that the $CaCO_3$ is not completely leached throughout the simulations (Meyer, 2012; Meyer et al., 2014). The amount and distribution of initial solid calcite does not change the timing of calcite accumulation in HYDRUS (Meyer, 2012).

We assume that the composition of the initial soil solution and incoming solution (rainwater) is 0.013 meq/L of Ca and 0.0015 meq/L of Na (Table 4-2). These values are

calculated to represent the amount of dust-deposited calcite that can be transported downward by rain (Meyer, 2012; Reheis, 2006).

CO_2 production parameters are the same as in Meyer et al. (2014); these parameters were used by the authors to successfully reproduce measured soil CO_2 data for their location in central New Mexico (Table 4-6, Table 4-7, Table 4-8). Further discussion of parameter choices for CO_2 production can be found elsewhere (Šimůnek et al., 2009; Suarez and Šimůnek, 1997). In HYDRUS, CO_2 content in soils is not sensitive to the optimal CO_2 production values because production is usually limited by water content and temperature (Suarez and Šimůnek, 1993). However, CO_2 content is sensitive to soil grain size because of the difference in gas diffusivity (Suarez and Šimůnek, 1993); we vary soil grain size parameters to explore this sensitivity.

We assign decreasing root spacing at depth following an empirical function for semi-arid grassland (Jackson et al., 1996; Meyer et al., 2014) (Table 4-10). Leaf area index (LAI) is held constant at a value of 1. This parameterization maximizes root-water uptake throughout the simulation (i.e., no plant dormancy). This approach differs from that of Meyer et al. (2014); those authors explicitly vary the timing of plant growth by including root growth and by allowing HYDRUS to calculate potential evapotranspiration based on varying LAI, maximum rooting depth, and surface reflectivity. Their work shows that varying the timing of plant growth affects the timing of carbonate accumulation in HYDRUS. Thus, in this work we keep plant-related variables constant in order to isolate the effect of changing precipitation regime. Our approach includes proscribing a potential evapotranspiration that does not depend on rooting parameters (described below).

4.3.3.3 Time-varying parameters: surface temperature, potential evapotranspiration, and rainfall

We use meteorological data from 2011-2015 from the Adams Ranch SCAN station for the time-varying boundary conditions in our simulations. First, we force the temperature at the top of the soil profile using data from soil temperatures measured from 5 cm deep at Adams Ranch (using air temperature as the boundary condition is problematic because the model does not include snowpack (insulation) or radiative heating (Appendix C)). We also input daily range in air temperature, which HYDRUS uses as the amplitude of a sinusoidal function to estimate temperature at sub-daily timesteps. Potential evapotranspiration (ET_0) is varied on a daily basis. We force the model with ET_0 values that are calculated using the Hargreaves Equation (Hargreaves and Samani, 1985):

$$ET_0 = 0.0023\, R_a\, (T_{mean} + 17.8)(T_{max} - T_{min})^{0.5} \qquad \text{Equation 4-5}$$

Where T_{mean}, T_{max}, and T_{min} are mean, maximum, and minimum daily temperature and R_a (mm day^{-1})) is extraterrestrial radiation for a daily period:

$$R_a = 0.408 * \frac{24(60)}{\pi} G_{sc} d_r [\omega_s \sin(\varphi)\sin(\delta) + \cos(\varphi)\cos(\delta)\sin(\omega_s)] \qquad \text{Equation 4-6}$$

G_{sc} is the solar constant (0.082 MJ m^{-2} min^{-1}),

φ is latitude (in radians, $\varphi = \frac{\pi}{180} * decimal\ degrees$),

d_r is the inverse relative distance Earth-Sun:

$$d_r = 1 + 0.033 \cos\frac{2\pi}{365}\varphi \qquad \text{Equation 4-7}$$

δ is solar declination in radians:

$$\delta = 0.409 \sin\left(\frac{2\pi}{365}\varphi - 1.39\right) \qquad \text{Equation 4-8}$$

and ω_s is sunset hour angle:

$$\omega_s = arcos(\tan^{-1} \varphi \tan \delta) \qquad \text{Equation 4-9}$$

During rain events, ET_0 is set to 0 to ensure that the water enters the soil column.

Precipitation (rain) is proscribed on a daily basis. Herein we use 'rain' to describe any water that falls from the sky, to avoid confusion with calcite precipitation. We vary the input rainfall with four different scenarios (Table 4-11, Table C-1). We use real, daily rainfall records because previous numerical modelers have shown that using stochastic rain events, rather than mean climatology, results in more accurate descriptions of soil carbonate formation (Marion et al., 2008, 1985). For the first experiment, we use the daily rainfall record from the Adams Ranch SCAN station for 2011-2015. Then, holding all other parameters constant, we vary the 5-year rainfall record (Table C-1). We consider the influence of the seasonality (timing) of rain by shifting the 2011-2015 Adams Ranch record by 182 days (6 months). Then we consider the influence of annual unevenness of rainfall. We use 5 years of daily rainfall data from two locations that are end-members in their unevenness in precipitation (Pendergrass and Knutti, 2018). Five consecutive years with complete data are randomly chosen from the data available from the NOAA Global Historical Climatology Network – Daily (Menne et al., 2012a, 2012b). Daily rainfall is scaled so that the total rain over 5 years is within 15 cm (12 %) of the Adams Ranch total. Scaling removes artifacts that would result from the long-observed relationship between precipitation amount and depth of carbonate formation (Arkley, 1963; Jenny, 1941; Retallack, 2005). To simulate a realistic but still relatively evenly distributed rainfall, we use rainfall data from Prince Rupert, BC, Canada (54.28N, -130.38E, 52 m) from 1958–1962 (scaled by 0.1). To simulate rainfall that is very uneven, we use precipitation data from New Delhi, India (28.57N, 77.12E, 233 m) from 1965–1970 (scaled by 0.33).

4.3.4 Calculating Predicted Clumped Isotope Temperature from HYDRUS-1D

We calculate a synthetic clumped isotope temperature ($T\Delta47_{syn}$) for each experiment in three ways. For all methods, we assume that calcite growth temperature is the soil temperature at the depth of interest in the soil profile at the time of carbonate formation. The first (and simplest) method of calculating clumped isotope temperature is an amount-weighted mean temperature of the soil temperatures from each time step when calcite forms (i.e., when there is a positive change in the solid Ca^{2+} content) ($T\Delta47_{syn1}$). $T\Delta47_{syn1}$ is an average of the growth temperature of any and all calcite that forms, even if it that material is subsequently dissolved. We also calculate a second estimate, $T\Delta47_{syn2}$, that only considers *accumulated* calcite. We do this by assuming 'first-in, last-out' of carbonate growth temperatures; this method implies that calcite grows outwardly, and dissolution would evenly remove the outermost layer(s) of calcite. This simplification does not represent uneven dissolution/precipitation that could more realistically describe soil carbonates (Zamanian et al., 2016). Third, we calculate $T\Delta47_{syn3}$ as follows: after each timestep with an increase in calcite, we re-calculate the synthetic clumped isotope temperature with an amount-weighted mean. After each timestep with a decrease in calcite, we remove that amount of calcite from the running total. If the total calcite is negative, then the temperature is reset. Thus the $T\Delta47_{syn3}$ is an amount-weighted mean of every positive timestep, but considers dissolution – this is an attempt to mimic uneven dissolution and precipitation in natural carbonates. To simplify comparisons between simulations, we calculate $T\Delta47_{syn}$ at a depth of 40 cm in all simulation except where variation with depth is explicitly considered. These synthetic clumped isotope temperatures are useful to compare results from the model simulations but might not be an accurate prediction for any particular location in the real world.

4.4 Results

First, we ran the Adams Ranch experiment (sandy clay loam) for 5 years. A comparison between the physical parameters predicted by HYDRUS and those measured at the Adams Ranch SCAN station can be found in Appendix C.

Each simulation ran for 5 years (two soil-texture experiments, four rainfall experiments). For all simulations, soil temperatures vary primarily with seasons. At shallow depths, the soil temperature fluctuates on a daily basis. The daily fluctuations in temperature are dampened below a depth of approximately 40 cm in the soil profile. Water content changes in response to incoming rain, evaporation, and rootwater uptake. CO_2 production and CO_2 content increase in response to rain and increasing temperature. In all experiments, calcite is mostly leached out of the top 40 cm of the soil profile (Figure 4-1). Calcite accumulates in varying amounts at depths >40 cm (Figure 4-1), which is the maximum rooting depth. The total amount of calcite accumulation in each simulation is similar (about 2 Ca^{2+} meq/kg equivalent total) as a result of scaling the total rainfall amount to be similar amongst the simulations.

The three methods for calculating synthetic clumped isotope values produce similar results. The difference between $T\Delta47_{syn1}$, $T\Delta47_{syn2}$, and $T\Delta47_{syn3}$ is 1°C or less for all simulations except the 'uneven' rain simulation (Table 4-12). It is most different in the 'uneven' rain simulation because calcite formation is also most uneven; the $T\Delta47_{syn2}$ only captures the temperature during the large (and hot) calcite accumulation events. The $T\Delta47_{syn2}$ is most useful because it also calculates the day of calcite accumulation. $T\Delta47_{syn2}$ is primarily used to compare the simulations in the subsequent discussion.

In the Adams Ranch simulation (~late summer (July, August, September) rain), calcite accumulates most often in August and September (an exception is the calcite that accumulates in winter-early spring of year 2). This carbonate accumulation timing results in a $T\Delta47_{syn2}$ of 18.3 °C (at a depth of 40 cm) (Figure 4-4, Table 4-12). In the Adams Ranch Shifted simulation (~late winter (January, February, March) rain) calcite accumulates most often from March to June, resulting in a $T\Delta47_{syn2}$ of 15.2 °C (Figure 4-5, Table 4-12). In the 'uneven' rain simulation, calcite accumulates primarily in August and September, resulting in a $T\Delta47_{syn2}$ of 22.3 °C (Figure 4-6, Table 4-12). In the 'even' rain simulation, calcite precipitates sporadically throughout the year in small amounts, resulting in a $T\Delta47_{syn2}$ of 15.2 °C (Figure 4-7, Table 4-12).

4.5 Discussion

We examine the relationship between calcite accumulation and physical soil parameters (CO_2, water content, and temperature) in an attempt to disentangle the relative importance of various physical processes in promoting calcite accumulation. We discuss the sensitivity of CO_2 content and calcite accumulation to soil texture. Next, we discuss that shifting the timing of rainfall shifts when accumulated calcite forms. We also discuss how a change in the annual evenness in rainfall can change the pattern and timing of calcite accumulation. Then we explore if/how the timing of calcite accumulation varies with depth in a soil profile. These findings have implications for how to interpret the stable isotope composition of soil carbonates.

4.5.1 Sensitivity of calcite accumulation to physical soil parameters

In the HYDRUS-1D model simulations, calcite formation is sensitive to soil CO_2 and water content (Figure 4-2). This finding is consistent with the understanding of calcite solubility outlined in Equation 4-1 and Equation 4-2. In the Adams Ranch simulation, calcite forms throughout the year (secular increase in solid Ca^{2+} in bottom panel, Figure 4-4). However, the accumulated calcite forms as a result of relatively large dissolution and re-precipitation events (vertical bars in Figure 4-4). These accumulation events are correlated with large percent changes in CO_2 content and water content (Figure 4-2). In contrast, calcite accumulation events are not well correlated with percent changes in soil temperature or in amount of Ca^{2+} in solution (Figure 4-2). The calcite accumulation events frequently occur when changes in CO_2 content correlated with changes in soil water content (Figure 4-2).

The co-variation of CO_2 and water content in the soil is a direct result of the parameterization that HYDRUS uses to calculate calcite. In HYDRUS, CO_2 production is positively correlated with water content and temperature (Šimůnek et al., 2009; Suarez and Šimůnek, 1997) – relationships that have been observed in nature (Bond-Lamberty and Thomson, 2010; Bowling et al., 2011; Liu et al., 2002; Vargas and Allen, 2008). This parameterization in HYDRUS results spikes in soil CO_2 concentrations during rain events, and calcite dissolution/re-precipitation that follows rain. Larger spikes in CO_2 concentrations result in larger dissolution and re-precipitation events. Thus, calcite accumulation post-rain events make up a large proportion of the total calcite accumulation in each simulation.

Calcite accumulation is sensitive to soil CO_2 content, which is sensitive to two main parameters: 1) the rate of gas diffusion out of the soil pores as determined soil texture (parameters in Table 4-1, Table 4-5) and 2) soil water content (Suarez and Šimůnek, 1993). We

subsequently explore soil texture and soil water content (through rainfall) affect soil CO_2 and the timing of calcite formation and accumulation.

4.5.2 Soil Texture, soil CO_2 content, and timing of calcite accumulation

Our simulations confirm that in HYDRUS, CO_2 diffusion in the soil profile is sensitive to soil texture parameterization (Meyer, 2012; Suarez and Šimůnek, 1993). We observe that soil CO_2 contents increase with decreasing soil grain size (highest soil CO_2 in the fine-grained soil, clay loam) (Figure 4-3). Fine-grained soil textures trap CO_2 and maintain high soil CO_2 conditions (Bouma and Bryla, 2000). Also, fine-grained soils maintain higher water contents (Figure 4-3), resulting in more CO_2 production in HYDRUS (Suarez and Šimůnek, 1997).

The differing parameterization of in soil texture results in differing patterns of calcite accumulation in HYDRUS. In all simulations, calcite accumulates after rain-induced spikes in CO_2 and soil water content (Figure 4-3). In all simulations, calcite forms during the extended soil drying that occurs months after a 'rain event' (increase Ca^{2+} in bottom panel of Figure 4-3). However, in the fine and medium-grained simulations (sandy clay loam and clay loam), that calcite is dissolved in subsequent rain-induced CO_2 spikes and is not accumulated. The CO_2 spikes do not occur in the coarse-grained simulation (sandy loam), so calcite formed beforehand is preserved. This results in comparatively more days with calcite accumulation in the coarse-grained simulation (39 vs 119 timesteps in coarse vs. fine simulations respectively) (vertical bars in Figure 4-3). Despite these differences in the pattern of calcite accumulation, the $T\Delta47_{syn2}$ values of these three simulations are within 1° C (Table 4-12). Soil texture influences soil CO_2, water contents, and patterns of calcite accumulation. Fine-grained soils promote calcite

accumulation that is more biased toward large storm events, while coarse-grained soils promote calcite accumulation that is more evenly distributed annually.

4.5.3 Effect of the timing of rainfall on calcite accumulation

Rainfall directly affects soil moisture, and thus we predicted that altering the timing of rainfall would alter the timing of calcite accumulation. Shifting the 5-year precipitation record from Adams Ranch by 182 days (6 months) is a simple experiment that allows us to decipher the sensitivity of the timing of carbonate formation to the timing of rainfall. Shifting the timing of rain imparts two major changes on the predicted physical parameters. First, annual peaks in water content shift from spring to fall (Figure 4-4, Figure 4-5). Second, the annual evolution of CO_2 concentration changes. In the shifted simulation, CO_2 concentrations are relatively high in the spring (due to high water content/rainfall) and continue to stay relatively high through mid-summer (due to high temperatures). This timing differs from the un-manipulated Adams Ranch experiment where peak temperatures and peak water contents coincide. This difference results in lower maximum soil CO_2 concentrations in the shifted experiment compared to the un-manipulated experiment.

As a result of these changes in physical parameters, the timing of calcite accumulation also changes. The preserved calcite forms earlier in the year (April through June) (Figure 4-5), still coinciding with major changes in soil CO_2 (and water content) as in the un-manipulated Adams Ranch experiment (Figure 4-4). This shift in timing reduces the predicted $T\Delta47_{syn}$ from 18.3 °C (un-manipulated) to 15.2 °C (shifted) (Figure 4-8, Table 4-12). This result suggests that changes in the timing of regional rainfall patterns through geologic time can change the seasonal bias recorded in the isotopic composition of soil carbonates. The predicted difference of 3 °C in

clumped isotope temperature is at the limit of what would be resolvable in the geologic record, but one could imagine several scenarios where a change in the annual timing of rainfall could cause a larger change in $T\Delta_{47}$ (i.e., the three months of primary rainfall shifts from June, July, August to December, January, February precipitation, rather than the shift from July, August September to January February March as currently tested). Differences in the timing of rainfall in natural settings likely also result in differing seasonal biases of calcite accumulation in soils– this mechanism was previously used to explain varied biases in Holocene soil carbonates (Peters et al., 2013).

4.5.4 Effect of precipitation regime on calcite formation and accumulation

Altering the character of rainfall driving the simulations allows us to investigate the more nuanced effects that rainfall regime might have on soil water and CO_2 contents, and thus the timing of carbonate formation. We compare the Adams Ranch simulation to simulations run with annually even rain and annually uneven rain (Table 4-11, Figure 4-8).

In the 'uneven' rain simulation, calcite accumulation mimics the uneven rainfall pattern. Accumulated calcite forms immediately after large dissolution/rain events, generally in early August. This pattern of calcite accumulation is similar to the pattern observed in the original Adams Ranch simulation, except that the calcite formation starts slightly earlier in the summer (resulting in a higher $T\Delta47_{syn}$). There is not a marked difference in calcite formation due to unevenness in precipitation between the Adams Ranch and the 'uneven' simulation.

In contrast, the 'even' rain simulation results in calcite accumulation that is evenly distributed throughout the year. The simulated physical parameters (e.g., CO_2 and water content), and thus the calcite accumulation is not as seasonally variable as in the other simulations. Most

importantly, soil CO_2 concentrations do not vary strongly with seasons as observed in the Adams Ranch and the uneven rain simulations (Figure 4-4, Figure 4-5). As a result, the calcite dissolution/re-precipitation events are smaller in magnitude than in the other simulations (Figure 4-7). The preserved calcite can form throughout the year, irrespective of changes in water content and temperature. This contrasts the other simulations where calcite formation occurs more discretely and more consistently at the same time of year in step with large fluctuations in CO_2 and water content. The $T\Delta47_{syn2}$ is 15.2 °C for the even rain experiment, which we note is identical to the Adams Ranch shifted experiment, despite resulting from an average of temperatures recorded throughout the year rather than an average of springtime temperatures.

Put together, these rainfall regime experiments suggest that the character of rainfall influences the timing of calcite formation (Figure 4-8). Annually uneven rainfall results in annually uneven calcite formation. Conversely, annually even rainfall results in annually even calcite formation. Our numerical modelling simulations suggest that such changes in the annual evenness of rainfall will change when soil carbonate accumulates.

4.5.5 Synchronous and asynchronous calcite accumulation at various depths in a soil profile

Because soil CO_2, temperature, and water content vary with depth in the soil profile, previous workers have hypothesized that soil carbonates at varying depths might form at different times in the year (Burgener et al., 2016; Ringham et al., 2016). We examine the Adams Ranch simulation (sandy clay loam) to test this hypothesis.

We observe that in some events, calcite accumulates synchronously at various depths within the soil profile, while in other events calcite only accumulates at certain depths. In year 2 of the model run, we observe that calcite accumulates only at a depth of 40 cm (Figure 4-4). That

year's rainfall is characterized by smaller events (Table 4-11, Figure 4-8) that only promote sizeable carbonate accumulation at relatively shallow depths in the profile. In contrast, in year 3 of the model we observe simultaneous calcite accumulation at depths of 40, 60 and 80 cm (Figure 4-9). The rainfall in that year includes a relatively large single event in September (Figure 4-8); this rainfall event promotes calcite accumulation at all depths (Figure 4-9). This contemporaneous accumulation results in similar $T\Delta47_{syn2}$ predicted at all depths (range of 18.3-19.8 °C, where $T\Delta47_{syn2}$ increases with depth) (Figure 4-9). The increase in $T\Delta_{47}$ with depth is because throughout the typical months in which calcite formation occurs in this simulation (September through January), the surface temperature is lower than temperatures at depth in the soil column (Figure 4-10). The pattern of $T\Delta_{47}$ with depth would differ if formation occurred during a different season (i.e., calcite accumulation events in the spring would result in decreasing $T\Delta_{47}$ with depth as surface temperatures are warmer than soil temperatures), as predicted with the physics of heat diffusion (Hillel, 1982; Quade et al., 2013; Radcliffe and Šimůnek, 2010). However, we note that the difference in $T\Delta_{47}$ with depth (1.5 °C) would be difficult to resolve with clumped isotope analyses of natural soil carbonates (usually have a minimum precision of ± 2 ℃). This modeling evidence for simultaneous and non-simultaneous calcite formation at all depths agrees with previous interpretations of clumped isotope data: uniform clumped isotope temperatures of Holocene soil carbonates collected at various depths have been interpreted to indicate unsynchronized carbonate formation where deep carbonates form after large rain events and shallow carbonates form more frequently after smaller rain events (Burgener et al., 2016; Ringham et al., 2016).

4.5.6 Caveats: where the numerical simulations fail to describe nature and future work

In these simple experiments where we have only varied soil texture and rainfall individually, we neglect some natural complications that might enhance or diminish the effect that these of environment factors have on calcite accumulation. First, we are not considering interactions between soil texture and rainfall regime; their interplay could and should be further investigated with HYDRUS. It would be beneficial to be able to numerically model gravelly soils for comparison to many Holocene soil carbonate sites (perhaps using HYDRUS 2-D or 3-D). It would be more difficult to account for feedbacks between soil moisture and air temperature or feedbacks between soil moisture and rainfall (review by Seneviratne et al., 2010).

Also, model simulations run for > 5 years might produce more robust results, given the annual variations in rainfall data that was randomly chosen. For example, year 2 of the Adams Ranch simulation has less rain than the other years (13.5 cm total annual rainfall in year 2, compared to >20 cm of annual rainfall in the other years) (Table 4-11). The reduced total rainfall results from an absence of days with >1 cm of rain (Figure 4-8). The absence of large storms changes the soil physics and chemistry: there is no seasonal increase in CO_2, and soil water content decreases fairly constantly throughout the year at depths of 40 cm (Figure 4-4). As a result, calcite accumulation does not follow the marked dissolution/re-precipitation patterns of the other years, instead calcite accumulates more sporadically throughout the year. This difference shows that one year with slightly different rainfall patterns can influence $T\Delta47_{syn}$ (in this case, model year 2 reduced the $T\Delta47_{syn2}$ by 1 °C). Such climatologically anomalous years are likely not relevant for paleoclimate purposes given that soil carbonates accumulate over hundreds to thousands of years (Gile et al., 1966). Simulations run for > 5 years with additional rainfall data would be useful to average out anomalous years.

An abundance of other environmental factors is neglected in this work. We are not considering snow or snowpack in these simulations. The presence of snowpack in early spring would likely affect calcite formation by saturating the soil with melt water, by preventing plant activity, and/or by acting as thermal insulation (Zhang, 2005). We are not considering feedbacks between seasonal timing of rainfall and rootwater uptake/evapotranspiration. In these simulations, we allow plants to be active year-round, which permits rootwater uptake to promote calcite supersaturation by moving solution upward, even at times of the year where plant activity is not necessarily realistic (i.e., midwinter). We would likely observe less calcite formation if plant growth season did not coincide with the rainy season (Meyer et al., 2014). However, the timing of plant growth is likely sensitive to the timing of rainfall in nature (Hall and Scurlock, 1991; Stephenson, 1990), so perhaps our parameterization of year-round potential rootwater uptake partially accounts for this potential feedback. Previous workers have used HYDRUS to demonstrate the importance of plant processes in calcite accumulation (Meyer et al., 2014). Future work could continue to explore how the parameterization of plants and rootwater uptake in HYDRUS changes the timing of calcite formation. We are not accounting for other plant-related feedbacks like change in vegetative cover, which would affect temperature (Cermak et al., 2017; Tan and Layne, 1993) or runoff/infiltration (Abrahams et al., 1995).

Also, there are a few parameterization choices that fall short of describing natural soils. Our simulations are not limited by Ca^{2+} ions: we start with seed calcite and have relatively high Ca^{2+} concentrations in the soil solution. This parameterization best represents natural soils with abundant Ca^{2+}, like soils with volcanic or marine sedimentary protoliths. In some natural soils, the rate of calcite accumulation is limited by Ca^{2+} (Landi et al., 2003); this might restrict calcite formation to periods when Ca^{2+} is available, rather than allowing calcite to form during changes

in soil CO_2 and water content. Also, we do not consider the presence of organic material in these HYDRUS simulations. Organic material can limit calcite formation by through poisoning nucleation sites (Inskeep and Bloom, 1986; Lebrón and Suarez, 1996; Lebrón and Suárez, 1998), preventing the formation of soil carbonate even in supersaturated conditions (Suarez and Rhoades, 1982). Future modeling efforts could explore how Ca^{2+} limitations and/or the presence of organic carbon could change the timing of calcite formation.

4.5.7 Implications for paleoclimate interpretations of the isotopic composition of soil carbonate

The magnitude of the difference in $T\Delta47_{syn}$ between some of the simulations is large enough to concern paleoclimatologists. We observe a maximum 7 °C difference between the rainfall scenarios. For comparison, the Paleocene-Eocene Thermal Maximum caused 5-8 °C of global temperature increase (McInerney and Wing, 2011). These results suggest that a shift in the timing of carbonate accumulation due to changes in rainfall regime could potentially amplify or dampen clumped isotope temperatures by an amount that is significant compared to secular changes in climate (Page et al., 2019). However, combining geologic and other contextual information with an understanding of calcite accumulation from numerical simulations could be a powerful way to use the soil carbonate proxy.

Soil texture can and should be directly observed during sampling. Paleo-hydrologic information is more difficult to find, but our model simulations show that information on the seasonal pattern and spacing of storms would be useful in interpreting the isotopic composition of soil carbonates. Sedimentology (from fluvial deposits or from the presence of slickensides) (Foreman et al., 2012; Foreman, 2014; Schmitz and Pujalte, 2007) and fossils (Gushulak et al., 2016; West et al., 2015; Wilf et al., 1998) can be used as independent constraints on paleo-

hydrology. Predictions from global climate models may also provide information about potential shifts in hydrologic regime and the seasonal range in temperature at a specific location (Carmichael et al., 2015, 2017, 2018; Fricke et al., 2010; Huber and Goldner, 2012). Also, we show that calcite accumulation is sensitive to soil CO_2 production. Thus, any geologic information about paleo-CO_2 production could be useful. The $\delta^{13}C$ of soil carbonates can be used to estimate soil respiration (given known atmospheric CO_2 concentrations and the proportion of C_3/C_4 vegetation) (Caves et al., 2016; Cerling, 1999; Quade et al., 1989). Less quantitatively, organic carbon content and root traces in paleosols could indicate relative productivity in soils. Alternatively, independent constraints on soil temperatures like lipid biomarkers (Inglis et al., 2017; Tierney, 2012; Yang et al., 2016) or the major elemental composition of soil matrix (Gallagher and Sheldon, 2013; Sheldon et al., 2002; Stinchcomb et al., 2016) could be paired with Δ_{47} values to learn about paleo-hydrology, although each proxy has its own complications to keep in mind. We are optimistic that a numerical model (like HYDRUS) could be forced with various paleo-environmental conditions with the purpose of predicting the seasonal bias of a soil carbonate clumped isotope temperature and the uncertainty around that bias.

4.6 Conclusions

The timing of calcite accumulation is influenced by soil texture and by the timing and style of rainfall. In HYDRUS-1D, calcite accumulation results from changes in soil CO_2 concentrations that are often caused by large rain events. We show that, while holding all other environmental variables constant, varying soil texture, varying the annual timing of rainfall and varying the annual evenness of the rainfall each change the pattern of carbonate accumulation.

Our soil texture simulations result in $T\Delta47_{syn}$ values that are within 1 °C of each other, despite the fact that coarse-grained soils accumulate calcite throughout a larger percentage of the year. We find that changing rainfall patterns results in a maximum change of 7 °C in $T\Delta47_{syn}$, but we speculate that the change could be larger in nature. The sensitivity to CO_2 production suggests that biological processes (plants and microbes) might be important in controlling soil carbonate accumulation. Numerical models, like HYDRUS, could be used to model a paleosol environment and to estimate the seasonal bias of ancient pedogenic carbonates. Additionally, the sensitivity of calcite accumulation to rainfall could be exploited by paleoclimatologists to investigate paleo-hydrologic processes.

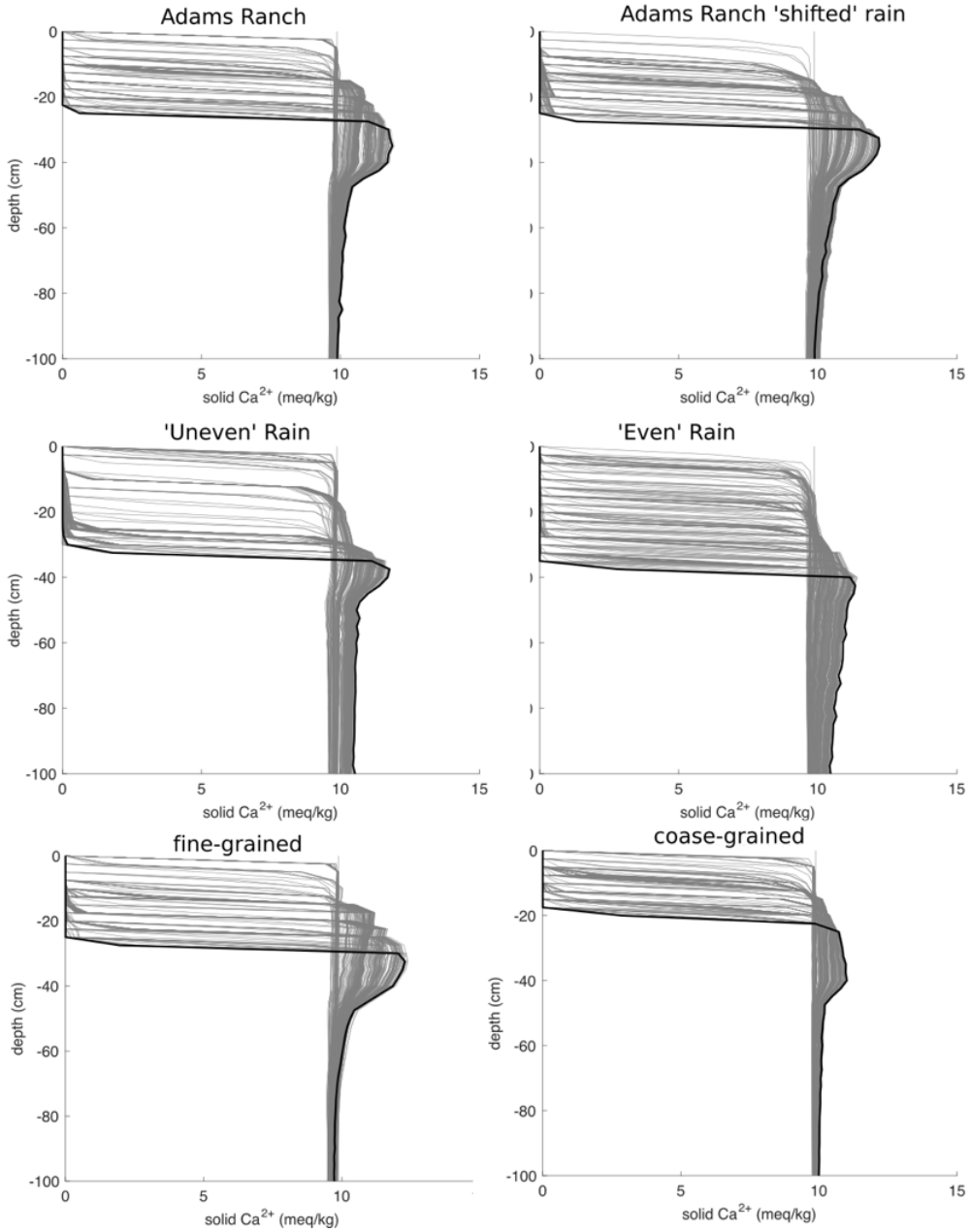

Figure 4-1: Solid Ca^{2+} profiles for each experiment.

Gray lines are time steps (all simulations start with 10 meq/kg of Ca^{2+} at all depths). Thick black line is the final time step of the simulation (day 1826).

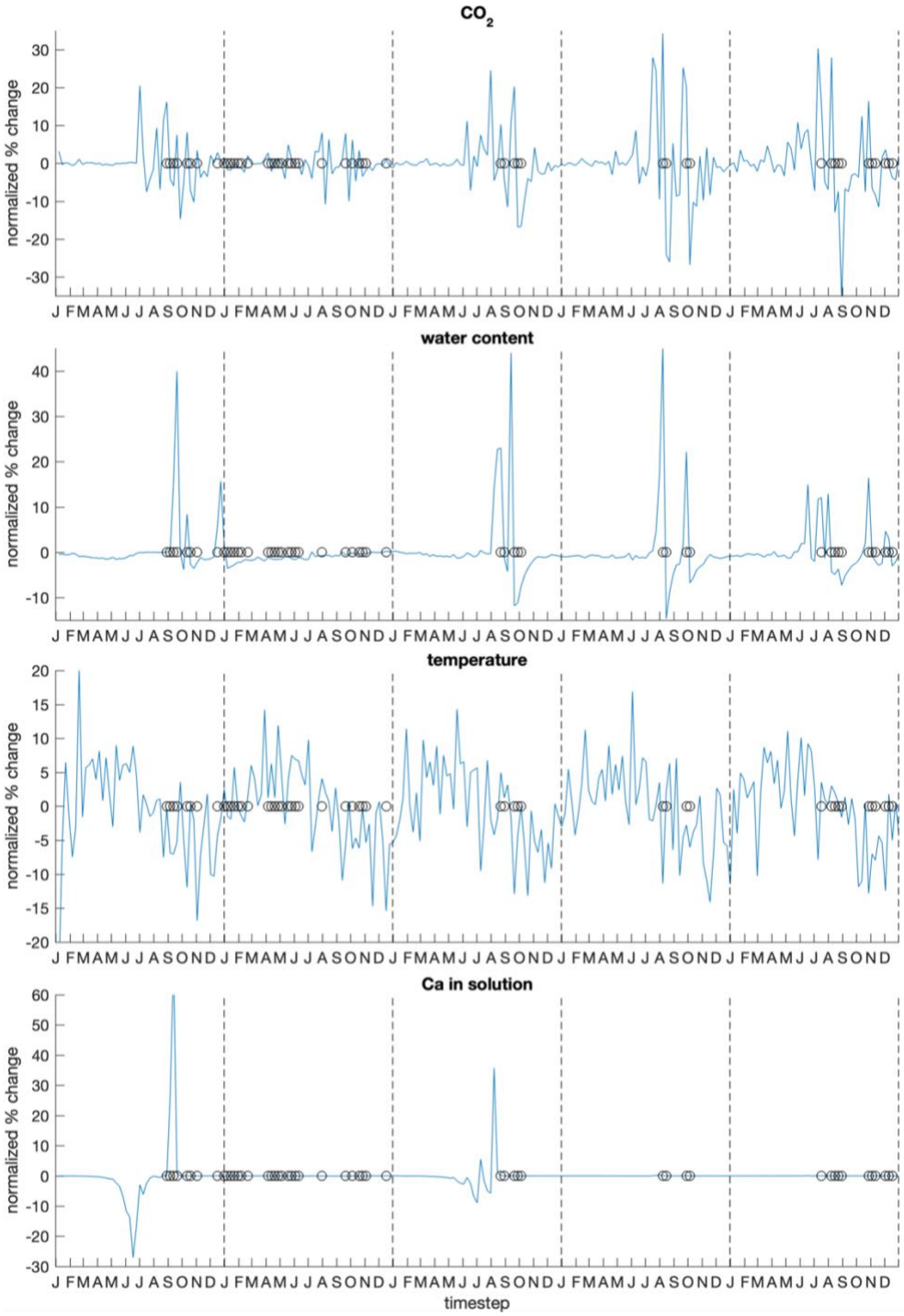

Figure 4-2: Percent change in physical soil parameters during calcite accumulation events.

Timesteps when accumulated calcite forms are indicated by black circles. Percent change of each physical parameter is calculated as the difference from the previous time step divided by the range in that physical parameter throughout the course of the experiment, multiplied by 100.

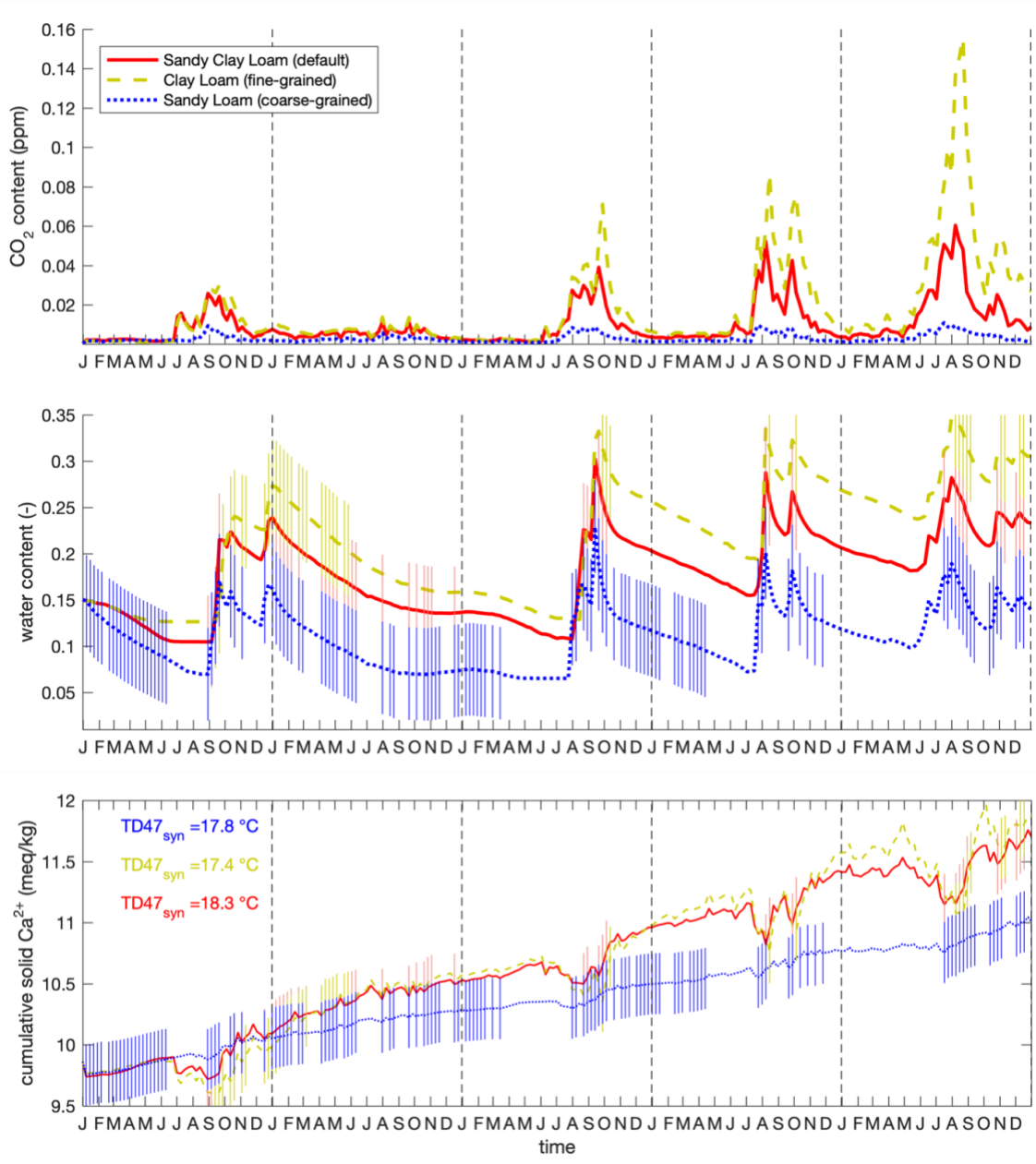

Figure 4-3: Adams Ranch simulation with varying soil texture parameters

Line color and texture indicate the soil texture parameters varied between the simulations (given in Table 4-1 and Table 4-5). All other input parameters are held constant. Vertical bars in middle and bottom panel indicate the timestep in which accumulation calcite forms (bars removed from top panel for clarity).

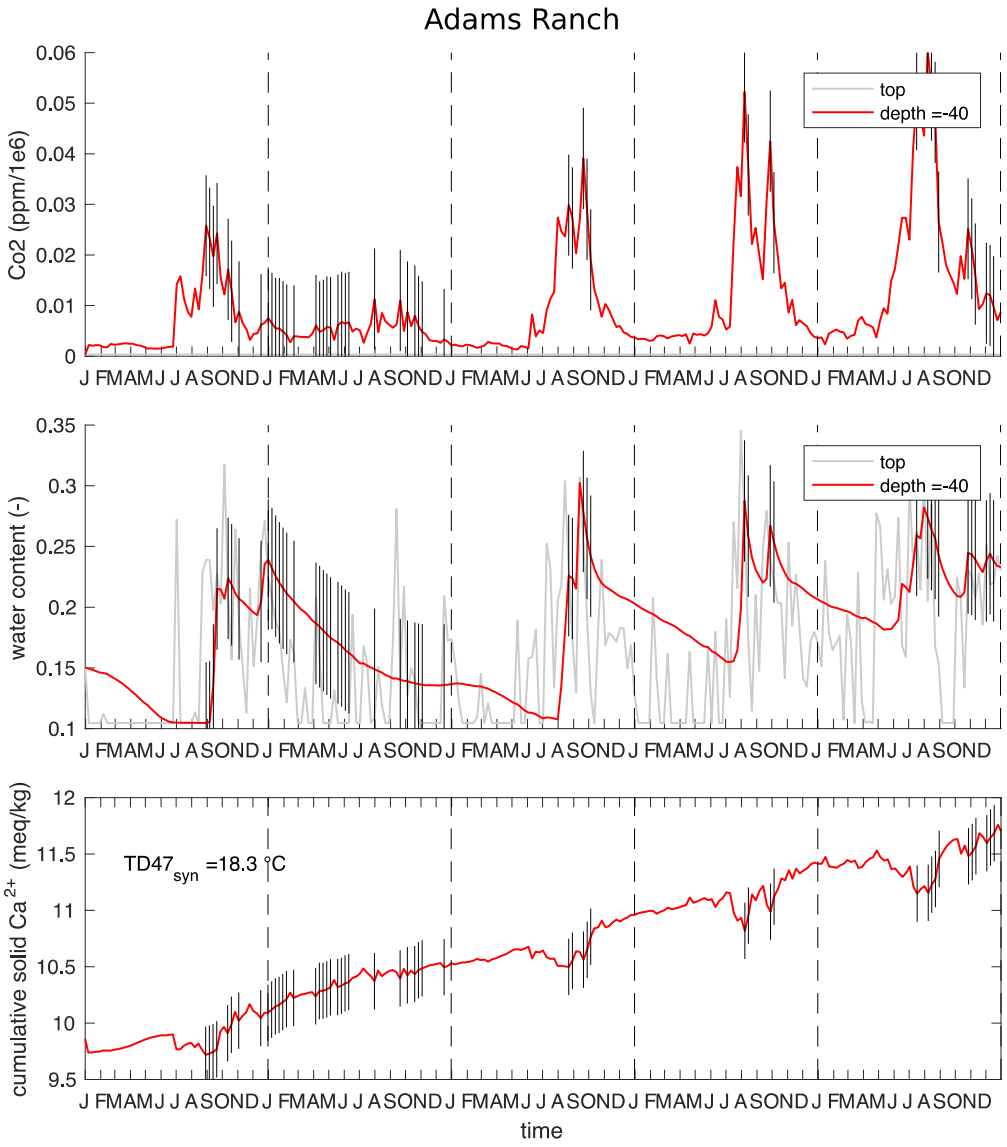

Figure 4-4: Physical parameters for the Adams Ranch simulation at 40 cm.

Data in red are from 40 cm depth, data in light gray are from the surface. Dashed vertical lines indicate breaks in the calendar year. Short, solid vertical lines centered on data in all other panels indicate the time step of calcite accumulation (all lines are same length, length chosen for visual clarity and not based on amount of accumulation).

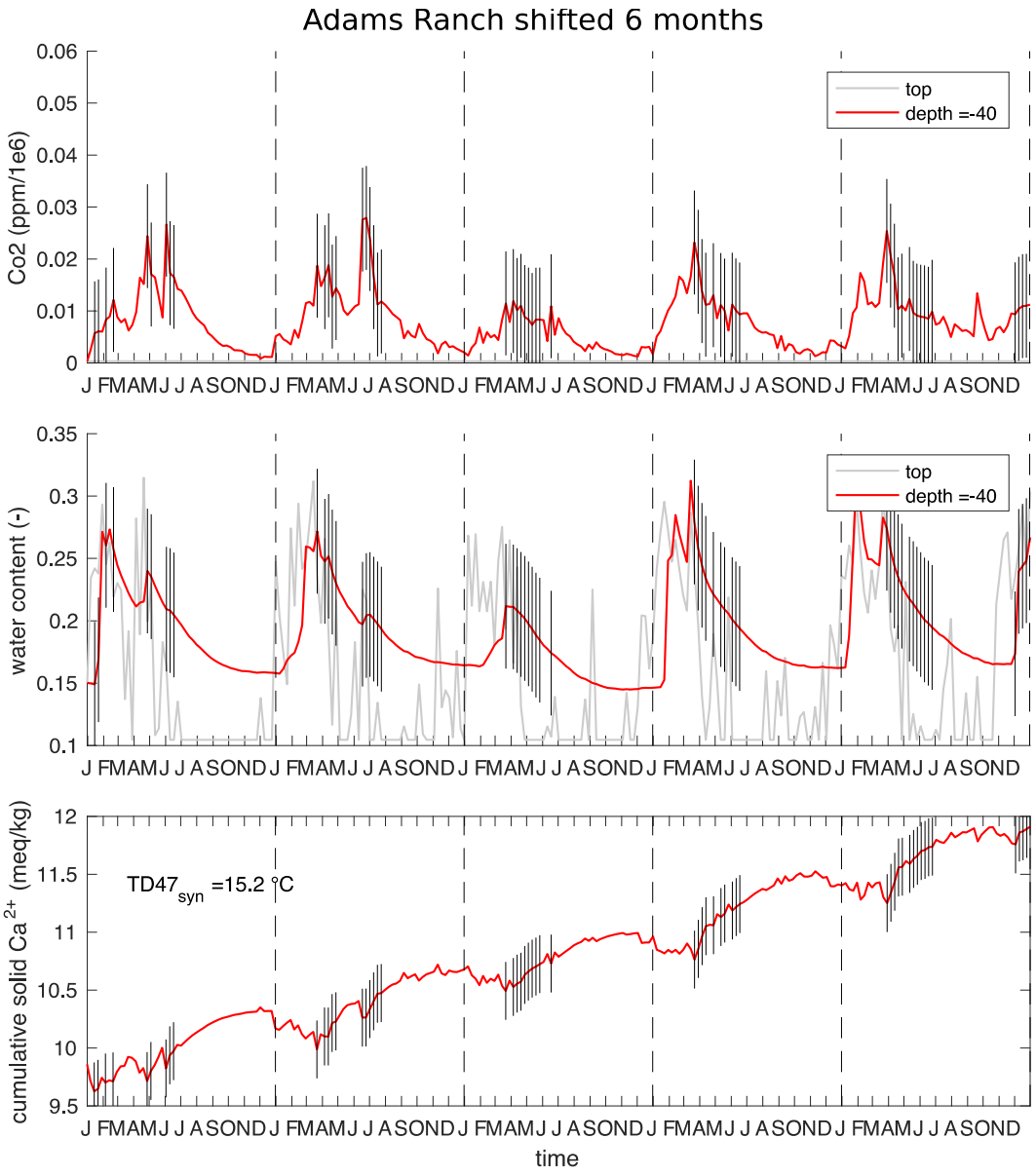

Figure 4-5: Physical parameters for the Adams Ranch Shifted Rain Simulation at 40 cm.

Data in red are from 40 cm depth, data in light gray are from the surface. Dashed vertical lines indicate breaks in the calendar year. Short, solid vertical lines centered on data in all other panels indicate the time step of calcite accumulation.

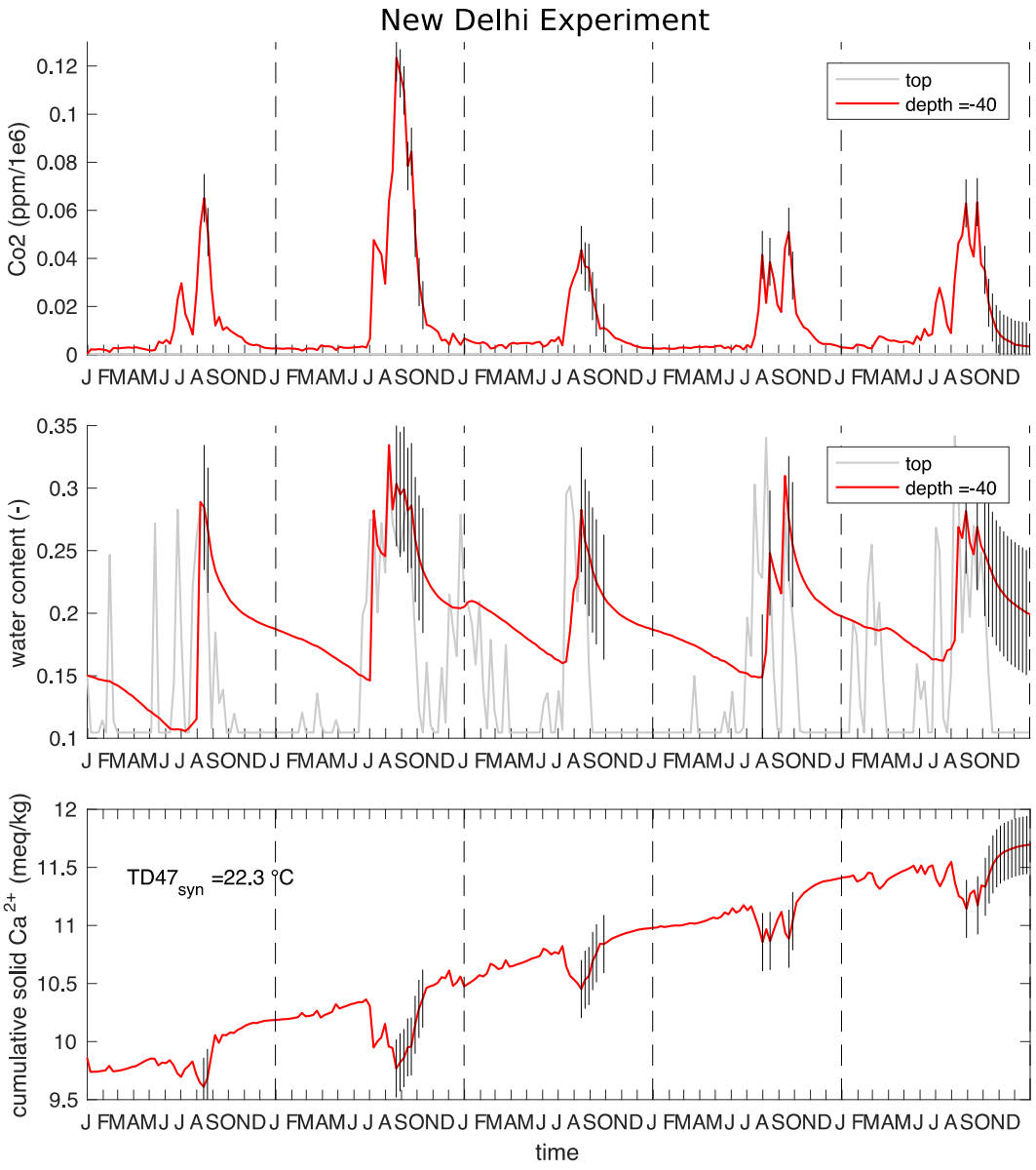

Figure 4-6: Physical parameters for the Uneven Rain (New Delhi) Simulation at 40 cm.

Data in red are from 40 cm depth, data in light gray are from the surface. Dashed vertical lines indicate breaks in the calendar year. Short, solid vertical lines centered on data in all other panels indicate the time step of calcite accumulation.

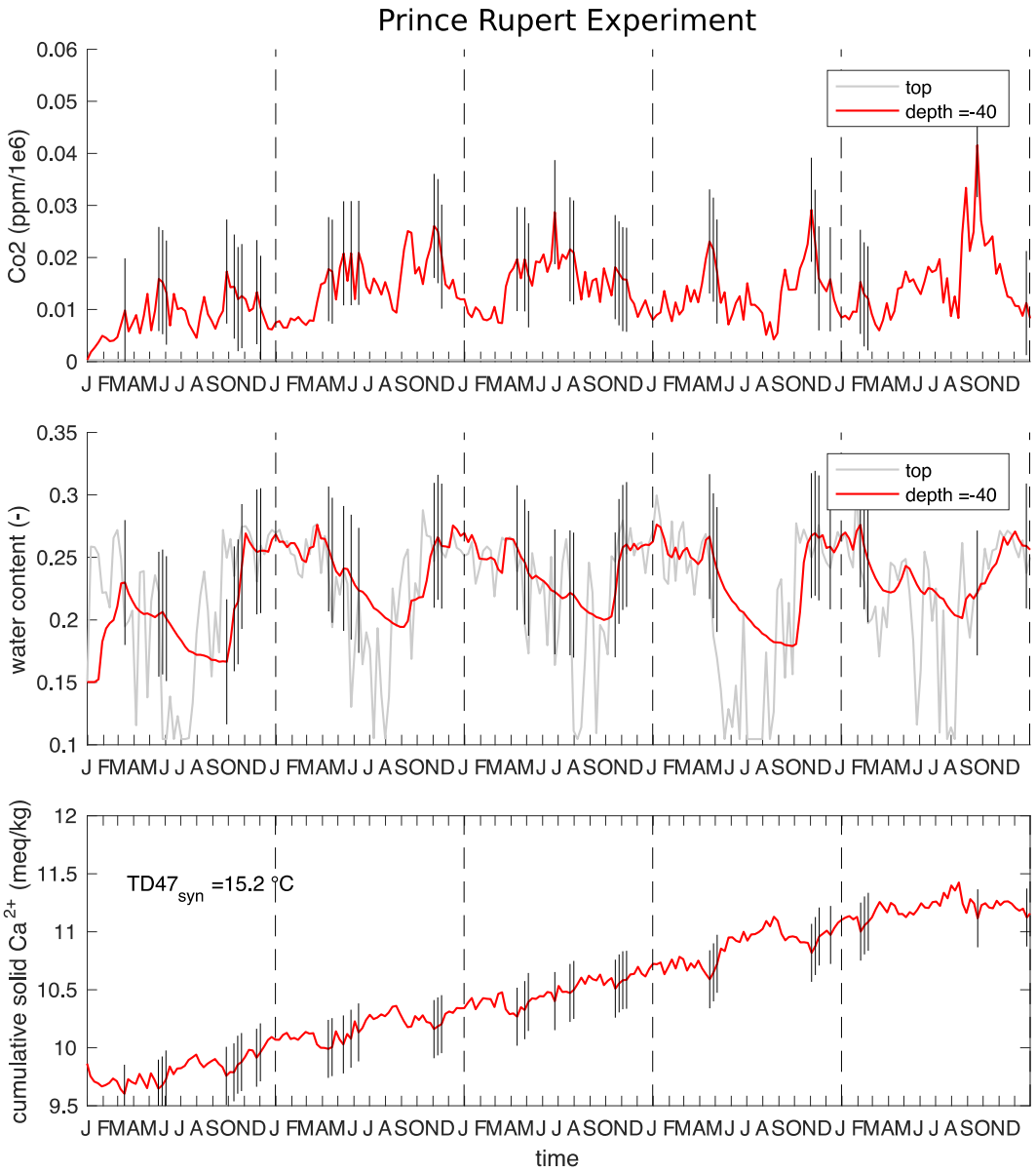

Figure 4-7: Physical parameters for the Even Rain (Prince Rupert) Simulation at 40 cm.

Data in red are from 40 cm depth, data in light gray are from the surface. Dashed vertical lines indicate breaks in the calendar year. Short, solid vertical lines centered on data in all other panels indicate the time step of calcite accumulation.

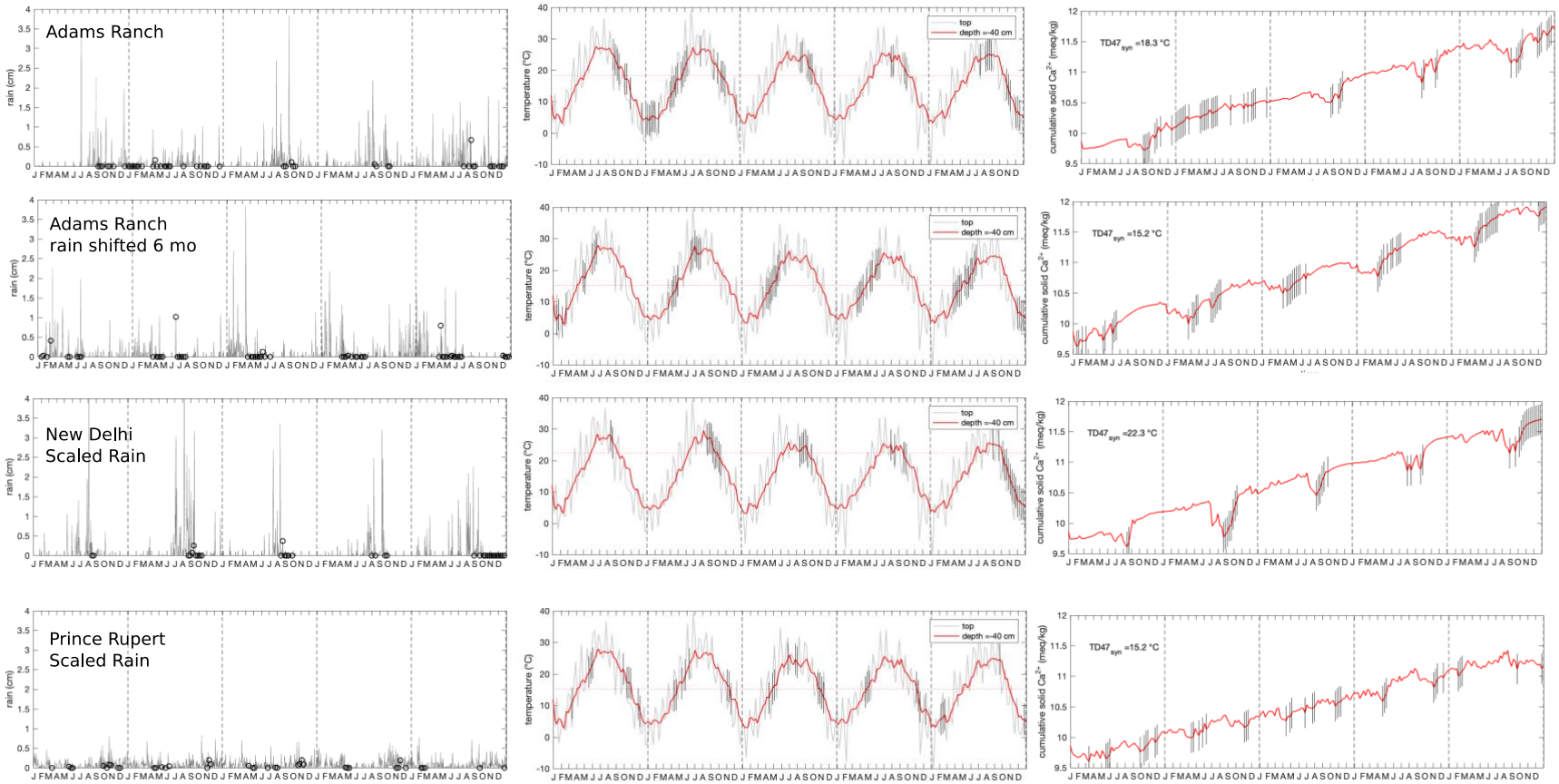

Figure 4-8: Summary of rainfall experiments – inputs, temperature, and calcite accumulation.

Left column: Daily rainfall for each simulation (black lines). Circles indicate the timestep of calcite accumulation. **Middle column:** temperature from each simulation (surface temperature is identical in all simulations). Short, solid vertical lines centered on data indicate the time step of calcite accumulation. Horizontal red dotted line is $T\Delta47_{syn}$. **Right column:** calcite accumulation for each simulation at 40 cm. Short, solid vertical lines centered on data in all indicate the time step of calcite accumulation

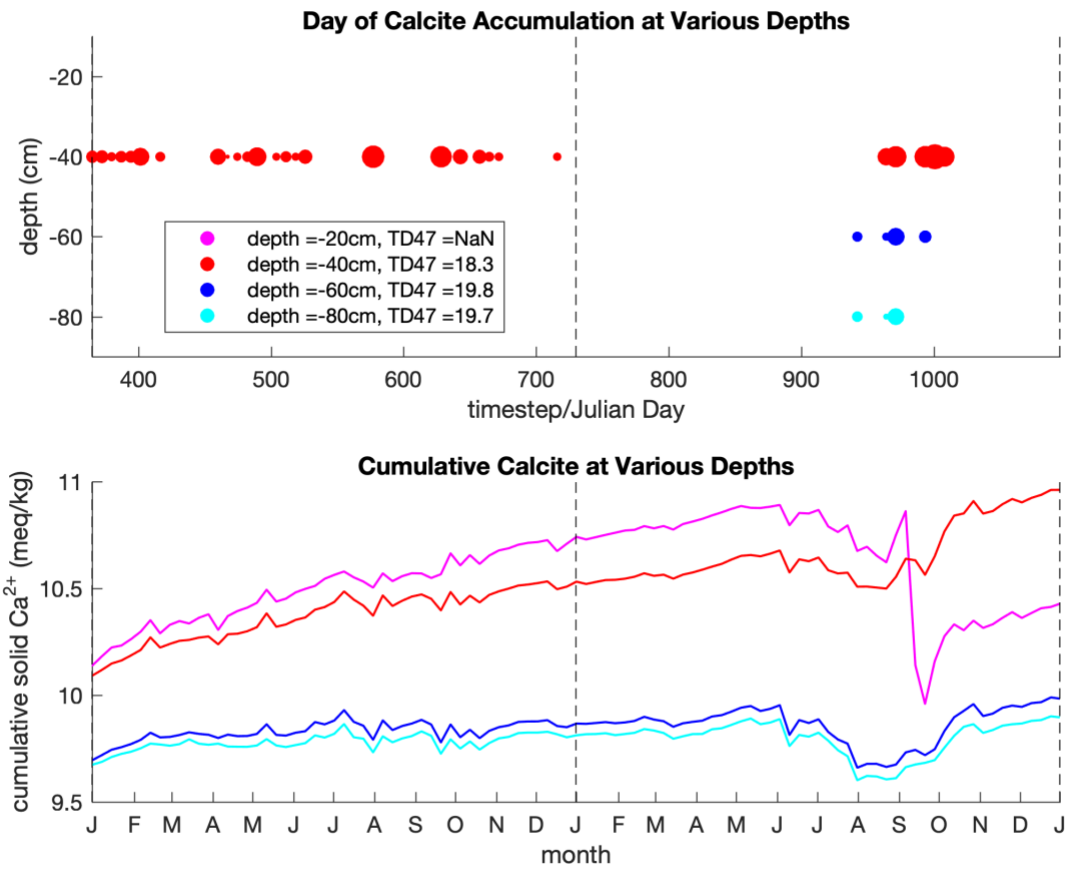

Figure 4-9: Calcite formation at various depths in the Adams Ranch experiment.

Only model years two and three are shown. Top: dots indicate a timestep/day when calcite accumulates at various depths in the soil profile. Size of dot indicates amount of calcite accumulation. Bottom: cumulative calcite at the same depths. Vertical dashed lines indicate the break between years 2 and 3 of the model run. No calcite accumulates at 20 cm in the shown model years.

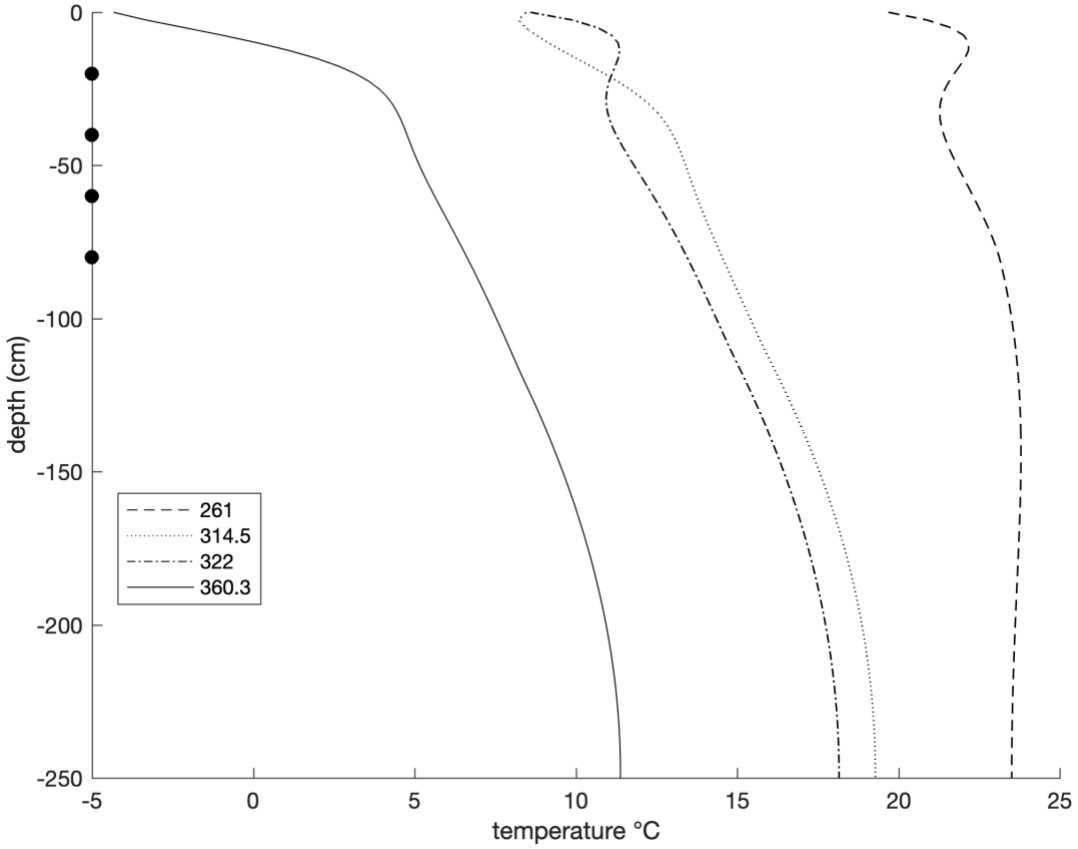

Figure 4-10: Temperature profiles during the Adams Ranch simulation

Each line represents the temperature profile at the given time step (in Julian Date) for the third year of the Adams Ranch simulation (sandy clay loam). Black dots on the x-axis give the depths for which calcite accumulation is plotted in Figure 4-9.

Table 4-1: Water Flow Parameters for Soil Material

	Qr (-)	Qs (-)	Alpha (1/cm)	n (-)	Ks (cm/day)	I (-)
sandy clay loam	0.1	0.39	0.059	1.48	31.44	0.5
"fine-grained" experiment - clay loam	0.095	0.41	0.019	1.31	6.24	0.5
"coarse-grained" experiment - sandy loam	0.065	0.41	0.075	1.89	106.1	0.5

Table 4-2: Solution Composition (meq/L)

Ca	Mg	Na	K	Alk	SO4	Cl	Tracer
0.013	0	0.0015	0	0	0	0	0

Table 4-3: Precipitated Concentration (meq/kg)

Calcite	Gypsum	Dolomite	HydroMg	Nesqoh	Sepiolite
10	0	0	0	0	0

Table 4-4: Solute Transport and Reaction Parameters

Bulk density	Dw (molecular coefficeint in free water, L2/T)	Dispersivity	CEC (Cation Exchange Capacity)	Calc.SA (Calcite surface area)	Dolom.SA (Dolomite surface area)	K [Ca/Mg]	K [Ca/Na]	K [Ca/K]
1.5	0	10	0	0.007	0	0	0	0

Table 4-5: Heat Transport Parameters for Soil Material

	Solid	Org. M.	Disp	b1	b2	b3	Cn	Co	Cw
Loam	0.57	0	5	1.57E+16	2.53E+16	9.89E+16	1.43E+14	1.87E+14	3.12E+14
Clay	0.601	0	5	-1.27E+16	-6.20E+16	1.63E+17	1.43E+14	1.87E+14	3.12E+14
Sand	0.601	0	5	1.47E+16	-1.55E+17	3.17E+17	1.43E+14	1.87E+14	3.12E+14

Table 4-6: Carbon Dioxide Transport Parameters

Air Diff	Water Diff	Disper.	Upper Boundary Condition:		Lower Boundary Condition:	
13737.6	1.526	5	Concentration BC	0.000333	Concentration BC	0

Table 4-7: Carbon Dioxide Production - Microorganisms

Optimal Carbon Dioxide Production	0.3
Activation Energy	7677
Michaelis' Constant	0.19
Optimal Pressure Head	-100
Critical Pressure Head	-1.00E+06
Salinity Stress Coefficient	3
Salinity Stress Coefficient h50	1000
Space Distribution	
Exponential Distribution Constant	0.085

Table 4-8: Carbon Dioxide Production – Plant Roots

Optimal Carbon Dioxide Production	0.28
Activation Energy	6014
Michaelis' Constant	0.14
Degree Days to Maximum Production	0

Table 4-9: Root Water Uptake Parameters (Feddes)

PO (cm)	-10
POpt (cm)	-50
P2H (cm)	-200
P2L (cm)	-800
P3 (cm)	-90000
r2H (cm/days)	0.37
r2L (cm/days)	0.01

Table 4-10: Soil Profile Inputs and Initial Conditions

Nodes (depth, cm)	Root concentrations	water content (-)	CO2
0	1	0.15	0.0033
2.5	0.938666977	0.15	0.0033
5	0.881095693	0.15	0.0033
7.5	0.827055431	0.15	0.0033
10	0.776329621	0.15	0.0033
12.5	0.728714978	0.15	0.0033
15	0.684020686	0.15	0.0033
17.5	0.642067629	0.15	0.0033
20	0.60268768	0.15	0.0033
22.5	0.565723023	0.15	0.0033
25	0.531025519	0.15	0.0033
27.5	0.498456119	0.15	0.0033
30	0.467884298	0.15	0.0033
32.5	0.43918754	0.15	0.0033
35	0.41225084	0.15	0.0033
37.5	0.38696625	0.15	0.0033
40	0.36323244	0.15	0.0033
42.5	0.340954296	0.15	0.0033
45	0	0.15	0.0033
47.5	0	0.15	0.0033
50	0	0.15	0.0033
52.5	0	0.15	0.0033
55	0	0.15	0.0033
57.5	0	0.15	0.0033
60	0	0.15	0.0033
62.5	0	0.15	0.0033
65	0	0.15	0.0033
67.5	0	0.15	0.0033
70	0	0.15	0.0033
72.5	0	0.15	0.0033
75	0	0.15	0.0033
77.5	0	0.15	0.0033
80	0	0.15	0.0033
82.5	0	0.15	0.0033
85	0	0.15	0.0033

(continued)

87.5	0	0.15	0.0033
90	0	0.15	0.0033
92.5	0	0.15	0.0033
95	0	0.15	0.0033
97.5	0	0.15	0.0033
100	0	0.15	0.0033
102.5	0	0.15	0.0033
105	0	0.15	0.0033
107.5	0	0.15	0.0033
110	0	0.15	0.0033
112.5	0	0.15	0.0033
115	0	0.15	0.0033
117.5	0	0.15	0.0033
120	0	0.15	0.0033
122.5	0	0.15	0.0033
125	0	0.15	0.0033
127.5	0	0.15	0.0033
130	0	0.15	0.0033
132.5	0	0.15	0.0033
135	0	0.15	0.0033
137.5	0	0.15	0.0033
140	0	0.15	0.0033
142.5	0	0.15	0.0033
145	0	0.15	0.0033
147.5	0	0.15	0.0033
150	0	0.15	0.0033
152.5	0	0.15	0.0033
155	0	0.15	0.0033
157.5	0	0.15	0.0033
160	0	0.15	0.0033
162.5	0	0.15	0.0033
165	0	0.15	0.0033
167.5	0	0.15	0.0033
170	0	0.15	0.0033
172.5	0	0.15	0.0033

(continued)

175	0	0.15	0.0033
177.5	0	0.15	0.0033
180	0	0.15	0.0033
182.5	0	0.15	0.0033
185	0	0.15	0.0033
187.5	0	0.15	0.0033
190	0	0.15	0.0033
192.5	0	0.15	0.0033
195	0	0.15	0.0033
197.5	0	0.15	0.0033
200	0	0.15	0.0033
202.5	0	0.15	0.0033
205	0	0.15	0.0033
207.5	0	0.15	0.0033
210	0	0.15	0.0033
212.5	0	0.15	0.0033
215	0	0.15	0.0033
217.5	0	0.15	0.0033
220	0	0.15	0.0033
222.5	0	0.15	0.0033
225	0	0.15	0.0033
227.5	0	0.15	0.0033
230	0	0.15	0.0033
232.5	0	0.15	0.0033
235	0	0.15	0.0033
237.5	0	0.15	0.0033
240	0	0.15	0.0033
242.5	0	0.15	0.0033
245	0	0.15	0.0033
247.5	0	0.15	0.0033
250	0	0.15	0.0033

Table 4-11: Summary of Rainfall Regimes Used in Experiments

	Adams Ranch		**'Even' rain**		**'Uneven' rain**	
	total annual rain (cm)	# of days with rain	total annual rain (cm)	# of days with rain	total annual rain (cm)	# of days with rain
Year 1	20.4	45	24.7	226	22.1	65
Year 2	13.5	56	27.3	255	43.5	77
Year 3	23.6	63	25.5	241	14.8	45
Year 4	23.9	69	26.5	212	20.8	50
Year 5	32.4	88	24.7	239	26.1	59
TOTAL	**113.6**	**321 (of 1826)**	**128.7**	**1173 (of 1826)**	**127.3**	**296 (of 1826)**

Table 4-12: Synthetic Clumped Isotope Temperatures from HYDRUS experiments

	coarse-grained	**fine-grained**	**Adams Ranch**	**Adams Ranch shifted**	**'Even' rain**	**'Uneven' rain**
$T\Delta47_{syn1}$	17.2	17.3	17.3	15.9	15.7	19.2
$T\Delta47_{syn2}$	17.8	17.4	18.3	15.2	15.2	22.3
$T\Delta47_{syn3}$	17.2	18.3	17.4	15.4	16.1	19.3

Chapter 5 Warm terrestrial subtropics during the Paleocene and Eocene: Carbonate clumped isotope (Δ_{47}) evidence from the Tornillo Basin, Texas (USA)

Abstract

Records of subtropical climate on land from the early Paleogene offer insights into how the earth system responds to greenhouse climate conditions. Fluvial and floodplain deposits of the Tornillo Basin (Big Bend National Park, Texas, USA) preserve a record of environmental and climatic change of the Paleocene and the early Eocene. We report carbon, oxygen, and clumped isotopic compositions ($\delta^{13}C$, $\delta^{18}O$, and Δ_{47}) of paleosol carbonate nodules from this basin. Mineralogical, geochemical and thermal modeling evidence suggests that the measured isotopic values preserve primary environmental signals with a summer bias with the exception of data from two nodules reset by local igneous intrusions. The unaltered nodules record Δ_{47} temperatures of 25 ±4°C and 32 ±2°C for the Paleocene and early Eocene nodules, respectively, showing an increase in average summer temperatures of 7 ±3°C. Calculations of $\delta^{18}O$ of soil water are -2.8 ±0.7‰ and -0.8 ±0.4‰ (SMOW) for the early-mid Paleocene and late Paleocene-early Eocene, showing an increase of 2.0 ±0.9‰. The increase in temperature and $\delta^{18}O$ values likely relates to a rise in atmospheric pCO_2, although we cannot rule out that changes in paleosol texture and regional precipitation patterns also influence the record. Comparison with Δ_{47} estimates of summer temperature from the Green River and Bighorn Basins (WY) highlights that terrestrial surface temperatures are heterogeneous, and latitudinal temperature gradients on land remain undetermined. Previously published paleoclimate models predict summer temperatures that are 2 to 6°C higher than our estimate; discrepancies between climate models and proxy data persist at lower latitudes.

5.1 Introduction

Reconstructions of ancient greenhouse climates can help inform our understanding of future climates that could be similarly forced by high concentrations of atmospheric CO_2. Greenhouse climates of the early Paleogene provide examples of Earth's long-term sensitivity of climate to high CO_2 (Haywood et al., 2011; Lunt et al., 2013, 2012; Valdes, 2011); the early Paleogene contains peak global temperatures of the Cenozoic during the Early Eocene Climatic Optimum (EECO, ~52 to 50 Ma), and those maximum temperatures correspond with high concentrations of atmospheric CO_2 (Anagnostou et al., 2016; Beerling and Royer, 2011; Hyland and Sheldon, 2013; Jagniecki et al., 2015; Lowenstein and Demicco, 2006; Pagani et al., 2005; Pearson et al., 2007; Zachos et al., 2008). Continuous records of ocean temperature exist from the Paleogene (Lauretano et al., 2015; Thomas et al., 2011; Zachos et al., 2008, 2001), but few terrestrial records span the entirety of the Paleocene and the transition into the early Eocene. The need for proxy estimates of temperature on land during this past greenhouse period is highlighted by predictions that terrestrial warming can outpace oceanic warming (Diffenbaugh and Field, 2013).

Fundamental questions about the nature and dynamics of early Paleogene climates remain unanswered. In particular, latitudinal temperature gradients in the early Eocene are enigmatic because shallow gradients estimated by proxies are challenging to reproduce with climate models (Bernard et al., 2017; Heinemann et al., 2009; Ho and Laepple, 2016; Huber and Caballero, 2011; Lunt et al., 2016, 2012; Matthew and Sloan, 2001; Roberts et al., 2009; Sagoo et al., 2013; Sewall and Sloan, 2001, 2006; Shellito et al., 2009, 2003; Sloan, 1994; Sloan and Barron, 1990; Thrasher and Sloan, 2009; Tierney et al., 2017; Winguth et al., 2010). Both geochemical proxies and fossils generally predict early Paleogene high-latitude temperatures that are much higher than modern, often by 20 degrees or more (Brinkhuis et al., 2006; Eberle et al., 2010; Eberle & Greenwood, 2012; Greenwood & Wing, 1995; Hollis et al., 2009; Maxbauer et al., 2014; Pross et

al., 2012; Royer et al., 2002; Sluijs et al., 2008, 2009, 2006; Smith et al., 2009; Spicer & Parrish, 1990; Weijers et al., 2007). Global climate models have been able to reproduce this high latitude warmth with large radiative forcing (Huber and Caballero, 2011; Lunt et al., 2012). However, these models also predict extremely high temperatures at low latitudes that, in some cases, exceed the physiological temperature limit for plant and animal survival (Huber, 2008; Sherwood and Huber, 2010). They are thus difficult to reconcile with fossil records that suggest mild tropical climates and/or abundant tropical life (Head et al., 2009; Spicer et al., 2014; Wheeler and Lehman, 2005; Wing et al., 2005, 2009; Wing and Greenwood, 1993) and disagree with some geochemical proxy reconstructions of mild tropical climates (Bijl et al., 2009; Evans et al., 2018; Keating-Bitonti et al., 2011). However, other studies voice concerns about the accuracy and interpretation of some geochemical ($\delta^{18}O$ and TEX_{86}) proxy reconstructions of low-latitude Paleogene climate due to problematic calibrations and/or sample preservation (Aze et al., 2014; Frieling et al., 2017; Hollis et al., 2012; Kozdon et al., 2011; Pearson et al., 2001, 2007). Furthermore, some fossil records provide evidence for heat stressed organisms and hot tropical temperatures that are more consistent with model predictions (Frieling et al., 2017; Harrington and Jaramillo, 2007; Head et al., 2009; Jaramillo et al., 2006). Additional quantitative proxy estimates of the amount of subtropical warming on land during greenhouse periods such as the early Paleogene offer a crucial opportunity to test model predictions and expand the representation of low-latitude temperatures in proxy datasets.

Early Paleogene warming was also accompanied by global hydrologic changes that remain poorly understood and likely varied with geography and with the temporal scale of interest (Anhäuser et al., 2018; Carmichael et al., 2015, 2016, 2017; Foreman et al., 2012; Kraus et al., 2015; Kraus & Riggins, 2007; McInerney & Wing, 2011; Schmitz & Pujalte, 2007; Smith et al.,

2014). It has been hypothesized that increased warming during greenhouse periods is associated with a more intense hydrologic cycle (e.g., Held and Soden, 2006), which could be manifested partly as increased summertime precipitation in North America (Huber and Goldner, 2012; Schubert et al., 2012; Sewall and Sloan, 2006; Thrasher and Sloan, 2009). Improved understanding of patterns of hydroclimate in the early Paleogene would offer potential to test this prediction and document specific characteristics of the water cycle of greenhouse climates.

Here, we expand our understanding of subtropical terrestrial temperatures and hydrology during the Paleocene and the early Eocene by applying the carbonate clumped isotope paleothermometer (Δ_{47}) to a suite of paleosols in the Tornillo Basin in Big Bend National Park, Texas (Figure 5-1). The paleosol sequence in the Tornillo Basin preserves a long, well-sampled record of environmental change from the early Paleocene through early Eocene (Atchley et al., 2004; Bataille et al., 2018, 2016). Carbonate clumped isotopes can provide information on both soil temperatures and meteoric waters at the time of carbonate growth, which allows us to provide a quantitative estimate of terrestrial environmental changes across this important greenhouse interval in the previously under-sampled subtropics.

5.2 Materials and Methods

5.2.1 Paleogeographic, geologic, and environmental setting

The paleosols studied in this work are from the Tornillo Basin in Big Bend National Park, Texas (USA), approximately 29° 25'N, 103° 09'W (Figure 5-1). The Tornillo Basin formed as the southernmost extent of the Laramide orogeny (Lehman, 1991; Lehman and Busbey, 2007; Schiebout et al., 1987; Turner et al., 2011), and during the early Paleogene was likely at or near the same subtropical latitude as it is today (van Hinsbergen et al., 2015). There is some evidence

for syndepositional deformation in the studied Paleocene and Eocene sediments (Lehman and Busbey, 2007). The basin was likely a distal foreland basin with relatively low sediment accumulation rates (Schiebout et al., 1987). During the Paleogene the basin was close to the proto-Gulf of Mexico shoreline, and thus preserves a record of a more coastal environment than exists at modern Big Bend (e.g., Galloway et al., 2011; Sharman et al., 2017).

We focus on Paleocene to early Eocene sediments in the Black Peaks and Hannold Hill Formations (Figure 5-1, Figure D-1, Figure D-2). These sediments consist of alternating channel deposits and over-bank floodplain deposits with evidence of pedogenesis (Bataille et al., 2016; Lehman and Busbey, 2007; White and Schiebout, 2008). Identifiable paleosols have been measured and described from these sections (Figure **5-2** and Figure D-1), and some of the pedogenic horizons yield carbonate nodules. An age model for these sediments was developed using carbon isotope stratigraphy, magnetostratigraphy, and sparse vertebrate fossils (Bataille et al., 2018, 2016; Rapp et al., 1983; Schiebout et al., 1987), and agrees well with a paleomagnetically-constrained age model for a section with overlapping stratigraphic coverage that is exposed about 38 km to the west (Leslie et al., 2018).

5.2.2 Field Methods

Stratigraphic sections were measured in two adjacent locations exposing the target formations, at Tornillo Flats and at Grapevine Hills (Figure **5-2**, Figure D-1, Figure D-2)Sections were correlated primarily via two distinct marker beds: the Exhibit Ridge sandstone, and the uppermost black paleosol of the Black Peaks Fm. Between these marker beds, sections were correlated based on similar lithologies and thicknesses and measurements of dip (Bataille et al., 2016; Figure D-1). Paleosols were identified in the field based on pedogenic features such as

horizonation, coloring, root traces and burrowing, gleying, and/or the presence of carbonate nodules. Paleosols were trenched to enable accurate description, and samples were collected from at least 20 cm below the modern outcrop surface to avoid modern contamination and exposure weathering. Carbonate nodules were sampled from the middle of the Bk horizon. The depth to the Bk horizon ranged from 0.1–4 m below the approximate top of the paleosol horizon; however, there is significant uncertainty in this estimate because the tops of most paleosols were either truncated or indistinct due to continual aggradation and pedogenesis. The shallowest of these carbonates (~0.1 m) were collected from truncated paleosols, and the true formation depth is unknown. We collected bulk A and B horizon material and pedogenic carbonate nodules where present.

5.2.3 Carbonate analysis methods

5.2.3.1 Nodule characterization and sampling

Each carbonate nodule was cut open and polished for examination, and selected carbonate nodules were made into thin sections. The carbonate nodules from Tornillo Flats were prepared and described as part of an MS thesis (Watford, 2015), and five of those nodules had thin sections that were examined with transmitted light. We collected additional nodules from Grapevine Hills, and representative nodules from that section were made into thin sections that were examined with both transmitted light and cathodoluminescent (CL) microscopy. The CL scope used is a Luminoscope ELM-3R, and was operated at 5–10 kV, 0.5 mA and 50–100 mTorr. Nodules were classified as homogeneous, heterogeneous, or radial, based on their internal textures, where homogeneous nodules were dominated by homogeneous micritic carbonate, heterogeneous nodules showed appreciable brecciation, grainification, and/or phreatic

sparry calcite cement, and radial nodules exhibited a distinctive radial-fibrous fabric (example images in Watford, 2015 and Bataille et al., 2016). With one exception, radial nodules were not analyzed for Δ_{47} given previous work suggesting that they represented distinctive, groundwater-dominated growth environments characterized by unusual isotopic values (Bataille et al., 2016; Schmidt, 2009). For all nodules, the target carbonate material was sampled from the cut and polished nodule surface using a micro mill, a mounted dental drill, or by hand with a drill tool. One nodule was too small to be cut open (< 0.5 cm in diameter), so the entire nodule was ground and homogenized (PS3); this sampling method offers considerably more opportunity for unintentional sampling of altered material.

5.2.3.2 $\delta^{18}O$, $\delta^{13}C$, and Δ_{47} methods

Soil carbonates grow in near-equilibrium conditions (Quade et al., 2007a; 2013), and thus can provide a reliable record of growth temperature and isotopic composition of the source fluid and gases. Carbonate clumped isotope thermometry uses the thermodynamic preference for an increase in the abundance of ^{13}C-^{18}O bonds with decreasing temperature in order to measure the growth temperature of a carbonate mineral (e.g., Affek, 2012; Eiler, 2007; Ghosh et al., 2006a). Paired with the simultaneously-measured oxygen isotope ($\delta^{18}O$) composition of carbonate, the $T\Delta_{47}$ also allows for the calculation of the $\delta^{18}O$ of the water in which the carbonate grew (here denoted $\delta^{18}O_w$) (e.g., Eiler, 2011; Huntington and Lechler, 2015; Quade et al., 2013).

The $\delta^{18}O$, $\delta^{13}C$, and Δ_{47} compositions of the carbonate nodules were measured at the University of Washington IsoLab in Seattle, WA. First, 6–10 mg carbonate-equivalent of sample powder was digested in a common bath of phosphoric acid with a specific gravity of 1.904–1.970 g/cm^3 held at 90°C. We do not observe a change in measured Δ_{47} in our carbonate

standards across this range in specific gravity. The evolved CO_2 gas was then cryogenically purified using an offline, automated vacuum system. The purified CO_2 gas was measured on a Thermo MAT 253 mass spectrometer configured to measure m/z 44–49. Details of the purification and the measurements, including the pressure baseline, absolute reference frame, and ^{17}O correction are described elsewhere (Burgener et al., 2016; Kelson et al., 2017; Schauer et al., 2016). For every ~4 sample unknowns a carbonate standard was run, which rotated between a tropical Porites coral (Coral), two in-house reagent-grade synthetic carbonates (C64 and C2), and four synthetic carbonates distributed by ETH Zurich (ETH1–4) (Bernasconi et al., 2018; Meckler et al., 2014). We regularly purified and measured heated gases (1000°C) and equilibrated gases (4 and 60°C) to place samples into the absolute reference frame (Dennis et al., 2011). The sample analyses span four reference frames: a reference frame from 02/2014 to 10/2014, a reference frame from 10/2014 to 4/2015, a reference frame from 10/2015 to 12/2016, and a reference frame from 12/2016 to 04/2018.

Δ_{47} was calculated using standard methods (Dennis et al., 2011; Huntington et al., 2009), with two exceptions: we used the Brand et al. (2010) parameters to correct for ^{17}O interference (Daëron et al., 2016; Schauer et al., 2016), and we did not add an acid fractionation factor to our Δ_{47} values (values are presented in the '90°C reference frame'). Each nodule was analyzed in replicate 2–8 times (replication is defined as an individual acid digestion of a subset of the sample powder). We calculated temperatures from Δ_{47} values ($T\Delta_{47}$) with the calibration presented in Kelson et al. (2017), equation 2, which is similar to other recent clumped isotope calibrations (e.g., Bonifacie et al., 2017), and was produced at IsoLab with the same methods (also calculated with the Brand et al. (2010) parameters and uses carbonates digested in 90°C acid). We report two estimates of error: 1) standard error (S.E.), which was calculated as the

larger of either the standard deviation of the sample Δ_{47} or our external error of 0.021‰ (estimated by the long term standard deviation of our zeros), divided by the square root of the number of replicates for that sample, and 2) the 95% confidence interval (CI), which was calculated as the student's t-value for the number of replicates multiplied by the S.E. Although errors on individual samples can be quite large, robust estimates for temperature can be made by using an error-weighted average of samples from similar time periods and reporting the 95% CI on those means (Fernandez et al., 2017). The $\delta^{18}O$ composition of the fluids from which the carbonates grew ($\delta^{18}O_w$) was estimated using the $T\Delta_{47}$ and the calcite-water fractionation factors from Kim and O'Neil (1997). The error in the $T\Delta_{47}$ measurement was propagated to estimate the error in the $\delta^{18}O_w$ calculation.

5.3 Results

5.3.1 Carbonate nodule texture observations

Most of the carbonate nodules (>70%) were characterized as homogenous, and micritic material from those nodules was targeted for isotopic analysis. Examination of thin sections in plane light showed that some of the homogenous nodules contained some secondary spar (>10 μm). The spar was isolated to veins or inclusions and made up less than 10% of the total nodule, which enabled us to sample exclusively micrite for isotopic analysis. In two nodules (BB-TF2-14-036 and BB-TF3-14-003), we were able to isolate and sample the spar material for isotopic analysis (Table 5-1). Thin section imagery revealed that the sparry calcite exhibited red or orange luminescence that was distinct from the micritic material, which was uniformly non-luminescent (Figure D-3) The minor amount of spar, together with textural observations from

CL, suggest that examination in plane light was likely sufficient to allow sampling for isotopic analyses that avoided most secondary or diagenetic calcite material.

5.3.2 $\delta^{18}Oc$, $\delta^{13}C$, Δ_{47}, and $\delta^{18}O_w$ results

Micritic carbonate samples have $\delta^{18}O_c$ values that range from -3.6 to -10.1‰ (VPDB) with an average S.E. of 0.04‰, and $\delta^{13}C$ values that range from -8.9 to -11.8‰ (VPDB) with an average S.E. of 0.09‰. Mean Δ_{47} values of the micritic carbonate nodules range from 0.456 to 0.646‰, with S.E. that ranges from 0.009 to 0.029‰ (Table 5-1, Figure **5-2**). This corresponds to $T\Delta_{47}$ values that range from 13 to 89°C with 95% CI that ranges from 7 to 47°C. Using the $\delta^{18}O_c$ and $T\Delta_{47}$ from individual carbonate nodules, we calculate a range in $\delta^{18}O_w$ of -5.8 to 3.0‰ (SMOW) with error ranging from 0.5 to 1.5‰ (Table 5-1, Figure 5-4 and Figure 5-5).

5.4 Discussion

5.4.1 Recognizing diagenesis

Post-depositional alteration can destroy the primary climate signal in a pedogenic carbonate nodule. Alteration can occur either through secondary precipitation of calcite or through solid-state reordering of the ^{13}C-^{18}O bonds. Recrystallization or precipitation of secondary calcite can cause the Δ_{47}, and conditionally also the $\delta^{13}C$ and $\delta^{18}O$, values of carbonate nodules to reflect the temperature and isotopic composition of the secondary fluid. Solid-state reordering can occur if a carbonate mineral is held at temperatures >100°C for an extended amount of time (>10^6 years), thus changing Δ_{47} but not $\delta^{18}O$ or $\delta^{13}C$ of carbonate (Henkes et al., 2014; Lloyd et al., 2017;

Passey and Henkes, 2012; Stolper and Eiler, 2015). Here, we discuss the possibility that these two processes have altered the Big Bend carbonate nodules.

5.4.1.1 Spar indicates localized recrystallization

In Big Bend, fluids associated with late Eocene-early Oligocene magmatic intrusions could have recrystallized the carbonate nodules. Thin sections of the nodules reveal distinct accumulations of luminescent spar (Figure D-3) which can be explained by increased concentrations in trace metals that are associated with secondary precipitation (e.g., Finnegan et al., 2011). Indeed, our two measured spar samples have $T\Delta_{47}$, $\delta^{13}C$ and $\delta^{18}O$ compositions that are distinctly higher than those of micrite samples (Table 5-1). The range in bulk isotopic composition among these samples (~10‰ in both $\delta^{13}C$ and $\delta^{18}O$) might be due to multiple phases of recrystallization with fluids varying in composition. We carefully sampled carbonate nodules where possible in order to avoid contamination from diagenetic spar material and believe that our isotopic analyses of micrite are not significantly contaminated with recrystallized post-burial phases.

5.4.1.2 Potential solid-state reordering of micritic samples due to heating from burial and local laccoliths

Solid-state reordering does not necessarily change the visible texture or bulk elemental structure of carbonates, which makes it nearly impossible to observe from thin-section imagery alone. Here we use thermal modeling to explore the possibility that our sample carbonate nodules could have experienced partial or complete reordering.

It is unlikely that the sampled sediments reached burial temperatures higher than 100°C because they were never deeply buried (also assumed by Atchley et al., 2004; Nordt et al., 2011) (heating due to local volcanic deposits is considered later). The combined Black Peaks, Hannold Hill, and Canoe Formations, are approximately 720–820 m thick (Turner et al., 2011). The Chisos Formation (~1000 m thick) is time-correlative with the Canoe Formation, but its distribution is limited to a local basin southwest of the stratigraphic sections measured and thus it does not overlie the sediments of interest (Turner et al., 2011). No other potential Paleogene overburden is mapped in this area. There are late Tertiary to Quaternary alluvial sediments in the region, but their deposition is localized in fault-bounded basins and any such alluvial accumulation in the vicinity of Tornillo Flats and Grapevine Hills likely had an insignificant effect on burial temperatures of the study formations (Turner et al., 2011). Therefore, the sediments of the Black Peaks and Hannold Hill Formations were buried <1 km, and so a remarkably high geothermal gradient would have been required to heat the carbonates studied here to >100°C. Even if late Tertiary Basin and Range extension elevated the geothermal gradient in the region to a high gradient like that of continental magmatic arc regions, ~40 to 50°C km^{-1} (Rothstein and Manning, 2003), the sediments would have been buried at maximum temperatures of 60–70°C. Heating of temperatures <100°C could have promoted modest reordering (an increase in apparent temperature of 10°C) if the carbonate samples resided at those elevated temperatures for hundreds of millions of years (Stolper and Eiler, 2015), but these samples have a maximum depositional age of 70 Ma that rules out such a long burial history. Thus, heating due to burial alone is unlikely to have significantly altered the clumped isotope bonding in our carbonate nodules.

Several kilometer-scale laccoliths were emplaced in the region at ~32 Ma (Miggins et al., 2007) and could have provided enough heat to locally enable solid state reordering. The Grapevine Hills section is so-named due to the Grapevine Laccolith that is as close as 0.8 km to our stratigraphic section (Figure D-2). Geophysical measurements of the Grapevine Laccolith suggest that it is about 3.5 km wide and 200 m thick, and that the laccolith does not extend laterally beyond its surface expression (Turner et al., 2011). We model the heating of the country rock using the 1D error function solution to the Fourier conduction equation (e.g., Turcotte and Schubert, 2014). We model the laccolith as a body of basaltic composition that is 200 m thick with a starting temperature of 1400°C (this starting temperature includes an adjustment for the latent heat of crystallization, e.g., Philpotts (1990)) and a thermal diffusivity of $1e^{-6}$ m^2s^{-1}. At a distance of 800 m from the laccolith (our closest sampling location), the country rock reaches simulated temperatures of up to 113°C for ~2 Ma (Figure 5-3). This estimate is inherently an overestimate of the heat at this sampling location because we model heat conduction in only one dimension, and in reality, heat can diffuse into the country rock in several directions. Also, the sample is located off of the edge of the laccolith, so the sample location would experience lower maximum temperatures. The relatively low temperatures predicted by our thermal modeling are consistent with the absence of evidence for contact metamorphism in sediments and paleosols surrounding the laccolith at Grapevine Hills (i.e., no color or textural changes). Given this thermal history, the Passey and Henkes (2012) model for re-ordering of clumped isotopes in carbonate predicts an increase in apparent clumped isotope temperature of <1°C using the Arrhenius parameters from a brachiopod (WA-CB-13), a result which is not sensitive to the assumed starting $T\Delta_{47}$ (Figure 5-3). This increase in temperature is too small to resolve with current Δ_{47} precision. In conclusion, it is unlikely that the Grapevine Laccolith provided enough

heat to promote measurable solid-state reordering of the clumped isotope bonds in our sampled carbonates.

The Rosillos Laccolith north of Tornillo Flats should also be considered as a heat source that could enable solid state reordering in nearby samples. The Rosillos Laccolith is 600 m thick on its north end, thinning to 200 m on its south end (Turner et al., 2011). The two Cretaceous Javelina Formation samples collected in northern Tornillo Flats are as close as 1 km to the south end of the laccolith (Figure D-2). We model the Rosillos Laccolith conservatively as 450 m thick, with the same temperature and thermal diffusivity as above. Using the Passey and Henkes (2012) reordering model and a starting sample depositional temperature of 25°C, we predict an apparent $T\Delta_{47}$ of 28°C at a distance of 1.6 km, an apparent $T\Delta_{47}$ of 50°C at a distance of 1.3 km, and an apparent $T\Delta_{47}$ of 192°C at a distance of 0.6 km (Figure 5-3). Note that these predicted temperatures imply that partial resetting could occur depending on the proximity to the intrusion; the apparent temperature predicted is less than the maximum temperature the sample at that distance experiences. Again, these are likely overestimates of the effect of heating because we have modeled the heat diffusion in only one direction and the samples are at the edge of the laccolith where the heat is able to diffuse in multiple directions. The carbonate nodules that are <1.3 km away from the Rosillos Laccolith have relatively high measured $T\Delta_{47}$: BB-TF2-14-002 has a temperature of 49 ±32°C, and BB12-077 has a temperature of 47 ±11°C. These measurements are consistent with modeled temperature effects, and so we interpret these high temperatures as potentially indicating that these samples experienced solid state reordering when the Rosillos Laccolith was emplaced. Therefore, we exclude these two samples from our environmental interpretations, but maintain that all other measured samples are unlikely to have experienced solid-state reordering.

5.4.1.3 Problematic carbonate nodules

Carbonate nodule PS3 was too small (~2 mm in diameter) to make a thin section or microsample, so the entire nodule was ground up and analyzed. If secondary carbonate phases were present in this nodule, they would have been included in our clumped isotope sample and may have affected the resulting data. Indeed, this nodule has a clumped isotope temperature that is hotter than plausible earth surface temperatures (T >55°C), but consistent with a mixture of spar and micrite. We exclude this carbonate nodule from our paleoclimate reconstruction.

The only carbonate nodule sampled from a black paleosol (BB-TF2-14-030) exhibited a radial fabric and has a relatively high clumped isotope temperature (48 ±14°C). Carbonate nodules from black paleosols in this formation were previously excluded from $\delta^{13}C$ chemostratigraphy because these paleosols indicate carbonate growth in a water-saturated environment where the carbonates might incorporate a higher contribution of carbon from respired soil CO_2 compared to carbonate nodules from other soils in the section (Bataille et al., 2016; Mintz et al., 2011). The carbonate growth process is poorly understood in Histosol-like soils such as the black paleosols in the Black Peaks Formation, and could involve disequilibrium processes, so we also exclude this nodule from our climate reconstruction.

5.4.2 Increase in temperatures from the Paleocene to the Eocene

The most robust conclusions about climate arise from averaging multiple Δ_{47} analyses of multiple carbonate nodules; uncertainty in clumped isotope measurements prevents robust conclusions to be drawn from 3–5 analyses of a single carbonate sample (e.g., Fernandez et al., 2017). Thus, we only interpret the average temperatures of the multiple carbonate nodules that can be calculated by separating the record at the Paleocene-Eocene boundary. We choose this

boundary because it is known to be of geologic significance (e.g., McInerney and Wing, 2011). Statistical evidence that supports treating the data as a constant piece-wise function with a breakpoint at ~56 Ma can be found in the Appendix D and Figure D-4.

Our measurements show that on average the Eocene clumped isotope temperatures are higher than those from the Paleocene (32 ±2°C and 25 ±3°C, respectively; means are error-weighted, and error is 95% CI of the mean, mean of all data is 28 ±1.5°C) (Figure 5-4). A *t*-test using the mean $T\Delta_{47}$ of each nodule finds that the Paleocene and Eocene have temperatures that are different by 7 ±3°C ($p = 0.025$). A *t*-test using the individual Δ_{47} replicates confirms a statistically significant difference between the Paleocene and Eocene Δ_{47} values ($p = 0.0049$).

Although the Paleocene samples are dominantly from Tornillo Flats and the Eocene samples are dominantly from Grapevine Hills, it is unlikely that the shift in temperatures between the Paleocene and Eocene could be explained only by differences between these closely situated localities. Bias due to the change in section sampled seems unlikely because the stratigraphy is similar between the two sections and they are less than 3 km apart. Furthermore, a *t*-test suggests that there is no statistical difference between the Eocene-aged nodules from Tornillo Flats vs. the nodules from Grapevine Hills ($p = 0.5027$). Additionally, if the samples from Grapevine Hills are removed, and a *t*-test for the Paleocene vs. Eocene samples from Tornillo Flats is performed, the difference in temperature between the two periods of time is confirmed ($p = 0.0136$).

To interpret the significance of the temperature difference between the Paleocene and the Eocene, we must consider the seasonal bias of our proxy. Soil carbonate typically accumulates when an increase in soil temperature promotes soil matrix drying, and soil water reaches supersaturation with respect to carbonate (Breecker et al., 2009). This often occurs in summer months, and most studied modern soil carbonates with Δ_{47} data thus far record summer-biased

temperatures (Burgener et al., 2016; Hough et al., 2014; Passey et al., 2010; Quade et al., 2013; Ringham et al., 2016). However, some soil carbonates record temperatures closer to mean annual temperature, likely due to differences in local precipitation and soil moisture regimes (Burgener et al., 2016; Gallagher and Sheldon, 2016; Peters et al., 2013). Thus, it is possible to hypothesize that the observed increase in temperature from the Paleocene to the Eocene could be related to an enhanced summer bias in the Eocene soils rather than a global increase in air temperatures.

Sedimentological observations do suggest differences in precipitation and soil texture between the Paleocene and the early Eocene in Big Bend, but these factors are unlikely to lead to a shift in the seasonal bias of pedogenic carbonate accumulation that would fully explain temperature differences between these periods. The Paleocene environment in Big Bend was likely subtropical and humid with year-round precipitation (Wheeler, 1991): dark purple Alfisols alternating with black, Histosol-like horizons (Lehman, 1990) suggest the soils were relatively poorly drained. In these humid conditions, soil carbonate accumulation is most likely to occur during the summer because higher temperatures would increase the amount of soil water lost due to evaporation and uptake by plant roots. In the Eocene, climate models suggest precipitation in the region may have been more seasonal with stronger summer monsoon rainfall than the Paleocene (Carmichael et al., 2015; Sewall and Sloan, 2006; Thrasher and Sloan, 2009)—a shift that has also been inferred from the sandstone sedimentology in Big Bend (Bataille et al., 2018) and in the Green River Basin (Krueger, 2017). Some soils in strongly seasonal rainfall regimes experience delayed drying and record mean annual rather than summer temperatures (e.g., Peters et al., 2013). However, the Early Eocene soils at Big Bend were well drained (Bataille et al., 2016; White & Schiebout, 2008) and likely dried shortly after summer rain events (as observed by Breecker et al., 2009 and Ringham et al., 2016), resulting in a summer bias, as we infer for

Paleocene carbonate accumulation. Therefore, it is unlikely that a change in the seasonal bias of the soil carbonates can explain the temperature difference we observe in the Paleocene and the Eocene samples.

The shift in temperatures at the start of the Eocene more likely relates to a contemporaneous gradual rise in the concentration of atmospheric pCO_2 (Anagnostou et al., 2016; Beerling and Royer, 2011; Cui and Schubert, 2017; Hyland and Sheldon, 2013; Jagniecki et al., 2015; Maxbauer et al., 2014; Royer et al., 2014). The increase in temperatures at Big Bend is also contemporaneous with an increase in $\delta^{18}O$ of benthic foraminifera, which suggests an increase in deep ocean temperatures of about 5°C from the mid-Paleocene to the peak warming of the EECO (Zachos et al., 2008). Our measured temperature increase of 7°C from the Paleocene to the Eocene is larger than that observed in the deep ocean, although our uncertainty of ±3°C (95% CI from a *t*-test) permit this terrestrial estimate to be closer to the oceanic estimate. It is not unreasonable for inland tropical temperatures to increase more than oceanic temperatures as a result of continentality (Rohling et al., 2012), an effect which has been noted in other terrestrial records from the Paleogene (e.g., Hyland et al., 2017; McInerney and Wing, 2011) and in the modern (Diffenbaugh and Field, 2013).

5.4.3 Increase in $\delta^{18}O_w$ from the mid Paleocene to the late Paleocene/early Eocene

We interpret the $\delta^{18}O_w$ data by taking the mean of the $\delta^{18}O$ values of several nodules from periods of time that appear to be similar or near-constant. For $\delta^{18}O_w$, we divide the record at ~59 Ma (between nodules with ages of 59.7 and 58.4 Ma) because this breakpoint minimizes the misfit from the means (Appendix D and Figure D-5). This analysis suggests that an apparent increase in $\delta^{18}O_w$ may have occurred ~2–3 Ma before the apparent increase in temperatures in the

same record (which occurs at ~ 56 Ma). However, dividing the $\delta^{18}O_w$ record at 56 Ma only results <1% increase in RMS error (if the analysis is performed with sample replicate data, Figure D-5). Therefore, these data are insufficient to justify speculation about lags between hydrologic and global temperature change.

We observe that the average $\delta^{18}O_w$ is 2.1 ± 0.9‰ higher in the late Paleocene/early Eocene than in the early to mid-Paleocene (-0.81 ± 0.35‰ and -2.8 ± 0.74‰, respectively, p = 0.00004 from a *t*-test) (Figure 5-4). We hypothesize that this increase in $\delta^{18}O_w$ relates to the contemporaneous increase in surface temperatures through one or more of the following processes: 1) increased evaporative enrichment in soil water, 2) increased $\delta^{18}O_w$ of the summertime rainfall and/or 3) an increased proportion of summer rainfall recorded in the Eocene carbonates.

Increased evaporation of soil water can cause an increase in $\delta^{18}O_w$. Evaporative effects can increase soil water $\delta^{18}O_w$ values relative to local rainfall by up to ~10‰ in extreme conditions such as the Atacama desert (Quade et al., 2007b). As noted earlier, the Eocene soils in Big Bend are generally better drained than those from the Paleocene, so it is likely that soil waters in the Eocene were more enriched in ^{18}O due to enhanced evaporation. This evaporative effect could be partially offset by the observation that Eocene carbonates generally formed deeper in the soil than the Paleocene carbonates (Figure D-1, also described in Bataille et al., 2016), although these apparent depths are imprecise due to indistinct soil tops and truncation. Increased evaporation likely contributes to the observed increase in $\delta^{18}O_w$ between the Paleocene and the Eocene.

It is also possible that the $\delta^{18}O$ of rainfall at Big Bend was higher during the Eocene than during the Paleocene and could contribute to increased $\delta^{18}O$ values of the soil water from which

our carbonate samples precipitated. Higher local temperatures are spatially and temporally correlated with higher $\delta^{18}O$ values in the modern, although this relationship is relatively weak at low latitudes and in the summer when precipitation is more convective (Rozanski et al., 1993; Vachon et al., 2010). All else equal, an increase in condensation temperature of 10°C would increase the $\delta^{18}O$ of rainfall by on the order of 3‰ (Vachon et al., 2010)– roughly the magnitude of the shift observed in both temperature and $\delta^{18}O_w$ across the Paleocene-Eocene boundary in our record. Additionally, an isotope-enabled general circulation model (GCM) predicts that the $\delta^{18}O$ value of the proto-Gulf of Mexico in the Eocene was about 1‰ higher than modern (after correcting for ice volumes) (Tindall et al., 2010). Although the difference in $\delta^{18}O_w$ of the Gulf between the Paleocene and the Eocene was likely smaller than predicted for the difference between Eocene and modern, it is possible that a similar change in source water compositions could contribute to the enrichment in ^{18}O recorded by the soil carbonates.

Finally, the increase in reconstructed $\delta^{18}O_w$ from the Paleocene to the Eocene could also relate to an increase in the relative proportion of summertime rainfall recorded by those carbonates. Modern summer precipitation in western Texas comes primarily from the Gulf of Mexico through a monsoon-like system, and is more enriched in ^{18}O than winter precipitation that originates primarily from frontal systems forced by cool air masses that have traveled overland from the Pacific (Licht et al., 2017; Nativ and Riggio, 1990; Vachon et al., 2010; Vera et al., 2006) (Figure D-7). Recent work shows that soils yield carbonates with calculated $\delta^{18}O_w$ that resembles the $\delta^{18}O$ of rainfall during the months in which the carbonates grew (Gallagher and Sheldon, 2016; Hough et al., 2014). Thus, assuming that these moisture source patterns were similar to modern throughout the Paleogene (as Fricke et al. (2010) predict for the Cretaceous North America), an increase in $\delta^{18}O$ of rainfall in the Eocene could also be explained

by preferential carbonate accumulation during summer rain events from moisture derived from the proto-Gulf of Mexico. Thus, it might be possible that a slight difference in the timing of carbonate accumulation and/or timing of moisture traveling inland from the proto-Gulf could also contribute to the difference in $\delta^{18}O_w$ observed in the Eocene and Paleocene.

Although reconstructed soil water $\delta^{18}O_w$ values increase from the Paleocene to the Eocene, the average $\delta^{18}O_w$ values for those time periods are both similar to the $\delta^{18}O$ of modern summer rainfall in the region. The isotopic composition of modern rainfall in south Texas has a strong seasonal cycle (range of ~6‰, Figure D-7(estimates from the Oxygen Isotopes in Precipitation Calculator, version 3.1, http://waterisotopes.org, Bowen and Revenaugh, 2003). We find a mean Paleogene $\delta^{18}O_w$ of -1.4 ‰, while modern rainfall in the region is about -3‰ in June and 0‰ in July and August. The similarity between mean Paleogene $\delta^{18}O_w$ reconstructed from the Big Bend carbonates and the $\delta^{18}O$ values of modern rainfall during summer months is consistent with the hypothesis that Paleocene and Eocene moisture patterns were not dissimilar from modern (Figure D-7), given our interpretation of a summer bias of the clumped isotope proxy. The relatively high $\delta^{18}O$ of Paleogene Big Bend waters (-1.4‰) might suggest that the ancient North American summer monsoon did not impart a strong amount effect (a depletion in ^{18}O with intense rainfall) on the summer soil waters of this area. Similarly, the amount effect is not observed in modern summer precipitation in the North American monsoon (Eastoe and Dettman, 2016). These results suggest that the Paleocene/Eocene North American monsoon was not particularly more intense or more deeply convective than the modern monsoon, despite modeling predictions to the contrary (Held and Soden, 2006; Huber and Goldner, 2012; Keery et al., 2018; Licht et al., 2014).

Despite this result, it is possible that the predicted intense monsoons may have occurred during transient periods of extreme Paleocene-Eocene warmth that are not recorded in our pedogenic carbonate data. It has been hypothesized that hyperthermals during this period are represented in the stratigraphy as distinctive sand bodies in the Tornillo Basin (Bataille et al., 2018, 2016). Indeed, the spacing and thickness of the Tornillo Basin sandstones may be consistent with the hypothesis that intense seasonal precipitation during hyperthermals caused an increase in erosion and flushing of sediment, as described in other Laramide basins (Foreman, 2014; Foreman et al., 2012). If true, it is possible that the intense, convective hydrological cycle predicted for the early Eocene occurred during hyperthermals, but due to the absence of nodules in the sandstone units, our paleosol carbonate record in the Tornillo Basin is stratigraphically biased against these events.

5.4.4 Comparison to previous clumped isotope records in North America from the Paleogene and modern air temperatures

Our clumped isotope data from the Tornillo Basin add to the existing sparse data available from terrestrial North America in the Paleogene and examining these data together can elucidate variability and temperature differences with latitude. Here, we compare our temperature results to temperature estimates produced from fourteen late Paleocene and Early Eocene carbonate nodules collected in the Bighorn Basin, WY (Snell et al., 2013), and fourteen Early Eocene carbonate nodules collected in the Green River Basin, WY (Hyland et al., 2018) (Figure 5-5).

Direct comparison of our results to the Δ_{47} values and temperature estimates from the Bighorn Basin reported by Snell et al. (2013) is complicated by recent developments in clumped isotope methods. The Δ_{47} data in Snell et al. (2013) were produced at Caltech between 2006 and 2011 when standard practice was to use the ^{17}O correction parameters of Santrock et al. (1985)

for calculations and present data in the 'Ghosh' or 'Caltech' reference frame. Our Δ_{47} values are calculated using updated ^{17}O correction parameters (Brand et al., 2010) following recent recommendations (Daeron et al., 2016; Schauer et al., 2016), and are normalized to the absolute reference frame (Dennis et al., 2011), which is now standard practice. Unfortunately, the data do not exist to recalculate the earlier Snell et al. (2013) Δ_{47} values to make them quantitatively comparable to the Δ_{47} values presented here. Comparing the temperatures calculated from the Δ_{47} values in the two studies is actually more appropriate, because each study used the Δ_{47} -temperature calibration based on empirical data generated in the same laboratory and calculated using the same methods as their sample data. However, analytical differences make it inappropriate to use the same Δ_{47} -temperature calibration for both datasets, so this temperature comparison likely introduces unquantified error on the order of a couple of degrees.

The average clumped isotope temperature from the fourteen Bighorn Basin carbonate nodules is 36 ±3°C (Snell et al., 2013). Snell et al. (2013) adjusted their clumped isotope soil temperature to account for radiative heating of the soil surface: they subtracted 5 °C from the measured carbonate temperature, yielding an estimate of 31 ±3°C for summer air temperature. We do not adjust our temperature estimates for radiative heating because tree fossils indicate that the Tornillo Basin was forested (Lehman and Busbey, 2007; Wheeler, 1991; Wheeler and Lehman, 2005), and so it is unlikely that the soils experienced enough heating from incident solar radiation to cause large differences in soil vs. air temperatures as has been observed for bare soils (Passey et al., 2010; Quade et al., 2013). The soils in the Bighorn Basin were likely not bare either (Wing et al., 2005, references within), but for comparison purposes we adopt the authors' judgment with respect to the solar heating effect on their record (the average Bighorn

Basin clumped isotope temperature without this adjustment is plotted for reference in Figure 5-5).

Direct comparison between the Tornillo and Green River Basin data is considerably simpler because the Green River Δ_{47} data were also produced at the University of Washington IsoLab, following the same procedures, and during the same time period, thus removing the concern of interlaboratory discrepancies or temperature calibration differences between these two data sets. The average clumped isotope values from the fourteen carbonate nodules from the Green River Basin yield summer temperature estimates of 24 ±3°C including the peak warming of the EECO, and 19 ±1°C excluding the peak-EECO samples (Hyland et al., 2018); these estimates are interpreted as summer temperatures by the authors (no correction for radiative heating). A single nodule from the latest Eocene in Sage Creek, MT provides a clumped isotope temperature estimate of 20 ±5°C (Methner et al., 2016) (Figure 5-5), which is similar to the temperature estimate from Green River; however, the Sage Creek estimate is more error-prone because it comes from a single nodule, and thus is not discussed further.

Despite their similarity in latitude, the Bighorn Basin Δ_{47} data and the Green River Basin Δ_{47} data yield very different temperatures (Figure 5-5). It is possible that the disparity in temperatures between these basins is due to differences in paleo-elevation. Although many studies suggest that both basins were likely at <1 km in elevation during the Eocene (Fan et al., 2011; Fricke, 2003; Morrill and Koch, 2002), some data suggest surface uplift in the Cordillera in the earliest Eocene (Feng and Poulsen, 2016; Mix et al., 2011). The disparity between the Bighorn and Green River data could also be due to differences in radiative heating due to local topography or aspect, distance from bodies of water that could provide cooling, unaccounted for

differences in the intra-annual timing of accumulation of the soil carbonates, or unquantifiable differences due to improvements in clumped isotope methods.

The disparate temperatures from the mid-latitude Bighorn and Green River Basins imply very different latitudinal gradients for Eocene North America when compared to our lower-latitude temperatures from the Tornillo Basin. The Eocene summer temperature estimate from the Tornillo Basin (32 ±3°C) is within error of the Bighorn Basin temperatures (31 ±3°C), which would imply a flat latitudinal temperature gradient (Figure 5-5). In contrast, the Tornillo Basin clumped isotope temperatures are hotter than the Green River Basin temperatures by 8 ±4°C (difference and 95% CI from a *t*-test); this difference approximates the temperature difference that exists in the modern between sites at those two latitudes (i.e., mean June-July-August (JJA) temperatures in San Antonio and modern Green River Basin are 10°C different) (Figure 5-5), which would imply a latitudinal temperature gradient similar to modern.

The difficulty of reconstructing Paleogene latitudinal temperature gradients from local temperature reconstructions is not surprising given that land temperatures and latitudinal temperature gradients are heterogeneous, which can be illustrated by considering modern reanalysis data (Kalnay et al., 1996). While the modern latitudinal temperature gradient at the longitude of San Antonio (97°W) conforms to the simple prediction of decreasing temperatures with increasing latitude, the gradient at the longitude of the Green River Basin (107°W) does not, due to the influence of topography (Figure 5-5). Furthermore, modern JJA temperatures near Big Bend, TX (from the west coast of North America to the west coast of the Gulf of Mexico at latitudes of 29–30°N) range widely, from 18–30 °C. Land cover likely contributes to significant variability in earth surface temperatures. These observations might explain why our estimated summer temperature for the forested Paleocene environment is slightly cooler than JJA

temperature for modern San Antonio shrubland environment (Figure 5-5), even though the Paleogene was globally warmer than modern. San Antonio might also be cooler because it is not the correct locality to compare to the Tornillo Basin: we use it here due to similar latitude and distance to the coast, but the variability in local temperatures suggest that there are other factors that control surface temperature. Given inherent variability in surface temperatures on land, a more complete understanding of summer temperatures in the Eocene in North America could emerge with refinement of paleo-topography, paleo-vegetation, and additional clumped isotope data from basins over a larger range in longitudes and latitudes.

5.4.5 Comparison to predictions from Eocene General Circulation Models

The temperature record from the Tornillo Basin provides an opportunity to test model predictions for temperatures on land at subtropical latitudes. While it is common to average several model grid cells centered on the preferred proxy location (e.g., Snell et al., 2013), at Tornillo Basin that method would involve including cells that are different in temperature due to differing distance from the coast. The range in temperatures predicted in grid cells surrounding Big Bend is larger than the range in temperatures predicted at a single cell by various simulations of a general circulation model from the UK Met Office (HadCM3L, Figure D-8). With this caveat in mind, we compare our $T\Delta_{47}$ estimate from the Tornillo Basin to predictions from available Eocene GCMs (most of which are described in Lunt et al, 2012) using JJA temperature from the grid cell that best approximates the paleo-location of the Tornillo Basin (Figure D-8).

Most of the Eocene GCMs presented here predict summer temperatures that are hotter than our estimate from clumped isotopes (Figure 5-6). Only three of thirteen simulations predict temperatures that are within error of our clumped isotope temperatures: HadCM3L-1 (Lunt et al.,

2010) for the x4 CO_2 forcing scenario, HadCM3L-2 (Loptson et al., 2014) for the x4 CO_2 forcing scenario with homogeneous shrubs, and CCSM-W (Winguth et al., 2010) for the x4 CO_2 forcing scenario (Figure 5-6). The HadCM3L simulations that predict temperatures higher than our maximum proxy estimate are run at higher pCO_2 forcings (x6 CO_2) (HadCM3L-1, Lunt et al., 2010), with dynamic vegetation (HadcM3L-2, Loptson et al., 2014), or with varied paleogeography (HadCM3L-3, Inglis et al., 2017; Valdes et al., 2017). The CCSM-H and CCSM-W simulations (Huber and Caballero, 2011; Winguth et al., 2010) overestimate our proxy-derived summer temperatures at Tornillo Basin by 2–4°C. The CCSM-K simulations (Kiehl and Shields, 2013) overestimate the Tornillo Basin temperatures by 2–6°C with lower CO_2 forcing; those simulations have modified aerosol parameters that change cloud condensation properties to reduce discrepancies with high latitude proxy data.

In summary, some simulations predict summer temperatures that are within error of our estimates (Figure 5-6), but most simulations predict summer temperatures that are higher than the low-latitude terrestrial temperatures estimated here. These temperature discrepancies of 2–7°C are similar in size to those reported between low-latitude sea surface temperature (SST) proxies and models (Evans et al., 2018). The simulations that predict warmer temperatures than our low-latitude terrestrial proxy estimates and the low-latitude SST estimates from Evans et al. (2018) are the same simulations that have been interpreted as generally agreeing with proxy data from high latitudes or with proxy-based marine latitudinal temperature gradients (see Huber and Caballero, 2011; Kiehl and Shields, 2013; Loptson et al., 2014). Thus, our data provide additional evidence that in order to match the proxy latitudinal temperature gradients and/or high latitude temperatures predicted by proxies, models tend to overheat lower latitude temperatures (Evans et al., 2018; Keating-Bitonti et al., 2011; Kozdon et al., 2011; Pearson et al., 2001; Spicer

et al., 2014; Tripati et al., 2003). Our results imply that the summer surface temperatures of >36°C predicted by models are unlikely for this coastal environment, and that temperatures lower than the thermal threshold for survival of organisms occurred at least locally during greenhouse climates. Our results suggest that coastal, subtropical climates remained relatively mild throughout background greenhouse climates, and thus proxy-model discrepancy persists at low latitudes.

5.5 Conclusions

We measure the $\delta^{13}C$, $\delta^{18}O$, and Δ_{47} composition of paleosol carbonate nodules from the Paleocene to the early Eocene from the Tornillo Basin in Big Bend National Park, Texas (USA). These analyses provide insight into a subtropical, near-coastal environment during a greenhouse climate regime. We find that most of our measured carbonate nodules record primary environmental signals, and two of our nodules have been reset by thermal heating from an adjacent laccolith. We estimate an average $T\Delta_{47}$ of 25 ±3°C through the Paleocene, and a statistically significant increase to 32 ± 2°C in the early Eocene. The increase in temperature recorded across this interval also corresponds to an increase in the calculated $\delta^{18}O$ of soil water from -2.8 ±0.74 to -0.81 ±0.35‰ (SMOW) that occurs at ~59 Ma. The shift in temperatures and water compositions is likely correlated with increasing atmospheric CO_2 (Anagnostou et al., 2016; Beerling and Royer, 2011).

Our data provide quantitative constraints on subtropical temperatures during the Paleocene and early Eocene that can inform our understanding of greenhouse climates. A comparison between the summer temperature estimate from the Tornillo Basin Δ_{47} data and similar data from the Bighorn Basin and the Green River Basin demonstrates the complexity and

heterogeneity of terrestrial temperature records. Reliable estimates of latitudinal temperature gradients on land likely await more data. While some Eocene GCM simulations agree within error of our estimate of summer temperature in the Tornillo Basin, most simulations overestimate summer temperature at this locality. The simulations that overestimate summer temperature are the simulations that have previously been interpreted as improvements to modeling Eocene climate because they show general agreement with other proxy estimates of latitudinal temperature gradients or temperatures from high latitudes. The tendency of these models to overestimate terrestrial subtropical paleo-temperatures from Tornillo Basin mimics their tendency to overestimate low latitude sea surface temperatures. Our results suggest that discrepancies remain between Eocene climate models and proxy data at low latitudes.

Acknowledgments, Samples, and Data

JRK was supported by the National Science Foundation Graduate Research Fellowship Program under Grant No. DGE-125082. Laboratory analyses were supported by US NSF grants EAR- 1156134 and EAR-1252064 to KWH. CPB was supported by the University of Ottawa faculty of Science start-up funds. Work by the University of Utah group was supported by ACS-PRF award number 52222-ND2 and US NSF grant EAR-1502786 to GJB. We gratefully acknowledge funding from the Quaternary Research Center and the Earth and Space Sciences Department at the University of Washington. Thanks to Andrew Schauer for endless support in IsoLab and to Landon Burgener for field assistance. Samples in Big Bend National Park were collected under NPS permit #s BIBE-2016-SCI-0024 and BIBE-2014-SCI-0015; thanks to Don Corrick for assistance in the permitting process. Thanks to Dan Peppe, an anonymous reviewer, and associate editor Stephen Barker for suggestions that improved this manuscript. Isotope data,

including individual replicate analyses, carbonate standards, and reference frame gases can be found in the supplemental tables.

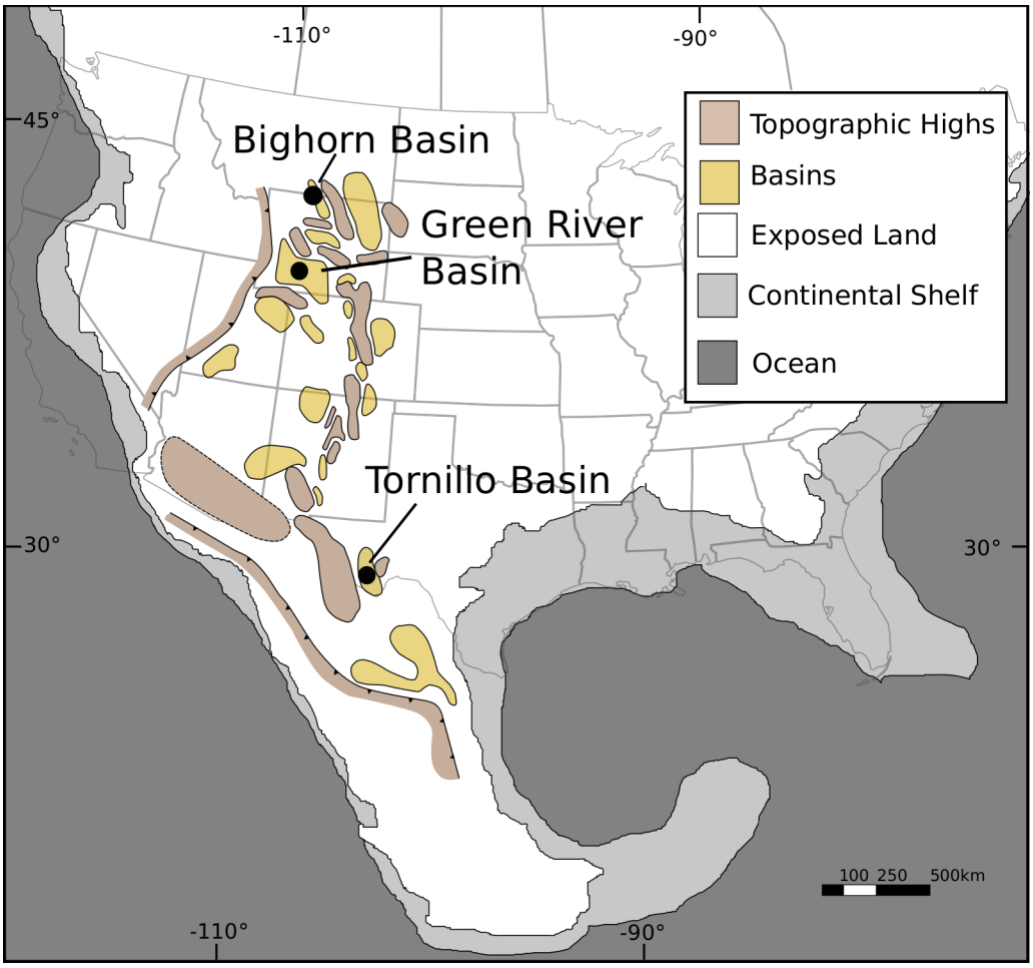

Figure 5-1: Location of the Tornillo Basin, Texas.

Laramide Basins and the proto-Gulf of Mexico modified from Galloway et al. (2011).

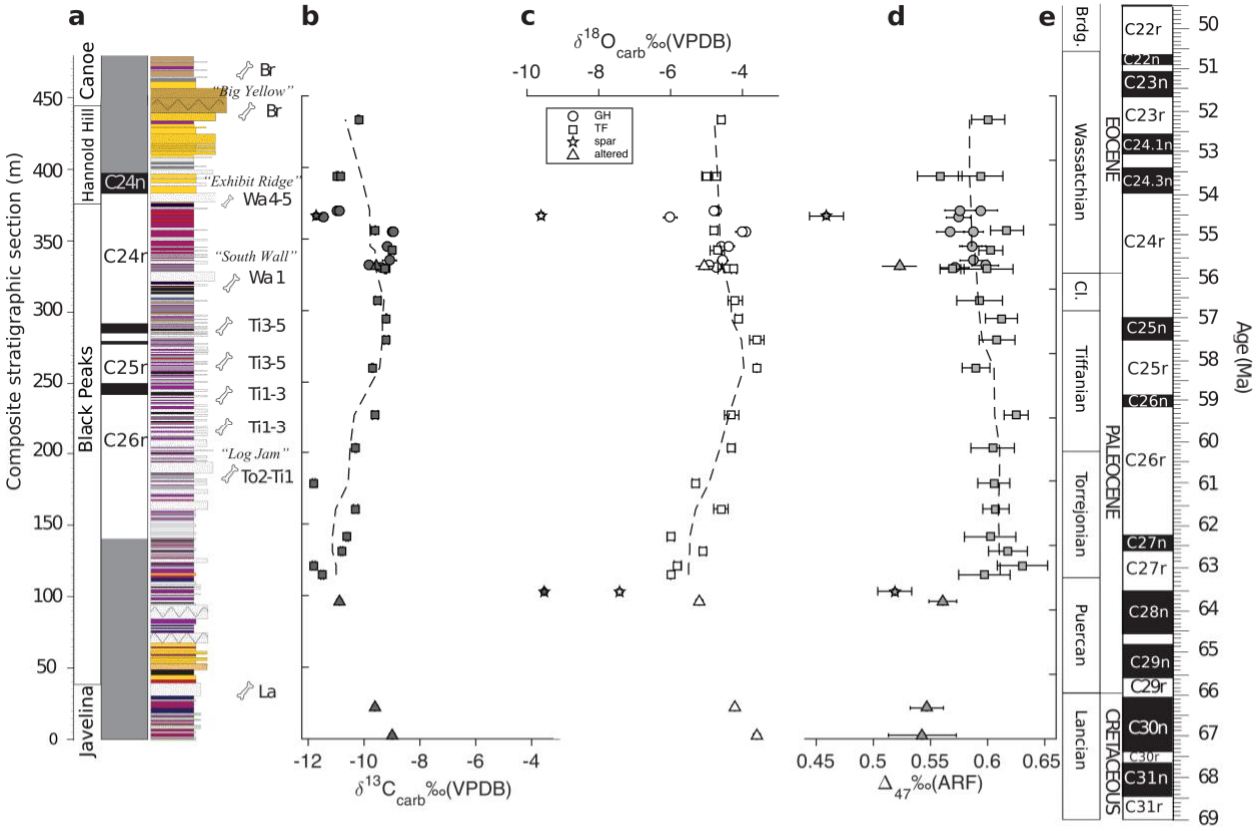

Figure 5-2: Stratigraphy and isotopic composition of carbonate nodules.

Stratigraphy of the Tornillo Group modified from Bataille et al., (2016, 2018). **a)** Composite stratigraphy from Tornillo Flats and Grapevine Hills. Magnetostratigraphic and biostratigraphic data are linked to the composite section (Rapp et al., 1983; Schiebout et al., 1987). The gray shading in the magnetostratigraphic data are unstudied intervals. **b), c),** and **d)** Symbols indicate sampling section (GH = Grapevine Hills, TF = Tornillo Flats), star and triangle symbols are either spar or diagenetically altered samples, as discussed in *Section 4.1*. Errors for $\delta^{13}C$ and $\delta^{18}O$ are S.D. and are generally smaller than the symbols. Errors for Δ_{47} are S.E. Dashed lines are a moving average of the isotopic data, excluding the spar and altered samples. **e)** Timescale with geologic epochs and ages, global magnetic polarity zones, and North American Land Mammal Ages.

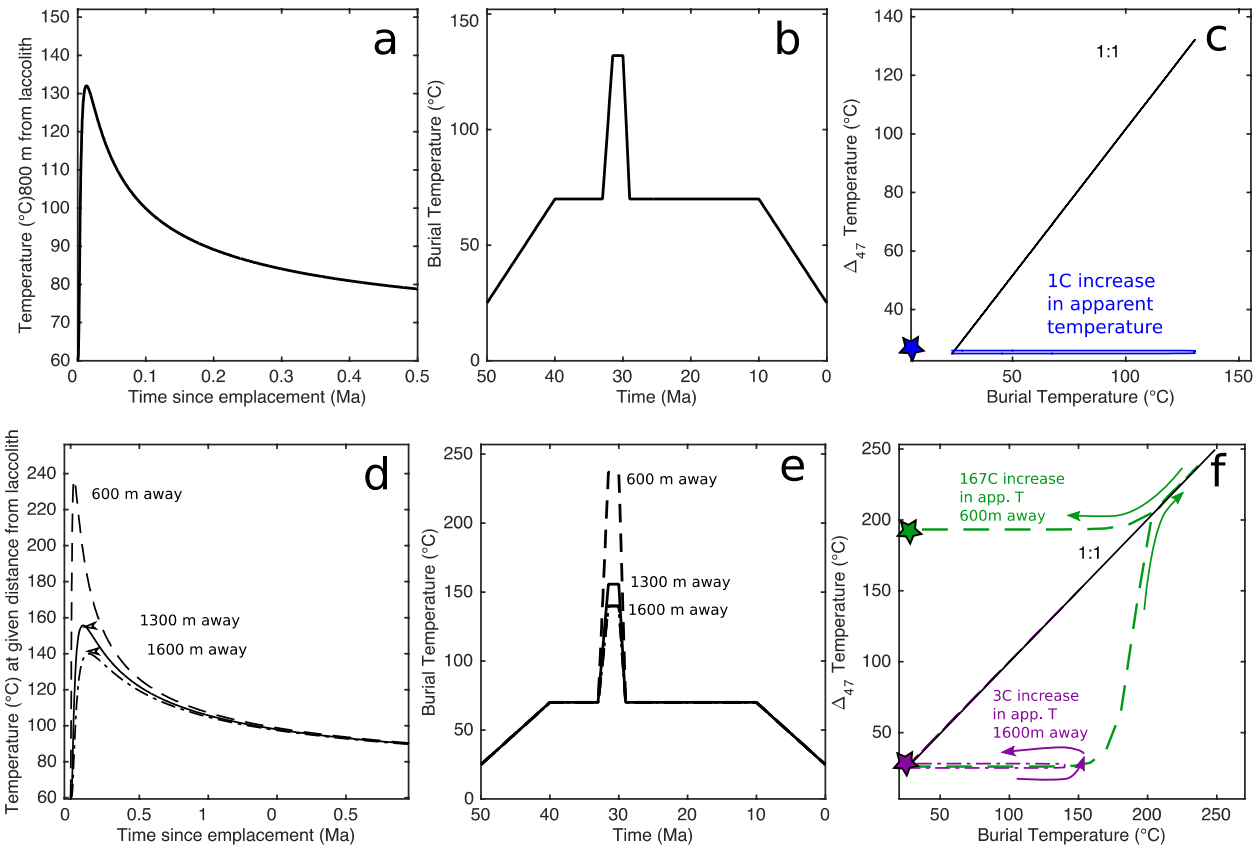

Figure 5-3: Modeled thermal history of the two sample locales in the Tornillo Basin

Grapevine Hills (**a-c**) and Tornillo Flats (**d-f**). **a)** For a laccolith that is 200 m thick, a 1D equation for heat diffusion predicts that a location 0.8 km away from the laccolith edge would reach ~130°C, then cool to temperatures less than 100°C by < 0.1 Ma. **b)** An approximate thermal history of the basin, where sediments start at 35°C on the surface, are buried to 70°C, are heated by a laccolith at 33 Ma to 113°C for 2 Ma, cool to 70°C, then are rapidly exhumed to the surface starting at 10 Ma. Apparent $T\Delta_{47}$ calculations are not sensitive to temperatures <100°C, so details of the thermal history below that temperature are not important. **c)** The solid-state reordering model of Henkes et al. (2014) predicts an increase of <1°C in the apparent $T\Delta_{47}$. The black line is a 1:1 line. The blue line is the temperature path for the carbonate. The blue star indicates the final apparent temperature. **d)** For a laccolith that is 450 m thick, we show predictions for temperatures experienced at 600, 1300, and 1600 m away from the laccolith. **e)** Thermal histories for the sediments at those distances from the laccolith, where sediments start at 25°C on the surface, are buried to 70°C, are heated by a laccolith at 33 Ma, cool to 70°C, then are exhumed to the surface starting at 10 Ma. **f)** Reordering calculations at distances of 600 and 1600 m in green and purple, respectively (1300 m omitted for clarity), the colored stars indicate the final apparent temperature.

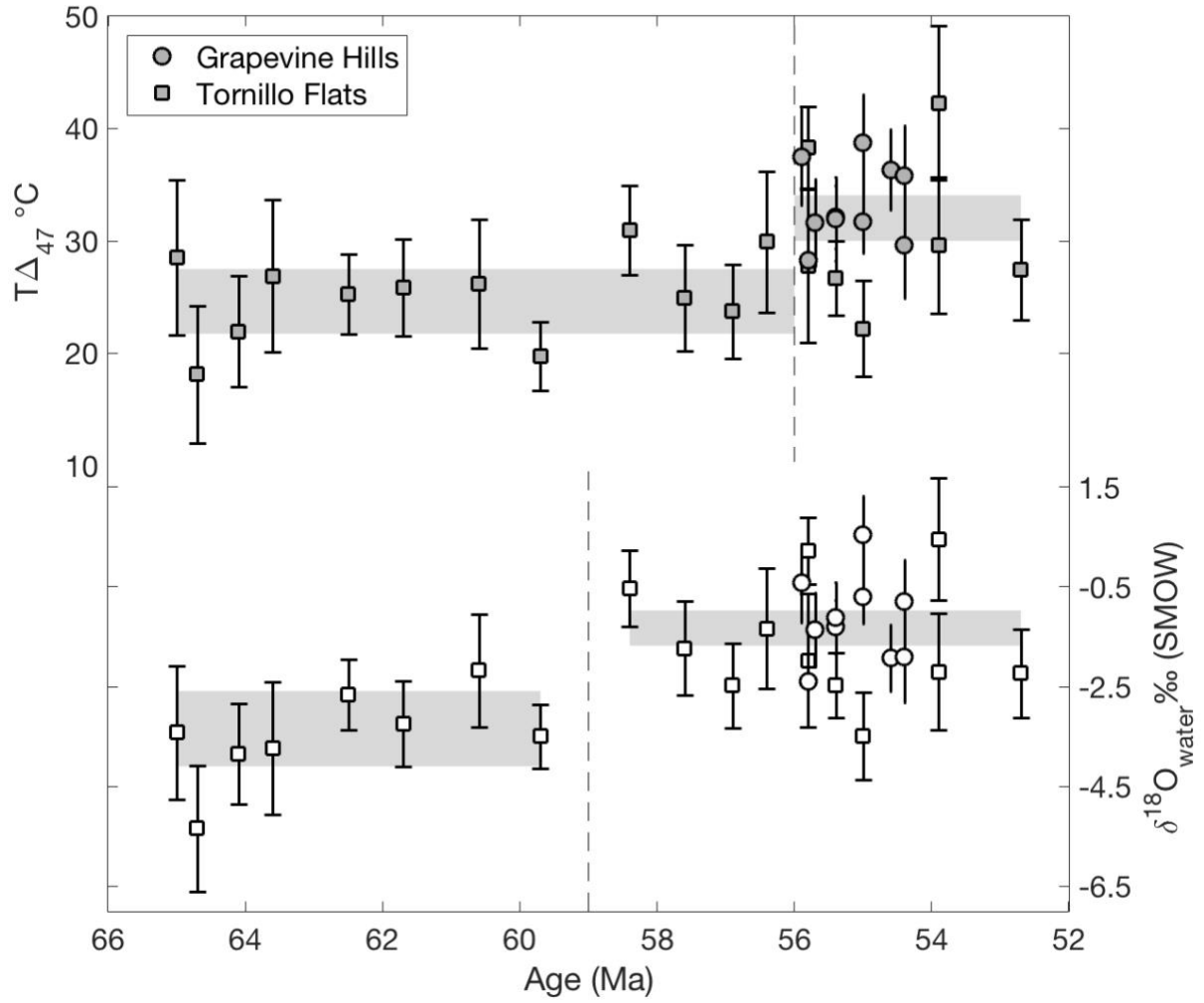

Figure 5-4: Calculated TΔ_{47} and $\delta^{18}O_w$ values for carbonate nodules.

Only carbonate nodules that record primary environmental values are shown. Error bars on individual nodules in black are 1 S.E. (the error normally reported for clumped isotope data). The vertical dashed line marks the point in time that minimizes RMS misfit when modeling the data as two periods of time with a constant mean (56 Ma for TΔ47 and 59 Ma for δ18Ow). The gray rectangles are the 95% CI centered on the error-weighted mean of the carbonate nodules for the given time period.

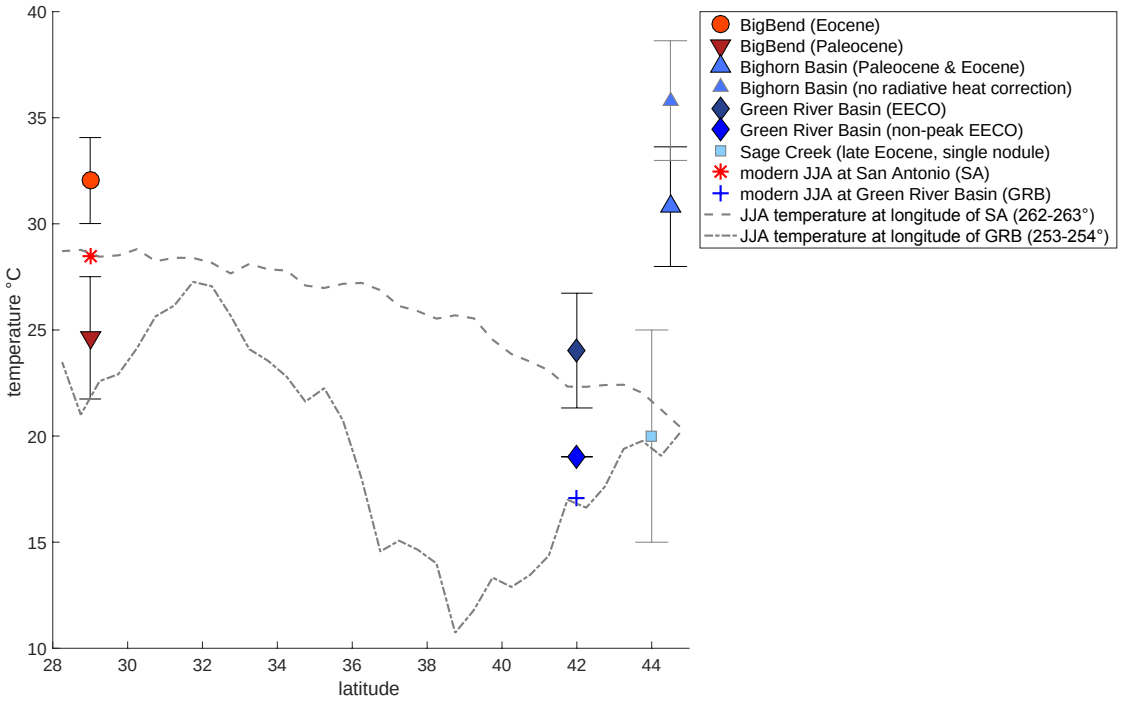

Figure 5-5: Latitudinal patterns in Δ_{47} temperatures and modern JJA temperatures

Clumped isotope temperatures (filled symbols) and modern JJA average temperatures from NCEP/NCAR Reanalysis data (Kalnay et al., 1996) (star/cross symbols and dashed lines) versus latitude for relevant locations in North America. The error bars shown for the clumped isotope data are the 95% CI of the mean of several nodules. The Green River Basin data is from the EECO (Hyland et al., 2018), and the Bighorn Basin data is from the late Paleocene and early Eocene (Snell et al., 2013), shown with and without the 5°C correction for radiative heating. The late Eocene Sage Creek single nodule is from Methner et al. (2016).

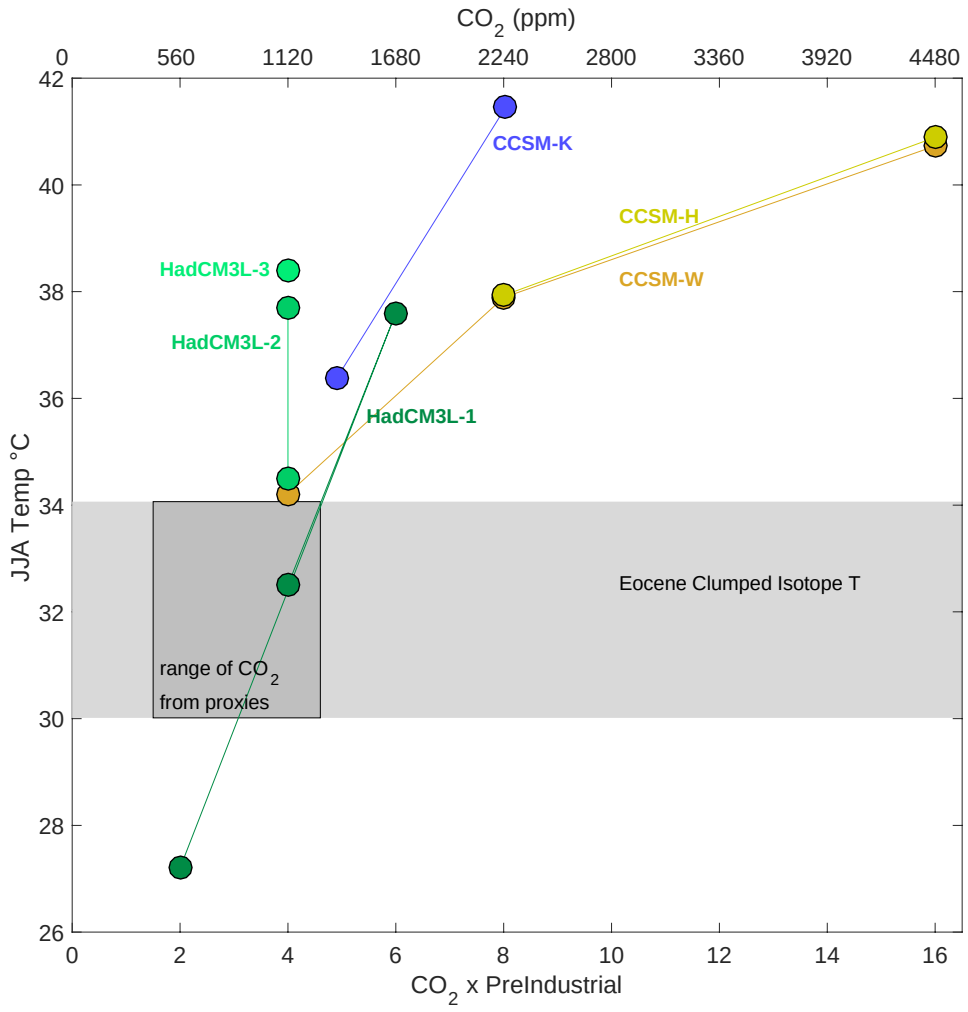

Figure 5-6: GCM predicted temperatures and Δ_{47} temperatures from the Tornillo Basin

JJA average temperature at the Tornillo Basin predicted by Eocene general circulation model simulations with atmospheric CO_2 concentrations of 1 to 16x preindustrial CO_2. The horizontal dashed line is the Eocene clumped isotope temperature estimate from Big Bend, with the 95% CI in light gray shading. The dark gray rectangle is atmospheric CO_2 concentrations from Anagnostou et al. (2016). Model citations are as follows: CCSM-H - Huber and Caballero (2011); CCSM-K - Kiehl and Shields (2013); CCSM-W - Winguth et al. (2010); HadCM3L-1 - Lunt et al. (2010); HadCM3L-2 - Loptson et al. (2014); and HadCM3L-3 - Lunt et al. (2016), Inglis et al. (2017), and Valdes et al. (2017).

Table 5-1: Stable isotope values for soil carbonate samples from the Tornillo Basin

Sample_ID	Age (Ma)	Epoch	Section	Type	$\delta^{13}C$ carb	$\delta^{13}C$ SD	$\delta^{13}C$ SE	$\delta^{18}O$ carb	$\delta^{18}O$ SD	$\delta^{18}O$ SE	$\Delta47$ [a]	$\Delta47$ SD	$\Delta47$ SE	n	T($\Delta47$) [b]	T($\Delta47$) SE	T($\Delta47$) 95 % CI	$\delta^{18}O$ water	$\delta^{18}O$ w error
BB-TF2-14-002	68.9	Cret.	TF	Micrite	-9.0	0.04	0.04	-3.6	0.1	0.1	0.5429	0.042	0.030	2	48	11	47	3.1	-2.6
BB12-077	68.0	Cret	TF	Micrite	-9.6	0.04	0.02	-4.2	0.0	0.0	0.5468	0.029	0.015	4	47	5	15	2.3	-1.1
BB-TF2-14-030	66.0	Cret	TF	Radial	-10.9	0.04	0.03	-5.2	0.1	0.1	0.5608	0.021	0.012	3	41	4	14	0.3	-1.0
BB-TF2-14-036	65.7	Paleo.	TF	Spar	-3.6	0.04	0.04	-7.4	0.0	0.0	0.5187	0.021	0.015	2	58	6	27	1.0	-1.4
BB12-098	65.0	Paleo.	TF	Micrite	-11.5	0.05	0.03	-6.0	0.0	0.0	0.5972	0.045	0.023	4	29	7	19	-2.9	-1.5
BB12-102	64.7	Paleo.	TF	Micrite	-11.8	0.05	0.03	-5.8	0.1	0.1	0.6305	0.044	0.022	4	18	6	17	-4.8	-1.5
BB-TF2-14-064	64.1	Paleo.	TF	Micrite	-10.8	0.04	0.02	-5.1	0.1	0.1	0.6178	0.034	0.017	4	22	5	14	-3.3	-1.2
BB12-047	63.6	Paleo.	TF	Micrite	-10.6	0.04	0.02	-6.0	0.1	0.1	0.6022	0.045	0.023	4	27	7	19	-3.2	-1.5
BB12-056	62.5	Paleo.	TF	Micrite	-10.3	0.08	0.05	-4.6	0.2	0.1	0.6073	0.023	0.012	4	25	4	10	-2.2	-0.8
BB12-062	61.7	Paleo.	TF	Micrite	-11.8	0.05	0.03	-5.3	0.1	0.1	0.6054	0.028	0.014	4	26	4	12	-2.7	-1.0
BB12-071	60.6	Paleo.	TF	Micrite	-10.3	0.03	0.02	-4.3	0.1	0.1	0.6044	0.038	0.019	4	26	6	16	-1.7	-1.3
BB12-041	59.7	Paleo.	TF	Micrite	-9.6	0.10	0.06	-4.3	0.2	0.1	0.6250	0.021	0.011	4	20	3	9	-3.0	-0.7
BB12-013	58.4	Paleo.	TF	Micrite	-9.7	0.03	0.02	-3.6	0.0	0.0	0.5899	0.021	0.012	3	31	4	13	0.0	-0.9
BB10-001	57.6	Paleo.	TF	Micrite	-9.2	0.08	0.04	-3.6	0.2	0.1	0.6083	0.035	0.016	5	25	5	12	-1.2	-1.0
BB10-011	56.9	Paleo.	TF	Micrite	-9.2	0.02	0.01	-4.1	0.1	0.1	0.6121	0.028	0.014	4	24	4	12	-2.0	-1.0
BB10-019	56.4	Paleo.	TF	Micrite	-9.5	0.10	0.06	-4.2	0.2	0.1	0.5930	0.040	0.020	4	30	6	17	-0.8	-1.4
BB-TF1-14-004B	55.8	Eo.	TF	Micrite	-9.2	0.03	0.01	-4.4	0.3	0.1	0.5994	0.056	0.023	6	28	7	17	-1.5	-1.5
BB-TF1-14-004Bnod2	55.8	Eo.	TF	Micrite	-9.3	0.02	0.01	-4.2	0.1	0.0	0.5689	0.021	0.011	4	38	4	10	0.7	-0.8
BB10-032	55.4	Eo.	TF	Micrite	-9.0	0.08	0.05	-4.7	0.2	0.1	0.6028	0.021	0.011	4	27	3	9	-2.0	-0.7
BB10-035	55.0	Eo.	TF	Micrite	-9.6	0.01	0.01	-4.8	0.1	0.1	0.6170	0.025	0.014	3	22	4	14	-3.0	-1.1
BB-TF3-14-003	54.7	Eo.	TF	Spar	-11.7	0.03	0.03	-9.6	0.1	0.1	0.4590	0.021	0.015	2	88	8	34	3.3	-1.5
BB-TF3-14-012	53.9	Eo.	TF	Micrite	-11.0	0.03	0.02	-5.0	0.1	0.1	0.5939	0.039	0.020	4	30	6	17	-1.7	-1.4
BB-TF3-14-012nod2	53.9	Eo.	TF	Micrite	-10.9	0.07	0.04	-4.7	0.1	0.1	0.5581	0.039	0.020	4	42	7	19	1.0	-1.4

BB-TF3-14-027	52.7	Eo.	TF	Micrite	-10.2	0.03	0.02	-4.6	0.1	0.1	0.6005	0.029	0.015	4	27	5	13	-1.7	-1.0
PS2-Bk	55.9	Eo.	GH	Micrite	-9.4	0.18	0.09	-4.7	0.1	0.1	0.5712	0.028	0.013	5	37	4	11	0.1	-0.9
PS3-Bk	55.85	Eo.	GH	unknown	-9.6	0.02	0.02	-5.1	0.2	0.2	0.5228	0.021	0.015	2	56	6	26	3.1	-1.4
PS4-Bk	55.8	Eo.	GH	Micrite	-9.8	0.12	0.05	-4.9	0.1	0.0	0.5979	0.033	0.012	8	28	4	8	-1.9	-0.8
PS5-Bk	55.7	Eo.	GH	Micrite	-9.1	0.25	0.10	-4.6	0.2	0.1	0.5880	0.032	0.012	7	32	4	9	-0.9	-0.8
PS7-Bk1	55.4	Eo.	GH	Micrite	-9.2	0.13	0.06	-4.6	0.2	0.1	0.5864	0.021	0.009	6	32	3	7	-0.8	-0.6
PS7-Bk2	55.4	Eo.	GH	Micrite	-9.2	0.16	0.07	-4.4	0.2	0.1	0.5870	0.028	0.011	6	32	4	9	-0.6	-0.8
PS12-Bk	55	Eo.	GH	Micrite	-9.0	0.10	0.04	-3.9	0.1	0.0	0.5877	0.021	0.009	6	32	3	7	-0.2	-0.6
PS12-Bknod2	55	Eo.	GH	Micrite	-8.9	0.01	0.01	-4.0	0.2	0.1	0.5676	0.021	0.012	3	39	4	14	1.0	-1.0
PS22-Bk	54.6	Eo.	GH	Micrite	-11.4	0.05	0.03	-6.0	0.2	0.1	0.5744	0.021	0.011	4	36	4	10	-1.4	-0.8
GH14-002	54.4	Eo.	GH	Micrite	-11.0	0.00	0.00	-4.7	0.0	0.0	0.5938	0.021	0.015	2	30	5	21	-1.4	-1.3
GH14-002nod2	54.4	Eo.	GH	Micrite	-10.9	0.02	0.01	-4.8	0.1	0.1	0.5759	0.023	0.013	3	36	5	14	-0.3	-1.0

[a] in the Absolute Reference Frame of Dennis et al., 2011, except with no acid fractionation factor added for acid digestion at 90 °C, and that the values have been calculated using the 17O parameters of Brand et al. (2010).

[b] temperature calculated from Δ47 with the calibration equation from Kelson et al. (2017): $\Delta_{47} = (0.0417 \times 10^6)/T^2 + 0.139$, where T is in Kelvin

Chapter 6 Conclusions: State of the proxy and applications to terrestrial paleoclimate

The research set forth in this dissertation, as well as other contemporaneous work, has significantly advanced our ability to reconstruct terrestrial climates using the carbonate clumped isotope thermometer. Foremost, a typical long-term reproducibility of Δ_{47} of 0.02‰ (from carbonate standards) allows for measurements of temperature with one standard error (S.E.) of ± 1–4 °C for samples grown near Earth-surface temperatures (0-50 °C) (the exact S.E. depends on number of replicate analyses and where the sample falls relative to the temperature range for calibration samples). This estimate of S.E. includes calibration error, although currently instrument precision and sample heterogeneity dominate the error (Petersen et al., 2019). One persistent challenge is that not all inter-laboratory discrepancies have been resolved, however, the discrepancies in sensitivity are significantly reduced in comparison to the early 2010s and may be eliminated as carbonate standards are adopted (Bernasconi et al., 2018). Regardless, especially when using an in-house Δ_{47} calibration, the resulting precision and accuracy is sufficient to address many paleoclimate questions (Chapter 2). For example, clumped isotope geochemistry should allow for the resolution of temperature changes relating to short-lived events like the PETM or the Eocene-Oligocene transition, as well as more gradual climate shifts like the Early Eocene Climatic Optimum and the mid-Miocene Climatic Optimum.

Pedogenic carbonates should continue to be widely used for paleoclimate. Recent research has led to the identification of the environmental factors that are most important in controlling the seasonal bias of formation. By developing and promoting a process-based understanding of carbonate precipitation, we can explain and predict the annual timing of soil

carbonate formation (Chapters 3 and 4). Understanding this seasonal bias facilitates direct comparisons between temperatures estimated from different regions, different proxies, and climate models. Furthermore, we may soon be able to leverage the seasonal biases in the isotopic composition of pedogenic carbonates to investigate new aspects of paleoclimate: Δ_{47} of pedogenic carbonates directly tells us temperature, but soon we may be able to use it in a multi-proxy framework to learn about seasonality and intensity of precipitation in geologic time.

Undoubtedly, there are still complications that cloud our vision into the crystal ball of Cenozoic climate. For example, we lack a reliable method of positively identifying primary preservation in pedogenic carbonates. We rely on a convoluted combination of textural descriptions, isotopic evidence, and thermal modeling to try to rule out the possibility of secondary alteration. Also, the spatial resolution and paleo-geographic boundary conditions used in most global climate models impede direct comparisons to proxy records. More spatially diverse proxy measurements of climate might help improve our ability to compare proxy and model estimates of temperature. If the regional differences in clumped isotope temperatures from the early Paleogene in North America (Chapter 5) describe real climate differences (are not an analytical artifact), identifying and describing those patterns could illuminate climate dynamics relating to continental interiors (or tectonics). This heterogeneity in regional climate would not be possible to observe through oceanic records. One strategy to bolster our understanding of temperature evolution of the Cenozoic may be to target complete stratigraphic sequences (rather than the dramatic changes in climate that have been the obvious primary targets). In conclusion, the clumped isotope geochemistry of soil carbonates can and has been used to reconstruct climate conditions on land in geologic deep time. The application of this proxy will allow us to understand and address novel challenges while providing insights into Cenozoic climate.

Bibliography

Abrahams, A.D., Parsons, A.J., Wainwright, J., 1995. Effects of vegetation change on interrill runoff and erosion, Walnut Gulch, southern Arizona. Geomorphology 13, 37–48. https://doi.org/10.1016/0169-555X(95)00027-3

Affek, H.P., 2013. Clumped isotopic equilibrium and the rate of isotope exchange between CO2 and water. Am. J. Sci. 313, 309–325. https://doi.org/10.2475/04.2013.02

Affek, H.P., 2012. Clumped Isotope Paleothermometry: Principles, Applications, and Challenges. Paleontol. Soc. Pap. 18, 101–114.

Affek, H.P., Eiler, J.M., 2006. Abundance of mass 47 CO2 in urban air, car exhaust, and human breath. Geochim. Cosmochim. Acta 70, 1–12. https://doi.org/10.1016/j.gca.2005.08.021

Affek, H.P., Matthews, A., Ayalon, A., Bar-Matthews, M., Burstyn, Y., Zaarur, S., Zilberman, T., 2014. Accounting for kinetic isotope effects in Soreq Cave (Israel) speleothems. Geochim. Cosmochim. Acta 143, 303–318. https://doi.org/10.1016/j.gca.2014.08.008

Affek, H.P., Zaarur, S., 2014. Kinetic isotope effect in CO2 degassing: Insight from clumped and oxygen isotopes in laboratory precipitation experiments. Geochim. Cosmochim. Acta 143, 319–330. https://doi.org/10.1016/j.gca.2014.08.005

Amundson, R.G., Lund, L.J., 1987. The Stable Isotope Chemistry of a Native and Irrigated Typic Natrargid in the San Joaquin Valley of California1. Soil Sci. Soc. Am. J. 51, 761–767. https://doi.org/10.2136/sssaj1987.03615995005100030034x

Anagnostou, E., John, E.H., Edgar, K.M., Foster, G.L., Ridgwell, A.J., Inglis, G.N., Pancost, R.D., Lunt, D.J., Pearson, P.N., 2016. Changing atmospheric CO2 concentration was the primary driver of early Cenozoic climate. Nature 533, 1–19. https://doi.org/10.1038/nature17423

Anhäuser, T., Hook, B.A., Halfar, J., Greule, M., Keppler, F., 2018. Earliest Eocene cold period and polar amplification - Insights from δ2H values of lignin methoxyl groups of mummified wood. Palaeogeogr. Palaeoclimatol. Palaeoecol. 505, 326–336. https://doi.org/10.1016/J.PALAEO.2018.05.049

Arkley, R.J., 1963. Calculation of carbonate and water movement in soil from climatic data. Soil Sci. 96, 239–248.

Atchley, S.C., Nordt, L.C., Dworkin, S.I., 2004. Eustatic Control on Alluvial Sequence Stratigraphy: A Possible Example from the Cretaceous-Tertiary Transition of the Tornillo Basin, Big Bend National Park, West Texas, U.S.A. J. Sediment. Res. 74, 391–404. https://doi.org/10.1306/102203740391

Aze, T., Pearson, P.N., Dickson, A.J., Badger, M.P.S., Bown, P.R., Pancost, R.D., Gibbs, S.J., Huber, B.T., Leng, M.J., Coe, A.L., Cohen, A.S., Foster, G.L., 2014. Extreme warming of tropical waters during the Paleocene-Eocene Thermal Maximum. Geology 42, 739–742. https://doi.org/10.1130/G35637.1

Bailey, I.W., Sinnott, E.W., 1915. A Botanical Index of Cretaceous and Tertiary Climates. Science (80-.). 41, 831–834. https://doi.org/0022-2836(91)90704-A [pii]

Bartlett, M.G., Chapman, D.S., Harris, R.N., 2006. A decade of ground-air temperature tracking at emigrant pass observatory, Utah. J. Clim. 19, 3722–3731. https://doi.org/10.1175/JCLI3808.1

Bataille, C.P., Ridgeway, K.D., Colliver, L., Liu, X.-M., 2018. An early Paleogene fluvial regime shift in response to global warming: a subtropical record from the Tornillo basin, West Texas, U.S.A. Geol. Soc. Am. Bull. https://doi.org/https://doi.org/10.1130/B31872.1.

Bataille, C.P., Watford, D., Ruegg, S., Lowe, A., Bowen, G.J., 2016. Chemostratigraphic age model for the Tornillo Group: A possible link between fluvial stratigraphy and climate. Palaeogeogr. Palaeoclimatol. Palaeoecol. 457, 277–289. https://doi.org/10.1016/j.palaeo.2016.06.023

Beerling, D.J., Royer, D.L., 2011. Convergent Cenozoic CO2 history. Nat. Geosci. 4, 418–420. https://doi.org/10.1038/ngeo1186

Behrensmeyer, A.K., Quade, J., Cerling, T.E., Kappelman, J., Khan, I.A., Copeland, P., Roe, L., Hicks, J., Stubblefield, P., Willis, B.J., Latorre, C., 2007. The structure and rate of late Miocene expansion of C4 plants: Evidence from lateral variation in stable isotopes in paleosols of the Siwalik Group, northern Pakistan. Bull. Geol. Soc. Am. 119, 1486–1505. https://doi.org/10.1130/B26064.1

Bernard, S., Daval, D., Ackerer, P., Pont, S., Meibom, A., 2017. Burial-induced oxygen-isotope re-equilibration of fossil foraminifera explains ocean paleotemperature paradoxes. Nat. Commun. 8, 1–10. https://doi.org/10.1038/s41467-017-01225-9

Bernasconi, S.M., Hu, B., Wacker, U., Fiebig, J., Breitenbach, S.F.M., Rutz, T., 2013. Background effects on Faraday collectors in gas-source mass spectrometry and implications for clumped isotope measurements. Rapid Commun. Mass Spectrom. 27, 603–12. https://doi.org/10.1002/rcm.6490

Bernasconi, S.M., Müller, I.A., Bergmann, K.D., Breitenbach, S.F.M., Fernandez, A., Hodell, D.A., Jaggi, M., Meckler, A.N., Millan, I.M., Ziegler, M., 2018. Reducing uncertainties in carbonate clumped isotope analysis through consistent carbonate-based standardization. Geochemistry, Geophys. Geosystems 1–20. https://doi.org/10.1029/2017GC007385

Bijl, P.K., Schouten, S., Sluijs, A., Reichart, G.-J., Zachos, J.C., Brinkhuis, H., 2009. Early palaeogene temperature evolution of the southwest Pacific Ocean. Nature 461, 776–779. https://doi.org/10.1038/nature08399

Birkeland, 1984. Soils and Geomorphology. Oxford University Press.

Blodgett, R.H., 1988. Calcareous paleosols in the Triassic Dolores Formation, southwestern Colorado. Geol. Soc. Am. Spec. Pap. 216.

Blodgett, R.H., 1985. Paleovertisols as indicators of climate. Am. Assoc. Pet. Geol. Bull. 69, 239.

Bond-Lamberty, B., Thomson, A., 2010. Temperature-associated increases in the global soil respiration record. Nature 464, 579–582. https://doi.org/10.1038/nature08930

Bonifacie, M., Calmels, D., Eiler, J.M., Horita, J., Chaduteau, C., Vasconcelos, C., Agrinier, P., Katz, A., Passey, B.H., Ferry, J.M., Bourrand, J.-J., 2017. Calibration of the dolomite clumped isotope thermometer from 25 to 350 °C, and implications for a universal calibration for all (Ca, Mg, Fe)CO3 carbonates. Geochim. Cosmochim. Acta 200, 255–279. https://doi.org/10.1016/J.GCA.2016.11.028

Borken, W., Davidson, E.A., Savage, K., Gaudinski, J., Trumbore, S.E., 2003. Drying and Wetting Effects on Carbon Dioxide Release from Organic Horizons. Soil Sci. Soc. Am. J. 67, 1888–1896. https://doi.org/10.2136/sssaj2003.1888

Bouma, T.J., Bryla, D.R., 2000. On the assessment of root and soil respiration for soils of different textures: Interactions with soil moisture contents and soil CO2 concentrations. Plant Soil 227, 215–221. https://doi.org/10.1023/A:1026502414977

Bowen, G.J., Beerling, D.J., 2004. An integrated model for soil organic carbon and CO 2 : Implications for paleosol carbonate p CO 2 paleobarometry . Global Biogeochem. Cycles 18, n/a-n/a. https://doi.org/10.1029/2003gb002117

Bowen, G.J., Revenaugh, J., 2003. Interpolating the isotopic composition of modern meteoric precipitation. Water Resour. Res. 39. https://doi.org/10.1029/2003WR002086
Bowling, D.R., Grote, E.E., Belnap, J., 2011. Rain pulse response of soil CO2 exchange by biological soil crusts and grasslands of the semiarid Colorado Plateau, United States. J. Geophys. Res. Biogeosciences 116, 1–17. https://doi.org/10.1029/2011JG001643
Braconnot, P., Harrison, S.P., Kageyama, M., Bartlein, P.J., Masson-Delmotte, V., Abe-Ouchi, A., Otto-Bliesner, B.L., Zhao, Y., 2012. Evaluation of climate models using palaeoclimatic data. Nat. Clim. Chang. 2, 417–424. https://doi.org/10.1038/nclimate1456
Brand, W., Assonov, S.S., Coplen, T.B., 2010. Correction for the 17O interference in δ(13C) measurements when analyzing CO2 with stable isotope mass spectrometry (IUPAC Technical Report). Pure Appl. Chem. 82, 1719–1733. https://doi.org/10.1351/PAC-REP-09-01-05
Breecker, D.O., McFadden, L.D., Sharp, Z.D., Martinez, M., Litvak, M.E., 2012. Deep Autotrophic Soil Respiration in Shrubland and Woodland Ecosystems in Central New Mexico. Ecosystems 15, 83–96. https://doi.org/10.1007/s10021-011-9495-x
Breecker, D.O., Sharp, Z.D., McFadden, L.D., 2010. Atmospheric CO2 concentrations during ancient greenhouse climates were similar to those predicted for A.D. 2100. Proc. Natl. Acad. Sci. U. S. A. 107, 576–580. https://doi.org/10.1073/pnas.0902323106
Breecker, D.O., Sharp, Z.D., McFadden, L.D., 2009. Seasonal bias in the formation and stable isotopic composition of pedogenic carbonate in modern soils from central New Mexico, USA. Bull. Geol. Soc. Am. 121, 630–640. https://doi.org/10.1130/B26413.1
Breshears, D.D., Nyhan, J.W., Heil, C.E., Wilcox, B.P., 1998. Effects of Woody Plants on Microclimate in a Semiarid Woodland: Soil Temperature and Evaporation in Canopy and Intercanopy Patches. Int. J. Plant Sci. 159, 1010–1017. https://doi.org/10.1086/314083
Brinkhuis, H., Schouten, S., Collinson, M.E., Sluijs, A., Damsté, J.S.S., Dickens, G.R., Huber, M., Cronin, T.M., Onodera, J., Takahashi, K., Bujak, J.P., Stein, R., van der Burgh, J., Eldrett, J.S., Harding, I.C., Lotter, A.F., Sangiorgi, F., Cittert, H. van K., de Leeuw, J.W., Matthiessen, J., Backman, J., Moran, K., Scientists, the E. 302, 2006. Episodic fresh surface waters in the Eocene Arctic Ocean. Nature 441, 606.
Burgener, L.K., Huntington, K.W., Hoke, G.D., Schauer, A.J., Ringham, M.C., Latorre, C., Díaz, F.P., 2016. Variations in soil carbonate formation and seasonal bias over >4 km of relief in the western Andes (30°S) revealed by clumped isotope thermometry. Earth Planet. Sci. Lett. 441, 188–199. https://doi.org/10.1016/j.epsl.2016.02.033
Burgener, L.K., Huntington, K.W., Sletten, R., Watkins, J.M., Quade, J., Hallet, B., 2018. Clumped isotope constraints on equilibrium carbonate formation and kinetic isotope effects in freezing soils. Geochim. Cosmochim. Acta 235, 402–430. https://doi.org/10.1016/J.GCA.2018.06.006
Burgener, L.K., Hyland, E.G., Huntington, K.W., Kelson, J.R., Sewall, J.O., 2019. Revisiting the equable climate problem during the Late Cretaceous greenhouse using paleosol carbonate clumped isotope temperatures from the Campanian of the Western Interior Basin, USA. Palaeogeogr. Palaeoclimatol. Palaeoecol. 516, 244–267. https://doi.org/10.1016/J.PALAEO.2018.12.004
Came, R.E., Brand, U., Affek, H.P., 2014. Clumped isotope signatures in modern brachiopod carbonate. Chem. Geol. 377, 20–30. https://doi.org/10.1016/j.chemgeo.2014.04.004
Came, R.E., Eiler, J.M., Veizer, J., Azmy, K., Brand, U., Weidman, C.R., 2007. Coupling of surface temperatures and atmospheric CO2 concentrations during the Palaeozoic era. Nature

449, 198.
Carmichael, M.J., Inglis, G.N., Badger, M.P.S., Naafs, B.D.A., Behrooz, L., Remmelzwaal, S., Monteiro, F.M., Rohrssen, M., Farnsworth, A., Buss, H.L., Dickson, A.J., Valdes, P.J., Lunt, D.J., Pancost, R.D., 2017. Hydrological and associated biogeochemical consequences of rapid global warming during the Paleocene-Eocene Thermal Maximum. Glob. Planet. Change 157, 114–138. https://doi.org/10.1016/j.gloplacha.2017.07.014
Carmichael, M.J., Lunt, D.J., Huber, M., Heinemann, M., Kiehl, J., LeGrande, A.N., Loptson, C.A., Roberts, C.D., Sagoo, N., Shields, C., Valdes, P.J., Winguth, A.M.E., Winguth, C., Pancost, R.D., 2016. A model-model and data-model comparison for the early Eocene hydrological cycle. Clim. Past 12, 455–481. https://doi.org/10.5194/cp-12-455-2016
Carmichael, M.J., Lunt, D.J., Pancost, R.D., 2015. Insights into the early Eocene hydrological cycle from an ensemble of atmosphere-ocean GCM simulations 17, 8839. https://doi.org/10.5194/cpd-11-3277-2015
Carmichael, M.J., Pancost, R.D., Lunt, D.J., 2018. Changes in the occurrence of extreme precipitation events at the Paleocene–Eocene thermal maximum. Earth Planet. Sci. Lett. 501, 24–36. https://doi.org/10.1016/J.EPSL.2018.08.005
Carsel, R.F., Parrish, R.S., 1988. Developing joint probability distributions of soil water retention characteristics. Water Resour. Res. Resour. Res. 24, 755–769.
Caves, J.K., Moragne, D.Y., Ibarra, D.E., Bayshashov, B.U., Gao, Y., Jones, M.M., Zhamangara, A., Arzhannikova, A. V., Arzhannikov, S.G., Chamberlain, C.P., 2016. The Neogene de-greening of Central Asia. Geology 44, 887–890. https://doi.org/10.1130/G38267.1
Cerling, T.E., 1999. Stable carbon isotopes in palaeosol carbonates. Specoal Publ. int. Ass Sediment Palaeoweathering, Palaeosurfaces, Relat. Cont. Depos. 27, 43–60.
Cerling, T.E., 1984. The stable isotopic composition of modern soil carbonate and its relation to climate. Earth Planet. Sci. Lett. 71, 229-240.
Cerling, T.E., Hay, R.L., 1986. An isotopic study of paleosol carbonates from Olduvai Gorge. Quat. Res. 25, 63–78.
Cerling, T.E., Quade, J., 1993. Stable carbon and oxygen isotopes in soil carbonates. Geophys. Monogr. 78, 217–231. https://doi.org/10.1029/GM078p0217
Cerling, T.E., Quade, J., Wang, Y., Bowman, J.R., 1989. Carbon isotopes in soils and palaeosols as ecology and palaeoecology indicators. Nature 341, 138–139. https://doi.org/10.1038/341138a0
Cerling, T.E., Solomon, D.K., Quade, J., Bowman, J.R., 1991. On the isotopic composition of carbon in soil carbon dioxide. Geochim. Cosmochim. Acta 55, 3403–3405. https://doi.org/10.1016/0016-7037(91)90498-T
Cermak, V., Bodri, L., Kresl, M., Dedecek, P., Safanda, J., 2017. Eleven years of ground–air temperature tracking over different land cover types. Int. J. Climatol. 37, 1084–1099. https://doi.org/10.1002/joc.4764
Chen, M., Willgoose, G.R., Saco, P.M., 2014. Spatial prediction of temporal soil moisture dynamics using HYDRUS-1D. Hydrol. Process. 28, 171–185. https://doi.org/10.1002/hyp.9518
Cotton, J.M., Sheldon, N.D., 2012. New constraints on using paleosols to reconstruct atmospheric pCO 2. Bull. Geol. Soc. Am. 124, 1411–1423. https://doi.org/10.1130/B30607.1
Csank, A.Z., Tripati, A.K., Patterson, W.P., Eagle, R.A., Rybczynski, N., Ballantyne, A.P., Eiler, J.M., 2011. Estimates of Arctic land surface temperatures during the early Pliocene from

two novel proxies. Earth Planet. Sci. Lett. 304, 291–299. https://doi.org/10.1016/J.EPSL.2011.02.030
Cui, Y., Schubert, B.A., 2017. Atmospheric pCO2 reconstructed across five early Eocene global warming events. Earth Planet. Sci. Lett. 478, 225–233. https://doi.org/10.1016/J.EPSL.2017.08.038
Daëron, M., Blamart, D., Peral, M., Affek, H.P., 2016. Absolute isotopic abundance ratios and the accuracy of Δ47 measurements. Chem. Geol. 442, 83–96. https://doi.org/10.1016/j.chemgeo.2016.08.014
Daëron, M., Drysdale, R.N., Peral, M., Huyghe, D., Blamart, D., Coplen, T.B., Lartaud, F., Zanchetta, G., 2019. Most Earth-surface calcites precipitate out of isotopic equilibrium. Nat. Commun. 10, 1–7. https://doi.org/10.1038/s41467-019-08336-5
Daëron, M., Guo, W., Eiler, J.M., Genty, D., Blamart, D., Boch, R., Drysdale, R., Maire, R., Wainer, K., Zanchetta, G., 2011. 13C18O clumping in speleothems: Observations from natural caves and precipitation experiments. Geochim. Cosmochim. Acta 75, 3303–3317. https://doi.org/10.1016/j.gca.2010.10.032
Defliese, W.F., Hren, M.T., Lohmann, K.C., 2015. Compositional and temperature effects of phosphoric acid fractionation on Δ47 analysis and implications for discrepant calibrations. Chem. Geol. 396, 51–60. https://doi.org/10.1016/j.chemgeo.2014.12.018
DeLuca, V., Vullo, D., Scozzafava, A., Carginale, V., Rossi, M., Capasso, C., 2013. An α-carbonic anhydrase from the thermophilic bacterium Sulphurihydrogenibium azorense is the fastest enzyme known for the CO2 hydration reaction. Bioorg. Med. Chem. 21, 1465–1469. https://doi.org/10.1016/j.bmc.2012.09.047
Dennis, K.J., Affek, H.P., Passey, B.H., Schrag, D.P., Eiler, J.M., 2011. Defining an absolute reference frame for 'clumped' isotope studies of CO2. Geochim. Cosmochim. Acta 75, 7117–7131. https://doi.org/10.1016/j.gca.2011.09.025
Dennis, K.J., Schrag, D.P., 2010. Clumped isotope thermometry of carbonatites as an indicator of diagenetic alteration. Geochim. Cosmochim. Acta 74, 4110–4122. https://doi.org/10.1016/j.gca.2010.04.005
DePaolo, D.J., 2011. Surface kinetic model for isotopic and trace element fractionation during precipitation of calcite from aqueous solutions. Geochim. Cosmochim. Acta 75, 1039–1056. https://doi.org/10.1016/j.gca.2010.11.020
Diffenbaugh, N.S., Field, C.B., 2013. Changes in ecologically critical terrestrial climate conditions. Science (80-.). 341, 486–92. https://doi.org/10.1126/science.1237123
Ding, Z.L., Yang, S.L., 2000. C3/C4 vegetation evolution over the last 7.0 Myr in the Chinese Loess Plateau: evidence from pedogenic carbonate δ13C. Palaeogeogr. Palaeoclimatol. Palaeoecol. 160, 291–299. https://doi.org/10.1016/S0031-0182(00)00076-6
Drever, J.I., 1982. The Geochemistry of Natural Waters. Prentice Hall, New York.
Dworkin, S.I., Nordt, L.C., Atchley, S.C., 2005. Determining terrestrial paleotemperatures using the oxygen isotopic composition of pedogenic carbonate. Earth Planet. Sci. Lett. 237, 56–68. https://doi.org/10.1016/j.epsl.2005.06.054
Eagle, R.A., Eiler, J.M., Tripati, A.K., Ries, J.B., Freitas, P.S., Hiebenthal, C., Wanamaker, A.D., Taviani, M., Elliot, M., Marenssi, S., Nakamura, K., Ramirez, P., Roy, K., 2013a. The influence of temperature and seawater carbonate saturation state on 13C–18O bond ordering in bivalve mollusks. Biogeosciences 10, 4591–4606. https://doi.org/10.5194/bg-10-4591-2013
Eagle, R.A., Risi, C., Mitchell, J.L., Eiler, J.M., Seibt, U., Neelin, J.D., Li, G., Tripati, A.K.,

2013b. High regional climate sensitivity over continental China constrained by glacial-recent changes in temperature and the hydrological cycle. Proc. Natl. Acad. Sci. U. S. A. 110, 8813–8. https://doi.org/10.1073/pnas.1213366110
Eagle, R.A., Schauble, E.A., Tripati, A.K., Tütken, T., Hulbert, R.C., Eiler, J.M., 2010. Body temperatures of modern and extinct vertebrates from (13)C-(18)O bond abundances in bioapatite. Proc. Natl. Acad. Sci. U. S. A. 107, 10377–10382. https://doi.org/10.1073/pnas.0911115107
Eastoe, C.J., Dettman, D.L., 2016. Isotope amount effects in hydrologic and climate reconstructions of monsoon climates: Implications of some long-term data sets for precipitation. Chem. Geol. 430, 78–89. https://doi.org/10.1016/j.chemgeo.2016.03.022
Eberle, J.J., Fricke, H.C., Humphrey, J.D., Hackett, L., Newbrey, M.G., Hutchison, J.H., 2010. Seasonal variability in Arctic temperatures during early Eocene time. Earth Planet. Sci. Lett. 296, 481–486. https://doi.org/10.1016/j.epsl.2010.06.005
Eberle, J.J., Greenwood, D.R., 2012. Life at the top of the greenhouse Eocene world—A review of the Eocene flora and vertebrate fauna from Canada's High Arctic. GSA Bull. 124, 3–23. https://doi.org/https://doi.org/10.1130/B30571.1
Ehlers, T.A., Poulsen, C.J., 2009. Influence of Andean uplift on climate and paleoaltimetry estimates. Earth Planet. Sci. Lett. 281, 238–248. https://doi.org/10.1016/j.epsl.2009.02.026
Eiler, J.M., 2011. Paleoclimate reconstruction using carbonate clumped isotope thermometry. Quat. Sci. Rev. 30, 3575–3588. https://doi.org/10.1016/j.quascirev.2011.09.001
Eiler, J.M., 2007. "Clumped-isotope" geochemistry—The study of naturally-occurring, multiply-substituted isotopologues. Earth Planet. Sci. Lett. 262, 309–327. https://doi.org/10.1016/j.epsl.2007.08.020
Eiler, J.M., Bergquist, B., Bourg, I., Cartigny, P., Farquhar, J., Gagnon, A.C., Guo, W., Halevy, I., Hofmann, A., Larson, T.E., Levin, N.E., Schauble, E.A., Stolper, D.A., 2014. Frontiers of stable isotope geoscience. Chem. Geol. 372, 119–143. https://doi.org/10.1016/j.chemgeo.2014.02.006
Eiler, J.M., Clog, M., Magyar, P., Piasecki, A., Sessions, A.L., Stolper, D.A., Deerberg, M., Schlueter, H.-J., Schwieters, J., 2013. A high-resolution gas-source isotope ratio mass spectrometer. Int. J. Mass Spectrom. 335, 45–56. https://doi.org/10.1016/j.ijms.2012.10.014
Eiler, J.M., Schauble, E.A., 2004. 18O13C16O in Earth's atmosphere. Geochim. Cosmochim. Acta 68, 4767–4777. https://doi.org/10.1016/j.gca.2004.05.035
Ekart, D.D., Cerling, T.E., Montañez, I.P., Tabor, N.J., 1999. A 400 million year carbon isotope record of pedogenic carbonate: Implications for paleoatmospheric carbon dioxide. Am. J. Sci. https://doi.org/10.2475/ajs.299.10.805
Evans, D., Sagoo, N., Renema, W., Cotton, L.J., Müller, W., Todd, J.A., Saraswati, P.K., Stassen, P., Ziegler, M., Pearson, P.N., Valdes, P.J., Affek, H.P., 2018. Eocene greenhouse climate revealed by coupled clumped isotope-Mg/Ca thermometry. Proc. Natl. Acad. Sci. 115, 1174–1179. https://doi.org/10.1073/pnas.1714744115
Fan, M., Carrapa, B., 2014. Late Cretaceous – early Eocene Laramide uplift, exhumation, and basin subsidence in Wyoming: Crustal responses to fl at slab subduction. Tectonics 509–529. https://doi.org/10.1002/2012TC003221.Received
Fan, M., DeCelles, P.G., Gehrels, G.E., Dettman, D.L., Quade, J., Peyton, S.L., 2011. Sedimentology, detrital zircon geochronology, and stable isotope geochemistry of the lower Eocene strata in the Wind River Basin, central Wyoming. GSA Bull. 123, 979–996. https://doi.org/10.1130/B30235.1

Fan, M., Hough, B.G., Passey, B.H., 2014. Middle to late Cenozoic cooling and high topography in the central Rocky Mountains: Constraints from clumped isotope geochemistry. Earth Planet. Sci. Lett. 408, 35–47. https://doi.org/10.1016/j.epsl.2014.09.050
Feddes, R.A., 1978. Simulation of field water use and crop yield, in: Simulation Monographs. Pudoc, Wageningen.
Feng, R., Poulsen, C.J., 2016. Refinement of Eocene lapse rates, fossil-leaf altimetry, and North American Cordilleran surface elevation estimates. Earth Planet. Sci. Lett. 436, 130–141. https://doi.org/10.1016/j.epsl.2015.12.022
Fenter, P., Kerisit, S., Raiteri, P., Gale, J.D., 2013. Is the calcite-water interface understood? Direct comparisons of molecular dynamics simulations with specular X-ray reflectivity data. J. Phys. Chem. C 117, 5028–5042. https://doi.org/10.1021/jp310943s
Fenter, P., Sturchio, N.C., 2012. Calcite (104)–water interface structure, revisited. Geochim. Cosmochim. Acta 97, 58–69. https://doi.org/10.1016/j.gca.2012.08.021
Fenter, P., Sturchio, N.C., 2004. Mineral–water interfacial structures revealed by synchrotron X-ray scattering. Prog. Surf. Sci. 77, 171–258. https://doi.org/10.1016/j.progsurf.2004.12.001
Fernandez, A., Müller, I.A., Rodríguez-Sanz, L., van Dijk, J., Looser, N., Bernasconi, S.M., 2017. A reassessment of the precision of carbonate clumped isotope measurements: Implications for calibrations and paleoclimate reconstructions. Geochemistry, Geophys. Geosystems 1–12. https://doi.org/10.1002/2017GC007106
Fernandez, A., Tang, J., Rosenheim, B.E., 2014. Siderite 'clumped' isotope thermometry: A new paleoclimate proxy for humid continental environments. Geochim. Cosmochim. Acta 126, 411–421. https://doi.org/10.1016/j.gca.2013.11.006
Fiebig, J., Hofmann, S., Löffler, N., Lüdecke, T., Methner, K., Wacker, U., 2016. Slight pressure imbalances can affect accuracy and precision of dual inlet-based clumped isotope analysis. Isotopes Environ. Health Stud. 6016, 1–17. https://doi.org/10.1080/10256016.2015.1010531
Finnegan, S., Bergmann, K.D., Eiler, J.M., Jones, D.S., Fike, D.A., Eisenman, I., Hughes, N.C., Tripati, A.K., Fischer, W.W., 2011. The Magnitude and Duration of Late Ordovician-Early Silurian Glaciation. Science (80-.). 331, 903–906.
Fischer, H., Meissner, K.J., Mix, A.C., Abram, N.J., Austermann, J., Brovkin, V., Capron, E., Colombaroli, D., Daniau, A.L., Dyez, K.A., Felis, T., Finkelstein, S.A., Jaccard, S.L., McClymont, E.L., Rovere, A., Sutter, J., Wolff, E.W., Affolter, S., Bakker, P., Ballesteros-Cánovas, J.A., Barbante, C., Caley, T., Carlson, A.E., Churakova, O., Cortese, G., Cumming, B.F., Davis, B.A.S., De Vernal, A., Emile-Geay, J., Fritz, S.C., Gierz, P., Gottschalk, J., Holloway, M.D., Joos, F., Kucera, M., Loutre, M.F., Lunt, D.J., Marcisz, K., Marlon, J.R., Martinez, P., Masson-Delmotte, V., Nehrbass-Ahles, C., Otto-Bliesner, B.L., Raible, C.C., Risebrobakken, B., Sánchez Goñi, M.F., Arrigo, J.S., Sarnthein, M., Sjolte, J., Stocker, T.F., Velasquez Alvárez, P.A., Tinner, W., Valdes, P.J., Vogel, H., Wanner, H., Yan, Q., Yu, Z., Ziegler, M., Zhou, L., 2018. Palaeoclimate constraints on the impact of 2 °c anthropogenic warming and beyond. Nat. Geosci. 11, 474–485. https://doi.org/10.1038/s41561-018-0146-0
Foreman, B.Z., 2014. Climate-driven generation of a fluvial sheet sand body at the Paleocene-Eocene boundary in north-west Wyoming (USA). Basin Res. https://doi.org/10.1111/bre.12027
Foreman, B.Z., Heller, P.L., Clementz, M.T., 2012. Fluvial response to abrupt global warming at the Palaeocene/Eocene boundary. Nature 491, 92–95. https://doi.org/10.1038/nature11513
Fox, D.L., Koch, P.L., 2004. Carbon and oxygen isotopic variability in Neogene paleosol

carbonates: constraints on the evolution of the C4-grasslands of the Great Plains, USA. Palaeogeogr. Palaeoclimatol. Palaeoecol. 207, 305–329. https://doi.org/10.1016/J.PALAEO.2003.09.030
Fredlund, D.G., Xing, A., 1994. Equations for the soil-water characteristic curve. Can. Geotech. J. 31, 521–532.
Fricke, H.C., 2003. Investigation of early Eocene water-vapor transport and paleoelevation using oxygen isotope data from geographically widespread mammal remains 1088–1096.
Fricke, H.C., Foreman, B.Z., Sewall, J.O., 2010. Integrated climate model-oxygen isotope evidence for a North American monsoon during the Late Cretaceous. Earth Planet. Sci. Lett. 289, 11–21. https://doi.org/10.1016/J.EPSL.2009.10.018
Friedl, M.A., Sulla-Menashe, D., Tan, B., Schneider, A., Ramankutty, N., Sibley, A., Huang, X., 2010. MODIS Collection 5 global land cover: Algorithm refinements and characterization of new datasets. Remote Sens. Environ. 114, 168–182. https://doi.org/10.1016/J.RSE.2009.08.016
Frieling, J., Gebhardt, H., Huber, M., Adekeye, O.A., Akande, S.O., Reichart, G.-J., Middelburg, J.J., Schouten, S., Sluijs, A., 2017. Extreme warmth and heat-stressed plankton in the tropics during the Paleocene-Eocene Thermal Maximum. Sci. Adv. 3. https://doi.org/10.1126/sciadv.1600891
Gabitov, R.I., Watson, E.B., Sadekov, A., 2012. Oxygen isotope fractionation between calcite and fluid as a function of growth rate and temperature: An in situ study. Chem. Geol. 306–307, 92–102. https://doi.org/10.1016/j.chemgeo.2012.02.021
Gallagher, T.M., Sheldon, N.D., 2016. Combining soil water balance and clumped isotopes to understand the nature and timing of pedogenic carbonate formation. Chem. Geol. 435, 79–91. https://doi.org/10.1016/j.chemgeo.2016.04.023
Gallagher, T.M., Sheldon, N.D., 2013. A new paleothermometer for forest paleosols and its implications for Cenozoic climate. Geology 41, 647–650. https://doi.org/10.1130/G34074.1
Galloway, W.E., Whiteaker, T.L., Ganey-curry, P., 2011. History of Cenozoic North American drainage basin evolution, sediment yield, and accumulation in the Gulf of Mexico basin. Geosphere 7, 938–973. https://doi.org/10.1130/GES00647.1
Garzione, C.N., Auerbach, D.J., Jin-Sook Smith, J., Rosario, J.J., Passey, B.H., Jordan, T.E., Eiler, J.M., 2014. Clumped isotope evidence for diachronous surface cooling of the Altiplano and pulsed surface uplift of the Central Andes. Earth Planet. Sci. Lett. 393, 173–181. https://doi.org/10.1016/j.epsl.2014.02.029
Garzione, C.N., Hoke, G.D., Libarkin, J.C., Withers, S., MacFadden, B., Eiler, J.M., Ghosh, P., Mulch, A., 2008. Rise of the Andes. Science 320, 1304–7. https://doi.org/10.1126/science.1148615
Garzione, C.N., Quade, J., DeCelles, P.G., English, N.B., 2000. Predicting paleoelevation of Tibet and the Himalaya from δ18O vs. altitude gradients in meteoric water across the Nepal Himalaya. Earth Planet. Sci. Lett. 183, 215–229. https://doi.org/10.1016/S0012-821X(00)00252-1
Gazis, C., Feng, X., 2004. A stable isotope study of soil water: evidence for mixing and preferential flow paths. Geoderma 119, 97–111. https://doi.org/10.1016/S0016-7061(03)00243-X
Geiger, R., Aron, R.H., Todhunter, P., 2009. The climate near the ground, 7th ed. Rowman & Littlefield.
Geissbühler, P., Fenter, P., DiMasi, E., Srajer, G., Sorensen, L.B., Sturchio, N.C., 2004. Three-

dimensional structure of the calcite–water interface by surface X-ray scattering. Surf. Sci. 573, 191–203. https://doi.org/10.1016/j.susc.2004.09.036
Ghosh, P., Adkins, J.F., Affek, H.P., Balta, B., Guo, W., Schauble, E.A., Schrag, D.P., Eiler, J.M., 2006a. 13C–18O bonds in carbonate minerals: A new kind of paleothermometer. Geochim. Cosmochim. Acta 70, 1439–1456. https://doi.org/10.1016/j.gca.2005.11.014
Ghosh, P., Eiler, J.M., Campana, S.E., Feeney, R.F., 2007. Calibration of the carbonate 'clumped isotope' paleothermometer for otoliths. Geochim. Cosmochim. Acta 71, 2736–2744. https://doi.org/10.1016/j.gca.2007.03.015
Ghosh, P., Garzione, C.N., Eiler, J.M., 2006b. Rapid Uplift of the Altiplano Revealed Through 13C-18O Bonds in Paleosol Carbonates. Science 311, 511–515. https://doi.org/10.1126/science.1119365
Gile, L.H., Peterson, F.F., Grossman, R.B., 1966. Morphological and Genetic Sequences of Carbonate Accumulation in Desert Soils. Soil Sci. 101, 347–360.
Goudie, A., 1973. Duricrusts in Tropical and Subtropical Landscapes. Oxford University Press.
Grauel, A.-L., Schmid, T.W., Hu, B., Bergami, C., Capotondi, L., Zhou, L., Bernasconi, S.M., 2013. Calibration and application of the 'clumped isotope' thermometer to foraminifera for high-resolution climate reconstructions. Geochim. Cosmochim. Acta 108, 125–140. https://doi.org/10.1016/j.gca.2012.12.049
Greenwood, D.R., Wing, S.L., 1995. Eocene continental climates and latitudinal temperature gradients. Geology 23, 1044–1048. https://doi.org/10.1130/0091-7613(1995)023<1044:ECCALT>2.3.CO;2
Guo, W., 2009. Carbonate Clumped Isotope Thermometry: Application to Cabonaceous Chondrites & Effects of Kinetic Isotope Fractionations. California Institute of Technology. https://doi.org/10.1017/CBO9781107415324.004
Guo, W., Mosenfelder, J.L., Goddard, W.A., Eiler, J.M., 2009. Isotopic fractionations associated with phosphoric acid digestion of carbonate minerals: Insights from first-principles theoretical modeling and clumped isotope measurements. Geochim. Cosmochim. Acta 73, 7203–7225. https://doi.org/10.1016/j.gca.2009.05.071
Gupta, P., Noone, D., Galewsky, J., Sweeney, C., Vaughn, B.H., 2009. Demonstration of high-precision continuous measurements of water vapor isotopologues in laboratory and remote field deployments using wavelength-scanned and cavity ring-down spectroscopy (WS-CRDS) technology. Rapid Commun. Mass Spectrom. 23, 2534–2542. https://doi.org/10.1002/rcm
Gushulak, C.A.C., West, C.K., Greenwood, D.R., 2016. Paleoclimate and precipitation seasonality of the Early Eocene McAbee megaflora, Kamloops Group, British Columbia. Can. J. Earth Sci. 53, 591–604. https://doi.org/10.1139/cjes-2015-0160
Hall, D.O., Scurlock, J.M.O., 1991. Climate change and productivity of natural grasslands. Ann. Bot. 49–55.
Harden, J.W., Taylor, E.M., Hill, C., Mark, R.K., McFadden, L.D., Reheis, M.C., Sowers, J.M., Wells, S.G., 1991. Rates of soil development from four soil chronosequences in the southern Great Basin. Quat. Res. 35, 383–399. https://doi.org/10.1016/0033-5894(91)90052-7
Hargreaves, G.H., Samani, Z.A., 1985. Reference crop evapotranspiration from temperature. Appl. Eng. Agric. 1, 96–99.
Harrington, G.J., Jaramillo, C.A., 2007. Paratropical floral extinction in the Late Palaeocene-Early Eocene. J. Geol. Soc. London. 164, 323–332. https://doi.org/10.1144/0016-76492006-

027
Harrison, S.P., Bartlein, P.J., Izumi, K., Li, G., Annan, J., Hargreaves, J., Braconnot, P., Kageyama, M., 2015. Evaluation of CMIP5 palaeo-simulations to improve climate projections. Nat. Clim. Chang. 5, 735–743. https://doi.org/10.1038/nclimate2649
Haywood, A.M., Ridgwell, A.J., Lunt, D.J., Hill, D.J., Pound, M.J., Dowsett, H.J., Dolan, A.M., Francis, J.E., Williams, M., 2011. Are there pre-Quaternary geological analogues for a future greenhouse warming? Philos. Trans. R. Soc. A Math. Phys. Eng. Sci. 369, 933–956. https://doi.org/10.1098/rsta.2010.0317
He, B., Olack, G.A., Colman, A.S., 2012. Pressure baseline correction and high-precision CO 2 clumped-isotope (Δ 47) measurements in bellows and micro-volume modes. Rapid Commun. Mass Spectrom. 26, 2837–2853. https://doi.org/10.1002/rcm.6436
Head, J.J., Bloch, J.I., Hastings, A.K., Bourque, J.R., Cadena, E.A., Herrera, F.A., Polly, P.D., Jaramillo, C.A., 2009. Giant boid snake from the Palaeocene neotropics reveals hotter past equatorial temperatures. Nature 457, 715–717. https://doi.org/10.1038/nature07671
Heinemann, M., Jungclaus, J.H., Marotzke, J., 2009. Warm Paleocene/Eocene climate as simulated in ECHAM5/MPI-OM. Clim. Past 5, 785–802.
Held, I.M., Soden, B.J., 2006. Robust responses of the hydrological cycle to global warming. J. Clim. 19, 5686–5699. https://doi.org/10.1175/JCLI3990.1
Henkes, G.A., Passey, B.H., Grossman, E.L., Shenton, B.J., Pérez-Huerta, A., Yancey, T.E., 2014. Temperature limits for preservation of primary calcite clumped isotope paleotemperatures. Geochim. Cosmochim. Acta 139, 362–382.
Henkes, G.A., Passey, B.H., Wanamaker, A.D., Grossman, E.L., Ambrose, W.G., Carroll, M.L., 2013. Carbonate clumped isotope compositions of modern marine mollusk and brachiopod shells. Geochim. Cosmochim. Acta 106, 307–325. https://doi.org/10.1016/j.gca.2012.12.020
Hill, P.S., Tripati, A.K., Schauble, E. a., 2014. Theoretical constraints on the effects of pH, salinity, and temperature on clumped isotope signatures of dissolved inorganic carbon species and precipitating carbonate minerals. Geochim. Cosmochim. Acta 125, 610–652. https://doi.org/10.1016/j.gca.2013.06.018
Hillel, D., 1982. Introduction to soil physics, Academic Press, Inc.
Hirmas, D.R., Amrhein, C., Graham, R.C., 2010. Spatial and process-based modeling of soil inorganic carbon storage in an arid piedmont. Geoderma 154, 486–494. https://doi.org/10.1016/j.geoderma.2009.05.005
Ho, S.L., Laepple, T., 2016. Flat meridional temperature gradient in the early Eocene in the subsurface rather than surface ocean. Nat. Geosci. 9. https://doi.org/10.1038/ngeo2763
Hoke, G.D., Garzione, C.N., Araneo, D.C., Latorre, C., Strecker, M.R., Williams, K.J., 2009. The stable isotope altimeter: Do Quaternary pedogenic carbonates predict modern elevations? Geology 37, 1015–1018. https://doi.org/10.1130/G30308A.1
Hollis, C.J., Handley, L., Crouch, E.M., Morgans, H.E.G., Baker, J.A., Creech, J.B., Collins, K.S., Gibbs, S.J., Huber, M., Schouten, S., Zachos, J.C., Pancost, R.D., 2009. Tropical sea temperatures in the high-latitude South Pacific during the Eocene. Geology 37, 99–102. https://doi.org/10.1130/G25200A.1
Hollis, C.J., Taylor, K.W.R., Handley, L., Pancost, R.D., Huber, M., Creech, J.B., Hines, B.R., Crouch, E.M., Morgans, H.E.G., Crampton, J.S., Gibbs, S.J., Pearson, P.N., Zachos, J.C., 2012. Early Paleogene temperature history of the Southwest Pacific Ocean: Reconciling proxies and models. Earth Planet. Sci. Lett. 349–350, 53–66.

https://doi.org/10.1016/j.epsl.2012.06.024
Hough, B.G., Fan, M., Passey, B.H., 2014. Calibration of the clumped isotope geothermometer in soil carbonate in Wyoming and Nebraska, USA: Implications for paleoelevation and paleoclimate reconstruction. Earth Planet. Sci. Lett. 391. https://doi.org/10.1016/j.epsl.2014.01.008
Hren, M.T., Sheldon, N.D., 2012. Temporal variations in lake water temperature: Paleoenvironmental implications of lake carbonate δ18O and temperature records. Earth Planet. Sci. Lett. 337–338, 77–84. https://doi.org/10.1016/j.epsl.2012.05.019
Huber, M., 2008. A hotter greenhouse? 321, 353–354. https://doi.org/10.1126/science.1161170
Huber, M., Caballero, R., 2011. The early Eocene equable climate problem revisited. Clim. Past 7, 603–633. https://doi.org/10.5194/cp-7-603-2011
Huber, M., Goldner, A., 2012. Eocene monsoons. J. Asian Earth Sci. 44, 3–23. https://doi.org/10.1016/J.JSEAES.2011.09.014
Huntington, K.W., Eiler, J.M., Affek, H.P., Guo, W., Bonifacie, M., Yeung, L.Y., Thiagarajan, N., Passey, B.H., Tripati, A.K., Daëron, M., Came, R.E., 2009. Methods and limitations of "clumped" CO2 isotope (Δ47) analysis by gas-source isotope ratiomass spectrometry. J. Mass Spectrom. 44, 1318–1329. https://doi.org/10.1002/jms.1614
Huntington, K.W., Lechler, A.R., 2015. Carbonate clumped isotope thermometry in continental tectonics. Tectonophysics 647–648, 1–20. https://doi.org/10.1016/j.tecto.2015.02.019
Huntington, K.W., Saylor, J., Quade, J., Hudson, A.M., 2015. High late Miocene-Pliocene elevation of the Zhada Basin, southwestern Tibetan Plateau, from carbonate clumped isotope thermometry. Bull. Geol. Soc. Am. 127, 181–199. https://doi.org/10.1130/B31000.1
Huntington, K.W., Wernicke, B.P., Eiler, J.M., 2010. Influence of climate change and uplift on Colorado Plateau paleotemperatures from carbonate clumped isotope thermometry. Tectonics 29, n/a-n/a. https://doi.org/10.1029/2009TC002449
Huth, T.E., Cerling, T.E., Marchetti, D.W., Bowling, D.R., Ellwein, A.L., Passey, B.H., 2019. Seasonal bias in soil carbonate formation and its implications for interpreting high-resolution paleoarchives: evidence from southern Utah. J. Geophys. Res. Biogeosciences 0. https://doi.org/10.1029/2018JG004496
Hyland, E.G., Huntington, K.W., Sheldon, N.D., Reichgelt, T., 2018. Temperature seasonality in the North American continental interior during the early Eocene climatic optimum. Clim. Past Discuss. 2018, 1–39. https://doi.org/10.5194/cp-2018-28
Hyland, E.G., Sheldon, N.D., 2013. Coupled CO2-climate response during the Early Eocene Climatic Optimum. Palaeogeogr. Palaeoclimatol. Palaeoecol. 369, 125–135. https://doi.org/10.1016/j.palaeo.2012.10.011
Hyland, E.G., Sheldon, N.D., Cotton, J.M., 2017. Constraining the early Eocene climatic optimum: A terrestrial interhemispheric comparison. Geol. Soc. Am. Bull. 129, 244–252. https://doi.org/10.1130/B31493.1
IAEA/WMO, 2019. Global Network of Isotopes in Precipitation. The GNIP database. Accessible at: http://www.iaea.org/water.
Ingalls, M., Rowley, D.B., Olack, G.A., Currie, B., Li, S., Schmidt, J., Tremblay, M., Polissar, P., Shuster, D.L., Lin, D., Colman, A.S., 2018. Paleocene to Pliocene low-latitude, high-elevation basins of southern Tibet: Implications for tectonic models of India-Asia collision, Cenozoic climate, and geochemical weathering. Bull. Geol. Soc. Am. 130, 307–330. https://doi.org/10.1130/B31723.1
Inglis, G.N., Collinson, M.E., Riegel, W., Wilde, V., Farnsworth, A., Lunt, D.J., Valdes, P.J.,

Robson, B.E., Scott, A.C., Lenz, O.K., Naafs, B.D.A., Pancost, R.D., 2017. Mid-latitude continental temperatures through the early Eocene in western Europe. Earth Planet. Sci. Lett. 460, 86–96. https://doi.org/10.1016/j.epsl.2016.12.009

Inskeep, W.P., Bloom, P.R., 1986. Kinetics of Calcite Precipitation in the Presence of Water-Soluble Organic Ligands. Soil Sci. Soc. Am. J. 50, 1167–1172.

Jackson, R.B., Canadell, J., Ehleringer, J.R., Mooney, H.A., Sala, O.R., Schulze, E.D., 1996. A global analysis of root distributions for terrestrial biomes. Oecologia 108, 389–411. https://doi.org/10.1007/BF00333714

Jagniecki, E.A., Lowenstein, T.K.T.K., Jenkins, D.M., Demicco, R. V., 2015. Eocene atmospheric CO2 from the nahcolite proxy. Geology 43, 1075–1078. https://doi.org/10.1130/G36886.1

Jaramillo, C.A., Rueda, M.J., Mora, G., 2006. Cenozoic Plant Diversity in the Neotropics. Science (80-.). 311, 1893–1896. https://doi.org/10.1126/science.1121380

Jenny, H., 1941. Factors of Soil Formation: A system of Quantitative Pedology. McGraw-Hill Book Company, New York.

Ji, S., Nie, J., Lechler, A.R., Huntington, K.W., Heitmann, E.O., Breecker, D.O., 2018. A symmetrical CO2 peak and asymmetrical climate change during the middle Miocene. Earth Planet. Sci. Lett. 499, 134–144. https://doi.org/10.1016/J.EPSL.2018.07.011

Kaakinen, A., Sonninen, E., Lunkka, J.P., 2006. Stable isotope record in paleosol carbonates from the Chinese Loess Plateau: Implications for late Neogene paleoclimate and paleovegetation. Palaeogeogr. Palaeoclimatol. Palaeoecol. 237, 359–369. https://doi.org/10.1016/j.palaeo.2005.12.011

Kalnay, E., Kanamitsu, M., Kistler, R., Collins, W., Deaven, D., Gandin, L., Iredell, M., Saha, S., White, G., Woollen, J., Zhu, Y., Chelliah, M., Ebisuzaki, W., Higgins, W., Janowiak, J., Mo, K.C., Ropelewski, C., Wang, J., Leetmaa, A., Reynolds, R.L., Jenne, R., Joseph, D., 1996. The NCEP/NCAR 40-Year Reanalysis Project. Bull. Am. Meteorol. Soc. 77, 437–472. https://doi.org/10.1175/1520-0477(1996)077<0437:TNYRP>2.0.CO;2

Keating-Bitonti, C.R., Ivany, L.C., Affek, H.P., Douglas, P.M.J., Samson, S.D., 2011. Warm, not super-hot, temperatures in the early Eocene subtropics. Geology 39, 771–774. https://doi.org/10.1130/G32054.1

Keery, J.S., Holden, P.B., Edwards, N.R., 2018. Sensitivity of the Eocene Climate to CO2 and Orbital Variability. Clim. Past Discuss. 14, 215–238. https://doi.org/10.5194/cp-2017-60

Kele, S., Breitenbach, S.F.M., Capezzuoli, E., Meckler, A.N., Ziegler, M., Millan, I.M., Kluge, T., Deák, J., Hanselmann, K., John, C.M., Yan, H., Liu, Z., Bernasconi, S.M., 2015. Temperature dependence of oxygen- and clumped isotope fractionation in carbonates: a study of travertines and tufas in the 6-95°C temperature range. Geochim. Cosmochim. Acta 168, 172–192. https://doi.org/10.1016/j.gca.2015.06.032

Kelson, J.R., Huntington, K.W., Schauer, A.J., Saenger, C., Lechler, A.R., 2017. Toward a universal carbonate clumped isotope calibration: Diverse synthesis and preparatory methods suggest a single temperature relationship. Geochim. Cosmochim. Acta 197. https://doi.org/10.1016/j.gca.2016.10.010

Kelson, J.R., Watford, D., Bataille, C.P., Huntington, K.W., Hyland, E.G., Bowen, G.J., 2018. Warm terrestrial subtropics during the Paleocene and Eocene: Carbonate clumped isotope (Δ47) evidence from the Tornillo Basin, Texas (USA). Paleoceanogr. Paleoclimatology 1–20. https://doi.org/10.1029/2018PA003391

Kiehl, J., Shields, C., 2013. Sensitivity of the Palaeocene-Eocene Thermal Maximum climate to

cloud properties. Philos. Trans. R. Soc. A Math. Phys. Eng. Sci. 371, 20130093–20130093. https://doi.org/10.1098/rsta.2013.0093
Kim, S.T., O'Neil, J.R., 1997. Equilibrium and nonequilibrium oxygen isotope effects in synthetic carbonates. Geochim. Cosmochim. Acta 61, 3461–3475. https://doi.org/10.1016/S0016-7037(97)00169-5
Kluge, T., Affek, H.P., 2012. Quantifying kinetic fractionation in Bunker Cave speleothems using Δ47. Quat. Sci. Rev. 49, 82–94. https://doi.org/10.1016/j.quascirev.2012.06.013
Kluge, T., Affek, H.P., Dublyansky, Y., Spötl, C., 2014. Devils Hole paleotemperatures and implications for oxygen isotope equilibrium fractionation. Earth Planet. Sci. Lett. 400, 251–260. https://doi.org/10.1016/j.epsl.2014.05.047
Kluge, T., Affek, H.P., Marx, T., Aeschbach-Hertig, W., Riechelmann, D.F.C., Scholz, D., Riechelmann, S., Immenhauser, A., Richter, D.K., Fohlmeister, J., Wackerbarth, a., Mangini, a., Spötl, C., 2013. Reconstruction of drip-water δ18O based on calcite oxygen and clumped isotopes of speleothems from Bunker Cave (Germany). Clim. Past 9, 377–391. https://doi.org/10.5194/cp-9-377-2013
Kluge, T., John, C.M., Jourdan, A.-L., Davis, S., Crawshaw, J., 2015. Laboratory calibration of the calcium carbonate clumped isotope thermometer in the 25–250°C temperature range. Geochim. Cosmochim. Acta 157, 213–227. https://doi.org/10.1016/j.gca.2015.02.028
Koch, P.L., Zachos, J.C., Dettman, D.L., 1995. Stable isotope stratigraphy and paleoclimatology of the Paleogene Bighorn Basin (Wyoming, USA). Palaeogeogr. Palaeoclimatol. Palaeoecol. 115, 61–89. https://doi.org/10.1016/0031-0182(94)00107-J
Kozdon, R., Kelly, D.C., Kita, N.T., Fournelle, J.H., Valley, J.W., 2011. Planktonic foraminiferal oxygen isotope analysis by ion microprobe technique suggests warm tropical sea surface temperatures during the Early Paleogene. Paleoceanography 26. https://doi.org/10.1029/2010PA002056
Kraus, M.J., Riggins, S., 2007. Transient drying during the Paleocene–Eocene Thermal Maximum (PETM): Analysis of paleosols in the bighorn basin, Wyoming. Palaeogeogr. Palaeoclimatol. Palaeoecol. 245, 444–461. https://doi.org/10.1016/j.palaeo.2006.09.011
Kraus, M.J., Woody, D.T., Smith, J.J., Dukic, V., 2015. Alluvial response to the Paleocene–Eocene Thermal Maximum climatic event, Polecat Bench, Wyoming (U.S.A.). Palaeogeogr. Palaeoclimatol. Palaeoecol. 435, 177–192. https://doi.org/10.1016/J.PALAEO.2015.06.021
Krueger, R.C., 2017. Fluvial Response to Warming During the Early Eocene Climatic Optimum, Green River Basin, Wyoming. Northern Arizona University, ProQuest Dissertations Publishing, 2018. 10742725.
Landi, A., Mermut, A.., Anderson, D.., 2003. Origin and rate of pedogenic carbonate accumulation in Saskatchewan soils, Canada. Geoderma 117, 143–156. https://doi.org/10.1016/S0016-7061(03)00161-7
Lauretano, V., Littler, K., Polling, M., Zachos, J.C., Lourens, L.J., 2015. Frequency, magnitude and character of hyperthermal events at the onset of the Early Eocene Climatic Optimum. Clim. Past 11, 1313–1324. https://doi.org/10.5194/cp-11-1313-2015
Lebrón, I., Suarez, D.L., 1996. Calcite nucleatiom and precipitation kinetics as affected by dissolved organic matter at 25 C and pH > 7.5. Geochim. Cosmochim. Acta 60, 2765–2776.
Lebrón, I., Suárez, D.L., 1998. Kinetics and Mechanisms of Precipitation of Calcite as Affected by PCO2 and Organic Ligands at 25°C. Geochim. Cosmochim. Acta 62, 405–416. https://doi.org/10.1016/S0016-7037(97)00364-5
Lechler, A.R., Huntington, K.W., Breecker, D.O., Sweeney, M.R., Schauer, A.J., 2018. Loess–

paleosol carbonate clumped isotope record of late Pleistocene–Holocene climate change in the Palouse region, Washington State, USA. Quat. Res. 1–17. https://doi.org/10.1017/qua.2018.47
Lechler, A.R., Niemi, N.A., Hren, M.T., Lohmann, K.C., 2013. Paleoelevation estimates for the northern and central proto-Basin and Range from carbonate clumped isotope thermometry. Tectonics 32. https://doi.org/10.1002/tect.20016
Lee, X., Wu, H.-J., Sigler, J., Oishi, C., Siccama, T., 2004. Rapid and transient response of soil respiration to rain. Glob. Chang. Biol. 10, 1017–1026. https://doi.org/10.1111/j.1365-2486.2004.00787.x
Lehman, T.M., 1991. Sedimentation in the Laramide Tornillo Basin of West Texas. Geol. Soc. Am. Rocky Mt. Sect. Abstr. with programs. 23, 41.
Lehman, T.M., 1990. Paleosols and the Cretaceous/Tertiary transition in the Big Bend region of Texas. Geology 18, 362–364. https://doi.org/10.1130/0091-7613(1990)018<0362:PATCTT>2.3.CO;2
Lehman, T.M., Busbey, A.B., 2007. Big Bend Field Trip Guide. Society of Vertebtrate Paleontology, 67th Annual Meeting, Field Trip Guidebook.
Leier, A., McQuarrie, N., Garzione, C.N., Eiler, J.M., 2013. Stable isotope evidence for multiple pulses of rapid surface uplift in the Central Andes, Bolivia. Earth Planet. Sci. Lett. 371–372, 49–58. https://doi.org/10.1016/j.epsl.2013.04.025
Leier, A., Quade, J., DeCelles, P.G., Kapp, P., 2009. Stable isotopic results from paleosol carbonate in South Asia: Paleoenvironmental reconstructions and selective alteration. Earth Planet. Sci. Lett. 279, 242–254. https://doi.org/10.1016/J.EPSL.2008.12.044
Leslie, C.E., Peppe, D.J., Williamson, T.E., Heizler, M., Jackson, M., Atchley, S.C., Nordt, L.C., Standhardt, B.R., 2018. Revised age constraints for Late Cretaceous to early Paleocene terrestrial strata from the Dawson Creek section, Big Bend National Park, west Texas. Geol. Soc. Am. Bull. 1–21. https://doi.org/10.1130/B31785.1
Levin, N.E., Brown, F.H., Behrensmeyer, A.K., Bobe, R., Cerling, T.E., 2011. Paleosol carbonates from the omo group: Isotopic records of local and regional environmental change in east africa. Palaeogeogr. Palaeoclimatol. Palaeoecol. 307, 75–89. https://doi.org/10.1016/j.palaeo.2011.04.026
Levitt, N.P., Eiler, J.M., Romanek, C.S., Beard, B.L., Xu, H., Johnson, C.M., 2018. Near Equilibrium 13C-18O Bonding During Inorganic Calcite Precipitation Under Chemo-Stat Conditions. Geochemistry, Geophys. Geosystems. https://doi.org/10.1002/2017GC007089
Li, Y., Zhang, W., Aydin, A., Deng, X., 2018. Formation of calcareous nodules in loess–paleosol sequences: Reviews of existing models with a proposed new "per evapotranspiration model." J. Asian Earth Sci. 154, 8–16. https://doi.org/10.1016/J.JSEAES.2017.12.002
Licht, A., Quade, J., Kowler, A., De Los Santos, M., Hudson, A.M., Schauer, A.J., Huntington, K.W., Copeland, P., Lawton, T.F., 2017. Impact of the North American Monsoon on Isotope Paleoaltimeters: Implications for the Paleoaltimetry of the American Southwest. Am. J. Sci. 317, 1–33. https://doi.org/10.2475/01.2017.01
Licht, A., Van Cappelle, M., Abels, H.A., Ladant, J.-B., Trabucho-Alexandre, J., France-Lanord, C., Donnadieu, Y., Vandenberghe, J., Rigaudier, T., Lécuyer, C., Terry, D., Adriaens, R., Boura, A., Guo, Z., Soe, A.N., Quade, J., Dupont-Nivet, G., Jaeger, J.J., 2014. Asian monsoons in a late Eocene greenhouse world. Nature 513, 501–506. https://doi.org/10.1038/nature13704
Liu, B., Phillips, F.M., Campbell, A.R., 1996. Stable carbon and oxygen isotopes of pedogenic

carbonates, Ajo Mountains, southern Arizona: implications for paleoenvironmental change. Palaeogeogr. Palaeoclimatol. Palaeoecol. 124, 233–246. https://doi.org/10.1016/0031-0182(95)00093-3
Liu, X., Wan, S., Su, B., Hui, D., Luo, Y., 2002. Response of soil CO2 efflux to water manipulation in a tallgrass prairie ecosystem. Plant Soil 240, 213–223. https://doi.org/10.1023/A:1015744126533
Lloyd, M.K., Eiler, J.M., Nabelek, P.I., 2017. Clumped isotope thermometry of calcite and dolomite in a contact metamorphic environment. Geochim. Cosmochim. Acta 197, 323–344. https://doi.org/10.1016/j.gca.2016.10.037
Loptson, C.A., Lunt, D.J., Francis, J.E., 2014. Investigating vegetation-climate feedbacks during the early Eocene. Clim. Past 10, 419–436. https://doi.org/10.5194/cp-10-419-2014
Lowenstein, T.K., Demicco, R. V., 2006. Elevated Eocene atmospheric CO2 and its subsequent decline. Science (80-.). 313, 1928. https://doi.org/10.1126/science.1129555
Lunt, D.J., Elderfield, H., Pancost, R.D., Ridgwell, A.J., Foster, G.L., Haywood, A.M., Kiehl, J., Sagoo, N., Shields, C., Stone, E.J., Valdes, P.J., 2013. Warm climates of the past--a lesson for the future? Philos. Trans. R. Soc. A Math. Phys. Eng. Sci. 371, 20130146–20130146. https://doi.org/10.1098/rsta.2013.0146
Lunt, D.J., Farnsworth, A., Loptson, C.A., L Foster, G., Markwick, P.J., O'Brien, C.L., Pancost, R.D., Robinson, S.A., Wrobel, N., 2016. Palaeogeographic controls on climate and proxy interpretation. Clim. Past 12, 1181–1198. https://doi.org/10.5194/cp-12-1181-2016
Lunt, D.J., Huber, M., Anagnostou, E., Baatsen, M.L.J., Caballero, R., Deconto, R.M., Dijkstra, H.A., Donnadieu, Y., Evans, D., Feng, R., Foster, G.L., Gasson, E.G.W., Von Der Heydt, A.S., Hollis, C.J., Inglis, G.N., Jones, S.M., Kiehl, J., Turner, S.K., Korty, R.L., Kozdon, R., Krishnan, S., Ladant, J.-B., Langebroek, P., Lear, C.H., LeGrande, A.N., Littler, K., Markwick, P.J., Otto-Bliesner, B.L., Pearson, P.N., Poulsen, C.J., Salzmann, U., Shields, C., Snell, K.E., Stärz, M., Super, J., Tabor, C.R., Tierney, J.E., Tourte, G.J.L., Tripati, A.K., Upchurch, G.R., Wade, B.S., Wing, S.L., Winguth, A.M.E., Wright, N.M., Zachos, J.C., Zeebe, R.E., 2017. The DeepMIP contribution to PMIP4: Experimental design for model simulations of the EECO, PETM, and pre-PETM (version 1.0). Geosci. Model Dev. 10, 889–901. https://doi.org/10.5194/gmd-10-889-2017
Lunt, D.J., Jones, T.D., Heinemann, M., Huber, M., LeGrande, A.N., Winguth, A.M.E., Loptson, C.A., Marotzke, J., Roberts, C.D., Tindall, J., Valdes, P.J., Winguth, C., 2012. A model-data comparison for a multi-model ensemble of early Eocene atmosphere-ocean simulations: EoMIP. Clim. Past 8, 1717–1736. https://doi.org/10.5194/cp-8-1717-2012
Lunt, D.J., Valdes, P.J., Jones, T.D., Ridgwell, A.J., Haywood, A.M., Schmidt, D.N., Marsh, R., Maslin, M., 2010. CO2-driven ocean circulation changes as an amplifier of Paleocene-Eocene thermal maximum hydrate destabilization. Geology 38, 875–878. https://doi.org/10.1130/G31184.1
MacGinitie, H.D., 1953. Fossil plants of the Florissant beds, Colorado. Carnegie Institution of Washington.
Machette, M.N., 1985. Calcic soils of the southwestern United States, in: Weide, D.L. (Ed.), Soils and Quaternary Geology of the Southwestern United States. Geological Society of America. https://doi.org/10.1130/SPE203
Marion, G.M., Schlesinger, W.H., 1994. Quantitative modeling of soil forming processes in deserts: The CALDEP and CALGYP models. Quant. Model. Soil Form. Process. 129–145.
Marion, G.M., Schlesinger, W.H., Fonteyn, P.J., 1985. CALDEP: A regional model for soil

CaCO3 (caliche) deposition in southwestern deserts. Soil Sci. 139.
Marion, G.M., Verburg, P.S.J., McDonald, E. V., Arnone, J.A., 2008. Modeling salt movement through a Mojave Desert soil. J. Arid Environ. 72, 1012–1033. https://doi.org/10.1016/J.JARIDENV.2007.12.005
Markwick, P.J., 1998. Fossil crocodilians as indicators of Late Cretaceous and Cenozoic climates: Implications for using palaeontological data in reconstructing palaeoclimate. Palaeogeogr. Palaeoclimatol. Palaeoecol. 137, 205–271. https://doi.org/10.1016/S0031-0182(97)00108-9
Mathieu, R., Bariac, T., 1996. An isotopic study (2H and 18O) of water movements in clayey soils under a semiarid climate. Waster Resour. Res. 32, 779–789.
Matthew, H., Sloan, L.C., 2001. Heat transport, deep waters, and thermal gradients: Coupled simulation of an Eocene greenhouse climate. Geophys. Res. Lett. 28, 3481–3484. https://doi.org/10.1029/2001GL012943
Maxbauer, D.P., Royer, D.L., LePage, B.A., 2014. High Arctic forests during the middle Eocene supported by moderate levels of atmospheric CO2. Geology 42, 1027–1030. https://doi.org/10.1130/G36014.1
Mayer, L., McFadden, L.D., Harden, J.W., 1989. Distribution of calcium carbonate in desert soils: A model. Geology 17, 190.
McCrea, J.M., 1950. On the Isotopic Chemistry of Carbonates and a Paleotemperature Scale. J. Chem. Phys. 18, 849–857. https://doi.org/10.1063/1.1747785
McDonald, E. V., Pierson, F.B., Flerchinger, G.N., McFadden, L.D., 1996. Application of a soil-water balance model to evaluate the influence of holocene climate change on calcic soils, Mojave Desert, California, U.S.A. Geoderma 74, 167–192. https://doi.org/10.1016/S0016-7061(96)00070-5
McFadden, L.D., 2013. Strongly dust-influenced soils and what they tell us about landscape dynamics in vegetated aridlands of the southwestern United States. Geol. Soc. Am. Spec. Pap. 500, 501–532. https://doi.org/10.1130/2013.2500(15)
McFadden, L.D., Amundson, R.G., Chadwick, O.A., 1991. Numerical Modeling Chemical, and Isotopic Studies of Carbonate Accumulation in of Arid Regions. Occur. Charact. Genes. carbonate, gypsum, silica accumulations soils 17–35.
McFadden, L.D., Tinsley, J.C., 1985. Rate and depth of pedogenic-carbonate accumulation in soils: Formulation and testing of a comparttment model. Soils Quat. Geol. Southwest. United States Geol. Soc. Am. Spec. Pap. 203, 23–41.
McInerney, F.A., Wing, S.L., 2011. The Paleocene-Eocene Thermal Maximum: A Perturbation of Carbon Cycle, Climate, and Biosphere with Implications for the Future. Annu. Rev. Earth Planet. Sci. 39, 489–516. https://doi.org/10.1146/annurev-earth-040610-133431
Meckler, A.N., Ziegler, M., Millán, M.I., Breitenbach, S.F.M., Bernasconi, S.M., 2014. Long-term performance of the Kiel carbonate device with a new correction scheme for clumped isotope measurements. Rapid Commun. Mass Spectrom. 28, 1705–1715. https://doi.org/10.1002/rcm.6949
Menne, M.J., Durre, I., Korzeniewski, B., McNeal, S., Thomas, K., Yin, X., Anthony, S., Ray, R., Vose, R.S., E.Gleason, B., Houston, T.G., 2012a. Global Historical Climatology Network - Daily (GCHN - Daily), Version 3. https://doi.org/10.7289/V5D21VHZ
Menne, M.J., Durre, I., Vose, R.S., Gleason, B.E., Houston, T.G., 2012b. An Overview of the Global Historical Climatology Network-Daily Database. J. Atmos. Ocean. Technol. 29, 897–910. https://doi.org/10.1175/JTECH-D-11-00103.1

Methner, K., Mulch, A., Fiebig, J., Wacker, U., Gerdes, A., Graham, S.A., Chamberlain, C.P., 2016. Rapid Middle Eocene temperature change in western North America. Earth Planet. Sci. Lett. 450, 132–139. https://doi.org/10.1016/j.epsl.2016.05.053

Meyer, H.W., 1992. Lapse rates and other variables applied to estimating paleoaltitudes from fossil floras. Palaeogeogr. Palaeoclimatol. Palaeoecol. 99, 71–99. https://doi.org/10.1016/0031-0182(92)90008-S

Meyer, N.A., 2012. Simulating the Accumulation of Calcite in Soils using the Soil Hydraulic Model HYDRUS-1D. The University of Texas at Austin.

Meyer, N.A., Breecker, D.O., Young, M.H., Litvak, M.E., 2014. Simulating the Effect of Vegetation in Formation of Pedogenic Carbonate. Soil Sci. Soc. Am. J. 78, 914. https://doi.org/10.2136/sssaj2013.08.0326

Mickler, P.J., Banner, J.L., Stern, L., Asmerom, Y., Edwards, R.L., Ito, E., 2004. Stable isotope variations in modern tropical speleothems: Evaluating equilibrium vs. kinetic isotope effects. Geochim. Cosmochim. Acta 68, 4381–4393. https://doi.org/10.1016/j.gca.2004.02.012

Miggins, D.P., Anthony, E., Ren, M., Wache, K., 2007. New 40Ar/39Ar ages, geochemistry, and stratigraphy for mafic and rhyolitic volcanic units from Big Bend National Park, in: Geological Society of America Abstracts with Programs. p. 635.

Mintz, J.S., Driese, S.G., Breecker, D.O., Ludvigson, G.A., 2011. Influence of Changing Hydrology on Pedogenic Calcite Precipitation in Vertisols, Dance Bayou, Brazoria County, Texas, U.S.A.: Implications for Estimating Paleoatmospheric PCO2. J. Sediment. Res. 81, 394–400. https://doi.org/10.2110/jsr.2011.36

Mix, H.T., Ibarra, D.E., Mulch, A., Graham, S.A., Chamberlain, C.P., 2016. A hot and high Eocene Sierra Nevada. Bull. Geol. Soc. Am. 128, 531–542. https://doi.org/10.1130/B31294.1

Mix, H.T., Mulch, A., Kent-Corson, M.L., Chamberlain, C.P., 2011. Cenozoic migration of topography in the North American Cordillera. Geology 39, 87–90. https://doi.org/10.1130/G31450.1

Monger, H.C., Cole, D.R., Buck, B.J., Gallegos, R.A., 2009. Scale and the isotopic record of C4 plants in pedogenic carbonate: from the biome to the rhizosphere. Ecology 90, 1498–1511. https://doi.org/10.1890/08-0670.1

Monger, H.C., Cole, D.R., Gish, J.., Giordano, T.., 1998. Stable carbon and oxygen isotopes in Quaternary soil carbonates as indicators of ecogeomorphic changes in the northern Chihuahuan Desert, USA. Geoderma 82, 137–172. https://doi.org/10.1016/S0016-7061(97)00100-6

Mora, C.I., Driese, S.G., 1993. A steep, mid- to late Paleozoic decline in atmospheric CO2: evidence from the soil carbonate CO2 paleobarometer. Chem. Geol. 107, 217–219. https://doi.org/10.1016/0009-2541(93)90177-K

Mora, C.I., Driese, S.G., Colarusso, L.A., 1996. Middle to Late Paleozoic Atmospheric CO_2 Levels from Soil Carbonate and Organic Matter. Science (80-.). 271, 1105 LP – 1107. https://doi.org/10.1126/science.271.5252.1105

Morrill, C., Koch, P.L., 2002. Elevation or alteration? Evaluation of isotopic constraints on paleoaltitudes surrounding the Eocene Green River Basin. Geology 151–154.

Mulch, A., 2016. Stable isotope paleoaltimetry and the evolution of landscapes and life. Earth Planet. Sci. Lett. 433, 180–191. https://doi.org/10.1016/J.EPSL.2015.10.034

Mulch, A., Sarna-Wojcicki, A.M., Perkins, M.E., Chamberlain, C.P., 2008. A Miocene to

Pleistocene climate and elevation record of the Sierra Nevada (California). Proc. Natl. Acad. Sci. 105, 6819–6824. https://doi.org/10.1073/pnas.0708811105
Müller, I.A., Fernandez, A., Radke, J., van Dijk, J., Bowen, D., Schwieters, J., Bernasconi, S.M., 2017. Carbonate clumped isotope analyses with the long-integration dual-inlet (LIDI) workflow: scratching at the lower sample weight boundaries. Rapid Commun. Mass Spectrom. 31. https://doi.org/10.1002/rcm.7878
Myers, T.S., Tabor, N.J., Jacobs, L.L., Bussert, R., 2016. Effects of Different Organic-Matter Sources On Estimates of Atmospheric and Soil p CO 2 Using Pedogenic Carbonate . J. Sediment. Res. 86, 800–812. https://doi.org/10.2110/jsr.2016.52
Nativ, R., Riggio, R., 1990. Precipitation in the Southern High Plains: meteorologic and isotopic features. J. Geophys. Res. 95.
Nielsen, L.C., DePaolo, D.J., De Yoreo, J.J., 2012. Self-consistent ion-by-ion growth model for kinetic isotopic fractionation during calcite precipitation. Geochim. Cosmochim. Acta 86, 166–181. https://doi.org/10.1016/j.gca.2012.02.009
Nordt, L.C., Atchley, S.C., Dworkin, S.I., 2003. Terrestrial evidence for two greenhouse events in the latest Cretaceous. GSA Today 13, 4–9. https://doi.org/10.1130/1052-5173(2003)013<4:TEFTGE>2.0.CO;2
Nordt, L.C., Dworkin, S.I., Atchley, S.C., 2011. Ecosystem response to soil biogeochemical behavior during the Late Cretaceous and early Paleocene within the western interior of North America. Bull. Geol. Soc. Am. 123, 1745–1762. https://doi.org/10.1130/B30365.1
Noy-Meir, I., 1973. Desert Ecosystems: Environment and Producers. Annu. Rev. Ecol. Syst. 25–51.
Oerter, E.J., Amundson, R.G., 2016. Climate controls on spatial temporal variations in the formation of pedogenic carbonate in the western Great Basin of North Americ. Bull. Geol. Soc. Am. 128, 1095–1104. https://doi.org/10.1130/B31367.1
Olack, G.A., Colman, A.S., 2016. Influence of 17 O correction parameters on calculation and calibration of Δ 47, in: Goldschmidt.
Oshun, J., Dietrich, W.E., Dawson, T.E., Fung, I., 2015. Dynamic, structured heterogeneity of water isotopes inside hillslopes. Water Resour. Res. 2616–2633. https://doi.org/10.1002/2015WR017485
Pagani, M., Caldeira, K., Archer, D.E., Zachos, J.C., 2006. An Ancient Carbon Mystery. Science 314, 1556–1557.
Pagani, M., Zachos, J.C., Freeman, K.H., Tipple, B.J., Bohaty, S.M., 2005. Marked Decline in Atmospheric Carbon Dioxide Concentrations During the Paleogene. Science (80-.). 309, 600–603. https://doi.org/10.1126/science.1110063
Page, M., Licht, A., Dupont-Nivet, G., Meijer, N., Barbolini, N., Hoorn, C., Schauer, A.J., Huntington, K.W., Bajnai, D., Fiebig, J., Mulch, A., Guo, Z., 2019. Synchronous cooling and decline in monsoonal rainfall in northeastern Tibet during the fall into the Oligocene icehouse. Geology 47, 203–206. https://doi.org/10.1130/g45480.1
Passey, B.H., 2012. Reconstructing Terrestrial Environments Using Stable Isotopes in Fossil Teeth and Paleosol Carbonates. Paleontol. Soc. Pap. 18.
Passey, B.H., Henkes, G.A., 2012. Carbonate clumped isotope bond reordering and geospeedometry. Earth Planet. Sci. Lett. 351–352, 223–236. https://doi.org/10.1016/j.epsl.2012.07.021
Passey, B.H., Levin, N.E., Cerling, T.E., Brown, F.H., Eiler, J.M., 2010. High-temperature environments of human evolution in East Africa based on bond ordering in paleosol

carbonates. Proc. Natl. Acad. Sci. U. S. A. 107, 11245–9. https://doi.org/10.1073/pnas.1001824107

Pearson, P.N., Ditchfield, P.W., Singano, J.M., Harcourt-Brown, K.G., Nicholas, C.J., Olsson, R.K., Shackleton, N.J., Hall, M.A., 2001. Warm tropical sea surface temperatures in the Late Cretaceous and Eocene epochs. Nature 413, 481–487. https://doi.org/10.1038/35097000

Pearson, P.N., Van Dongen, B.E., Nicholas, C.J., Pancost, R.D., Schouten, S., Singano, J.M., Wade, B.S., 2007. Stable warm tropical climate through the Eocene Epoch. Geology 35, 211–214. https://doi.org/http://dx.doi.org/10.1130/G23175A.1

Pendergrass, A.G., Knutti, R., 2018. The uneven nature of daily precipitation and its change. Geophys. Res. Lett. 1–9. https://doi.org/10.1029/2018GL080298

Peppe, D.J., Royer, D.L., Cariglino, B., Oliver, S.Y., Newman, S., Leight, E., Enikolopov, G., Fernandez-Burgos, M., Herrera, F.A., Adams, J.M., Correa, E., Currano, E.D., Erickson, J.M., Hinojosa, L.F., Hoganson, J.W., Iglesias, A., Jaramillo, C.A., Johnson, K.R., Jordan, G.J., Kraft, N.J.B., Lovelock, E.C., Lusk, C.H., Niinemets, Ü., Peñuelas, J., Rapson, G., Wing, S.L., Wright, I.J., 2011. Sensitivity of leaf size and shape to climate: Global patterns and paleoclimatic applications. New Phytol. 190, 724–739. https://doi.org/10.1111/j.1469-8137.2010.03615.x

Peral, M., Daëron, M., Blamart, D., Bassinot, F., Dewilde, F., Smialkowski, N., Isguder, G., Bonnin, J., Jorissen, F., Kissel, C., Michel, E., Vázquez Riveiros, N., Waelbroeck, C., 2018. Updated calibration of the clumped isotope thermometer in planktonic and benthic foraminifera. Geochim. Cosmochim. Acta 239, 1–16. https://doi.org/10.1016/j.gca.2018.07.016

Peters, N.A., Huntington, K.W., Hoke, G.D., 2013. Hot or not? Impact of seasonally variable soil carbonate formation on paleotemperature and O-isotope records from clumped isotope thermometry. Earth Planet. Sci. Lett. 361, 208–218. https://doi.org/10.1016/j.epsl.2012.10.024

Petersen, S. V., Defliese, W.F., Saenger, C., Daëron, M., Huntington, K.W., John, C.M., Kelson, J.R., Bernasconi, S.M., Colman, A.S., Kluge, T., Olack, G.A., Schauer, A.J., Bajnai, D., Bonifacie, M., Breitenbach, S.F.M., Fiebig, J., Fernandez, A., Henkes, G.A., Hodell, D.A., Katz, A., Winkelstern, I.Z., Kele, S., Lohmann, K.C., Passey, B.H., Petrizzo, D.A., Rosenheim, B.E., Tripati, A.K., Venturelli, R., Young, E.D., Wacker, U., 2019. Effects of Improved 17O Correction on Inter-Laboratory Agreement in Clumped Isotope Calibrations, Estimates of Mineral-Specific Offsets, and Acid Fractionation Factors. Geochemistry, Geophys. Geosystems.

Petersen, S. V., Winkelstern, I.Z., Lohmann, K.C., Meyer, K.W., 2015. The effects of Porapak(TM) trap temperature on d18O, d13C, and D47 values in preparing samples for clumped isotope analysis. Rapid Commun. Mass Spectrom. 30, 1–10. https://doi.org/10.1002/rcm.7438

Petrizzo, D.A., Young, E.D., 2014. High-precision determination of 13C–18O bonds in CO2 using multicollector peak hopping. Rapid Commun. Mass Spectrom. 28, 1185–1193. https://doi.org/10.1002/rcm.6888

Petrizzo, D.A., Young, E.D., Runnegar, B.N., 2014. Implications of high-precision measurements of 13C–18O bond ordering in CO2 for thermometry in modern bivalved mollusc shells. Geochim. Cosmochim. Acta 142, 400–410. https://doi.org/10.1016/j.gca.2014.07.017

Philpotts, A.R., 1990. Principles of igneous and metamorphic petrology, Prentice Hall. Englewood Cliffs, New Jersey.
Pross, J., Contreras, L., Bijl, P.K., Greenwood, D.R., Bohaty, S.M., Schouten, S., Bendle, J.A.P., Röhl, U., Tauxe, L., Raine, J.I., Huck, C.E., Van De Flierdt, T., Jamieson, S.S.R., Stickley, C.E., Van De Schootbrugge, B., Escutia, C., Brinkhuis, H., Klaus, A., Fehr, A., Williams, T., Carr, S.A., Dunbar, R.B., Gonzèlez, J.J., Hayden, T.G., Iwai, M., Jimenez-Espejo, F.J., Katsuki, K., Soo Kong, G., Mc Kay, R.M., Nakai, M., Olney, M.P., Passchier, S., Pekar, S.F., Riesselman, C.R., Sakai, T., Shrivastava, P.K., Sugisaki, S., Tuo, S., Welsh, K., Yamane, M., 2012. Persistent near–tropical warmth on the antarctic continent during the early Eocene epoch. Nature 488, 73–77. https://doi.org/10.1038/nature11300
Quade, J., Breecker, D.O., Daeron, M., Eiler, J.M., 2011. The paleoaltimetry of Tibet: An isotopic perspective. Am. J. Sci. 311, 77–115. https://doi.org/10.2475/02.2011.01
Quade, J., Cater, J.M.L., Ojha, T.P., Adam, J., Harrison, T.M., Erdei, B., Hir, J., 1995. Late Miocene environmental change in Nepal and the northern Indian subcontinent; stable isotopic evidence from Paleosols\nVegetation and climate reconstruction of Sarmatian (middle Miocene) sites from NE and W Hungary 107, 1381–1397.
Quade, J., Cerling, T.E., Bowman, J.R., 1989. Systematic variations in the carbon and oxygen isotopic composition of pedogenic carbonate along elevation trasects in the southern Great Basin, United States. Geol. Soc. Am. Bull. 101, 464–475. https://doi.org/10.1130/0016-7606(1989)101<0464:SVITCA>2.3.CO;2
Quade, J., Eiler, J.M., Daëron, M., Achyuthan, H., 2013. The clumped isotope geothermometer in soil and paleosol carbonate. Geochim. Cosmochim. Acta 105, 92–107. https://doi.org/10.1016/j.gca.2012.11.031
Quade, J., Garzione, C.N., Eiler, J.M., 2007a. Paleoelevation Reconstruction using Pedogenic Carbonates. Rev. Mineral. Geochemistry 66, 53–87. https://doi.org/10.2138/rmg.2007.66.3
Quade, J., Rech, J.A., Latorre, C., Betancourt, J.L., Gleeson, E., Kalin, M.T.K., 2007b. Soils at the hyperarid margin: The isotopic composition of soil carbonate from the Atacama Desert, Northern Chile. Geochim. Cosmochim. Acta 71, 3772–3795. https://doi.org/10.1016/j.gca.2007.02.016
Radcliffe, D.E., Šimůnek, J., 2010. Soil physics with HYDRUS: Modeling and applications. CRC press.
Rapp, S.D., MacFadden, B.J., Schiebout, J.A., 1983. Magnetic Polarity Stratigraphy of the Early Tertiary Black Peaks Formation , Big Bend National Park , Texas. J. Geol. 91, 555–572.
Reddy, M.M., 1995. Carbonate Precipitation in Pyramid Lake, Nevada, Mineral Scale Formation and Inhibition.
Reheis, M.C., 2006. A 16-year record of eolian dust in Southern Nevada and California, USA: Controls on dust generation and accumulation. J. Arid Environ. 67, 487–520. https://doi.org/10.1016/J.JARIDENV.2006.03.006
Reheis, M.C., Shroba, R.R., Harden, J.W., McFadden, L.D., 1989. Development rates of late Quaternary soils, Silver Lake playa, California. Soil Sci. Soc. Am. J. 53, 1127–1140.
Retallack, G.J., 2009. Refining a pedogenic-carbonate CO2 paleobarometer to quantify a middle Miocene greenhouse spike. Palaeogeogr. Palaeoclimatol. Palaeoecol. 281, 57–65. https://doi.org/10.1016/J.PALAEO.2009.07.011
Retallack, G.J., 2007. Cenozoic Paleoclimate on Land in North America. J. Geol. 115, 271–294. https://doi.org/10.1086/512753
Retallack, G.J., 2005. Pedogenic carbonate proxies for amount and seasonality of precipitation in

paleosols. Geology 33, 333–336. https://doi.org/10.1130/G21263.1
Ringham, M.C., Hoke, G.D., Huntington, K.W., Aranibar, J.N., 2016. Influence of vegetation type and site-to-site variability on soil carbonate clumped isotope records, Andean piedmont of Central Argentina (32–34°S). Earth Planet. Sci. Lett. 440, 1–11. https://doi.org/10.1016/j.epsl.2016.02.003
Roberts, C.D., LeGrande, A.N., Tripati, A.K., 2009. Climate sensitivity to Arctic seaway restriction during the early Paleogene. Earth Planet. Sci. Lett. 286, 576–585. https://doi.org/10.1016/j.epsl.2009.07.026
Rohling, E.J., Sluijs, A., Dijkstra, H.A., Köhler, P., Van De Wal, R.S.W., Von Der Heydt, A.S., Beerling, D.J., Berger, A., Bijl, P.K., Crucifix, M., Deconto, R.M., Drijfhout, S.S., Fedorov, A., Foster, G.L., Ganopolski, A., Hansen, J., Hönisch, B., Hooghiemstra, H., Huber, M., Huybers, P., Knutti, R., Lea, D., Lourens, L.J., Lunt, D.J., Masson-Delmotte, V., Medina-Elizalde, M., Otto-Bliesner, B.L., Pagani, M., Pälike, H., Renssen, H., Royer, D.L., Siddall, M., Valdes, P.J., Zachos, J.C., Zeebe, R.E., 2012. Making sense of palaeoclimate sensitivity. Nature 491, 683–691. https://doi.org/10.1038/nature11574
Ross, S.M., 2003. Peirce's criterion for the elimination of suspect experimental data. J. Eng. Technol. 20, 1–12.
Rothstein, D., Manning, C., 2003. Geothermal gradients in continental magmatic arcs: Constraints from the eastern Peninsular Ranges batholith, Baja California, México. Geol. Soc. Am. Spec. Pap. 337–354. https://doi.org/10.1130/0-8137-2374-4.337
Royer, D.L., Donnadieu, Y., Park, J., Kowalczyk, J., Goddéris, Y., 2014. Error analysis of CO2 and O2 estimates from the long-term geochemical model GEOCARBSULF. Am. J. Sci. 314, 1259–1283. https://doi.org/10.2475/09.2014.01
Royer, D.L., Osborne, C.P., Beerling, D.J., 2002. High CO2 increases the freezing sensitivity of plants : Implications for paleoclimatic reconstructions from fossil floras. Geology 30, 963–966. https://doi.org/10.1130/0091-7613(2002)030<0963
Rozanski, K., Araguás-Araguás, L., Gonfiantini, R., 1993. Isotopic Patterns in Modern Global Precipitation. Clim. Chang. Cont. Isot. Rec. 1–36. https://doi.org/10.1029/GM078p0001
Saenger, C., Affek, H.P., Felis, T., Thiagarajan, N., Lough, J.M., Holcomb, M., 2012. Carbonate clumped isotope variability in shallow water corals: Temperature dependence and growth-related vital effects. Geochim. Cosmochim. Acta 99, 224–242. https://doi.org/10.1016/j.gca.2012.09.035
Sagoo, N., Valdes, P.J., Flecker, R., Gregoire, L.J., 2013. The Early Eocene equable climate problem: can perturbations of climate model parameters identify possible solutions? Philos. Trans. A. Math. Phys. Eng. Sci. 371, 20130123. https://doi.org/10.1098/rsta.2013.0123
Sándor, R., Fodor, N., 2012. Simulation of Soil Temperature Dynamics with Models Using Different Concepts. Sci. World J. 2012, 1–8. https://doi.org/10.1100/2012/590287
Santrock, J., Studley, S.A., Hayes, J.M., 1985. Isotopic analyses based on the mass spectrum of carbon dioxide. Anal. Chem. 57, 1444–1448. https://doi.org/10.1021/ac00284a060
Schauble, E.A., Ghosh, P., Eiler, J.M., 2006. Preferential formation of 13C–18O bonds in carbonate minerals, estimated using first-principles lattice dynamics. Geochim. Cosmochim. Acta 70, 2510–2529. https://doi.org/10.1016/j.gca.2006.02.011
Schauer, A.J., Kelson, J.R., Saenger, C., Huntington, K.W., 2016. Choice of 17O correction affects clumped isotope (Δ47) values of CO2 measured with mass spectrometry. Rapid Commun. Mass Spectrom. 30, 2607–2616. https://doi.org/10.1002/rcm.7743
Schiebout, J.A., Rigsby, C.A., Rapp, S.D., Hartnell, J.A., Standhardt, B.R., 1987. Stratigraphy of

the Cretaceous-Tertiary and Paleocene-Eocene Transition Rocks of Big Bend National Park, Texas. J. Geol. 95, 359–375.
Schmidt, D.R., 2009. Stable Isotope Geochemistry of Upper Cretaceous and Paleocene strata in Big Bend National Park, Texas. Dissertation. Texas Tech University.
Schmitz, B., Pujalte, V., 2007. Abrupt increase in seasonal extreme precipitation at the Paleocene-Eocene boundary. Geology 35, 215–218.
Schubert, B.A., Jahren, A.H., Eberle, J.J., Sternberg, L.S.L., Eberth, D.A., 2012. A summertime rainy season in the Arctic forests of the Eocene. Geology 40, 523–526. https://doi.org/10.1130/G32856.1
Seneviratne, S.I., Corti, T., Davin, E.L., Hirschi, M., Jaeger, E.B., Lehner, I., Orlowsky, B., Teuling, A.J., 2010. Investigating soil moisture–climate interactions in a changing climate: A review. Earth-Science Rev. 99, 125–161. https://doi.org/10.1016/J.EARSCIREV.2010.02.004
Sewall, J.O., Sloan, L.C., 2006. Come a little bit closer: A high-resolution climate study of the early Paleogene Laramide foreland. Geology 34, 81–84. https://doi.org/10.1130/G22177.1
Sewall, J.O., Sloan, L.C., 2001. Equable paleogene climates: The result of a stable, positive Arctic Oscillation? Geophys. Res. Lett. 28, 3693–3695. https://doi.org/10.1029/2001GL013776
Sharman, G.R., Covault, J.A., Stolper, D.A., Wroblewski, A.F.J., Bush, M.A., 2017. Early Cenozoic drainage reorganization of the United States Western Interior-Gulf of Mexico sediment routing system. Geology 45, 187–190. https://doi.org/10.1130/G38765.1
Sheldon, N.D., Retallack, G.J., Tanaka, S., 2002. Geochemical Climofunctions from North American Soils and Application to Paleosols across the Eocene-Oligocene Boundary in Oregon. J. Geol. 110, 687–696. https://doi.org/10.1086/342865
Sheldon, N.D., Tabor, N.J., 2009. Quantitative paleoenvironmental and paleoclimatic reconstruction using paleosols. Earth-Science Rev. 95, 1–52. https://doi.org/10.1016/j.earscirev.2009.03.004
Shellito, C.J., Lamarque, J., Sloan, L.C., 2009. Early Eocene Arctic climate sensitivity to pCO2 and basin geography. Geophys. Res. Lett. 36. https://doi.org/10.1029/2009GL037248
Shellito, C.J., Sloan, L.C., Huber, M., 2003. Climate model sensitivity to atmospheric CO2 levels in the Early-Middle Paleogene. Palaeogeogr. Palaeoclimatol. Palaeoecol. 193, 113–123. https://doi.org/10.1016/S0031-0182(02)00718-6
Sherwood, S.C., Huber, M., 2010. An adaptability limit to climate change due to heat stress. Proc. Natl. Acad. Sci. 107, 9552–9555. https://doi.org/10.1073/pnas.0913352107
Sikes, N.E., Ashley, G.M., 2007. Stable isotopes of pedogenic carbonates as indicators of paleoecology in the Plio-Pleistocene (upper Bed I), western margin of the Olduvai Basin, Tanzania. J. Hum. Evol. 53, 574–594. https://doi.org/10.1016/j.jhevol.2006.12.008
Šimůnek, J., Sejna, M., Saito, H., Sakai, M., van Genuchten, M.T., 2009. The HYDRUS 1D Software Package for Simulating the One-Dimensional Movement of Water, Heat, and Multiple Solutes in Variably-Saturated Media, Environmental Sciences. https://doi.org/10.1007/978-3-319-40238-3_60
Šimůnek, J., van Genuchten, M.T., Sejna, M., 2012. HYDRUS: Model Use, Calibration, and Validation. Trans. Am. Soc. Agric. Biol. Eng. 55, 1261–1274. https://doi.org/10.1080/19425120.2013.860065
Sloan, L.C., 1994. Equable climates during the early Eocene: significance of regional paleogeography for North American climate. Geology 22, 881–884.

https://doi.org/10.1130/0091-7613(1994)022<0881:ECDTEE>2.3.CO
Sloan, L.C., Barron, E.J., 1990. "Equable" climates during Earth history? Geology 18, 489–492. https://doi.org/10.1130/0091-7613(1990)018<0489:ECDEH>2.3.CO;2
Sluijs, A., Röhl, U., Schouten, S., Brumsack, H.-J., Sangiorgi, F., Damsté, J.S.S., Brinkhuis, H., 2008. Arctic late Paleocene–early Eocene paleoenvironments with special emphasis on the Paleocene-Eocene thermal maximum (Lomonosov Ridge, Integrated Ocean Drilling Program Expedition 302). Paleoceanography 23. https://doi.org/10.1029/2007PA001495
Sluijs, A., Schouten, S., Donders, T.H., Schoon, P.L., Röhl, U., Reichart, G.-J., Sangiorgi, F., Kim, J.-H., Sinninghe Damsté, J.S., Brinkhuis, H., 2009. Warm and wet conditions in the Arctic region during Eocene Thermal Maximum 2. Nat. Geosci. 2, 777. https://doi.org/http://dx.doi.org/10.1038/ngeo668
Sluijs, A., Schouten, S., Pagani, M., Woltering, M., Brinkhuis, H., Damsté, J.S.S., Dickens, G.R., Huber, M., Reichart, G.-J., Stein, R., Matthiessen, J., Lourens, L.J., Pedentchouk, N., Backman, J., Moran, K., Clemens, S., Cronin, T.M., Eynaud, F., Gattacceca, J., Jakobsson, M., Jordan, R., Kaminski, M., King, J., Koc, N., Martinez, N.C., McInroy, D., Moore, T.C., O'Regan, M., Onodera, J., Pälike, H., Rea, B., Rio, D., Sakamoto, T., Smith, D.C., St John, K.E.K., Suto, I., Suzuki, N., Takahashi, K., Watanabe, M., Yamamoto, M., 2006. Subtropical Arctic Ocean temperatures during the Palaeocene/Eocene thermal maximum. Nature 441, 610–613. https://doi.org/10.1038/nature04668
Smith, G.A., Wang, Y., Cerling, T.E., Geissman, J.W., 1993. Pleistocene climate in the western United States 691–694.
Smith, M.E., Carroll, A.R., Scott, J.J., Singer, B.S., 2014. Early Eocene carbon isotope excursions and landscape destabilization at eccentricity minima: Green River Formation of Wyoming. Earth Planet. Sci. Lett. 403, 393–406. https://doi.org/10.1016/j.epsl.2014.06.024
Smith, R.Y., Basinger, J.F., Greenwood, D.R., 2009. Depositional setting, fossil flora, and paleoenvironment of the Early Eocene Falkland site, Okanagan Highlands, British Columbia. Can. J. Earth Sci. 46, 811–822. https://doi.org/10.1139/E09-053
Snell, K.E., Koch, P.L., Druschke, P., Foreman, B.Z., Eiler, J.M., 2014. High elevation of the 'Nevadaplano' during the Late Cretaceous. Earth Planet. Sci. Lett. 386, 52–63. https://doi.org/10.1016/j.epsl.2013.10.046
Snell, K.E., Thrasher, B.L., Eiler, J.M., Koch, P.L., Sloan, L.C., Tabor, N.J., 2013. Hot summers in the Bighorn Basin during the early Paleogene. Geology 41, 55–58. https://doi.org/10.1130/G33567.1
Spencer, C., Kim, S.T., 2015. Carbonate clumped isotope paleothermometry: a review of recent advances in CO2 gas evolution, purification, measurement and standardization techniques. Geosci. J. https://doi.org/10.1007/s12303-015-0018-1
Spicer, R.A., Herman, A.B., Liao, W., Spicer, T.E.V., Kodrul, T.M., Yang, J., Jin, J., 2014. Cool tropics in the Middle Eocene: Evidence from the Changchang Flora, Hainan Island, China. Palaeogeogr. Palaeoclimatol. Palaeoecol. 412, 1–16. https://doi.org/10.1016/j.palaeo.2014.07.011
Spicer, R.A., Parrish, J.T., 1990. Late Cretaceous-early Tertiary palaeoclimates of northern high latitudes: a quantitative view. J. Geol. Soc. London. 147, 329–341. https://doi.org/10.1144/gsjgs.147.2.0329
Spooner, P.T., Guo, W., Robinson, L.F., Thiagarajan, N., Hendry, K.R., Rosenheim, B.E., Leng, M.J., 2016. Clumped isotope composition of cold-water corals: A role for vital effects? Geochim. Cosmochim. Acta 179, 123–141. https://doi.org/10.1016/J.GCA.2016.01.023

Sprenger, M., Mcnamara, J.P., Buttle, J., Carey, S.K., Shatilla, N.J., Soulsby, C., 2018. Storage , mixing , and fluxes of water in the critical zone across northern environments inferred by stable isotopes of soil water 1720–1737. https://doi.org/10.1002/hyp.13135

Stephenson, N.L., 1990. Climatic Control of Vegetation Distribution: The Role of the Water Balance. Am. Nat. 135, 649–670. https://doi.org/10.1086/285067

Stinchcomb, G.E., Nordt, L.C., Driese, S.G., Lukens, W.E., Williamson, F.C., Tubbs, J.D., 2016. A data-driven spline model designed to predict paleoclimate using paleosol geochemistry, American Journal of Science. https://doi.org/10.2475/08.2016.02

Stolper, D.A., Eiler, J.M., 2015. The kinetics of solid-state isotope-exchange reactions for clumped isotopes: A study of inorganic calcites and apatites from natural and experimental samples. Am. J. Sci. 315, 363–411. https://doi.org/10.2475/05.2015.01

Suarez, D.L., Rhoades, J.D., 1982. The Apparent Solubility of Calcium Carbonate in Soils 1. Soil Sci. Soc. Am. J. 46, 716–722.

Suarez, D.L., Šimůnek, J., 1997. UNSATCHEM: Unsaturated Water and Solute Transport Model with Equilibrium and Kinetic Chemistry. Soil Sci. Soc. Am. J. 61, 1633. https://doi.org/10.2136/sssaj1997.03615995006100060014x

Suarez, D.L., Šimůnek, J., 1993. Modeling of Carbon Dioxide Transport and Production in Soil. Water Resour. Res. 29, 487–497.

Suarez, M.B., Passey, B.H., Kaakinen, A., 2011. Paleosol carbonate multiple isotopologue signature of active East Asian summer monsoons during the late Miocene and Pliocene. Geology 39, 1151–1154. https://doi.org/10.1130/G32350.1

Tabor, N.J., Myers, T.S., Huffington, R.M., Sciences, E., Gulbranson, E., Rasmussen, C., Sheldon, N.D., 2013. Carbon stable isotope composition of mordern calcatrous soil profiles in California: implications for CO2 reconstructions from calcareous paleosols. SEPM Sepecial Pulication 17–34. https://doi.org/10.2110/sepmsp.104.07

Tan, C.S., Layne, R.E.C., 1993. Irrigation and ground cover management effect on soil temperature in a mature peach orchard. Can. J. Plant Sci. 73, 857–870. https://doi.org/10.4141/cjps93-112

Tan, H., Liu, Z., Rao, W., Jin, B., Zhang, Y., 2017. Understanding recharge in soil-groundwater systems in high loess hills on the Loess Plateau using isotopic data. CATENA 156, 18–29. https://doi.org/10.1016/J.CATENA.2017.03.022

Tang, J., Baldocchi, D.D., 2005. Spatial-temporal variation in soil respiration in an oak-grass savanna ecosystem in California and its partitioning into autotrophic and heterotrophic components. Biogeochemistry 73, 183–207. https://doi.org/10.1007/s10533-004-5889-6

Tang, J., Dietzel, M., Fernandez, A., Tripati, A.K., Rosenheim, B.E., 2014. Evaluation of kinetic effects on clumped isotope fractionation (Δ47) during inorganic calcite precipitation. Geochim. Cosmochim. Acta 134, 120–136. https://doi.org/10.1016/j.gca.2014.03.005

Thiagarajan, N., Adkins, J.F., Eiler, J.M., 2011. Carbonate clumped isotope thermometry of deep-sea corals and implications for vital effects. Geochim. Cosmochim. Acta 75, 4416–4425. https://doi.org/10.1016/j.gca.2011.05.004

Thomas, W., Ursula, R., Barbara, D., K., M.H., C., Z.J., 2011. A complete high-resolution Paleocene benthic stable isotope record for the central Pacific (ODP Site 1209). Paleoceanography 26. https://doi.org/10.1029/2010PA002092

Thrasher, B.L., Sloan, L.C., 2009. Carbon dioxide and the early Eocene climate of western North America. Geology 37, 807–810. https://doi.org/10.1130/G30090A.1

Tierney, J.E., 2012. GDGT Thermometry: Lipid Tools for Reconstructing Paleotemperatures.

Paleontol. Soc. Pap. 18, 115–132.
Tierney, J.E., Sinninghe Damsté, J.S., Pancost, R.D., Sluijs, A., Zachos, J.C., 2017. Eocene temperature gradients. Nat. Geosci. 10, 538–539. https://doi.org/10.1038/ngeo2997
Tindall, J., Flecker, R., Valdes, P.J., Schmidt, D.N., Markwick, P.J., Harris, J., 2010. Modelling the oxygen isotope distribution of ancient seawater using a coupled ocean–atmosphere GCM: Implications for reconstructing early Eocene climate. Earth Planet. Sci. Lett. 292, 265–273. https://doi.org/10.1016/j.epsl.2009.12.049
Tobin, T.S., Schauer, A.J., Lewarch, E., 2011. Alteration of micromilled carbonate δ18O during Kiel Device analysis. Rapid Commun. Mass Spectrom. 25, 2149–52. https://doi.org/10.1002/rcm.5093
Tobin, T.S., Wilson, G.P., Eiler, J.M., Hartman, J.H., 2014. Environmental change across a terrestrial Cretaceous-Paleogene boundary section in eastern Montana, USA, constrained by carbonate clumped isotope paleothermometry. Geology 42, 351–354. https://doi.org/10.1130/G35262.1
Tripati, A.K., Delaney, M.L., Zachos, J.C., Anderson, L.D., Kelly, D.C., Elderfield, H., K., T.A., L., D.M., C., Z.J., D., A.L., C., K.D., Harry, E., 2003. Tropical sea-surface temperature reconstruction for the early Paleogene using Mg/Ca ratios of planktonic foraminifera. Paleoceanography 18. https://doi.org/10.1029/2003PA000937
Tripati, A.K., Eagle, R.A., Thiagarajan, N., Gagnon, A.C., Bauch, H., Halloran, P.R., Eiler, J.M., 2010. 13C–18O isotope signatures and 'clumped isotope' thermometry in foraminifera and coccoliths. Geochim. Cosmochim. Acta 74, 5697–5717. https://doi.org/10.1016/j.gca.2010.07.006
Tripati, A.K., Hill, P.S., Eagle, R.A., Mosenfelder, J.L., Tang, J., Schauble, E.A., Eiler, J.M., Zeebe, R.E., Uchikawa, J., Coplen, T.B., Ries, J.B., Henry, D., 2015. Beyond temperature: Clumped isotope signatures in dissolved inorganic carbon species and the influence of solution chemistry on carbonate mineral composition. Geochim. Cosmochim. Acta 166, 344–371. https://doi.org/10.1016/j.gca.2015.06.021
Turcotte, D., Schubert, G., 2014. Geodynamics. Cambridge University Press.
Turner, K.J., Berry, M.E., Page, W.R., Lehman, T.M., Bohannon, R.G., Scott, R.B., Miggins, D.P., Budahn, J.R., Cooper, R.W., Drenth, B.J., Anderson, E.D., Williams, V.S., 2011. Geologic map of Big Bend National Park, Texas. U.S. Geol. Surv. Sci. Investig. Map 3142 84.
Uchikawa, J., Zeebe, R.E., 2012a. The effect of carbonic anhydrase on the kinetics and equilibrium of the oxygen isotope exchange in the CO 2-H 2O system: Implications for δ 18O vital effects in biogenic carbonates. Geochim. Cosmochim. Acta 95, 15–34. https://doi.org/10.1016/j.gca.2012.07.022
Uchikawa, J., Zeebe, R.E., 2012b. The effect of carbonic anhydrase on the kinetics and equilibrium of the oxygen isotope exchange in the CO2–H2O system: Implications for δ18O vital effects in biogenic carbonates. Geochim. Cosmochim. Acta 95, 15–34. https://doi.org/10.1016/j.gca.2012.07.022
Újvári, G., Kele, S., Bernasconi, S.M., Haszpra, L., Novothny, Á., Bradák, B., 2019. Clumped isotope paleotemperatures from MIS 5 soil carbonates in southern Hungary. Palaeogeogr. Palaeoclimatol. Palaeoecol. 518, 72–81. https://doi.org/10.1016/j.palaeo.2019.01.002
Vachon, R.W., Welker, J.M., White, J.W.C., Vaughn, B.H., 2010. Monthly precipitation isoscapes ($\delta^{18}O$) of the United States: Connections with surface temperatures, moisture source conditions, and air mass trajectories. J. Geophys. Res. Atmos. 115, 1–17.

https://doi.org/10.1029/2010JD014105
Valdes, P.J., 2011. Built for stability. Nat. Geosci. 4, 414–416. https://doi.org/10.1038/ngeo1200
Valdes, P.J., Armstrong, E., Badger, M.P.S., Bradshaw, C.D., Bragg, F., Davies-Barnard, T., Day, J.J., Farnsworth, A., Hopcroft, P.O., Kennedy, A.T., Lord, N.S., Lunt, D.J., Marzocchi, A., Parry, L.M., Roberts, W.H.G., Stone, E.J., Tourte, G.J.L., Williams, J.H.T., 2017. The BRIDGE HadCM3 family of climate models: HadCM3@Bristol v1.0. Geosci. Model Dev. Discuss. 1–42. https://doi.org/10.5194/gmd-2017-16
van Hinsbergen, D.J.J., de Groot, L. V, van Schaik, S.J., Spakman, W., Bijl, P.K., Sluijs, A., Langereis, C.G., Brinkhuis, H., 2015. A Paleolatitude Calculator for Paleoclimate Studies. PLoS One 10, e0126946. https://doi.org/10.1371/journal.pone.0126946
VanDeVelde, J.H., Bowen, G.J., Passey, B.H., Bowen, B.B., 2013. Climatic and diagenetic signals in the stable isotope geochemistry of dolomitic paleosols spanning the Paleocene–Eocene boundary. Geochim. Cosmochim. Acta 109, 254–267. https://doi.org/10.1016/j.gca.2013.02.005
Vargas, R., Allen, M.F., 2008. Diel patterns of soil respiration in a tropical forest after Hurricane Wilma. J. Geophys. Res. Biogeosciences 113. https://doi.org/10.1029/2007JG000620
Vera, C., Higgins, W., Amador, J., Ambrizzi, T., Garreaud, R., Gochis, D., Gutzler, D., Lettenmaier, D., Marengo, J., Mechoso, C.R., Nogues-Paegle, J., Silva Dias, P.L., Zhang, C., 2006. Toward a Unified View of the American Monsoon Systems. Am. Meteorol. Soc. 19, 4977–5000.
von der Heydt, A.S., Dijkstra, H.A., van de Wal, R.S.W., Caballero, R., Crucifix, M., Foster, G.L., Huber, M., Köhler, P., Rohling, E., Valdes, P.J., Ashwin, P., Bathiany, S., Berends, T., van Bree, L.G.J., Ditlevsen, P., Ghil, M., Haywood, A.M., Katzav, J., Lohmann, G., Lohmann, J., Lucarini, V., Marzocchi, A., Pälike, H., Baroni, I.R., Simon, D., Sluijs, A., Stap, L.B., Tantet, A., Viebahn, J., Ziegler, M., 2016. Lessons on Climate Sensitivity From Past Climate Changes. Curr. Clim. Chang. Reports 2, 148–158. https://doi.org/10.1007/s40641-016-0049-3
Wacker, U., Fiebig, J., Schoene, B.R., 2013. Clumped isotope analysis of carbonates: comparison of two different acid digestion techniques. Rapid Commun. Mass Spectrom. 27, 1631–42. https://doi.org/10.1002/rcm.6609
Wacker, U., Fiebig, J., Tödter, J., Schöne, B.R., Bahr, A., Friedrich, O., Tütken, T., Gischler, E., Joachimski, M.M., 2014. Empirical calibration of the clumped isotope paleothermometer using calcites of various origins. Geochim. Cosmochim. Acta 141, 127–144. https://doi.org/10.1016/j.gca.2014.06.004
Wang, X., Conway, W., Burns, R., McCann, N., Maeder, M., 2009. Comprehensive Study of the Hydration and Dehydration Reactions of Carbon Dioxide in Aqueous Solution. J. Phys. Chem. A 114, 1734–1740. https://doi.org/10.1021/jp909019u
Wang, Y., Cerling, T.E., Effland, W.R., 1993. Stable isotope ratios of soil carbonate and soil organic matter as indicators of forest invasion of prairie near Ames, Iowa. Oecologia 95, 365–369.
Wang, Y., McDonald, E. V., Amundson, R.G., McFadden, L.D., Chadwick, O.A., 1996. An isotopic study of soils in chronological sequences of alluvial deposits, Providence Mountains, California. Bull. Geol. Soc. Am. 108, 379–391. https://doi.org/10.1130/0016-7606(1996)108<0379:AISOSI>2.3.CO;2
Wang, Z., Schauble, E.A., Eiler, J.M., 2004. Equilibrium thermodynamics of multiply substituted isotopologues of molecular gases. Geochim. Cosmochim. Acta 68, 4779–4797.

https://doi.org/10.1016/j.gca.2004.05.039
Watford, D., 2015. An early Paleogene Terrestrial Paleoclimate Record from Big Bend National Park, Texas; Insights from Carbonate Clumped Isotope Thermometry. The University of Utah, ProQuest Dissertations Publishing, 2015. 10011603.
Watkins, J.M., Hunt, J.D., 2015. A process-based model for non-equilibrium clumped isotope effects in carbonates. Earth Planet. Sci. Lett. 432, 152–165. https://doi.org/10.1016/j.epsl.2015.09.042
Watkins, J.M., Hunt, J.D., Ryerson, F.J., DePaolo, D.J., 2014. The influence of temperature, pH, and growth rate on the δ18O composition of inorganically precipitated calcite. Earth Planet. Sci. Lett. 404, 332–343. https://doi.org/10.1016/j.epsl.2014.07.036
Watkins, J.M., Nielsen, L.C., Ryerson, F.J., DePaolo, D.J., 2013. The influence of kinetics on the oxygen isotope composition of calcium carbonate. Earth Planet. Sci. Lett. 375, 349–360. https://doi.org/10.1016/j.epsl.2013.05.054
Weijers, J.W.H., Schouten, S., Sluijs, A., Brinkhuis, H., Sinninghe Damsté, J.S., 2007. Warm arctic continents during the Palaeocene-Eocene thermal maximum. Earth Planet. Sci. Lett. 261, 230–238. https://doi.org/10.1016/j.epsl.2007.06.033
West, C.K., Greenwood, D.R., Basinger, J.F., 2015. Was the Arctic Eocene "rainforest" monsoonal? Estimates of seasonal precipitation from early Eocene megafloras from Ellesmere Island, Nunavut. Earth Planet. Sci. Lett. 427, 18–30. https://doi.org/10.1016/j.epsl.2015.06.036
Wheeler, E.A., 1991. Paleocene Dicotyledonous Trees from Big Bend National Park, Texas: Variability in Wood Types Common in the Late Cretaceous and Early Tertiary, and Ecological Inferences. Am. J. Bot. 78, 658–671.
Wheeler, E.A., Lehman, T.M., 2005. Upper Cretaceous-Paleocene conifer woods from Big Bend National Park, Texas. Palaeogeogr. Palaeoclimatol. Palaeoecol. 226, 233–258. https://doi.org/10.1016/j.palaeo.2005.05.014
White, P.D., Schiebout, J.A., 2008. Paleogene paleosols and changes in pedogenesis during the initial Eocene thermal maximum: Big Bend National Park, Texas, USA. Bull. Geol. Soc. Am. 120, 1347–1361. https://doi.org/10.1130/B25987.1
White, W., 2003. Isotope Geochemistry. Geochemistry Lect. Ser. 90–95. https://doi.org/10.1126/science.1064051
Wilf, P., Wing, S.L., Greenwood, D.R., Greenwood, C.L., 1998. Using fossil leaves as paleoprecipitation indicators : An Eocene example 1998–1999.
Wing, S.L., Greenwood, D.R., 1993. Fossils and fossil climate: The case for equable continental interiors in the Eocene. Philos. Trans. R. Soc. London B Biol. Sci. 341, 243–252. https://doi.org/10.1098/rstb.1993.0109
Wing, S.L., Harrington, G.J., Smith, F.A., Bloch, J.I., Boyer, D.M., Freeman, K.H., 2005. Transient Floral Change and Rapid Global Warming at the Paleocene-Eocene Boundary. Science 310, 993–996.
Wing, S.L., Herrera, F.A., Jaramillo, C.A., Gomez-Navarro, C., Wilf, P., Labandeira, C.C., 2009. Late Paleocene fossils from the Cerrejon Formation, Colombia, are the earliest record of Neotropical rainforest. Proc. Natl. Acad. Sci. 106, 18627–18632. https://doi.org/10.1073/pnas.0905130106
Winguth, A.M.E., Shellito, C.J., Shields, C., Winguth, C., 2010. Climate response at the Paleocene-Eocene thermal maximum to greenhouse gas forcing-a model study with CCSM3. J. Clim. 23, 2562–2584. https://doi.org/10.1175/2009JCLI3113.1

Wolfe, J.A., 1995. Paleoclimatic Estimates From Tertiary Leaf Assemblages. Annu. Rev. Earth Planet. Sci. 23, 119–42.
Yang, H., Pancost, R.D., Jia, C., Xie, S., 2016. The Response of Archaeal Tetraether Membrane Lipids in Surface Soils to Temperature: A Potential Paleothermometer in Paleosols. Geomicrobiol. J. 33, 98–109. https://doi.org/10.1080/01490451.2014.1002956
Yeung, L.Y., Hayles, J.A., Hu, H., Ash, J.L., Sun, T., 2018. Scale distortion from pressure baselines as a source of inaccuracy in triple-isotope measurements. Rapid Commun. Mass Spectrom. 32, 1811–1821. https://doi.org/10.1002/rcm.8247
York, D., Evensen, N.M., Martínez, M.L., De Basabe Delgado, J., 2004. Unified equations for the slope, intercept, and standard errors of the best straight line. Am. J. Phys. 72, 367. https://doi.org/10.1119/1.1632486
Young, M.H., Caldwell, T.G., Meadows, D.G., Fenstermaker, L.F., 2009. Variability of soil physical and hydraulic properties at the Mojave Global Change Facility, Nevada: Implications for water budget and evapotranspiration. J. Arid Environ. 73, 733–744. https://doi.org/10.1016/j.jaridenv.2009.01.015
Zaarur, S., Affek, H.P., Brandon, M.T., 2013. A revised calibration of the clumped isotope thermometer. Earth Planet. Sci. Lett. 382, 47–57. https://doi.org/10.1016/j.epsl.2013.07.026
Zaarur, S., Olack, G.A., Affek, H.P., 2011. Paleo-environmental implication of clumped isotopes in land snail shells. Geochim. Cosmochim. Acta 75, 6859–6869. https://doi.org/10.1016/J.GCA.2011.08.044
Zachos, J.C., Dickens, G.R., Zeebe, R.E., 2008. An early Cenozoic perspective on greenhouse warming and carbon-cycle dynamics. Nature 451, 279–283.
Zachos, J.C., Pagani, M., Sloan, L.C., Thomas, E., Billups, K., 2001. Trends, Global Rhythms, Aberrations in Global Climate 65Ma to Present. Science (80-.). 292, 686–693. https://doi.org/10.1126/science.1059412
Zamanian, K., Pustovoytov, K., Kuzyakov, Y., 2016. Pedogenic carbonates: Forms and formation processes. Earth-Science Rev. 157, 1–17. https://doi.org/10.1016/j.earscirev.2016.03.003
Zeebe, R.E., 2011. Where are you heading Earth? Nat. Geosci. 4, 416–417. https://doi.org/10.1038/ngeo1196
Zeebe, R.E., 2007. An expression for the overall oxygen isotope fractionation between the sum of dissolved inorganic carbon and water. Geochemistry, Geophys. Geosystems 8, 1–7. https://doi.org/10.1029/2007GC001663
Zeebe, R.E., 1999. An explanation of the effect of seawater carbonate concentration on foraminiferal oxygen isotopes. Geochim. Cosmochim. Acta 63, 2001–2007. https://doi.org/10.1016/S0016-7037(99)00091-5
Zhang, T., 2005. Influence of the seasonal snow cover on the ground thermal regime: an overview. Rev. Geophys. 43. https://doi.org/10.1029/2004RG000157

Appendix A. Supplementary materials to Chapter 2

A.1 Carbonic Anhydrase (CA) Activity Test

In order to ascertain that the batch of carbonic anhydrase that we attained was effective in our experimental conditions, we measured the isotopic composition of CO_2 gas as it equilibrated with solution identical to the solutions used in the mixed solution and actively degassing precipitation experiments. The $\delta^{18}O$ of the CO_2 gas was measured with a Thermo Finnegan Delta Plus IRMS approximately every 30 minutes until the gas approached equilibrium. The CO_2 gas, which came from a cylinder and started with a $\delta^{18}O$ composition of -19.22 ‰ (SMOW), reached isotopic equilibrium faster when carbonic anhydrase was in solution (Figure A-1). For the tests with experimental solution and CO_2, we observe an equilibration rate of 0.45 ‰/minute with CA and 0.30 ‰/minute without CA. We also equilibrated CO_2 gas with deionized water with and without CA, and again found the CO_2 reached equilibrium faster in the presence of CA. For the tests with just water and CO_2, we observe an equilibration rate of 0.30 ‰/minute with CA and 0.24 ‰/minute without CA.

A.2 Mineralogy and Crystal Size

Mineralogy does not measurably influence the Δ_{47} values of a given sample type, despite differences predicted in theoretical calculations (Guo et al., 2009). Samples of different mineralogy grown at the same temperature have Δ_{47} values that are within measurement error (Figure A-2).

Scanning electron microscope imagery was taken for twenty carbonate samples, including our in-house calcite standard, C64. Most samples displayed rhombic, fine-grained texture (Figure A-3). Aragonitic samples were not included in grain size analyses because of

their spindly texture (Figure A-3). C64 is characterized by a more bimodal grain distribution compared to the synthetic carbonates grown for this work (Figure A-3).

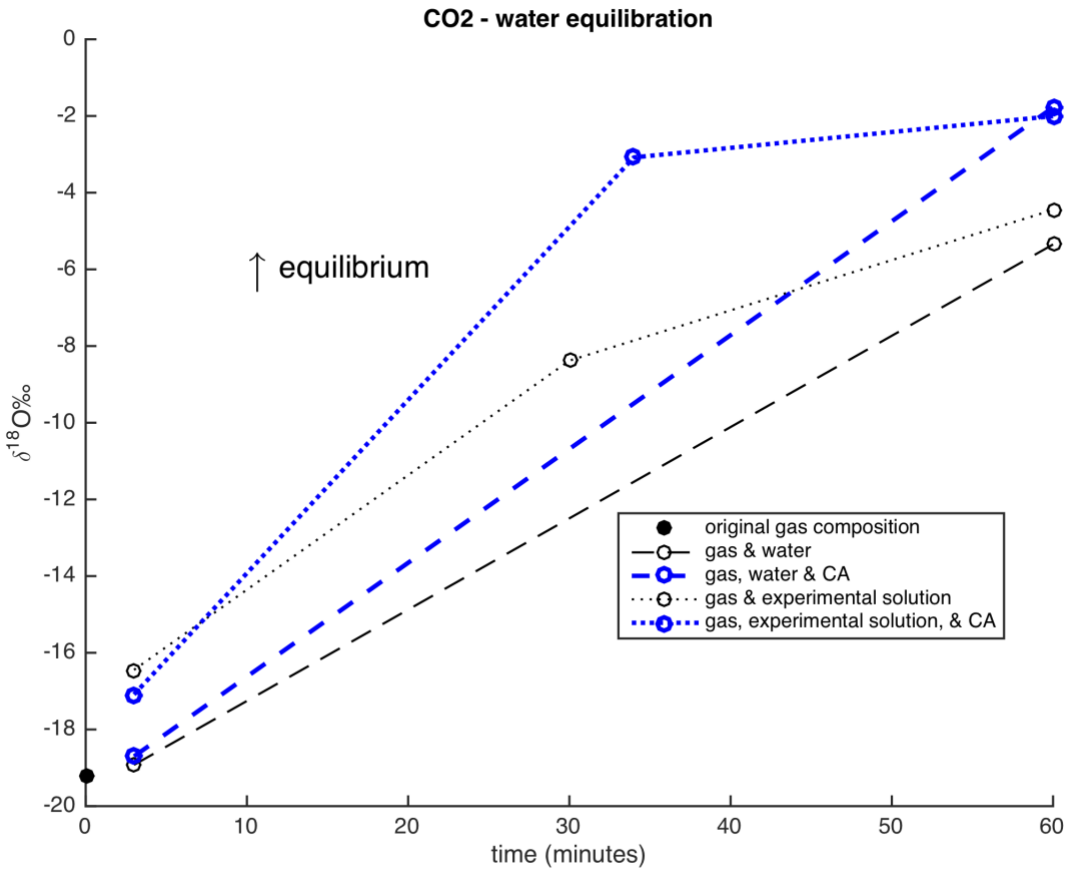

Figure A-1: $\delta^{18}O$ of CO_2 as it isotopically equilibrated, with and without CA

Equilibration for both water and solutions identical to those used in the precipitation experiments.

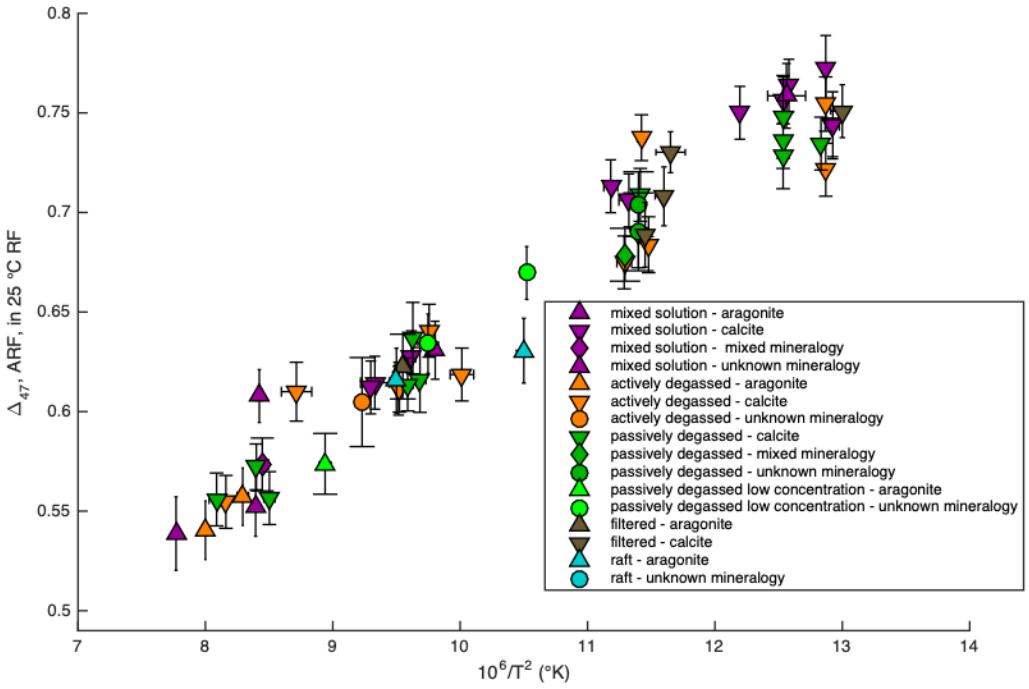

Figure A-2: Mineralogy and Δ_{47} values of synthetic samples from this study.

Symbol indicate mineralogy (up triangle is aragonite, down triangle is calcite, circle is unknown, diamond is mixed mineralogy). Color indicates method used to precipitate the sample.

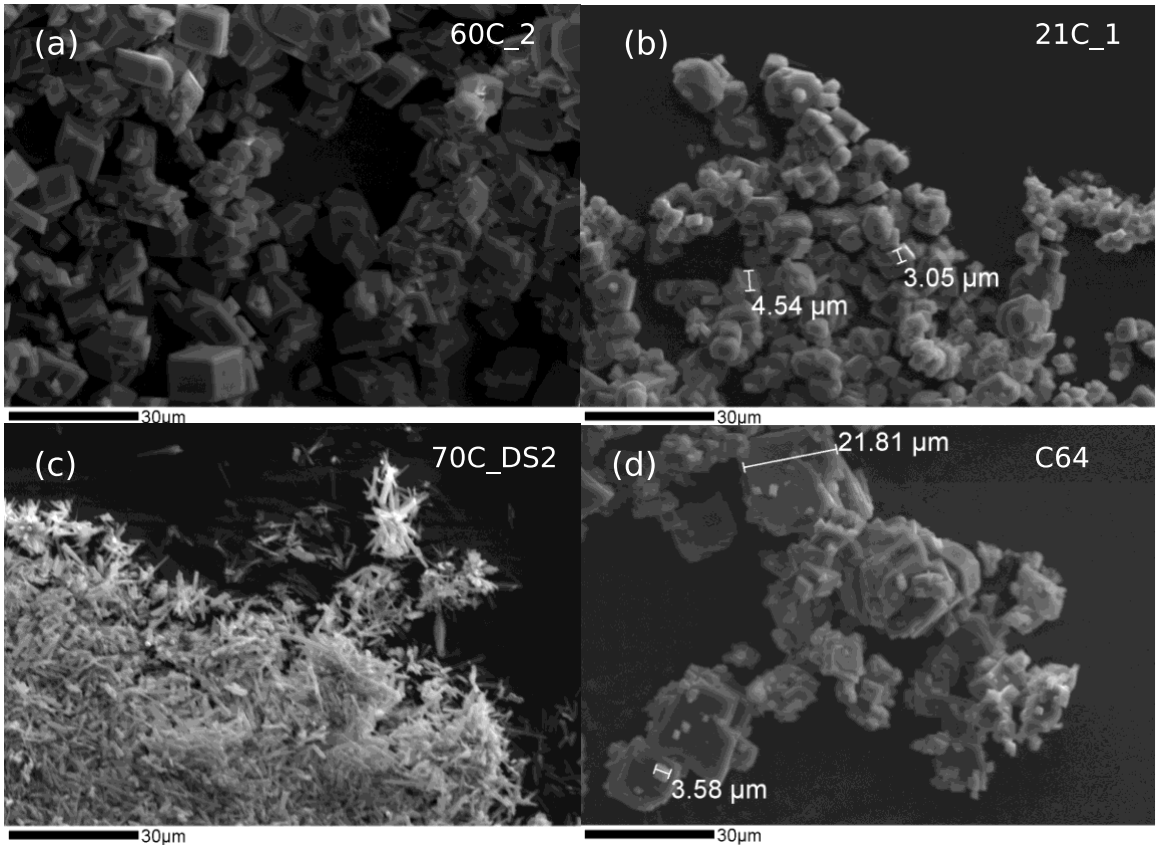

Figure A-3: SEM imagery of select carbonate samples used to measure grain size.

(a) Calcitic sample 60C_2 (actively degassed), **(b)** calcitic sample 21C_1 (actively degassed), **(c)** aragonitic sample 70C_DS2 (mixed solution), and **(d)** in-house synthetic calcite standard, C64. 60C_2, and 21C_1 have the rhombic, fine-grained texture observed in most samples. 70C_DS2 has the aragonitic, fine-grained spindly texture that was also observed. C64 has a bimodal grain sizes with step morphology. The morphology observed in C64 was unique to that carbonate and suggests that a larger range in grain size and carbonate morphology exists than was rigorously tested in this study.

Table A-1: Experimental conditions for synthetic calcite samples

Sample	Precipitation Method	Mean Growth Temp (°C)	S.D. of Temp (°C)	$NaHCO_3$ Molarity (mM)	Molarity $CaCl_2 \cdot H_2O$ (mM)	Molarity CA (in mM)	humidified N_2?	Growing Time (days)	Amount collected (grams)	Solution $\delta^{18}O$ - start, ‰ SMOW	Solution $\delta^{18}O$ - end ‰ SMOW	Solution pH - start	Solution pH - end	Grain Size (d50, in mm)	Morph-ology
UWcp14_4C_2	actively degassed	6	0.05	20	20	NA	no	18	0.84	-10.38	-10.34		7.0		calcite
UWcp14_4C_4	actively degassed	6	0.05	20	20	NA	yes	41	0.8	-9.61	-10.31	6.38	5.85		calcite
UWcp14_21C_1	actively degassed	22	0.22	20	20	NA	no	7	0.75	-10.62		6.75		3.1	calcite
UWcp14_40C_1	actively degassed	43	1.46	20	20	NA	no	1	0.74	-10.86	-10.71	5.36	8.13	4.7	calcite
UWcp14_50C_1	actively degassed	47	0.36	20	20	NA	no	7	0.7	-10.61	-10.54	7.62	8.19	4.7	calcite
UWcp14_50C_2	actively degassed	51	0.36	20	20	NA	no	4	0.82	-10.61	-10.59	7.78	7.81		calcite
UWcp14_60C_2	actively degassed	66	2.31	20	20	NA	no	2	0.80	-10.45	-10.4	6.70	7.08	4.2	calcite
UWcp14_80C_1	actively degassed	77	0.36	20	20	NA	no	3	0.92	-10.38	-10.45	8.27	7.79	4.0	calcite
UWcp14_80C_3	actively degassed	80	0.64	20	20	NA	no	4	0.93	-10.29	-10.22	6.65	7.82		aragonite (97.6%), calcite (2.4%)
UWcp14_24C_CA_1	actively degassed	24	0.76	20	20	25	no		0.25	-10.75	-10.78	7.70	7.58	3.7	calcite
UWcp14_20C_CA_16	actively degassed	23	0.42	20	20	24	yes	6	0.75			6.00	7.01		calcite
UWcp14_50C_CA_3	actively degassed	56	0.63	20	20	25	no	4	0.74	-10.69	-10.68	7.42	8.12		

UWcp14_70C_CA_1	actively degassed	74	0.95	20	20	25	no	2	0.88	-10.74	-10.58	7.54	8.16	7.0	aragonite
UWcp14_4C_3	passively degassed	6	0.05	20	20	NA	no	42	0.82	-9.91	-10.40	6.57	6.61		calcite
UWcp14_8C_2	passively degassed	9	0.12	20	20	NA	no	24	0.83	-10.28	-10.23	5.90			calcite
UWcp14_8C_3	passively degassed	9	0.12	20	20	NA	no	17	0.80	-10.16	-10.32		6.56		calcite
UWcp14_20C_9	passively degassed	23	0.33	20	20	NA	no	2	0.60	-10.51		6.71	7.24	3.6	calcite
UWcp14_20C_4	passively degassed	23	0.33	20	20	NA	no	11	0.08	-10.69	-10.67	7.61			
UWcp14_20C_10	passively degassed	24	0.43	20	20	NA	no	4	0.43	-10.68	-10.62	6.67	7.77		calcite (55.7%), vaterite (44.3%)
UWcp14_50C_5	passively degassed	48	0.77	20	20	NA	no	2	0.8	-10.51	-10.46	6.80	7.52	4.5	calcite
UWcp14_50C_3	passively degassed	49	0.12	20	20	NA	no	1	0.67	-10.43	-10.55	6.98	7.01		calcite
UWcp14_70C_4	passively degassed	72	0.43	20	20	NA	no	2	0.82	-10.54	-10.44	6.78	7.44	7.5	calcite
UWcp14_80C_2	passively degassed	78	1.28	20	20	NA	no	1	0.72	-10.42	-10.39	6.61	7.28		calcite
UWcp14_8C_CA_4	passively degassed	9	0.12	20	20	19	yes	34	0.87	-10.48	-10.44	5.71	7.07		calcite
UWcp14_20C_CA_5	passively degassed	23	0.33	20	20	25	no	11	0.05	-10.47	-10.49	7.48	7.62		
UWcp14_20C_CA_11	passively degassed	23	0.34	20	20	25	no	7	0.49	-10.50	-10.46	6.81	8.08	9.0	calcite
UWcp14_50C_CA_10	passively degassed	50	0.74	20	20	25	no	4	0.8	-10.20	-10.18	6.15	6.80	3.9	calite (98%), aragonite (1.7%)
UWcp14_70C_CA_5	passively degassed	70	0.89	20	20	25	no	3	0.86	-10.55	-10.46		7.91	5.9	calcite

UWcp14_35C_1	passively degassed	35	0.71	3.1	3.9		no	8	0.03	-10.63	-10.64	6.01	8.29		
UWcp14_50C_4	passively degassed	47	1.32	3.2	4.0		no	8	0.05		-10.60	6.14	8.15		
UWcp14_60C_1	passively degassed	61	0.86	3.0	3.9		no	6	0.08	-10.55	-10.45	6.15	8.08		aragonite
UWcp14_3C_2	mixed solution	9	1.67	3.1	3.9		no	88	0.04	-10.33	-10.18	8.77	7.09		
UWcp14_4C_1	mixed solution	6	0.05	3.2	4.0		no	35	0.06	-10.20	-9.12		7.20		calcite
UWcp14_4C_5	mixed solution	6	0.05	3.1	4.0		yes	42	0.05	-10.18	-10.04	6.80	7.16		calcite
UWcp14_4C_6	mixed solution	6	0.05	3.1	4.0		yes	20	0.04			7.63	6.89		calcite
UWcp14_8C_1	mixed solution	9	0.12	3.1	4.0		no		0.05	-10.24	-10.19	7.94	6.78		calcite
UWcp14_8C_6	mixed solution	9	0.15	3.2	4.0		yes	34	0.06			6.29	7.60		calcite
UWcp14_20C_DS	mixed solution	26	0.73	3.2	4.0		no	25	0.06	-10.37	-10.01	7.93	7.85	2.8	calcite
UWcp14_50C_7	mixed solution	54	1.98	3.2	4.0		no	4	0.04	-9.86	-10.30	8.54	8.26	6.2	calcite (94.6%), aragonite (5.4%)
UWcp14_50C_8	mixed solution	46	0.33	3.2	4.0		no	4	0.04	-10.37	-10.42	8.54	8.07		
UWcp14_50C_DS	mixed solution	55	0.32	3.1	4.0		no	5	0.06	-10.26	-10.34	8.59	8.22		calcite
UWcp14_50C_DS2	mixed solution	51	0.3	3.1	4.0		no	17	0.07	-10.40	-10.19	8.56	8.51		calcite
UWcp14_70C_DS2	mixed solution	72	0.38	3.1	4.0		no	16	0.09	-10.35	-9.85	8.29	8.73	2.2	aragonite
UWcp14_70C_2	mixed solution	71	0.45	3.2	4.0		no	2	0.10	-10.43	-9.26	8.50	8.28		aragonite
UWcp14_80C_DS	mixed solution	86	0.04	3.1	4.0		no	5	0.08	-10.03	-9.61	8.56	8.38		aragonite

UWcp14_8C_CA_5	mixed solution	13	0.12	3.2	4.0	20	yes	83	0.47	-9.95	-9.89	7.95	7.36		calcite
UWcp14_20C_CA_13	mixed solution	24	1.03	3.2	4.0	20	no	54	0.07	-10.28	-9.58	8.09	7.77		calcite
UWcp14_50C_CA_9	mixed solution	49	0.53	3.2	4.0	25	no	11	0.07	-10.31	-10.49	7.80	7.77	3.7	calcite
UWcp14_70C_CA_4	mixed solution	71	1.00	3.1	4.0	25	no	4	0.06	-10.34	-10.21	8.26	8.61	6.3	calcite (62.6%), aragonite (38.5%)
					Molarity of CaCO3 (mM)										
UWcp14_30C_Z_1	raft, filtered method	36	0.49		<12		yes	9	0.1466			6.10	7.19		aragonite
UWcp14_50C_Z_1	raft, filtered method	50	0.83		<12		yes	3	0.2169			6.40	7.82		aragonite (91.7%), vaterite (8.1%)
UWcp14_4C_Z_3	filtered	4	0.33		<13.2		yes	68	0.0324			5.99	8.00		calcite
UWcp14_20C_Z_15	filtered	20	1.45		<11.2		yes	20	0.3927			6.07	7.20		calcite
UWcp14_20C_G_14	filtered	21	0.49		<6.26		yes	7	0.32	-10.52	-10.63	6.02	7.24		calcite
UWcp14_20C_Z_2	filtered	22	0.17		<10.3		yes	30	0.4306			6.18	6.43		calcite (92.9%), aragonite (7.1%)
UWcp14_50C_Z_2	filtered	50	1		<13.2		yes	9	0.2984			5.94	7.59		aragonite

Table A-2: Isotopic Values of Synthetic Carbonates, processed with Brand et al. (2010) values

Sample	Precipitation Method	$\delta^{13}C$ vpdb ‰	$\delta^{13}C$ SD	$\delta^{18}O$ calcite ‰ VPDB	$\delta^{18}O$ SD	δ_{47} ‰	δ_{47} SD ‰	Δ_{47} ‰ digested in 90 °C (no acid correction)[a]	Number of replicates digested in 90°C acid (n)	Δ_{47} SE ‰ (digested in 90 °C acid) [b]	Δ_{47} ‰ digested in 25 °C (no acid correction)	Number of replicates digested in 25 °C acid (n)	Δ_{47} SE ‰ (digested in 25 °C acid) SE [c]	1000lna calcite water (SMOW)
UWcp14_4C_2	actively degassed	-25.67	0.004	-7.54	0.06	-16.50	0.074	0.6724	3	0.014	0.7577	3	0.012	33.5
UWcp14_4C_4	actively degassed	-23.52	0.017	-6.93	0.04	-13.82	0.037	0.6394	3	0.010				33.7
UWcp14_21C_1	actively degassed	-18.56	0.162	-11.61	0.46	-13.67	0.630	0.6018	3	0.014	0.7049	3	0.012	29.6
UWcp14_40C_1	actively degassed	-16.98	0.046	-15.19	0.10	-15.83	0.049	0.5366	3	0.014				26.0
UWcp14_50C_1	actively degassed	-22.92	0.008	-16.19	0.11	-22.61	0.100	0.5586	3	0.014	0.6413	3	0.032	24.8
UWcp14_50C_2	actively degassed	-18.26	0.045	-16.52	0.15	-18.44	0.134	0.5293	4	0.012				24.5
UWcp14_60C_2	actively degassed	-12.55	0.014	-18.53	0.06	-14.93	0.095	0.5280	3	0.015				22.2
UWcp14_80C_1	actively degassed	-21.13	0.215	-20.44	0.01	-25.26	0.209	0.4727	3	0.014	0.5576	3	0.012	20.3
UWcp14_80C_3	actively degassed	-12.42	0.017	-20.16	0.17	-17.23	0.164	0.4584	3	0.015				20.4

UWcp14_24C_CA_1	actively degassed	-21.04	0.014	-12.00	0.05	-16.50	0.041	0.5929	3	0.014				29.3
UWcp14_20C_CA_16	actively degassed	-18.66	1.083	-11.09	0.11	-13.31	1.164	0.6555	4	0.014				29.9
UWcp14_50C_CA_3	actively degassed	-15.27	0.024	-17.04	0.02	-16.07	0.055	0.5228	3	0.022				24.0
UWcp14_70C_CA_1	actively degassed	-22.31	0.013	-20.46	0.06	-26.72	0.096	0.4753	4	0.014	0.6039	3	0.012	20.5
UWcp14_4C_3	passively degassed	-21.76	0.671	-6.47	0.76	-11.63	0.212	0.6526	3	0.010				34.4
UWcp14_8C_2	passively degassed	-15.08	0.045	-8.15	0.09	-6.86	0.094	0.6660	3	0.021				32.8
UWcp14_8C_3	passively degassed	-16.46	0.023	-8.18	0.01	-8.25	0.010	0.6542	3	0.014				32.7
UWcp14_20C_9	passively degassed	-20.92	0.115	-11.28	0.09	-15.64	0.169	0.6075	3	0.017	0.6867	4	0.010	29.8
UWcp14_20C_4	passively degassed	-15.16	0.031	-10.41	0.05	-9.12	0.102	0.6083	4	0.020				30.9
UWcp14_20C_10	passively degassed	-17.89	0.004	-11.36	0.04	-12.76	0.030	0.5968	3	0.014				29.9
UWcp14_50C_5	passively degassed	-21.89	0.045	-15.85	0.08	-21.28	0.103	0.5339	2	0.017	0.6306	3	0.012	25.1

UWcp14_50C_3	passively degassed	-13.58	0.003	-16.27	0.03	-13.61	0.033	0.5549	3	0.018				24.6
UWcp14_70C_4	passively degassed	-17.67	0.101	-19.07	0.08	-20.53	0.176	0.4902	4	0.012				21.7
UWcp14_80C_2	passively degassed	-6.16	0.025	-20.75	0.03	-11.07	0.011	0.4739	3	0.014				19.9
UWcp14_8C_CA_4	passively degassed	-17.41	0.043	-8.17	0.06	-9.17	0.026	0.6462	2	0.013				32.9
UWcp14_20C_CA_5	passively degassed	-18.55	0.015	-10.67	0.03	-12.69	0.047	0.6222	2	0.017				30.4
UWcp14_20C_CA_11	passively degassed	-13.97	0.014	-11.26	0.00	-8.81	0.024	0.6268	3	0.014				29.8
UWcp14_50C_CA_10	passively degassed	-18.42	0.106	-15.89	0.05	-18.20	0.164	0.5316	3	0.013				24.7
UWcp14_70C_CA_5	passively degassed	-20.32	0.402	-19.40	0.21	-23.41	0.575	0.4746	3	0.014				21.4
UWcp14_35C_1	passively degassed	-23.02	0.013	-14.93	0.03	-21.41	0.048	0.5876	3	0.014				26.2
UWcp14_50C_4	passively degassed	-22.32	0.043	-16.02	0.24	-21.86	0.278	0.5521	3	0.015				25.0

UWcp14_60C_1	passively degassed	-25.45	0.025	-18.03	0.10	-27.30	0.114	0.4918	3	0.015				22.8
UWcp14_3C_2	mixed solution	-1.02	0.006	-8.78	0.03	6.11	0.028	0.6766	2	0.013				32.1
UWcp14_4C_1	mixed solution	0.10	0.007	-8.70	0.01	7.26	0.014	0.6623	2	0.013	0.7915	3	0.018	31.6
UWcp14_4C_5	mixed solution	-1.55	1.117	-7.62	0.41	6.80	0.683	0.6618	3	0.017				33.2
UWcp14_4C_6	mixed solution	-0.01	0.273	-7.81	0.61	8.08	0.383	0.6906	2	0.020				33.3
UWcp14_8C_1	mixed solution	0.03	0.009	-8.85	0.06	7.05	0.085	0.6746	4	0.009				32.0
UWcp14_8C_6	mixed solution	0.40	0.018	-8.88	0.02	7.36	0.043	0.6817	3	0.016				32.2
UWcp14_20C_DS	mixed solution	0.60	0.074	-12.18	0.01	4.06	0.070	0.6312	3	0.010				28.5
UWcp14_50C_7	mixed solution	-0.29	0.007	-17.69	0.05	-2.16	0.054	0.5325	3	0.014				22.8
UWcp14_50C_8	mixed solution	-0.89	0.002	-16.34	0.02	-1.32	0.037	0.5488	3	0.015				24.5
UWcp14_50C_DS	mixed solution	-0.15	0.074	-17.34	0.03	-2.16	0.093	0.5301	3	0.010				23.3
UWcp14_50C_DS2	mixed solution	0.40	0.079	-16.82	0.03	-1.08	0.092	0.5295	3	0.013				23.9
UWcp14_70C_DS2	mixed solution	0.92	0.067	-19.05	0.18	-3.29	0.155	0.4706	3	0.015	0.6041	5	0.010	21.4

UWcp14_70C_2	mixed solution	1.57	0.020	-19.48	0.10	-2.52	0.144	0.5258	3	0.014				20.7
UWcp14_80C_DS	mixed solution	0.75	0.046	-20.36	0.14	-4.84	0.119	0.4567	3	0.019				19.7
UWcp14_8C_CA_5	mixed solution	-1.82	1.413	-9.14	0.32	4.95	1.040	0.6681	3	0.010				31.4
UWcp14_20C_CA_13	mixed solution	-2.03	0.500	-12.01	0.15	1.69	0.321	0.6241	3	0.010	0.7077	2	0.014	28.5
UWcp14_50C_CA_9	mixed solution	-0.24	0.073	-16.76	0.03	-1.62	0.097	0.5453	3	0.010				24.0
UWcp14_70C_CA_4	mixed solution	-0.29	0.041	-19.83	0.04	-4.41	0.047	0.4914	3	0.014	0.5685	2	0.018	20.7
UWcp14_30C_Z_1	raft, filtered method	-23.26	0.350	-12.32	0.63	-19.40	0.292	0.5486	2	0.020				28.8
UWcp14_50C_Z_1	raft, filtered method	-22.99	0.007	-15.51	0.08	-22.42	0.069	0.5336	2	0.020				25.3
UWcp14_4C_Z_3	filtered	-25.32	0.942	-8.07	0.39	-16.61	1.293	0.6689	3	0.016				33.2
UWcp14_20C_Z_15	filtered	-22.68	0.008	-11.03	0.11	-17.11	0.123	0.6482	5	0.013				30.2
UWcp14_20C_Z_2	filtered	-23.74	0.949	-11.43	0.10	-18.57	0.831	0.6261	3	0.016				29.8
UWcp14_20C_G_14	filtered	-24.70	0.011	-11.62	0.01	-19.80	0.014	0.6068	2	0.013				29.5
UWcp14_50C_Z_2	filtered	-24.08	0.625	-15.49	0.06	-23.43	0.517	0.5406	2	0.020				25.1

chicken egg shell		-0.23	0.055	-7.41	0.06	8.57	0.10	0.5760	4	0.014				

[a]Values calculated with Brand et al. (2010) ^{17}O correction parameters.

[b]When the S.D> of the Δ_{47} was lower than the long-term S.D. of C64, SD of C64 was used to calculate S.E. of sample. For the first reference frame, C^4 S.D. = 0.024, for the second reference frame C64 S.D. = 0.028, for the third reference frame C64 S.D. = 0.28.

[c] Where the standard deviation of Δ_{47} of the sample was lower than the S.D. of C64 reacted at 25 °C (S.D. = 0.020), S.D> of C64 was used to calculate S.E. of the sample.

Table A-3: Isotopic Values of Synthetic Carbonates, processed with Santrock et al. (1985) values

Sample	Precipitation Method	$\delta^{13}C$ vpdb ‰	$\delta^{13}C$ SD ‰	$\delta^{18}O$ calcite vpdb ‰	$\delta^{18}O$ SD ‰	δ_{47} ‰	δ_{47} SD ‰	Δ_{47} ‰ digested in 90 °C (no acid correction)[a]	Number of reps digested in 90 °C acid (n	Δ_{47} SE ‰ (digested in 90 °C acid) [b]	Δ_{47} ‰ digested in 25 °C (no acid correction)	number of reps digested in 25 °C acid (n	Δ_{47} SE ‰ (digested in 25 °C acid) SE [c]
UWcp14_4C_2	actively degassed	-25.67	0.00	-7.56	0.06	-16.50	0.07	0.6403	3	0.014	0.7265	3	0.012
UWcp14_4C_4	actively degassed	-23.52	0.02	-6.94	0.04	-13.82	0.04	0.6114	3	0.010			
UWcp14_21C_1	actively degassed	-18.50	0.21	-11.61	0.46	-13.67	0.63	0.5872	3	0.014	0.6867	3	0.012
UWcp14_40C_1	actively degassed	-16.98	0.05	-15.19	0.10	-15.83	0.05	0.5247	3	0.014			
UWcp14_50C_1	actively degassed	-22.91	0.01	-16.10	0.20	-22.61	0.10	0.5365	3	0.014	0.6168	3	0.032
UWcp14_50C_2	actively degassed	-18.25	0.04	-16.52	0.15	-18.44	0.13	0.5153	4	0.012			
UWcp14_60C_2	actively degassed	-12.56	0.01	-18.53	0.06	-14.93	0.10	0.5242	3	0.015			
UWcp14_80C_1	actively degassed	-21.13	0.21	-20.44	0.01	-25.26	0.21	0.4538	3	0.014	0.5372	3	0.012
UWcp14_80C_3	actively degassed	-12.44	0.02	-20.56	0.17	-17.23	0.16	0.4524	3	0.015			
UWcp14_24C_CA_1	actively degassed	-21.11	0.01	-12.03	0.14	-16.50	0.04	0.5765	3	0.014			

UWcp14_20C_CA_16	actively degassed	-18.65	1.08	-11.10	0.11	-13.31	1.16	0.6408	4	0.014			
UWcp14_50C_CA_3	actively degassed	-15.28	0.02	-17.04	0.02	-16.07	0.05	0.5140	3	0.022			
UWcp14_70C_CA_1	actively degassed	-22.31	0.01	-20.46	0.06	-26.72	0.10	0.4544	4	0.014	0.5450	3	0.012
UWcp14_4C_3	passively degassed	-21.76	0.67	-6.48	0.76	-11.63	0.21	0.6277	3	0.010			
UWcp14_8C_2	passively degassed	-15.07	0.05	-8.17	0.09	-6.86	0.09	0.6533	3	0.021			
UWcp14_8C_3	passively degassed	-16.46	0.02	-8.20	0.01	-8.25	0.01	0.6391	3	0.014			
UWcp14_20C_9	passively degassed	-20.90	0.11	-11.28	0.09	-15.64	0.17	0.5882	3	0.017	0.6667	4	0.010
UWcp14_20C_4	passively degassed	-15.16	0.03	-10.41	0.05	-9.12	0.10	0.5994	4	0.020			
UWcp14_20C_10	passively degassed	-17.88	0.00	-11.36	0.04	-12.76	0.03	0.5830	3	0.014			
UWcp14_50C_5	passively degassed	-21.87	0.06	-15.88	0.07	-21.31	0.13	0.5060	2	0.017	0.6080	3	0.012
UWcp14_50C_3	passively	-13.59	0.00	-16.27	0.03	-13.61	0.03	0.5492	3	0.018			

	degassed												
UWcp14_70C_4	passively degassed	-17.68	0.10	-19.10	0.09	-20.53	0.18	0.4773	4	0.012			
UWcp14_80C_2	passively degassed	-6.20	0.02	-20.75	0.03	-11.07	0.01	0.4808	3	0.014			
UWcp14_8C_CA_4	passively degassed	-17.41	0.04	-8.19	0.06	-9.17	0.03	0.6294	2	0.013			
UWcp14_20C_CA_5	passively degassed	-18.54	0.01	-10.68	0.03	-12.69	0.05	0.6072	2	0.017			
UWcp14_20C_CA_11	passively degassed	-13.97	0.01	-11.26	0.00	-8.82	0.02	0.6156	3	0.014			
UWcp14_50C_CA_10	passively degassed	-18.43	0.11	-15.94	0.05	-18.20	0.16	0.5140	3	0.013			
UWcp14_70C_CA_5	passively degassed	-20.55	0.05	-19.40	0.21	-23.41	0.58	0.4568	3	0.014			
UWcp14_35C_1	passively degassed	-23.01	0.01	-14.93	0.03	-21.41	0.05	0.5647	3	0.014			
UWcp14_50C_4	passively degassed	-22.31	0.04	-16.02	0.24	-21.86	0.28	0.5306	3	0.015			

UWcp14_60C_1	passively degassed	-25.44	0.03	-18.03	0.10	-27.30	0.00	0.4647	3	0.015			
UWcp14_3C_2	mixed solution	-1.00	0.01	-8.80	0.03	6.11	0.03	0.6893	2	0.013			
UWcp14_4C_1	mixed solution	0.11	0.01	-8.72	0.01	7.26	0.01	0.6771	2	0.013	0.8047	3	0.018
UWcp14_4C_5	mixed solution	-1.54	1.12	-7.63	0.41	6.80	0.68	0.6736	3	0.017			
UWcp14_4C_6	mixed solution	0.00	0.27	-7.83	0.61	8.08	0.27	0.7088	2	0.020			
UWcp14_8C_1	mixed solution	0.04	0.01	-8.87	0.06	7.05	0.09	0.6893	4	0.009			
UWcp14_8C_6	mixed solution	0.41	0.02	-8.89	0.05	7.40	0.08	0.7006	3	0.016			
UWcp14_20C_DS	mixed solution	0.60	0.07	-12.21	0.01	4.06	0.07	0.6471	3	0.010			
UWcp14_50C_7	mixed solution	-0.33	0.01	-17.69	0.05	-2.16	0.05	0.5506	3	0.014			
UWcp14_50C_8	mixed solution	-0.92	0.00	-16.33	0.02	-1.32	0.04	0.5658	3	0.015			
UWcp14_50C_DS	mixed solution	-0.15	0.07	-17.39	0.03	-2.16	0.09	0.5455	3	0.010			
UWcp14_50C_DS2	mixed solution	0.40	0.08	-16.87	0.03	-1.08	0.09	0.5458	3	0.013			
UWcp14_70C_DS2	mixed solution	0.92	0.07	-19.11	0.19	-3.29	0.16	0.4882	3	0.015	0.5957	5	0.010

UWcp14_70C_2	mixed solution	1.52	0.02	-19.48	0.10	-2.52	0.14	0.5459	3	0.014			
UWcp14_80C_DS	mixed solution	0.75	0.05	-20.43	0.14	-4.84	0.12	0.4742	3	0.019			
UWcp14_8C_CA_5	mixed solution	-1.80	1.41	-9.17	0.32	4.95	1.04	0.6794	3	0.010			
UWcp14_20C_CA_13	mixed solution	-2.03	0.50	-12.05	0.16	1.69	0.32	0.6354	3	0.010	0.7183	2	0.014
UWcp14_50C_CA_9	mixed solution	-0.24	0.07	-16.81	0.03	-1.62	0.10	0.5604	3	0.010			
UWcp14_70C_CA_4	mixed solution	-0.33	0.04	-19.83	0.04	-4.41	0.05	0.5096	3	0.014	0.5828	2	0.018
UWcp14_30C_Z_1	raft, filtered method	-23.25	0.35	-12.63	0.58	-19.40	0.29	0.5257	2	0.020			
UWcp14_50C_Z_1	raft, filtered method	-22.99	0.00	-15.81	0.01	-22.70	0.07	0.5114	2	0.020			
UWcp14_4C_Z_3	filtered	-25.30	0.95	-8.08	0.39	-16.61	1.29	0.6419	3	0.016			
UWcp14_20C_Z_15	filtered	-23.17	0.01	-10.97	0.11	-17.53	0.12	0.6336	5	0.013			
UWcp14_20C_Z_2	filtered	-23.73	0.95	-11.44	0.10	-18.57	0.83	0.6022	3	0.016			
UWcp14_20C_G_14	filtered	-24.72	0.01	-11.65	0.01	-19.80	0.01	0.5770	2	0.013			
UWcp14_50C_Z_2	filtered	-24.08	0.62	-15.79	0.06	-23.43	0.52	0.5164	2	0.020			

chicken egg shell		-0.26	0.06	-7.41	0.06	8.57	0.10	0.5940	4	0.014			

[a]Values calculated with Brand et al. (2010) ^{17}O correction parameters.

[b]When the S.D> of the Δ_{47} was lower than the long-term S.D. of C64, SD of C64 was used to calculate S.E. of sample. For the first reference frame, C^4 S.D. = 0.024, for the second reference frame C64 S.D. = 0.028, for the third reference frame C64 S.D. = 0.28.

[c] Where the standard deviation of Δ_{47} of the sample was lower than the S.D. of C64 reacted at 25 °C (S.D. = 0.020), S.D> of C64 was used to calculate S.E. of the sample.

Appendix B. Supplementary materials to Chapter 3

B.1 Reprocessing Δ_{47} values with IUPAC ^{17}O correction parameters

Our projection of the Δ_{47} values into the CDES reference frame differs slightly from the approach of Petersen et al. (2019) in that we do not account for rounding errors in universal constants (speed of light, Planck's constant, Boltzmann's constant and conversion from Kelvin to °C) that were introduced in the theoretical equilibrium Δ_{47} values upon which the absolute reference frame is based (Wang et al.; 2004; Dennis et al., 2011). These rounding errors can lead to errors in Δ_{47} of up to 0.005 ‰ (up to about 1.5 °C) (Petersen et al. 2019). This potential error is an order of magnitude smaller than the seasonal biases that are the focus of this work. We recalculated each Δ_{47} value from Burgener et al., 2016; Ringham et al., 2016; and Hough et al., 2014. The change in Δ_{47} due to the change in parameters is denoted $\Delta\Delta47_{BR\text{-}S}$.

The largest $\Delta\Delta47_{BR\text{-}S}$ values occur in samples analyzed at the University of Washington (Burgener et al., 2016; Ringham et al., 2016) (Figure B-1). As previously documented, the $\Delta\Delta47_{BR\text{-}S}$ of samples analyzed at UW is dependent on their $\delta^{13}C$ composition (Kelson et al.,2017). The samples from Burgener et al. (2016) have $\delta^{13}C$ that is elevation dependent (i.e., Cerling and Quade 1993), so the maximum change in Δ_{47} is observed at high elevations ($\delta^{13}C$ of 10 ‰, $\Delta\Delta47_{BR\text{-}S}$ of -0.047‰) and at low elevations ($\delta^{13}C$ of -10 ‰, $\Delta\Delta47_{BR\text{-}S}$ of 0.024 ‰). The change in temperature ($\Delta T_{BR\text{-}S}$) ranges from -11 to 9 °C (note original calibration used was equation 5 from Kluge et al., 2015; reprocessed calibration is from Kelson et al. (2017) which was created in the same lab as the soil carbonates from Burgener et al. (2016)). The $\Delta\Delta47_{BR\text{-}S}$ for the data from Ringham et al. ranges from -0.02 to 0.003 ‰ and the $\Delta T_{BR\text{-}S}$ ranges from 0 to 8 °C

(note original calibration used was equation 5 from Kluge et al., 2015; reprocessed calibration is from Kelson et al. 2017) (Table B-4).

The $\Delta\Delta47_{BR\text{-}S}$ of the samples from Gallagher and Sheldon (2016), which were analyzed at the University of Michigan, ranges from -0.025 to -0.014 ‰ (Figure B-1). The $\Delta T_{BR\text{-}S}$ for these samples ranges from -5 to -2 °C (Figure B-1). This sample set has a relatively large change in $\Delta\Delta47_{BR\text{-}S}$ and small $\Delta T_{BR\text{-}S}$ due to the change calibration used for the reprocessed data (originally published with a composite calibration from Defliese et al. 2015, calculated here with a UM-specific calibration presented in Petersen et al. 2019) (Table B-4).

The $\Delta\Delta47_{BR\text{-}S}$ of the samples from Hough et al., which were analyzed at John Hopkins University ranges from -0.02 to -0.005 ‰ (Figure B-1). The $\Delta T_{BR\text{-}S}$ for these samples ranges from -9 to -6 °C (Figure B-1). This small change in Δ_{47} but large change in $\Delta T_{BR\text{-}S}$ can be explained by the change in the choice of empirical calibration. The original study used a calibration with a high sensitivity (Ghosh et al., 2006 recalculated in the ARF by Dennis et al. 2011): the sensitivity of this calibration is an outlier among the recent calibrations (e.g., Bonifacie et al., 2017; Fernandez et al., 2017; Kelson et al., 2017; Petersen et al., 2019). We now use a JHU-specific calibration presented in Petersen et al. (2019) calibration to calculate temperatures for this data (Table B-4).

We were not able to recalculate the Δ_{47} values for the carbonate samples from Peters et al., Quade et al., and Passey et al., 2010. All of those samples were analyzed for Δ_{47} at Caltech and the work was done before current replication standards were in place. Many of the samples from Quade et al. (47 of 52) and Passey et al. (19 of 28), and one out of 34 total samples from Peters et al., were analyzed for Δ_{47} once (no replication), and thus were not considered further for this synthesis. For the remaining samples with >1 replicate, it is difficult to predict what the

$\Delta\Delta47_{Br\text{-}S}$ would be. However, other recent studies have suggested that the Δ_{47} of samples analyzed at Caltech would change minimally (<0.01 ‰) with recalculation because Caltech employed a reference gas and a working gas that had similar $\delta^{13}C$ composition to each other (both about -3 ‰, Stolper et al., 2018, Appendix A1 and Bonifacie et al., 2017). Furthermore, the $\delta^{13}C$ of the samples is at most 4‰ different from the reported reference gas, so the $\Delta\Delta47_{BR\text{-}S}$ should be less than the reported error for the samples analyzed at Caltech (<0.02 ‰, as predicted in Schauer et al., 2016). Thus, in this synthesis dataset, we include samples from Caltech as originally calculated with the Santrock et al. (1985) parameters and the temperatures as originally calculated (see Table B-4 for study-specify calibrations).

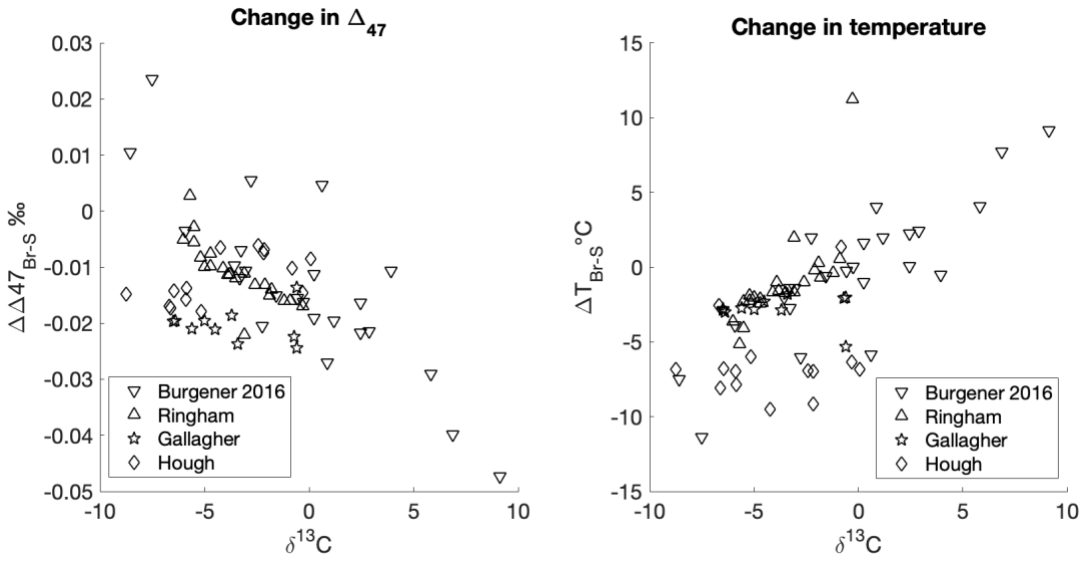

Figure B-1: Change in Δ_{47} and change in temperature due to ^{17}O reprocessing

Each symbol type represents samples from a different study. The samples in Burgener et al. (2018) and Ringham et al. (2016) were analyzed at the University of Washington. The samples of Gallagher and Sheldon (2016) were analyzed at the University of Michigan. The samples of Hough et al. (2014) were analyzed at Johns Hopkins University.

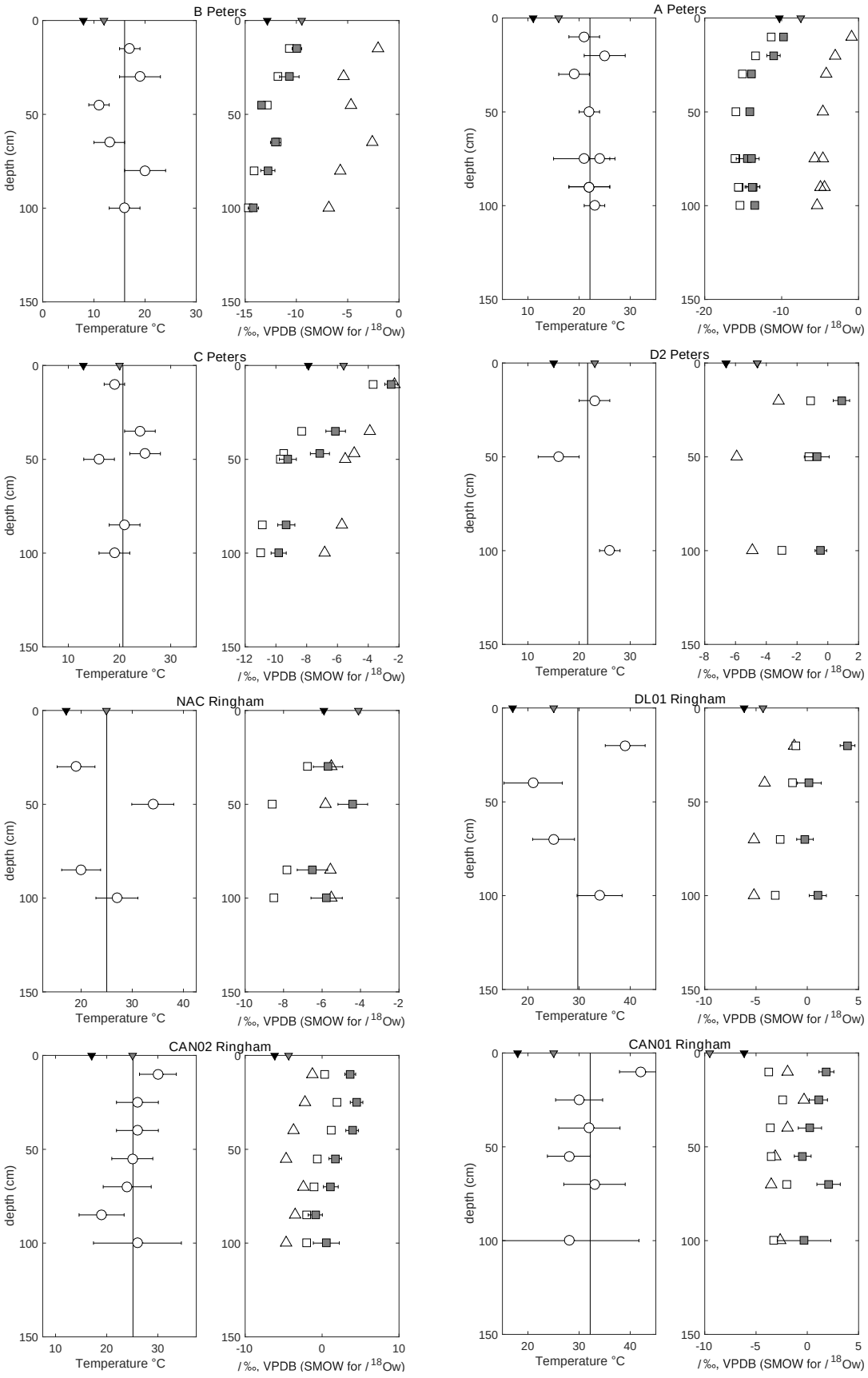
B Peters
A Peters
C Peters
D2 Peters
NAC Ringham
DL01 Ringham
CAN02 Ringham
CAN01 Ringham
depth (cm)
Temperature °C
/‰, VPDB (SMOW for /18Ow)

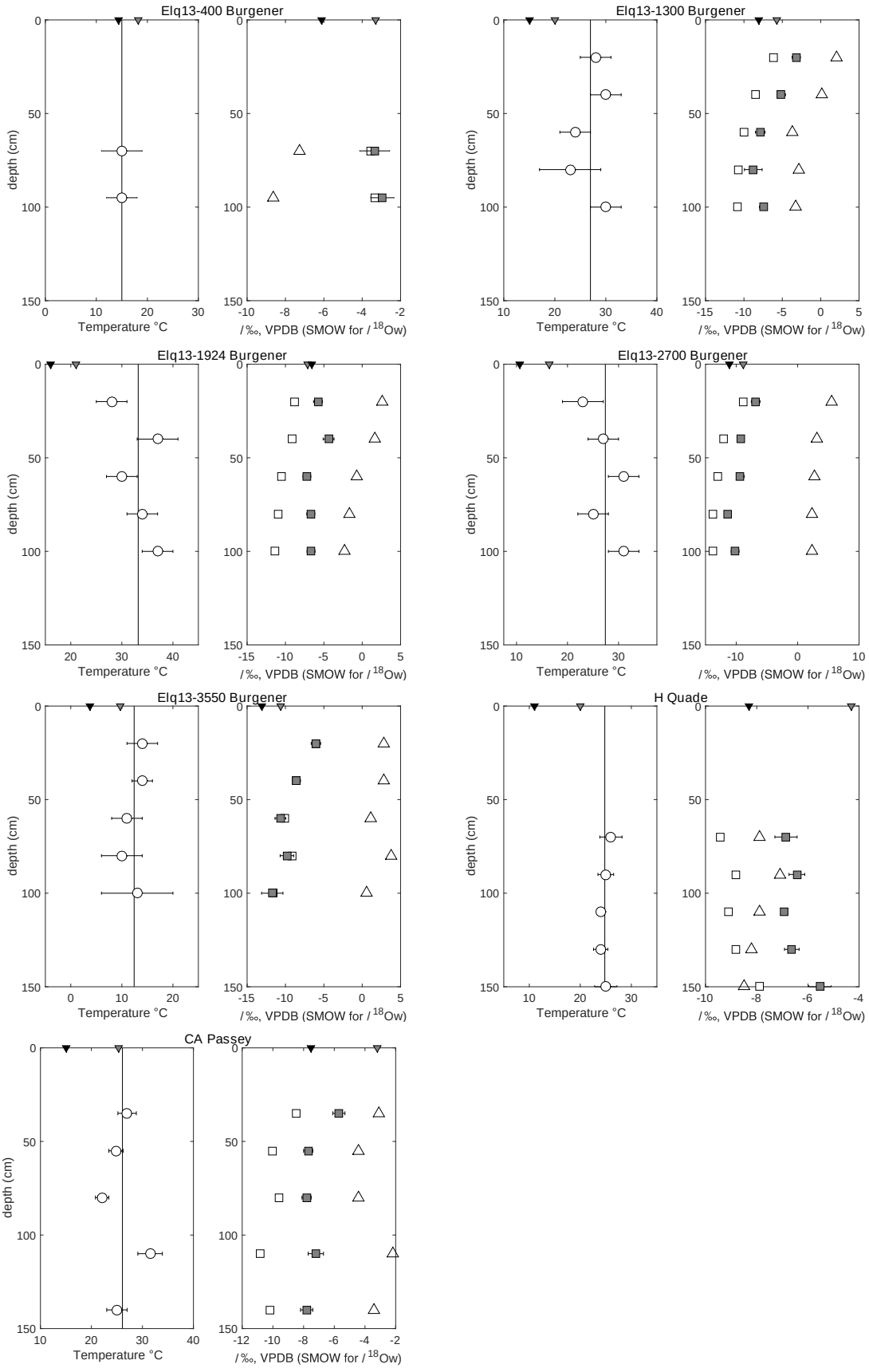
Elq13-400 Burgener
Elq13-1300 Burgener
Elq13-1924 Burgener
Elq13-2700 Burgener
Elq13-3550 Burgener
H Quade
CA Passey
depth (cm)
Temperature °C
/‰, VPDB (SMOW for /18Ow)

Figure B-2: Stable isotope data for all soil pits in this study

Data shown for each soil pit on the two previous pages. Left panel: open circles are $T\Delta_{47}$ values at specific depths. Gray band is soil pit mean $T\Delta_{47} \pm 1$ SE. Black/gray triangles on top of plot are MAAT/MWST. Right panel: open squares are $\delta^{18}O_c$, gray squares are calculated $\delta^{18}O_{gw.}$ Black/gray triangles on top of plot are $\delta^{18}O_{ann}/\delta^{18}O_{JJA}$ of rain from OIPC.

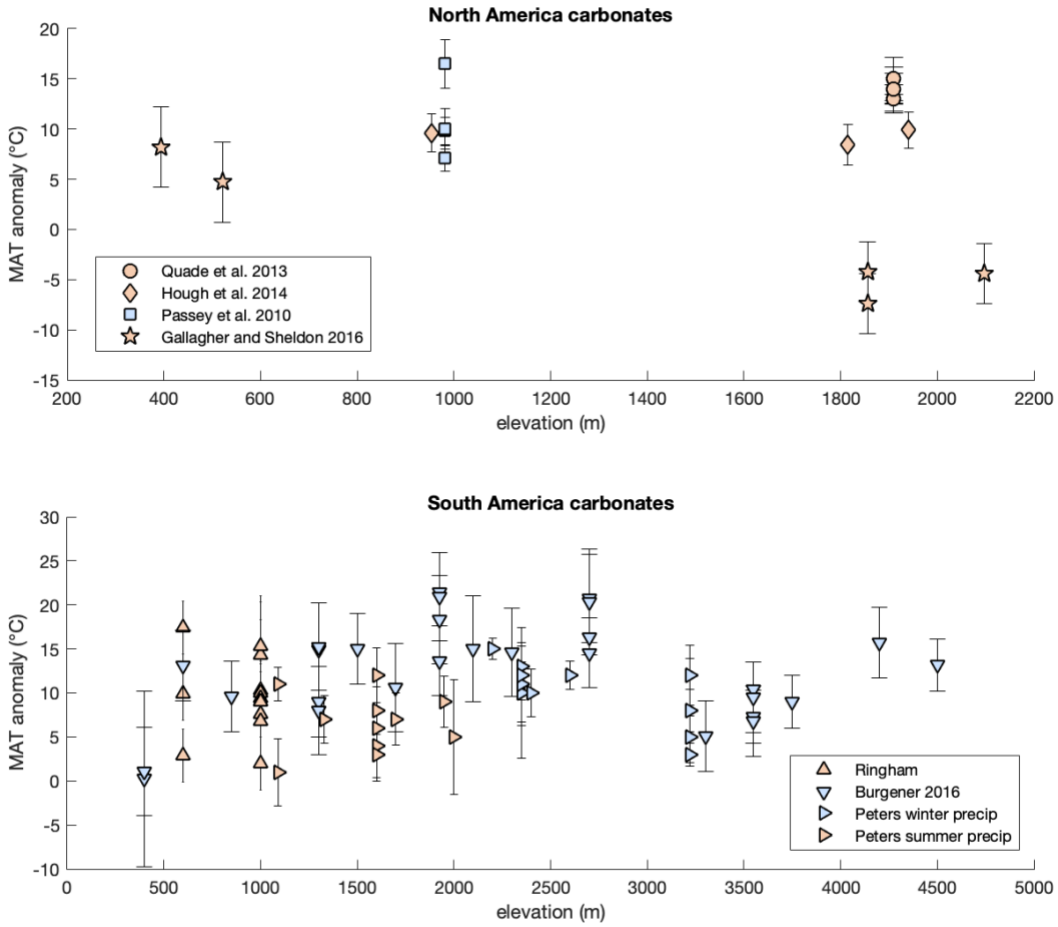

Figure B-3: Regional comparison to TΔ_{47} – MAAT for modern soil carbonates.

Symbol color represents primary season of precipitation (rain/snow) (blue is winter, red is summer).

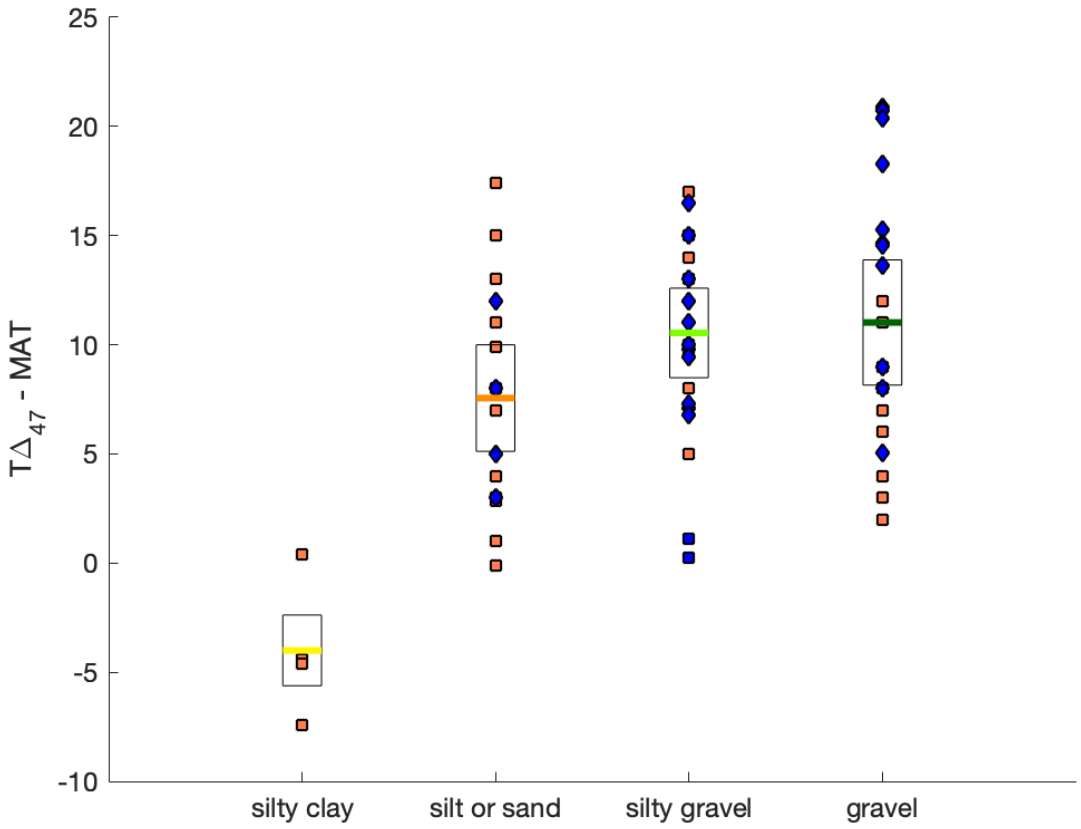

Figure B-4: Soil texture, precipitation season, and land cover for modern soil carbonates. Position on x-axis indicates soil texture; symbol color indicates primary season of precipitation (rain/winter) (blue is winter, red is summer); symbol type indicates land cover (square is vegetated, diamond is non-vegetated).

Table B-1: Holocene soil carbonate sample information

Sample	Study	Location	Depth (cm)	Latitude (°N)	Longitude (°E)	Elevation (m)
'GONJQ-305-1'	Passey et al. (2010)	Ehtiopia	50	11.1481	40.3357	694
'GON07-4.7-1'	Passey et al. (2010)	Ehtiopia	45	11.1653	40.495	637
'K2002-MAR-103-1'	Passey et al. (2010)	Kenya	NaN	-1.5466	35.0234	1477
'CN2008-DM-164-120cm-1'	Passey et al. (2010)	Inner Mongolia	120	42.0153	111.5743	1306
'CA08-BHS-001.1'	Passey et al. (2010)	California, USA	35	34.4212	-116.789	982
'CA08-BHS-002.1'	Passey et al. (2010)	California, USA	55	34.4212	-116.789	982
'CA08-BHS-003.1'	Passey et al. (2010)	California, USA	80	34.4212	-116.789	982
'CA08-BHS-004.1'	Passey et al. (2010)	California, USA	110	34.4212	-116.789	982
'CA08-BHS-005.1'	Passey et al. (2010)	California, USA	140	34.4212	-116.789	982
'H-70'	Quade et al. (2013)	Arizona, USA	70	31.455	-110.3732	1910
'H-90'	Quade et al. (2013)	Arizona, USA	90	31.455	-110.3732	1910
'H-110'	Quade et al. (2013)	Arizona, USA	110	31.455	-110.3732	1910
'H-130'	Quade et al. (2013)	Arizona, USA	130	31.455	-110.3732	1910
'H-150'	Quade et al. (2013)	Arizona, USA	150	31.455	-110.3732	1910
'NE11-C2'	Hough et al. (2014)	Nebraska, USA	0	41.93	-103.63	1236
'WY11-C5'	Hough et al. (2014)	Wyoming, USA	55	42.65	-106.84	1941
'WY11-C9'	Hough et al. (2014)	Wyoming, USA	40	43.73	-105.87	1815
'WY11-C10'	Hough et al. (2014)	Wyoming, USA	0	44.21	-107.39	2638
'WY11-C12'	Hough et al. (2014)	Wyoming, USA	0	43.24	-108.17	1448
'WY11-C19'	Hough et al. (2014)	Wyoming, USA	30	42.81	-108.89	2288
'WY11-C20'	Hough et al. (2014)	Wyoming, USA	30	41.89	-105.73	2131
'NE11-C24'	Hough et al. (2014)	Nebraska, USA	50	42.21	-101.65	954
'D2-20'	Peters et al. (2014)	Argentina	20	-33.0439	-69.0092	1090
'D2-50'	Peters et al. (2014)	Argentina	50	-33.0439	-69.0092	1090
'D2-100'	Peters et al. (2014)	Argentina	100	-33.0439	-69.0092	1090
'RM1333-11-60'	Peters et al. (2014)	Argentina	60	-33.0907	-69.1004	1330
'MODS07-03'	Peters et al. (2014)	Argentina	50	-32.814	-69.301	1600
'C10'	Peters et al. (2014)	Argentina	10	-32.8233	-69.2986	1600
'C35'	Peters et al. (2014)	Argentina	35	-32.8233	-69.2986	1600

'C47'	Peters et al. (2014)	Argentina	47	-32.8233	-69.2986	1600
'C50'	Peters et al. (2014)	Argentina	50	-32.8233	-69.2986	1600
'C85'	Peters et al. (2014)	Argentina	85	-32.8233	-69.2986	1600
'C100'	Peters et al. (2014)	Argentina	100	-32.8233	-69.2986	1600
'RM1695-11-60'	Peters et al. (2014)	Argentina	60	-32.7301	-69.3283	1700
'RM1647-11-60'	Peters et al. (2014)	Argentina	60	-32.6406	-69.4991	1950
'MODS07-05'	Peters et al. (2014)	Argentina	50	-32.662	-69.513	2000
'MODS07-06'	Peters et al. (2014)	Argentina	50	-32.769	-69.598	2200
'A10'	Peters et al. (2014)	Argentina	10	-32.8348	-69.7286	2350
'A20'	Peters et al. (2014)	Argentina	20	-32.8348	-69.7286	2350
'A30'	Peters et al. (2014)	Argentina	30	-32.8348	-69.7286	2350
'A50'	Peters et al. (2014)	Argentina	50	-32.8348	-69.7286	2350
'A74A'	Peters et al. (2014)	Argentina	75	-32.8348	-69.7286	2350
'A75B'	Peters et al. (2014)	Argentina	75	-32.8348	-69.7286	2350
'A901'	Peters et al. (2014)	Argentina	90	-32.8348	-69.7286	2350
'A902'	Peters et al. (2014)	Argentina	90	-32.8348	-69.7286	2350
'A100U'	Peters et al. (2014)	Argentina	100	-32.8348	-69.7286	2350
'MODS07-07'	Peters et al. (2014)	Argentina	50	-32.842	-69.744	2400
'MODS07-10'	Peters et al. (2014)	Argentina	50	-32.845	-69.827	2600
'B15'	Peters et al. (2014)	Argentina	15	-32.8118	-70.0645	3220
'B30'	Peters et al. (2014)	Argentina	30	-32.8118	-70.0645	3220
'B45'	Peters et al. (2014)	Argentina	45	-32.8118	-70.0645	3220
'B65'	Peters et al. (2014)	Argentina	65	-32.8118	-70.0645	3220
'B80'	Peters et al. (2014)	Argentina	80	-32.8118	-70.0645	3220
'B100'	Peters et al. (2014)	Argentina	100	-32.8118	-70.0645	3220
'MODS07-08B'	Peters et al. (2014)	Argentina	50	-32.812	-70.062	3220
'Kranzburg'	Gallagher & Sheldon (2016)	South Dakota, USA	40	44.428	-96.784	521
'Clamo'	Gallagher & Sheldon (2016)	South Dakota, USA	40	43.834	-97.993	394
'Plughat-1'	Gallagher & Sheldon (2016)	New Mexico, USA	60	37.023	-103.908	1856
'Plughat-2'	Gallagher & Sheldon (2016)	New Mexico, USA	60	37.023	-103.908	1856
'Montecito'	Gallagher & Sheldon (2016)	New Mexico, USA	35	36.392	-105.93	2261
'Witt'	Gallagher & Sheldon (2016)	New Mexico, USA	70	34.649	-106.343	2097
'Cornville'	Gallagher & Sheldon (2016)	Arizona, USA	35	34.603	-111.854	962
'Guvo'	Gallagher & Sheldon (2016)	Arizona, USA	20	32.752	-111.962	481
'Cross-Apache'	Gallagher & Sheldon (2016)	Arizona, USA	33	35.331	-112.805	1646
'Lavic'	Gallagher & Sheldon (2016)	California, USA	25	34.604	-117.454	859
'Muroc'	Gallagher & Sheldon (2016)	California, USA	21	34.918	-118.152	781
'CAN01-10'	Ringham et al. (2016)	Argentina	10	-32.5919	-68.9053	1000
'CAN01-25'	Ringham et al. (2016)	Argentina	25	-32.5919	-68.9053	1000
'CAN01-40'	Ringham et al. (2016)	Argentina	40	-32.5919	-68.9053	1000
'CAN01-55'	Ringham et al. (2016)	Argentina	55	-32.5919	-68.9053	1000

'CAN01-70'	Ringham et al. (2016)	Argentina	70	-32.5919	-68.9053	1000
'CAN01-100'	Ringham et al. (2016)	Argentina	100	-32.5919	-68.9053	1000
'CAN02-10'	Ringham et al. (2016)	Argentina	10	-32.6519	-68.9167	1000
'CAN02-25'	Ringham et al. (2016)	Argentina	25	-32.6519	-68.9167	1000
'CAN02-40'	Ringham et al. (2016)	Argentina	40	-32.6519	-68.9167	1000
'CAN02-55'	Ringham et al. (2016)	Argentina	55	-32.6519	-68.9167	1000
'CAN02-70'	Ringham et al. (2016)	Argentina	70	-32.6519	-68.9167	1000
'CAN02-85'	Ringham et al. (2016)	Argentina	85	-32.6519	-68.9167	1000
'CAN02-100'	Ringham et al. (2016)	Argentina	100	-32.6519	-68.9167	1000
'CAN03'	Ringham et al. (2016)	Argentina	50	-32.57	-68.9428	1000
'DL01-20'	Ringham et al. (2016)	Argentina	20	-32.8778	-68.9225	1000
'DL01-40'	Ringham et al. (2016)	Argentina	40	-32.8778	-68.9225	1000
'DL01-70'	Ringham et al. (2016)	Argentina	70	-32.8778	-68.9225	1000
'DL01-100'	Ringham et al. (2016)	Argentina	100	-32.8778	-68.9225	1000
'NAC-30'	Ringham et al. (2016)	Argentina	30	-34.05	-67.9028	600
'NAC-50'	Ringham et al. (2016)	Argentina	50	-34.05	-67.9028	600
'NAC-85'	Ringham et al. (2016)	Argentina	85	-34.05	-67.9028	600
'NAC-100'	Ringham et al. (2016)	Argentina	100	-34.05	-67.9028	600
'Elq13-400-70'	Burgener et al. (2016)	Chile	70	-29.9732	-70.9536	400
'Elq13-400-95'	Burgener et al. (2016)	Chile	95	-29.9732	-70.9536	400
'Elq13-600-50'	Burgener et al. (2016)	Chile	50	-30.0451	-70.8191	600
'Elq13-850-50'	Burgener et al. (2016)	Chile	50	-29.9876	-70.5694	850
'Eql13-1300-20'	Burgener et al. (2016)	Chile	20	-29.8576	-70.3649	1300
'Eql13-1300-40'	Burgener et al. (2016)	Chile	40	-29.8576	-70.3649	1300
'Elq13-1300-60'	Burgener et al. (2016)	Chile	60	-29.8576	-70.3649	1300
'Elq13-1300-80'	Burgener et al. (2016)	Chile	80	-29.8576	-70.3649	1300
'Elq13-1300-100'	Burgener et al. (2016)	Chile	100	-29.8576	-70.3649	1300
'Elq13-1500-50'	Burgener et al. (2016)	Chile	50	-29.9323	-70.294	1500
'Elq13-1700-50'	Burgener et al. (2016)	Chile	50	-29.9828	-70.2333	1700
'Elq13-1924-20'	Burgener et al. (2016)	Chile	20	-29.9543	-70.1754	1924
'Elq13-1924-40'	Burgener et al. (2016)	Chile	40	-29.9543	-70.1754	1924
'Elq13-1924-60'	Burgener et al. (2016)	Chile	60	-29.9543	-70.1754	1924
'Elq13-1924-80'	Burgener et al. (2016)	Chile	80	-29.9543	-70.1754	1924
'Elq13-1924-100'	Burgener et al. (2016)	Chile	100	-29.9543	-70.1754	1924
'Elq13-2100-50'	Burgener et al. (2016)	Chile	50	-29.9747	-70.0984	2100
'Elq13-2300-50'	Burgener et al. (2016)	Chile	50	-30.0532	-70.0954	2300
'Elq13-2700-20'	Burgener et al. (2016)	Chile	20	-30.1372	-70.0624	2700
'Elq13-2700-40'	Burgener et al. (2016)	Chile	40	-30.1372	-70.0624	2700
'Elq13-2700-60'	Burgener et al. (2016)	Chile	60	-30.1372	-70.0624	2700
'Elq13-2700-80'	Burgener et al. (2016)	Chile	80	-30.1372	-70.0624	2700
'Elq13-2700-100'	Burgener et al. (2016)	Chile	100	-30.1372	-70.0624	2700
'Elq13-3300-50'	Burgener et al. (2016)	Chile	50	-30.2715	-69.9734	3300
'Elq13-3550-20'	Burgener et al. (2016)	Chile	20	-30.2624	-69.9415	3550
'Elq13-3550-40'	Burgener et al. (2016)	Chile	40	-30.2624	-69.9415	3550
'Elq13-3550-60'	Burgener et al. (2016)	Chile	60	-30.2624	-69.9415	3550
'Elq13-3550-80'	Burgener et al. (2016)	Chile	80	-30.2624	-69.9415	3550
'Elq13-3550-100'	Burgener et al. (2016)	Chile	100	-30.2624	-69.9415	3550
'Elq13-3750-50'	Burgener et al. (2016)	Chile	50	-30.2064	-69.9161	3750

'Elq13-4200-50'	Burgener et al. (2016)	Chile	50	-30.1637	-69.862	4200
'Elq13-4500-50'	Burgener et al. (2016)	Chile	50	-30.1382	-69.8298	4500
'Tsangpo-19a'	Burgener et al. (2018)	Tibet	110	30.418	82.767	4800
'Tsangpo-19b'	Burgener et al. (2018)	Tibet	110	30.418	82.767	4800
'Tsangpo-21a'	Burgener et al. (2018)	Tibet	60	29.204	88.309	4016
'Tsangpo-21b'	Burgener et al. (2018)	Tibet	60	29.204	88.309	4016
'Tsangpo-22'	Burgener et al. (2018)	Tibet	55	29.317	88.942	3876
'Lhasa-4'	Burgener et al. (2018)	Tibet	60	29.636	91.292	3809
'Cannes-62'	Burgener et al. (2018)	Svalbard	62	78.937	11.455	60

Table B-2: Isotopic Data for Holocene soil carbonate samples

Sample	n	$\delta^{18}O_c$ (‰) VDPB	$\delta^{13}C_c$ (‰) VPDB	Δ47*	Δ47err+	TΔ47**	TΔ47err	$\delta^{18}O_{sw}$ (‰) SMOW***	$\delta^{18}O_{sw}$ error (‰) SMOW***	$\delta^{18}O_{MWS}$ (from OIPC)	$\delta^{18}O_{ann}$ (from OIPC)
'GONJQ-305-1'	2	-5.5	-2.5	0.628	0.008	29.1	1.8	-2.3	0.4	3.8	3.3
'GON07-4.7-1'	2	-3.5	-1.5	0.629	0.009	28.9	2.1	-0.3	0.4	3.9	3.4
'K2002-MAR-103-1'	2	-3.0	0.8	0.674	0.005	18.9	1.0	-1.9	0.2	-1.0	-8.2
'CN2008-DM-164-120cm-1'	2	-8.2	-3.9	0.696	0.006	14.4	1.2	-8.0	0.3	-6.6	-8.6
'CA08-BHS-001.1'	2	-8.5	-3.1	0.637	0.008	27	1.8	-5.7	0.4	-3.2	-7.5
'CA08-BHS-002.1'	3	-10.0	-4.4	0.647	0.006	24.8	1.4	-7.7	0.3	-3.2	-7.5
'CA08-BHS-003.1'	3	-9.6	-4.4	0.659	0.006	22.1	1.3	-7.8	0.3	-3.2	-7.5
'CA08-BHS-004.1'	2	-10.8	-2.2	0.618	0.01	31.5	2.4	-7.2	0.5	-3.2	-7.5
'CA08-BHS-005.1'	2	-10.2	-3.4	0.646	0.009	25	2.0	-7.8	0.4	-3.2	-7.5
				^not in ARF, in 'HG'							
'H-70'	4	-9.4	-7.9	0.710	0.0065	26	2.2	-6.9	0.4	-4.3	-8.3
'H-90'	4	-8.8	-7.1	0.710	0.0082	25	1.5	-6.4	0.3	-4.3	-8.3
'H-110'	3	-9.1	-7.9	0.710	0.0033	24	0.5	-6.9	0.1	-4.3	-8.3
'H-130'	4	-8.8	-8.2	0.720	0.0025	24	1.4	-6.6	0.3	-4.3	-8.3
'H-150'	5	-7.9	-8.5	0.710	0.0114	25	2.2	-5.5	0.4	-4.3	-8.3
NE11-C2'	2	-9.1	-2.4	0.7068	0.018	19	5.9	-7.9	1.2	-5.6	-10.6
WY11-C5'	2	-12.6	-6.5	0.7198	0.012	15	3.7	-12.4	0.8	-7.3	-13.9
WY11-C9'	2	-12.8	-8.7	0.7212	0.009	14	2.8	-12.7	0.6	-7.8	-13.8
WY11-C10'	2	-15.0	-6.6	0.7377	0.009	9	2.7	-16.0	0.6	-9.3	-16.3
WY11-C12'	2	-7.2	0.1	0.7105	0.012	18	4.0	-6.3	0.8	-7.3	-13.3
WY11-C19'	2	-12.7	-5.8	0.7283	0.009	12	2.8	-13.0	0.6	-7.8	-14.4
WY11-C20'	2	-8.5	-4.2	0.7305	0.021	12	6.1	-8.9	1.3	-7.1	-13.7

NE11-C24'	2	-8.7	-2.2	0.7082	0.009	19	3.0	-7.6	0.6	-5.1	-11.5
'D2-20'	2	-1.1	-3.2	0.654	0.013	23	3.0	0.9	0.5	-4.6	-6.6
'D2-50'	3	-1.2	-5.9	0.686	0.021	16	4.0	-0.7	0.8	-4.6	-6.6
'D2-100'	3	-3.0	-4.9	0.64	0.010	26	2.0	-0.5	0.4	-4.6	-6.6
'RM1333-11-60'	2	-11.4	-5.3	0.664	0.013	21	3.0	-9.9	0.6	-5.1	-7.3
'MODS07-03'	3	-7.7	-5.8	0.683	0.020	17	4.0	-7.0	0.8	-5.6	-7.9
'C10'	3	-3.7	-2.3	0.673	0.010	19	2.0	-2.5	0.4	-5.6	-7.9
'C35'	2	-8.3	-3.9	0.652	0.013	24	3.0	-6.1	0.6	-5.6	-7.9
'C47'	2	-9.5	-4.9	0.647	0.013	25	3.0	-7.1	0.6	-5.6	-7.9
'C50'	2	-9.7	-5.5	0.688	0.013	16	3.0	-9.2	0.6	-5.6	-7.9
'C85'	2	-10.9	-5.7	0.664	0.013	21	3.0	-9.3	0.6	-5.6	-7.9
'C100'	2	-11.0	-6.8	0.672	0.013	19	3.0	-9.8	0.5	-5.6	-7.9
'RM1695-11-60'	3	-11.7	-4.2	0.671	0.012	20	3.0	-10.4	0.6	-5.8	-8.2
'RM1647-11-60'	2	-12.3	-6.3	0.663	0.015	21	3.0	-10.8	0.6	-6.4	-8.9
'MODS07-05'	2	-7.3	-2.8	0.683	0.033	17	5.0	-6.6	1.4	-6.7	-9.1
'MODS07-06'	2	-14.4	-3.7	0.640	0.007	26	2	-11.9	0.2	-7.2	-9.7
'A10'	2	-11.3	-0.9	0.662	0.013	21	3	-9.8	0.5	-7.5	-10.3
'A20'	2	-13.4	-3.1	0.644	0.022	25	4	-11.1	0.9	-7.5	-10.3
'A30'	2	-15.1	-4.2	0.672	0.013	19	3	-14.0	0.5	-7.5	-10.3
'A50'	4	-15.9	-4.6	0.659	0.009	22	2	-14.2	0.4	-7.5	-10.3
'A74A'	2	-16.0	-4.6	0.664	0.036	21	6	-14.4	1.5	-7.5	-10.3
'A75B'	3	-16.0	-5.7	0.651	0.01	24	2	-13.9	0.5	-7.5	-10.3
'A901'	2	-15.5	-5.0	0.659	0.021	22	4	-13.7	0.9	-7.5	-10.3
'A902'	3	-15.6	-4.4	0.661	0.021	22	4	-13.8	1.0	-7.5	-10.3
'A100U'	4	-15.4	-5.4	0.653	0.009	23	2	-13.5	0.3	-7.5	-10.3
'MODS07-07'	2	-15.4	-5.6	0.662	0.015	21	3	-13.9	0.6	-7.6	-10.5
'MODS07-10'	2	-16.1	1.3	0.66	0.007	22	2	-14.3	0.3	-8.1	-11.1
'B15'	4	-10.7	-2.1	0.684	0.01	17	2	-9.9	0.5	-9.5	-12.8

'B30'	2	-11.8	-5.4	0.675	0.021	19	4	-10.7	0.9	-9.5	-12.8
'B45'	4	-12.8	-4.7	0.711	0.009	11	2	-13.4	0.3	-9.5	-12.8
'B65'	2	-11.9	-2.6	0.702	0.013	13	3	-12.0	0.5	-9.5	-12.8
'B80'	2	-14.1	-5.8	0.667	0.018	20	4	-12.8	0.7	-9.5	-12.8
'B100'	2	-14.7	-6.9	0.687	0.013	16	3	-14.2	0.5	-9.5	-12.8
'MODS07-08B'	3	-15.6	-6.9	0.688	0.03	16	6	-15.1	1.2	-9.5	-12.8
				^not in ARF, in 'HG'							
Kranzburg	3	-6.0	-0.6	0.715	0.0115	11	3	-6.6	0.8	-4.3	-8.3
'Clamo	3	-5.2	-0.5	0.6968	0.0115	17	4	-4.5	0.8	-4.0	-8
Plughat-1	3	-8.1	-6.3	0.7419	0.0115	3	3	-10.5	0.7	-4.6	-8.1
Plughat-2	3	-9.0	-6.4	0.7307	0.0115	6	3	-10.7	0.8	-4.6	-8.1
Montecito	3	-8.7	-4.4	0.7393	0.0115	4	3	-11.0	0.7	-5.5	-10.4
'Witt	3	-6.5	-4.9	0.7308	0.0115	6	3	-8.2	0.8	-4.4	-8.5
Cornville	3	-9.8	-0.5	0.69	0.0115	19	4	-8.7	0.8	-2.0	-5.7
Guvo	3	-5.3	-3.6	0.7078	0.0115	13	4	-5.5	0.8	-2.2	-6.4
Cross-Apache	3	-8.4	-6.4	0.7378	0.0115	4	3	-10.6	0.7	-4.4	-9
Lavic	3	-10.4	-3.4	0.7077	0.0115	13	4	-10.5	0.8	-3.0	-7.3
Muroc	3	-9.3	-5.5	0.7204	0.0115	9	3	-10.3	0.8	-2.8	-6.8
'CAN01-10'	3	-3.8	-1.9	0.646	0.011	42	4.1	1.9	0.7	-4.3	-6.2
'CAN01-25'	3	-2.4	-0.3	0.68	0.014	30	4.6	1.1	0.9	-4.3	-6.2
'CAN01-40'	3	-3.6	-1.9	0.674	0.018	32	6.0	0.3	1.1	-4.3	-6.2
'CAN01-55'	3	-3.5	-3.1	0.6858	0.013	28	4.2	-0.5	0.8	-4.3	-6.2
'CAN01-70'	3	-2.0	-3.5	0.6711	0.018	33	6.0	2.1	1.1	-4.3	-6.2
'CAN01-100'	3	-3.3	-2.7	0.6869	0.045	28	13.7	-0.3	2.6	-4.3	-6.2
'CAN02-10'	3	0.4	-1.3	0.682	0.011	30	3.6	3.7	0.7	-4.3	-6.2
'CAN02-25'	3	1.9	-2.2	0.693	0.013	26	4.1	4.5	0.8	-4.3	-6.2
'CAN02-40'	3	1.2	-3.8	0.6917	0.013	26	4.1	3.9	0.8	-4.3	-6.2
'CAN02-55'	3	-0.6	-4.6	0.6974	0.013	25	4.0	1.7	0.8	-4.3	-6.2

'CAN02-70'	3	-1.0	-2.4	0.6998	0.0155	24	4.7	1.1	1.0	-4.3	-6.2
'CAN02-85'	3	-2.0	-3.5	0.7156	0.0151	19	4.4	-0.9	0.9	-4.3	-6.2
'CAN02-100'	2	-2.0	-4.7	0.693	0.028	26	8.6	0.6	1.7	-4.3	-6.2
'CAN03'	3	-3.0	-4.7	0.6872	0.013	28	4.2	0.0	0.8	-4.3	-6.2
'DL01-20'	3	-1.1	-1.2	0.656	0.011	39	3.9	3.9	0.7	-4.3	-6.2
'DL01-40'	4	-1.4	-4.1	0.7079	0.0192	21	5.7	0.2	1.2	-4.3	-6.2
'DL01-70'	2	-2.6	-5.2	0.6957	0.013	25	4.1	-0.2	0.8	-4.3	-6.2
'DL01-100'	2	-3.1	-5.2	0.6697	0.013	34	4.4	1.0	0.8	-4.3	-6.2
'NAC-30'	3	-6.8	-5.5	0.7165	0.0125	19	3.7	-5.7	0.8	-4.1	-5.9
'NAC-50'	4	-8.6	-5.8	0.6679	0.012	34	4.1	-4.4	0.8	-4.1	-5.9
'NAC-85'	3	-7.8	-5.6	0.7127	0.013	20	3.8	-6.5	0.8	-4.1	-5.9
'NAC-100'	2	-8.5	-5.5	0.6901	0.013	27	4.1	-5.8	0.8	-4.1	-5.9
'Elq13-400-70'	2	-3.6	-7.3	0.7305	0.013	15	4	-3.4	0.8	-3.3	-6.1
'Elq13-400-95'	4	-3.3	-8.6	0.7275	0.01	15	3	-3.0	0.6	-3.3	-6.1
'Elq13-600-50'	5	-7.8	-6.0	0.6865	0.01	28	3	-4.8	0.6	-3.8	-6.6
'Elq13-850-50'	7	-6.6	-3.1	0.6973	0.011	25	3	-4.3	0.7	-4.6	-6.7
'Eql13-1300-20'	5	-6.1	2.0	0.6875	0.0085	28	3	-3.2	0.5	-5.8	-8.1
'Eql13-1300-40'	5	-8.5	0.2	0.6809	0.0085	30	3	-5.1	0.5	-5.8	-8.1
'Elq13-1300-60'	6	-10.0	-3.6	0.6993	0.01	24	3	-7.9	0.6	-5.8	-8.1
'Elq13-1300-80'	4	-10.7	-2.9	0.7025	0.019	23	6	-8.8	1.1	-5.8	-8.1
'Elq13-1300-100'	4	-10.9	-3.3	0.68	0.008	30	3	-7.5	0.5	-5.8	-8.1
'Elq13-1500-50'	6	-9.9	-0.4	0.6778	0.0078	31	3	-6.4	0.5	-6.2	-8.5
'Elq13-1700-50'	4	-12.0	-3.4	0.6911	0.0095	27	3	-9.3	0.6	-6.6	-9
'Elq13-1924-20'	5	-8.8	2.6	0.6864	0.0092	28	3	-5.8	0.6	-7.1	-6.6
'Elq13-1924-40'	4	-9.2	1.7	0.6591	0.011	37	4	-4.4	0.7	-7.1	-6.6
'Elq13-1924-60'	5	-10.5	-0.7	0.6815	0.008	30	3	-7.2	0.5	-7.1	-6.6
'Elq13-1924-80'	5	-10.9	-1.7	0.6679	0.008	34	3	-6.7	0.5	-7.1	-6.6
'Elq13-1924-100'	4	-11.4	-2.3	0.6605	0.008	37	3	-6.7	0.5	-7.1	-6.6

'Elq13-2100-50'	3	-11.8	0.1	0.6808	0.01	30	3	-8.5	0.6	-7.5	-9.9
'Elq13-2300-50'	3	-13.7	0.1	0.6879	0.011	28	4	-10.9	0.7	-7.9	-10.3
'Elq13-2700-20'	6	-8.9	5.5	0.7009	0.0115	23	4	-6.8	0.7	-8.8	-11.2
'Elq13-2700-40'	5	-12.1	3.2	0.6897	0.0085	27	3	-9.3	0.5	-8.8	-11.2
'Elq13-2700-60'	4	-13.0	2.7	0.6765	0.01	31	3	-9.3	0.6	-8.8	-11.2
'Elq13-2700-80'	5	-13.8	2.3	0.6953	0.008	25	3	-11.4	0.5	-8.8	-11.2
'Elq13-2700-100'	3	-13.7	2.3	0.6776	0.01	31	3	-10.2	0.6	-8.8	-11.2
'Elq13-3300-50'	4	-10.4	5.6	0.7469	0.012	10	3	-11.2	0.7	-10.1	-12.5
'Elq13-3550-20'	5	-6.0	2.8	0.7343	0.0103	14	3	-6.0	0.6	-10.6	-13.1
'Elq13-3550-40'	5	-8.6	2.8	0.7324	0.0085	14	2	-8.6	0.5	-10.6	-13.1
'Elq13-3550-60'	6	-10.1	1.1	0.7435	0.012	11	3	-10.7	0.7	-10.6	-13.1
'Elq13-3550-80'	4	-9.1	3.8	0.7453	0.015	10	4	-9.8	0.9	-10.6	-13.1
'Elq13-3550-100'	4	-11.6	0.6	0.7357	0.024	13	7	-11.7	1.4	-10.6	-13.1
'Elq13-3750-50'	5	-11.9	0.8	0.747	0.01	10	3	-12.7	0.6	-11.1	-13.5
'Elq13-4200-50'	4	-4.7	6.7	0.7372	0.01	13	3	-4.9	0.6	-12.1	-14.5
'Elq13-4500-50'	6	-9.4	8.9	0.7577	0.014	7	4	-10.8	0.8	-12.8	-15.2
'Tsangpo-19a'	3	-14.7	3.3	0.7453	0.0093	11	3	-15.3	-0.7	-13.2	-15.2
'Tsangpo-19b'	3	-14.2	3.8	0.7528	0.0093	8	2	-15.5	-0.4	-13.2	-15.2
'Tsangpo-21a'	3	-11.7	-2.9	0.748	0.0093	10	3	-12.5	-0.7	-14.6	-15
'Tsangpo-21b'	3	-13.6	-2.9	0.7128	0.0133	20	4	-12.3	-0.8	-14.6	-12.5
'Tsangpo-22'	4	-15.7	-1.5	0.7064	0.008	22	3	-14.0	-0.6	-15.3	-15.8
'Lhasa-4'	3	-17.3	-4.0	0.7235	0.0094	17	3	-16.6	-0.6	-15.3	-15.8
'Cannes-62'	3	-5.0	5.3	0.7659	0.0093	5	2	-7.0	-0.5	-10.2	-11.7

*in ARF (corrected for 25 C RF), except for Passey and Peters are not in ARF

(+) minimum SD used to calculate SE are as follows: 0.018 for Quade et al. (2013); 0.013 for Hough et al. (2014); 0.018 for Peters et al.(2013); 0.019 for Burgener et al. (2016); 0.019 for Ringham et al. (2016); 0.016 for Burgener et al. 2018

** See Calibrations Table for T-D47 calibration equation used

***calculated from δ^{18}Oc, TΔ47 and Kim and O'Neil equation

Table B-3: Climate and environmental parameters for Holocene soil carbonate samples

Sample	texture of soil matrix	MAT	MWST	Carbonate Type	Primary Season of Precipitation
'GONJQ-305-1'	fine	28.7	32.1	pendant	'summer'
'GON07-4.7-1'	medium	29	32.5	pendant	'summer'
'K2002-MAR-103-1'	-	19	20.2	pendant	'unknown'
'CN2008-DM-164-120cm-1'	coarse	4.6	19.4	nodule	'spring'
'CA08-BHS-001.1'	coarse	15	25.4	nodule	'winter'
'CA08-BHS-002.1'	coarse	15	25.4	nodule	'winter'
'CA08-BHS-003.1'	coarse	15	25.4	nodule	'winter'
'CA08-BHS-004.1'	coarse	15	25.4	nodule	'winter'
'CA08-BHS-005.1'	coarse	15	25.4	nodule	'winter'
'H-70'	coarse	11	20	pendant	'summer'
'H-90'	coarse	11	20	pendant	'summer'
'H-110'	coarse	11	20	pendant	'summer'
'H-130'	coarse	11	20	pendant	'summer'
'H-150'	coarse	11	20	pendant	'summer'
'NE11-C2'	-	9	21	-	'summer'
'WY11-C5'	-	5	17	pendant	'summer'
'WY11-C9'	-	6	18	pendant	'summer'
'WY11-C10'	-	-2	9	pendant	'summer'
'WY11-C12'	-	8	20	pendant	'summer'
'WY11-C19'	-	2	13	pendant	'summer'
'WY11-C20'	-	3	15	pendant	'summer'
'NE11-C24'	-	9	22	pendant	'summer'
'D2-20'	medium	15	23	pendant	'summer'
'D2-50'	medium	15	23	pendant	'summer'
'D2-100'	medium	15	23	pendant	'summer'
'RM1333-11-60'	-	14	22	pendant	'summer'
'MODS07-03'	very coarse	13	20	pendant	'summer'
'C10'	very coarse	13	20	pendant	'summer'
'C35'	very coarse	13	20	pendant	'summer'
'C47'	very coarse	13	20	pendant	'summer'
'C50'	very coarse	13	20	pendant	'summer'
'C85'	very coarse	13	20	pendant	'summer'

'C100'	very coarse	13	20	pendant	'summer'
'RM1695-11-60'	-	13	20	pendant	'summer'
'RM1647-11-60'	-	12	18	pendant	'summer'
'MODS07-05'	coarse	12	18	pendant	'summer'
'MODS07-06'	-	11	17	pendant	'winter'
'A10'	-	11	16	pendant	'winter'
'A20'	coarse	11	16	pendant	'winter'
'A30'	coarse	11	16	pendant	'winter'
'A50'	coarse	11	16	pendant	'winter'
'A74A'	coarse	11	16	pendant	'winter'
'A75B'	coarse	11	16	pendant	'winter'
'A901'	coarse	11	16	pendant	'winter'
'A902'	coarse	11	16	pendant	'winter'
'A100U'	coarse	11	16	pendant	'winter'
'MODS07-07'	-	11	16	pendant	'winter'
'MODS07-10'	very coarse	10	15	pendant	'winter'
'B15'	medium	8	12	pendant	'winter'
'B30'	medium	8	12	pendant	'winter'
'B45'	medium	8	12	pendant	'winter'
'B65'	medium	8	12	pendant	'winter'
'B80'	medium	8	12	pendant	'winter'
'B100'	medium	8	12	pendant	'winter'
'MODS07-08B'	medium	8	12	pendant	'winter'
'Kranzburg'	fine	6	20	nodule	'summer'
'Clamo'	fine	9	22	nodule	'summer'
'Plughat-1'	fine	10	22	nodule	'summer'
'Plughat-2'	fine	10	22	nodule	'summer'
'Montecito'	medium	9	20	nodule	'summer'
'Witt'	fine	11	20	nodule	'summer'
'Cornville'	medium	17	27	nodule	'summer'
'Guvo'	coarse	22	32	nodule	'summer'
'Cross-Apache'	medium	13	22	nodule	'summer'
'Lavic'	medium	16	25	nodule	'winter'
'Muroc'	medium	17	27	nodule	'winter'
'CAN01-10'	coarse	18	25	pendant	'summer'
'CAN01-25'	coarse	18	25	pendant	'summer'
'CAN01-40'	coarse	18	25	pendant	'summer'

'CAN01-55'	coarse	18	25	pendant	'summer'
'CAN01-70'	coarse	18	25	pendant	'summer'
'CAN01-100'	coarse	18	25	pendant	'summer'
'CAN02-10'	very coarse	17	25	pendant	'summer'
'CAN02-25'	very coarse	17	25	pendant	'summer'
'CAN02-40'	very coarse	17	25	pendant	'summer'
'CAN02-55'	very coarse	17	25	pendant	'summer'
'CAN02-70'	very coarse	17	25	pendant	'summer'
'CAN02-85'	very coarse	17	25	pendant	'summer'
'CAN02-100'	very coarse	17	25	pendant	'summer'
'CAN03'	very coarse	17	25	pendant	'summer'
'DL01-20'	coarse	17	25	pendant	'summer'
'DL01-40'	coarse	17	25	pendant	'summer'
'DL01-70'	coarse	17	25	pendant	'summer'
'DL01-100'	coarse	17	25	pendant	'summer'
'NAC-30'	medium	17	25	pendant	'summer'
'NAC-50'	medium	17	25	pendant	'summer'
'NAC-85'	medium	17	25	pendant	'summer'
'NAC-100'	medium	17	25	pendant	'summer'
'Elq13-400-70'	coarse	14.4	18.2	pendant	'winter'
'Elq13-400-95'	coarse	14.4	18.2	pendant	'winter'
'Elq13-600-50'	-	15	19	pendant	'winter'
'Elq13-850-50'	-	15	19	pendant	'winter'
'Eql13-1300-20'	very coarse	15	20	pendant	'winter'
'Eql13-1300-40'	very coarse	15	20	pendant	'winter'
'Elq13-1300-60'	very coarse	15	20	pendant	'winter'
'Elq13-1300-80'	very coarse	15	20	pendant	'winter'
'Elq13-1300-100'	very coarse	15	20	pendant	'winter'
'Elq13-1500-50'	coarse	16	20	pendant	'winter'
'Elq13-1700-50'	-	16	21	pendant	'winter'
'Elq13-1924-20'	very coarse	16	21	pendant	'winter'
'Elq13-1924-40'	very coarse	16	21	pendant	'winter'
'Elq13-1924-60'	very coarse	16	21	pendant	'winter'
'Elq13-1924-80'	very coarse	16	21	pendant	'winter'
'Elq13-1924-100'	very coarse	16	21	pendant	'winter'
'Elq13-2100-50'	-	15	20	pendant	'winter'
'Elq13-2300-50'	very coarse	13	19	pendant	'winter'
'Elq13-2700-20'	very coarse	10.7	16.4	pendant	'winter'

'Elq13-2700-40'	very coarse	10.7	16.4	pendant	'winter'
'Elq13-2700-60'	very coarse	10.7	16.4	pendant	'winter'
'Elq13-2700-80'	very coarse	10.7	16.4	pendant	'winter'
'Elq13-2700-100'	very coarse	10.7	16.4	pendant	'winter'
'Elq13-3300-50'	very coarse	5	11	pendant	'winter'
'Elq13-3550-20'	coarse	3.7	9.7	pendant	'winter'
'Elq13-3550-40'	coarse	3.7	9.7	pendant	'winter'
'Elq13-3550-60'	coarse	3.7	9.7	pendant	'winter'
'Elq13-3550-80'	coarse	3.7	9.7	pendant	'winter'
'Elq13-3550-100'	coarse	3.7	9.7	pendant	'winter'
'Elq13-3750-50'	-	1	7	pendant	'winter'
'Elq13-4200-50'	-	-3	3	pendant	'winter'
'Elq13-4500-50'	-	-6	1	pendant	'winter'
'Tsangpo-19a'	medium	4	14	pendant	'summer'
'Tsangpo-19b'	medium	4	14	pendant	'summer'
'Tsangpo-21a'	medium	7	15	pendant	'summer'
'Tsangpo-21b'	medium	7	15	pendant	'summer'
'Tsangpo-22'	medium	7	15	pendant	'summer'
'Lhasa-4'	medium	9	16	pendant	'summer'
'Cannes-62'	medium	-3	7	pendant	'winter'

Table B-4: Clumped Isotope Temperature Calibrations Used

Study	Analytical Lab	Reaction Temperature (°C)	Original T-Δ47 Calibration	Original AFF used	Updated T-Δ47 Calibration	Updated AFF used in calculating temperature	Updated AFF to project to 25 °C RF*
Passey et al. 2010	Caltech	90	Ghosh 2006 pre-ARF (1)	0.081	NA	NA	NA
Quade et al. 2013	Caltech	25	Ghosh 2006 post -ARF (2)	NA	NA	NA	NA
Peters et al. 2014	Caltech	25 & 90	Ghosh 2006 pre-ARF (1)	NA	NA	NA	NA
Hough et al. 2014	Johns Hopkins University	90	Ghosh 2006 post-ARF (2)	NA	JHU Brand (6)	0.088	0.088
Gallagher & Sheldon 2016	University of Michigan	75	Defliese et al. (2015) eq 6, a compilation of synthetic samples reacted at >70 °C (3)	0.067	UM Brand (7)	0.072	0.072
Ringham et al. 2016	University of Washington	90	Kluge et al. (2015) eq 5 (4)	NA	Kelson et al. 2017 (5)	NA	0.088
Burgener et al. 2016	University of Washington	90	Kluge et al. (2015) eq 5 (4)	NA	Kelson et al. 2017 (5)	NA	0.088
Burgener et al. 2018	University of Washington	90	Kelson et al. 2017 (5)	NA	Kelson et al. 2017 (5)	NA	0.088

*Acid digestion correction values from Petersen et al. (2019)

(1) Ghosh pre-ARF calibration, m = 0.0592 * 1e6, b = -0.02 (in 25C RF) (Ghosh et al. 2006)

(2) Ghosh post-CDES calibration, m = 0.0636, b = -0.0047 (in 25C RF) (Dennis et al. 2011 equation 9)

(3) Defliese et al. (2015) > 70 °C acid rxn compilation, m = 0.03712, b= 0.2784 (in 25C RF) (Defliese et al. 2015 eq 6)

(4) Kluge et al. (2015) 90 °C acid rxn only, m = -=0.0405, b = 0.167 (in 90C RF) (Kluge et al. 2015 equation 5)

(5) Kelson et al. (2017), m = 0.0417, b = 0.139 (in 90C RF) (Kelson et al. 2017 equation 1)

(6) JHU Brand updated (Passey & Henkes 2010 /Henkes 2013 combination), m = 0.0379, b = 0.263 (in 25C RF)

(Petersen et al. (2019) Supplementary Table S5)

(7) UM Brand updated (Defliese/Winkelstern combination), m = 0.0372, b= 0.254 (in 25C RF)

(Petersen et al. (2019) Supplementary Table S5)

Appendix C. Supplementary materials to Chapter 4

C.1 Testing HYDRUS-1D skill: comparing predicted and measured soil temperature and water content

HYDRUS has been used extensively, with success, to predict soil temperatures and water contents at specific locations (Chen et al., 2014; e.g., Radcliffe and Šimůnek, 2010; Sándor and Fodor, 2012; Šimůnek et al., 2012). While the primary goal of this study is not to model a specific location, we compare model predictions of soil temperatures and soil moistures to the measurements at Adams Ranch from 2011-2015.

First, we test which measured temperature (air vs. near-surface soil) is most appropriate to use for the time-varying boundary condition of temperature at the top of the simulated soil profile (measured temperatures in Figure C-1). When forcing the numerical simulation with measured air temperature as the surface boundary condition, the predicted soil temperature differs from the measured temperature by -10 to 5 °C (Figure C-2). The inaccuracy in temperature is especially pronounced in the summer, when HYDRUS predicts soil temperatures that are colder than those measured. This underestimate of soil temperature is likely because HYDRUS does not consider radiative heating (Burgener et al., 2019; Cermak et al., 2017; Passey et al., 2010). At the Adams Ranch station, the measured air temperature is about 5–10°C colder than measured soil temperature for summer months (Figure C-1). This underestimate of soil temperatures could result in an underestimate in the total amount of calcite precipitation. We observe more accurate soil temperatures when we force the model with the measured near-

surface soil temperatures (thermistor at 5 cm in depth). With this parameterization, the model predicts soil temperature at all depths to within ~2–3 °C (Figure C-3).

Next, we consider how well the model is able to predict soil water content. We force the model simulations with daily precipitation amounts as measured from a rain gauge. During rain events, potential evapotranspiration is set to equal 0 to ensure that rain enters the soil column (as in Meyers et al., 2014). Surface run-off is not considered. Because of these factors, we would expect the model to overestimate water content in the soil. Indeed, the model overestimates water content by a baseline of ~0.05, and up to 0.15 during rain events (Figure C-4). However, the model captures changes in water content that occur in response to rain events.

Altogether, our test of model skill is promising, considering that we only minimally tuned the model to fit the specific location. We are not including important environmental parameters like snowpack, layered soil materials, surface run off/ surface water ponding, site-specific vegetation, kinetic calcite precipitation and hysteresis– parameters which can be explicitly considered in HYDRUS-1D, but we choose to exclude for the purposes of this study. As is, the minimally-tuned Adams Ranch simulation captures major patterns and changes in temperature and soil moisture (Figure C-3, Figure C-4). We believe that this level of model skill is sufficient to allow us to test the first-order sensitivity of carbonate accumulation to various precipitation regimes.

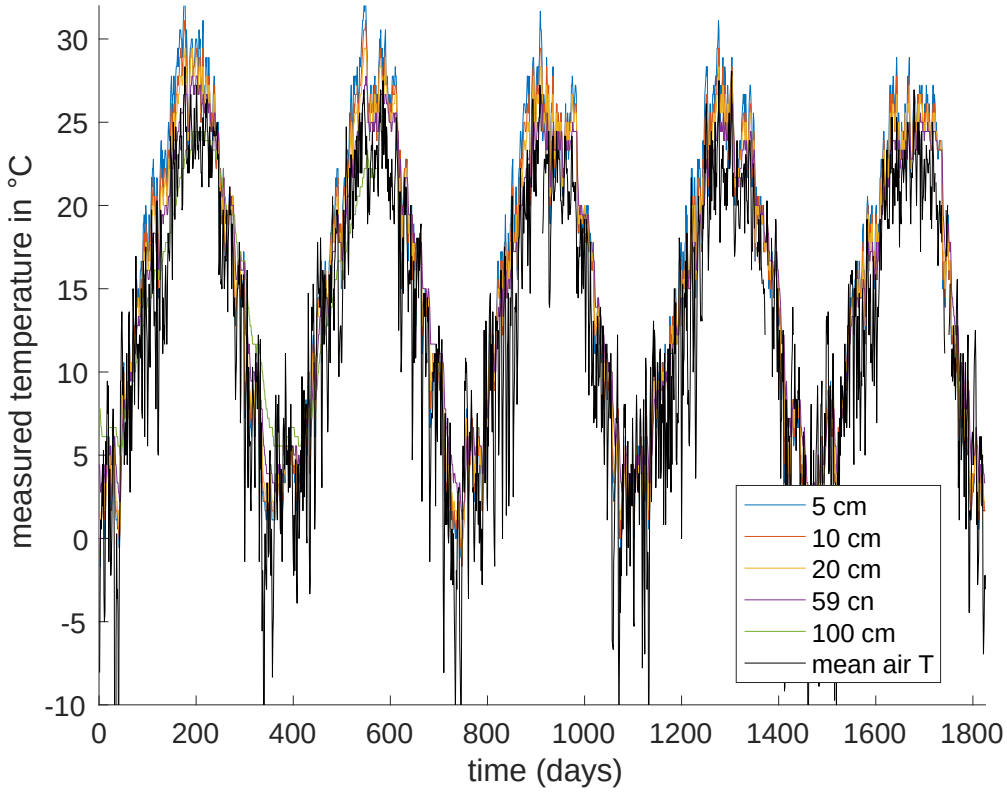

Figure C-1: Measured soil and air temperatures at Adams Ranch 2011-2015

Soil temperature at various depths (colors) and mean air temperature (black) measured at the SCAN station (https://wcc.sc.egov.usda.gov/nwcc/site?sitenum=2015).

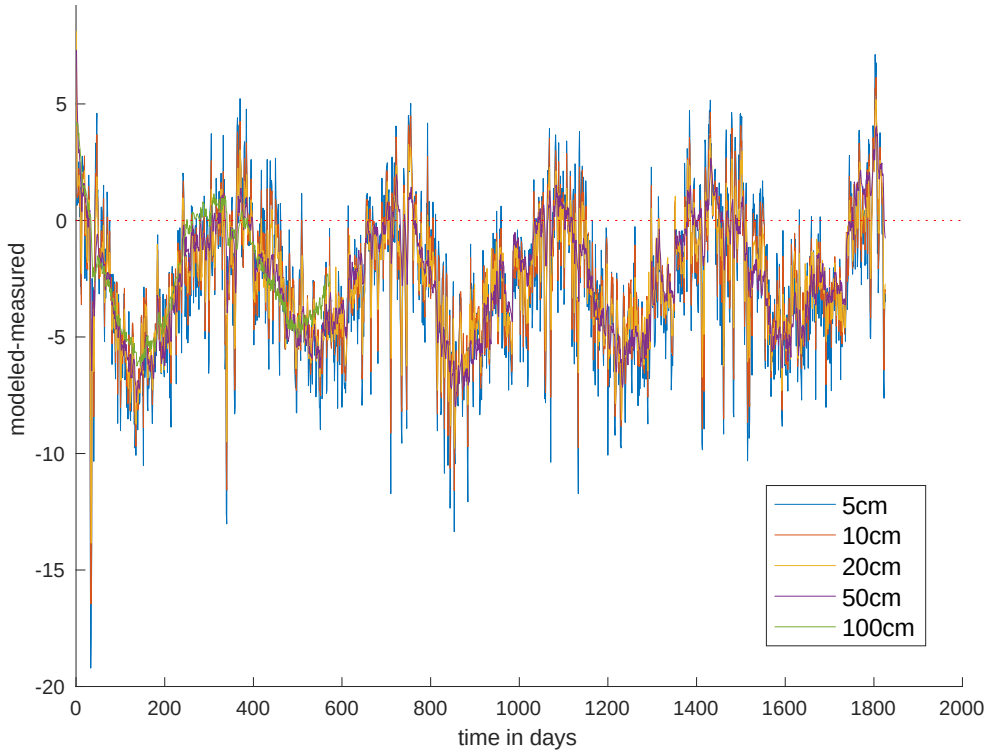

Figure C-2: Difference between measured and HYDRUS-simulated soil temperatures, v1

Soil temperatures measured at Adams Ranch SCAN station. HYDRUS soil temperatures simulated using measured air temperature (daily mean) as the time-varying boundary condition at the simulated soil surface. Each colored line is the model-measured difference at the given depth in the soil profile.

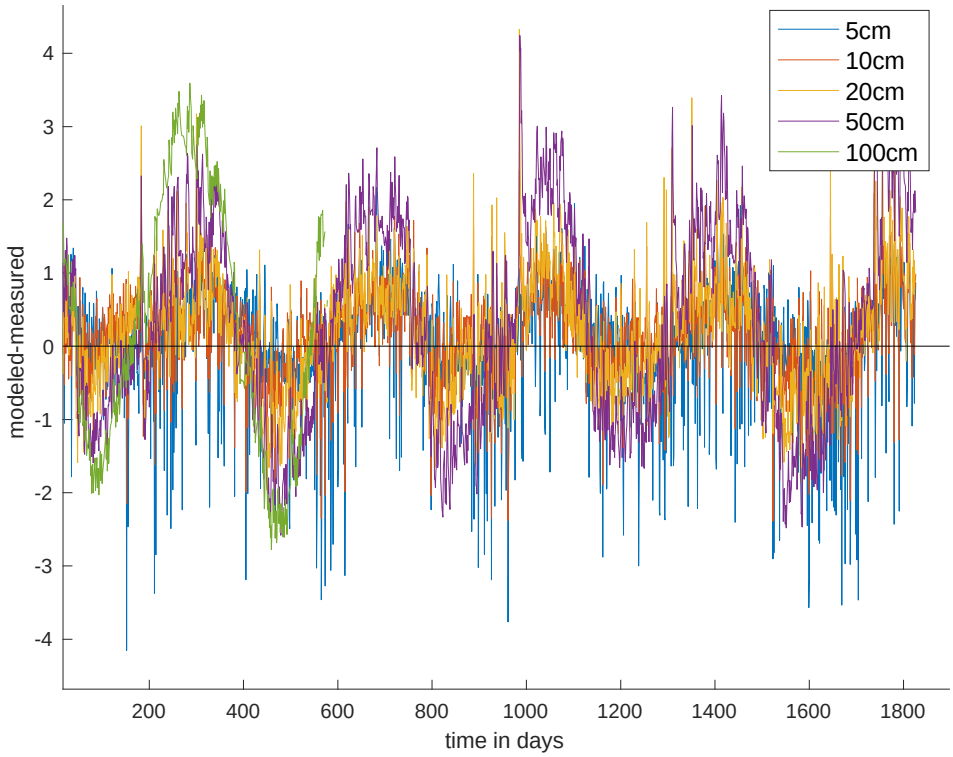

Figure C-3: Difference between measured and HYDRUS-simulated soil temperatures, v2

Soil temperatures measured at Adams Ranch SCAN station. HYDRUS soil temperatures simulated using measured 5-cm soil temperature as the time-varying boundary condition at the simulated soil surface. Each colored line is the model-measured difference at the given depth in the soil profile.

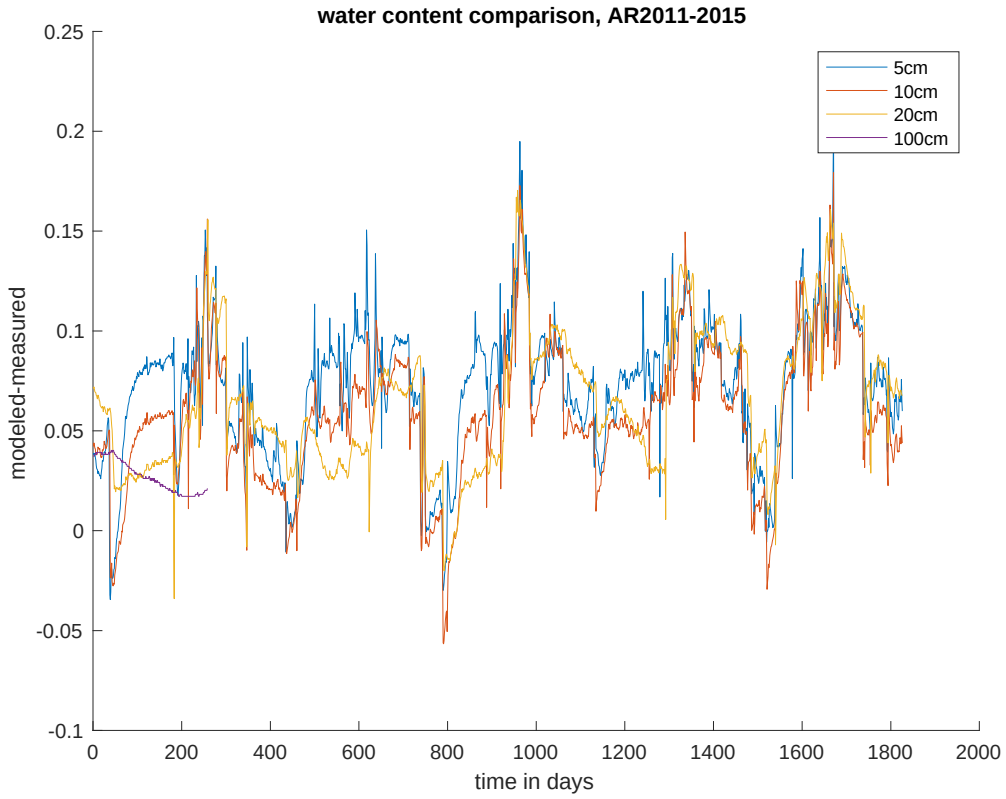

Figure C-4: Difference between measured and HYDRUS-simulated soil water content

Soil water contents measured at Adams Ranch SCAN station. HYDRUS water contents are simulated using daily precipitation as the input and the measured 5-cm soil temperature as the time-varying boundary condition at the simulated soil surface. Each colored line is the model-measured difference at the given depth in the soil profile.

Appendix D. Supplementary materials to Chapter 4

D.1 Description of Breakpoint Analysis

In this supplemental text, we provide additional analyses that support breaking the clumped isotope temperature record at the Paleocene-Eocene boundary and discuss the results of performing a moving average on the clumped isotope data. We use a piecewise constant function with a single break point to model the data. For each gap between two sample ages (a breakpoint), we divide the samples into two groups: one group of consisting of the samples that are older than the breakpoint, and the other group consisting of the samples that are younger than the breakpoint. Then, we find the mean value of the data in each of the two groups and calculate the total root mean square (RMS) misfit. We perform this statistical analysis using both: 1) the means of each carbonate sample, and 2) the individual replicate analyses for each carbonate sample, at each possible breakpoint. The RMS is calculated using the following formulation:

$$\sqrt{\sum_{i=1}^{n}(y_i - \hat{y}_i)^2/n}$$

Where $\hat{y}$ is the expected value (mean(young) or mean(old)) and n is the total number of samples. For $T\Delta_{47}$, the minimum RMS occurs using a breakpoint that separates the carbonate samples at 56.4 and 56.9 Ma, and the RMS between 56.4 and 55.9 is within 10% of the true minimum (Figure D-5). Both of those breakpoints produce groups with means that are statistically different in a *t*-test (p values range from $1e^{-4}$ to 0.01). This analysis supports dividing the samples between 55.8 Ma and 56.9 Ma, while the sample that is 56.4 Ma in age (BB10-019) could be placed in either the old (Paleocene) or the young (Eocene) group. Including/excluding this sample in either of the groups changes the means by <0.5 °C, which is less than our reported error. In the main text, we choose to divide the temperature record at 56 Ma, which is consistent with our results

from the breakpoint analysis and agrees with the reported age for the onset of the PETM from a recent astronomical calibration (55.930 ± 0.05 Ma, from Westerhold et al., 2015). The nodule BB10-019 (56.4 Ma) is thus included in the older/Paleocene group.

For $\delta^{18}O_w$, the minimum RMS occurs using a breakpoint that separates the carbonate samples at 58.4 and 59.7 Ma (Figure D-6). This breakpoint produces groups with means that are statistically different in a *t*-test (p value of 0.00004). In the main text, we divide the $\delta^{18}O_w$ record at 59 Ma.

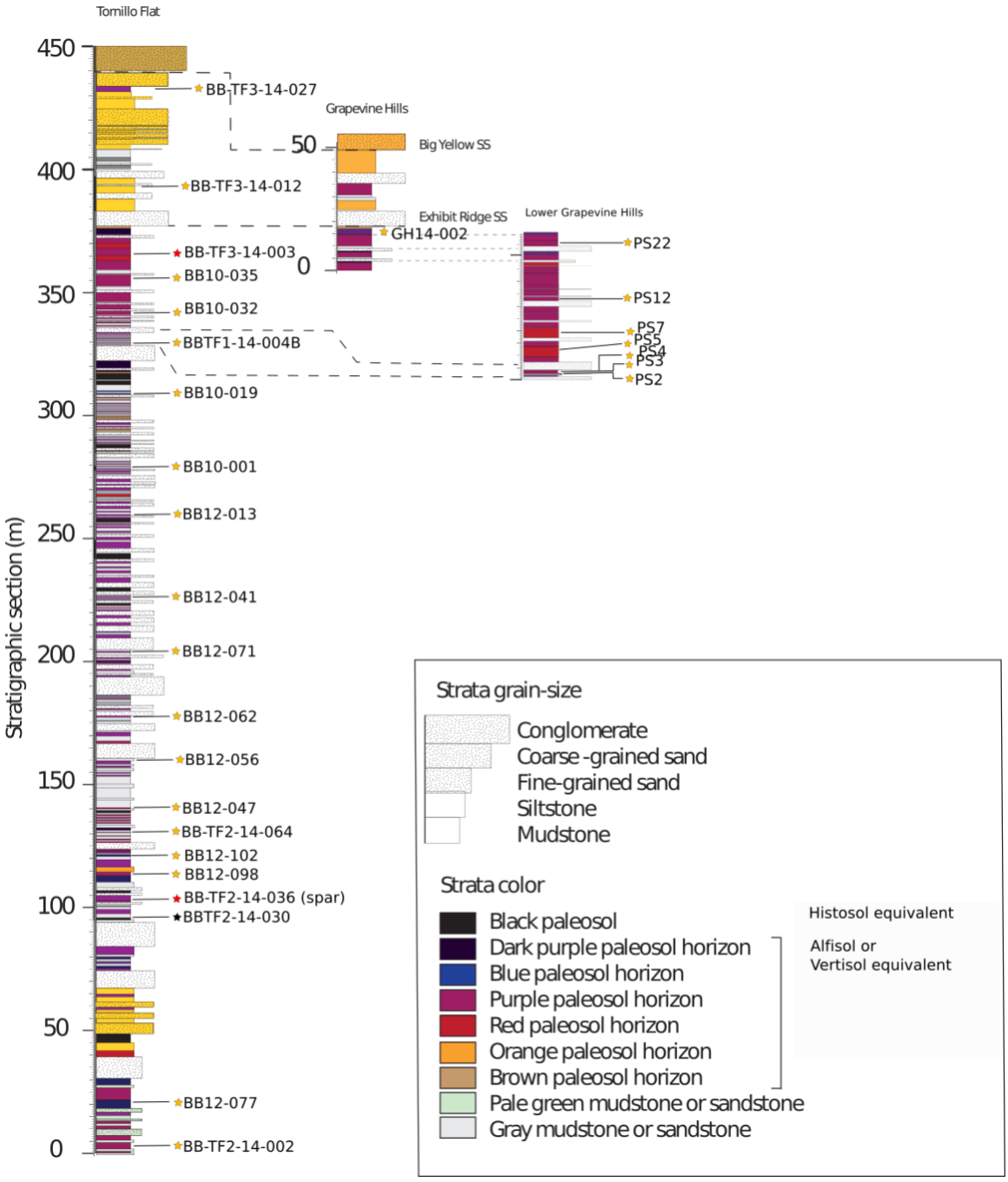

Figure D-1: Stratigraphic correlation between Tornillo Flats and Grapevine Hills

Stars indicate level of carbonate nodule collection; yellow indicates nodules that were sampled for micrite, red indicates nodules that were sampled for spar, and black indicates the carbonate nodule from a black paleosol.

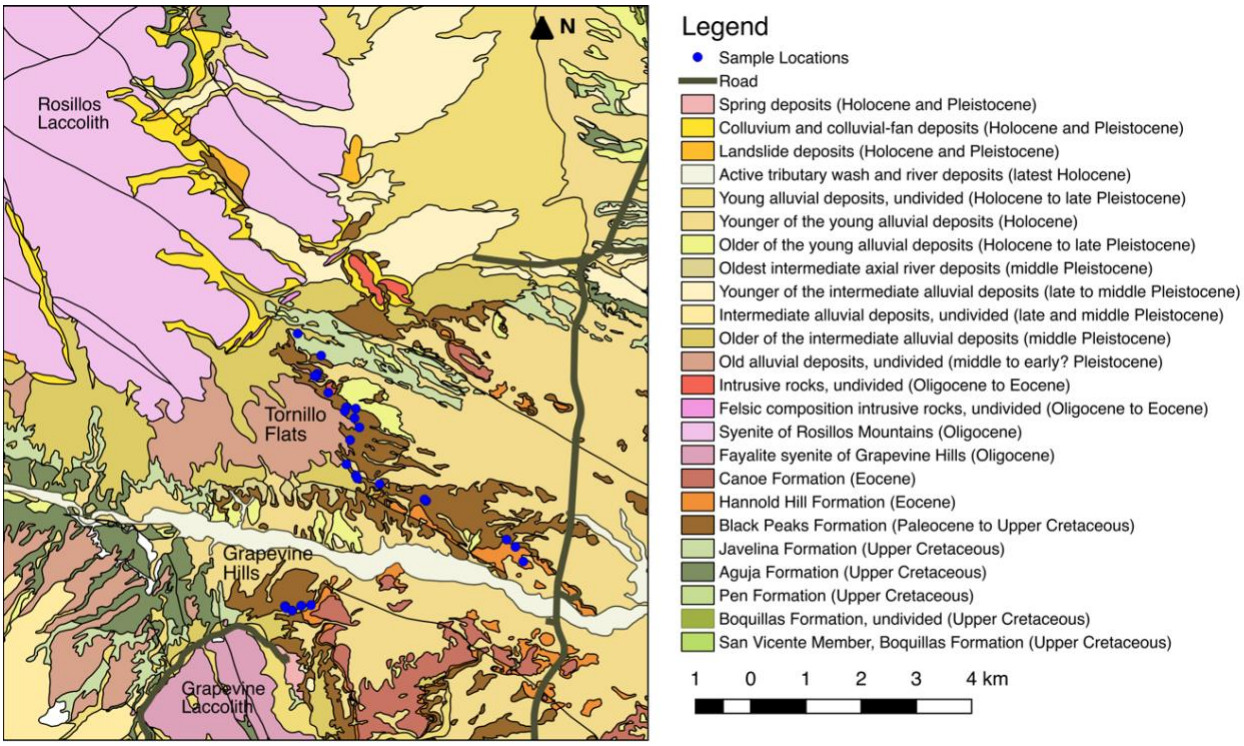

Figure D-2: Locations of the samples collected at Tornillo Flats and Grapevine Hills. Geology from Turner et al. (2011). Latitude, longitude, and stratigraphic section for each sample can be found Table D-1.

PS2 Bk nodule

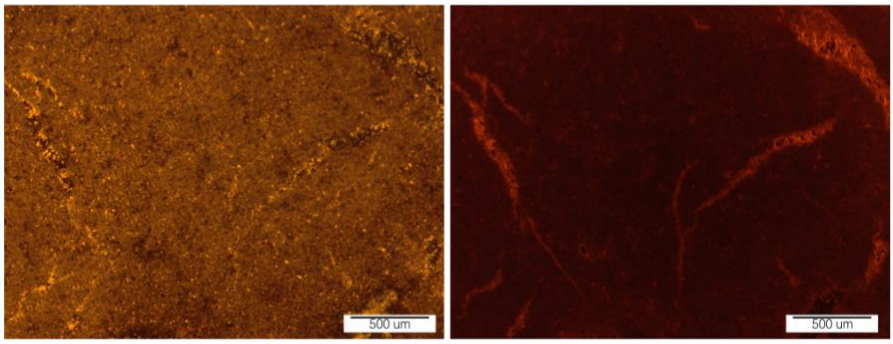

plane light cathodoluminescent

PS4 Bk nodule

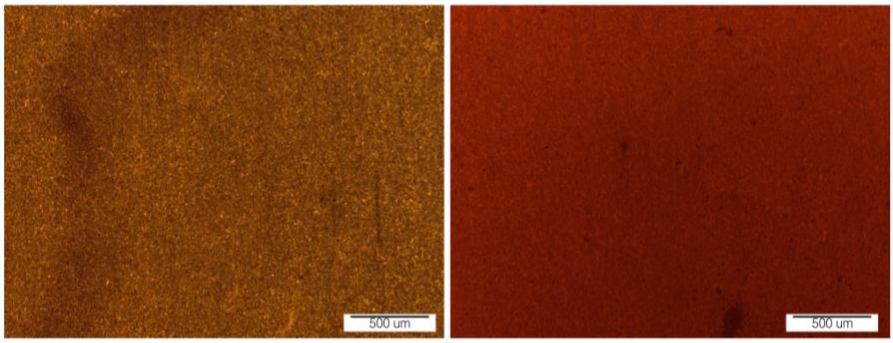

plane light cathodoluminescent

PS5 Bk

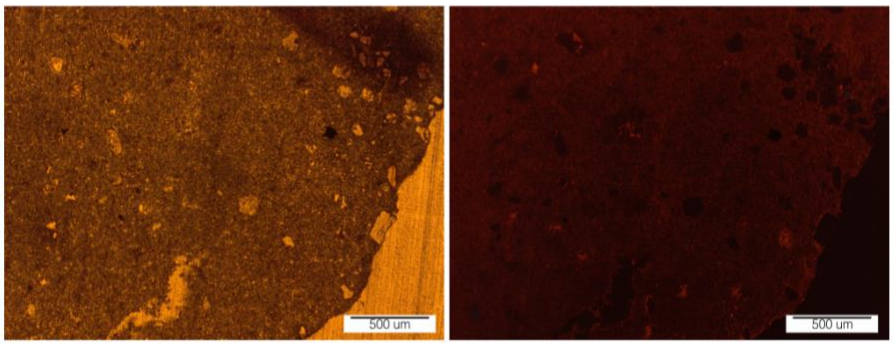

plane light cathodoluminescent

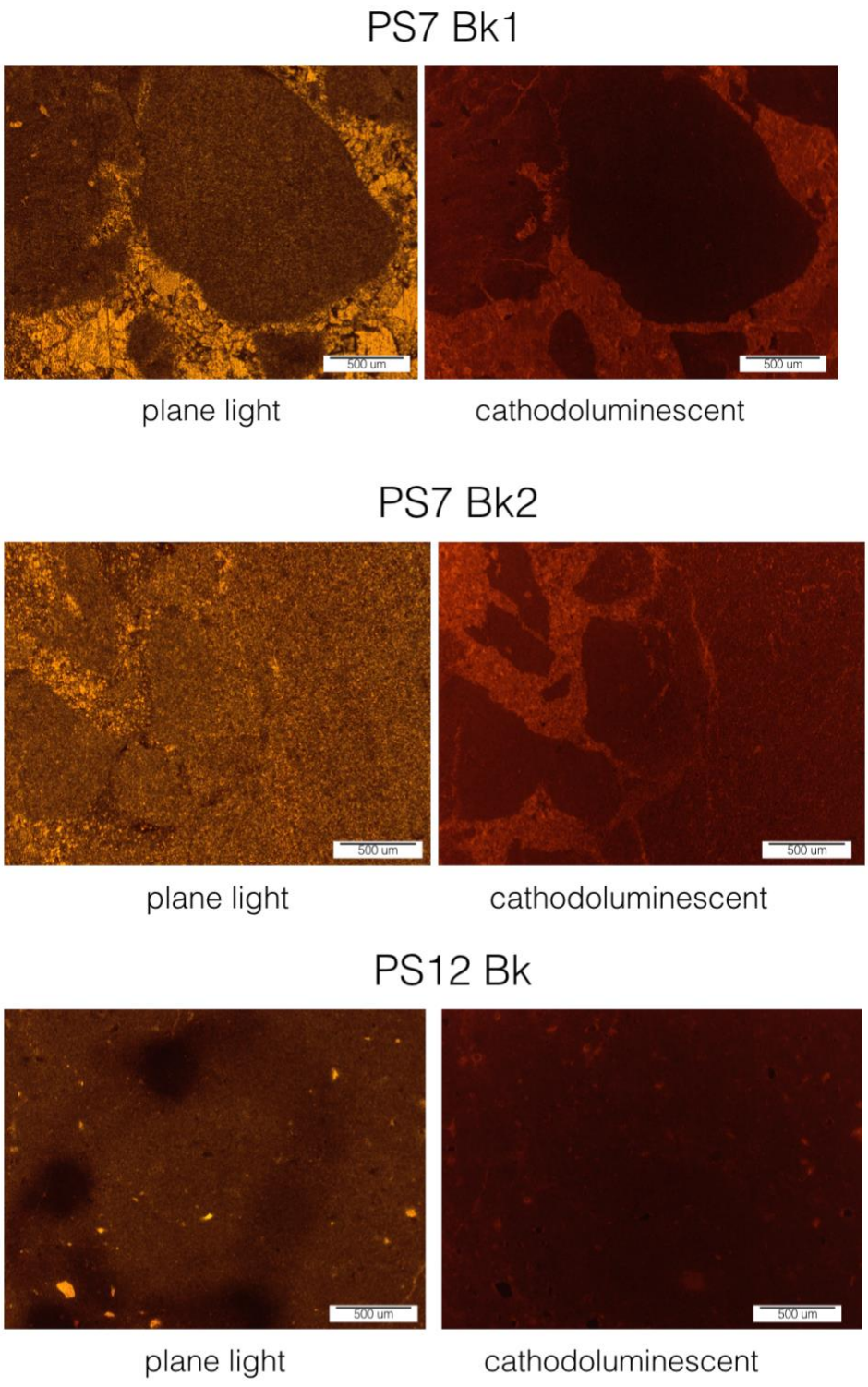

Figure D-3: Plane and cathodoluminescent light thin sections of the Grapevine Hills samples.

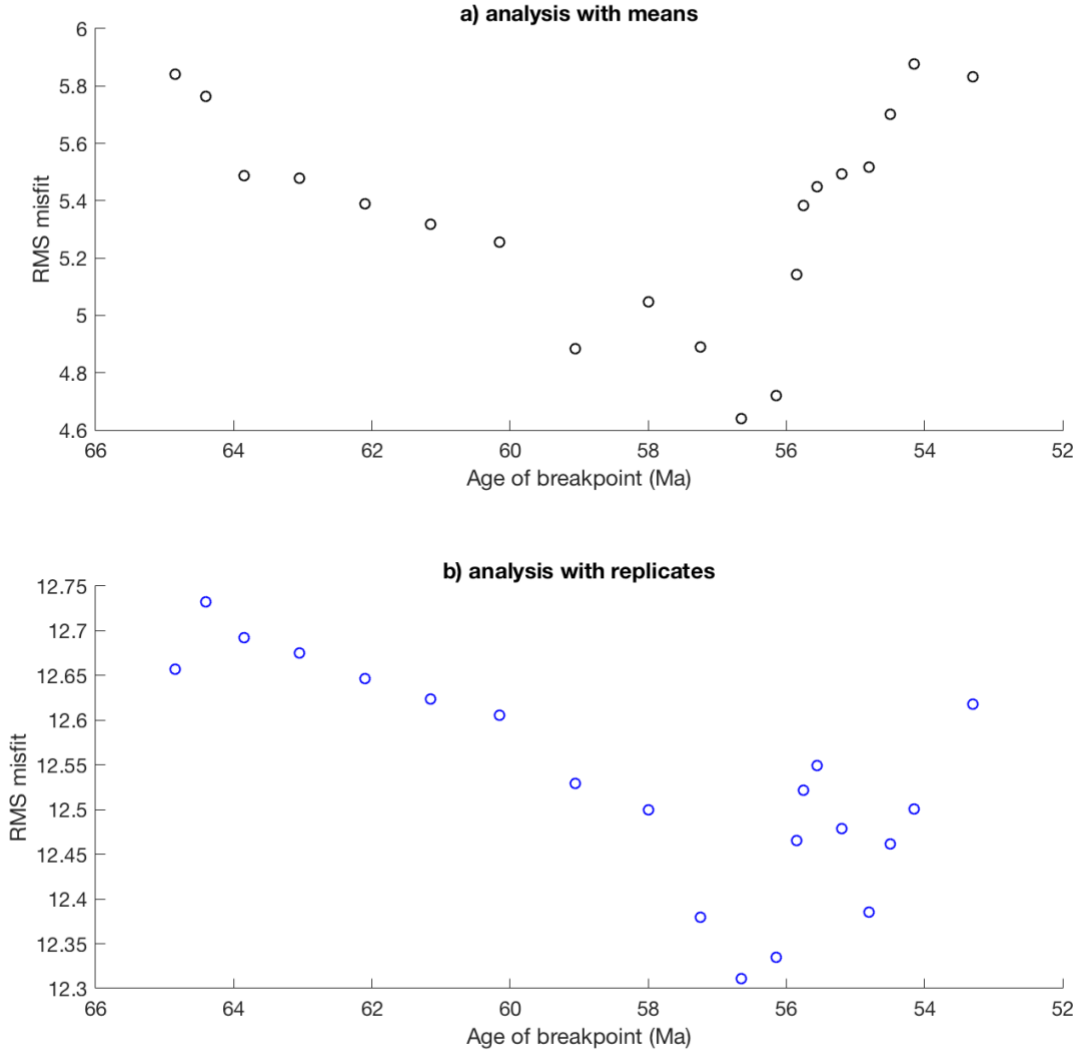

Figure D-4: RMS misfit for breakpoint analysis of $T\Delta_{47}$ record.

For $T\Delta_{47}$, we show RMS misfit calculated using the means of each carbonate sample (top) and the individual replicates (bottom). The minimum occurs at ~56 Ma.

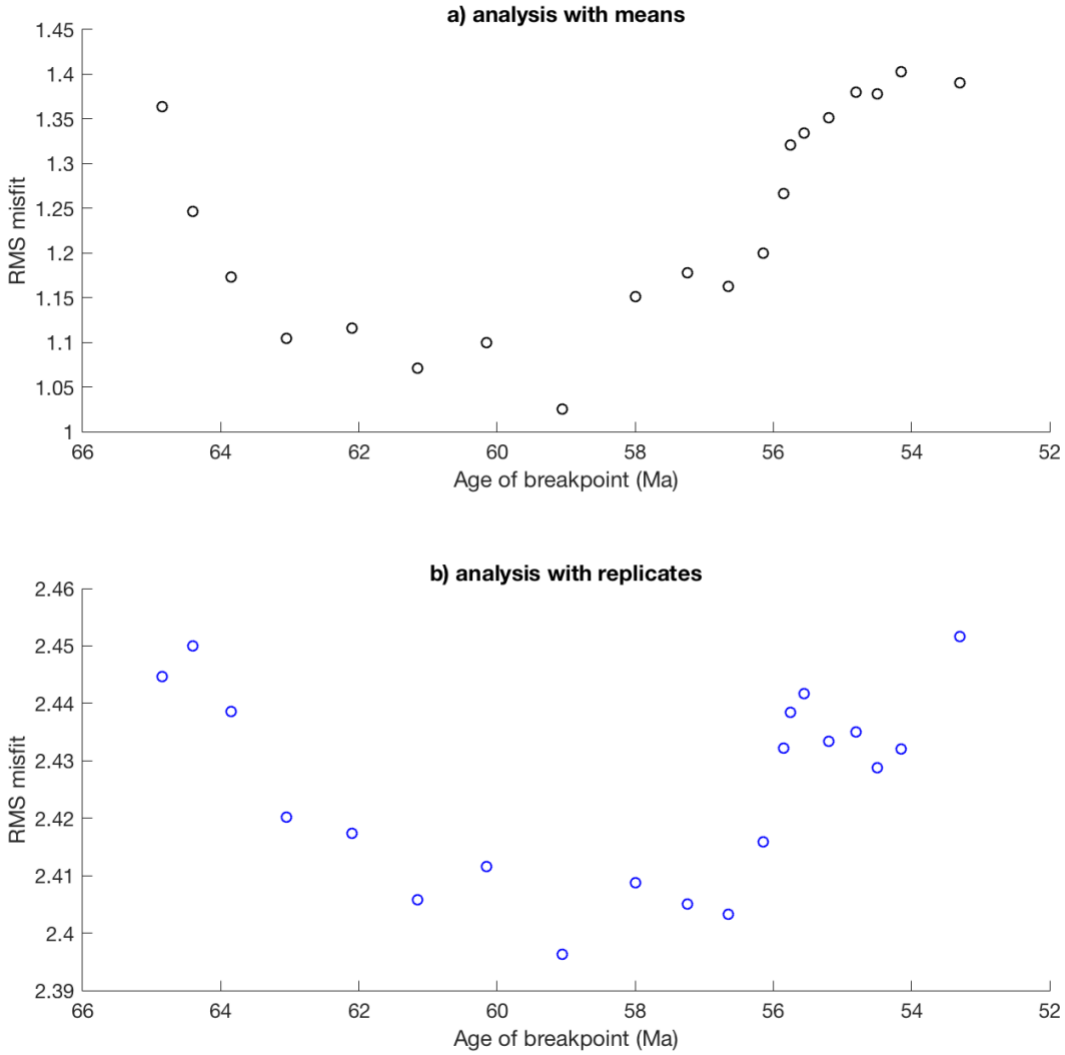

Figure D-5: RMS misfit for breakpoint analysis of $\delta^{18}O_w$ record.

For $\delta^{18}O_w$, we show RMS misfit calculated using the means of each carbonate sample (top) and the individual replicates (bottom). The minimum occurs at ~59 Ma. Breaking the record at ~56 Ma results in a 13% or a 0.28% increase in RMS misfit error (for analysis with means and replicates, respectively).

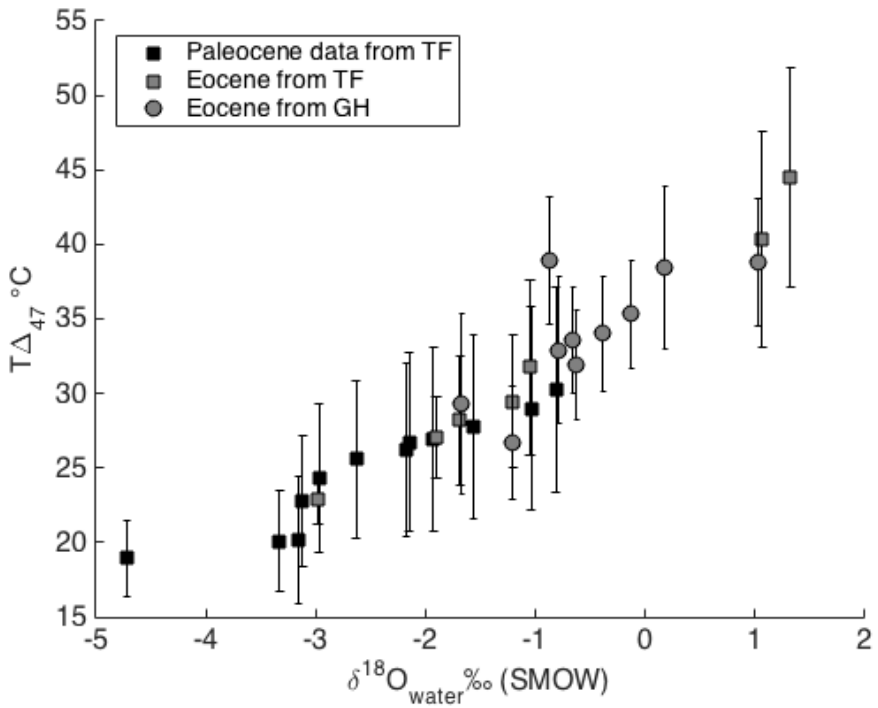

Figure D-6: $\delta^{18}O_w$ versus TΔ_{47} for soil carbonate samples from the Tornillo Basin. Squares denote samples from the Tornillo Flats (TF) section, circles denote samples from the Grapevine Hills section (GH). Samples that are older than 56 Ma are in black and samples that are younger than 56 Ma are plotted in gray.

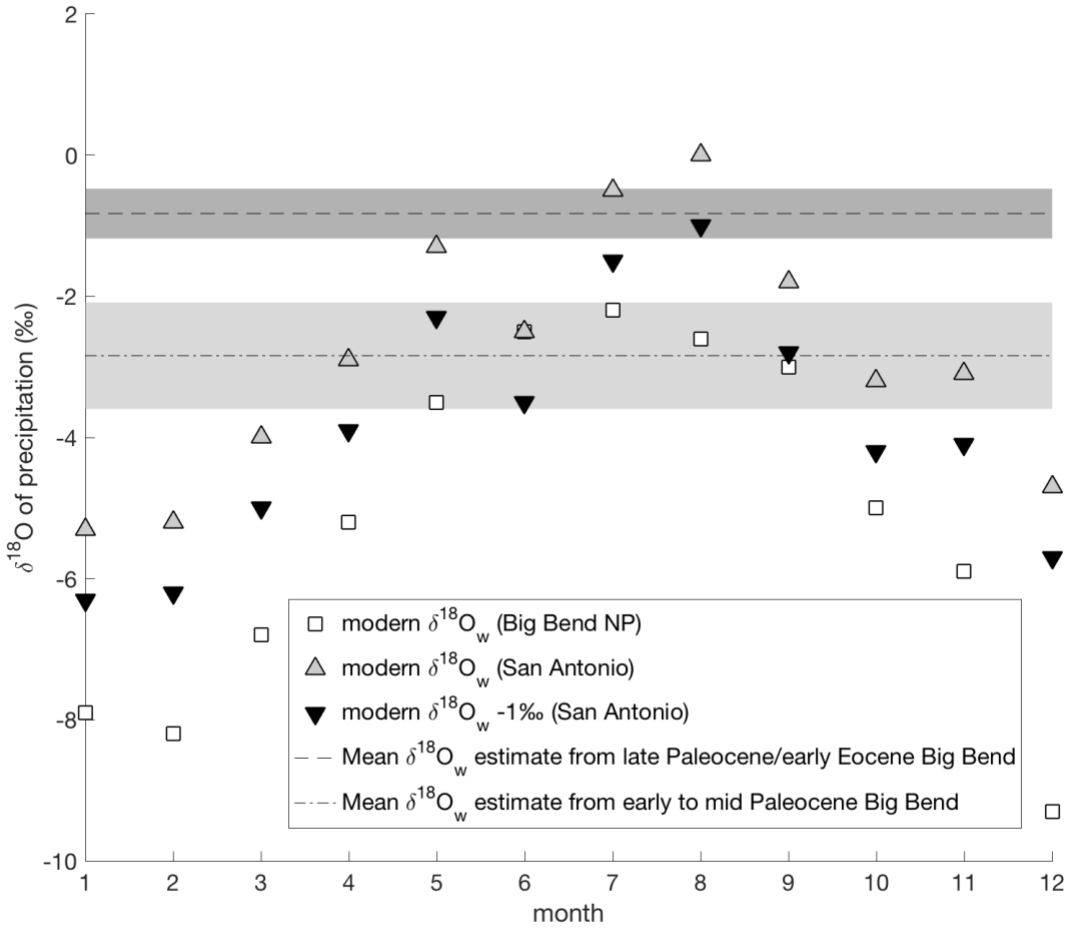

Figure D-7: $\delta^{18}O$ of modern rainfall compared to the mean calculated $\delta^{18}O_w$.

The $\delta^{18}O$ of modern rainfall from the Oxygen Isotopes in Precipitation Calculator. The mean calculated $\delta^{18}O_w$ is shown for the early to mid-Paleocene (69 to 59 Ma) and the late Paleocene to Early Eocene (59 to 54 Ma); this mean is shown as lines with the 95% confidence intervals of the mean shaded around the line. We show the modern $\delta^{18}O$ rainfall at San Antonio (TX), because San Antonio is at the same latitude but better approximates the Paleogene near-sea level elevation and the reconstructed distance between Big Bend and the early Paleogene coastline (Galloway et al., 2011). We adjust modern San Antonio $\delta^{18}O$ values by -1‰ in our comparison to account for an ice-free Paleocene/Eocene ocean (e.g., Tindall et al., 2010).

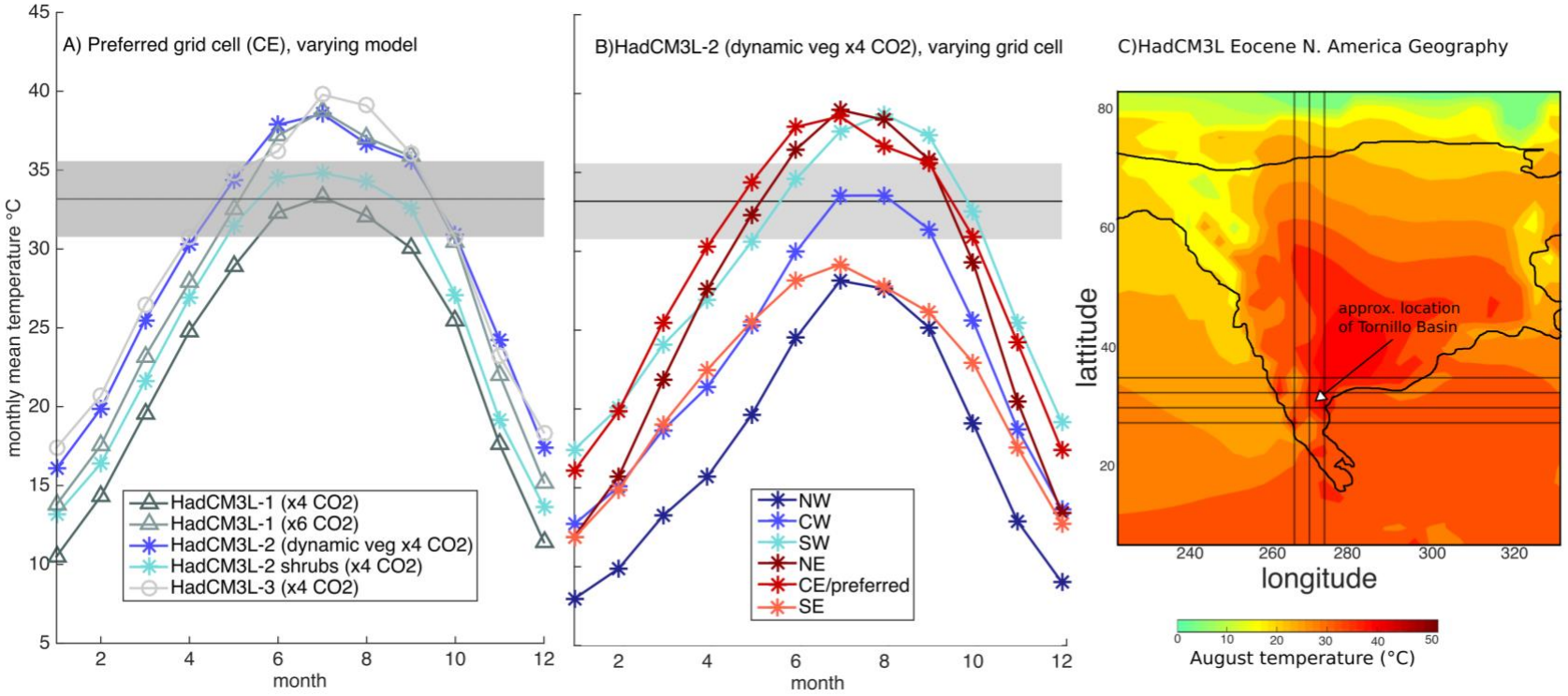

Figure D-8: HADCM3L predictions for surface temperature with Eocene configurations

HADCM3L model predictions from Lunt et al., (2010), Loptson et al., (2014), and Lunt et al., (2017). **a)** At the grid cell that most resembles the paleo-location of Tornillo Basin, the temperature predicted varies by 6 °C. **b)** For a single model at the grid cells near Big Bend, the temperature predicted varies by 13 °C (S = South, N = North, C= Center, E = East, W = West). **c)** Example output of the surface temperature in August for North America. The arrow points to the grid cell that most resembles the paleo-location (CE) of Tornillo Basin.

Table D-1: Tornillo Basin soil carbonate sample locations

Sample_ID	Latitude	Longitude	Section
BB-TF2-14-002	29.46413	-103.1851	TF
BB12-077	29.46825	-103.18947	TF
BB-TF2-14-030	29.46076	-103.18581	TF
BB-TF2-14-036	29.46029	-103.18599	TF
BB12-098	29.46033	-103.1863	TF
BB12-102	29.457225	-103.18376	TF
BB-TF2-14-064	29.45426	-103.17863	TF
BB12-047	29.4545	-103.18043	TF
BB12-056	29.4538	-103.18068	TF
BB12-062	29.45247	-103.17887	TF
BB12-071	29.45075	-103.17795	TF
BB12-041	29.4484	-103.1797	TF
BB12-013	29.44388	-103.18038	TF
BB10-001	29.4418	-103.17862	TF
BB10-011	29.44124	-103.17835	TF
BB10-019	29.4402	-103.17416	TF
BB-TF1-14-004B	29.43706	-103.16552	TF
BB10-032	29.4373	-103.16579	TF
BB10-035	29.4373	-103.16579	TF
BB-TF3-14-003	29.42984	-103.15048	TF
BB-TF3-14-012	29.42848	-103.14883	TF
BB-TF3-14-027	29.42575	-103.14737	TF
PS2-Bk	29.41744	-103.19181	GH
PS3-Bk	29.417417	-103.19186	GH
PS4-Bk	29.417039	-103.19161	GH
PS5-Bk	29.416601	-103.19048	GH
PS7-Bk	29.416601	-103.19048	GH
PS12-Bk	29.417493	-103.18881	GH
PS22-Bk	29.417493	-103.18881	GH
GH14-002	29.417615	-103.18699	GH